TECHNISCHE UNIVERSITÄT MÜNCHEN

Lehrstuhl für Methodik der Fernerkundung

Advanced Stacking Techniques and Applications in High Resolution SAR Interferometry

Kanika Goel

Vollständiger Abdruck der von der Ingenieurfakultät Bau Geo Umwelt der Technischen Universität München zur Erlangung des akademischen Grades eines

Doktor-Ingenieurs (Dr.-Ing.)

genehmigten Dissertation.

Vorsitzender: Univ.-Prof. Dr.-Ing. Uwe Stilla

Prüfer der Dissertation:

1. Univ.-Prof. Dr.-Ing. habil. Richard Bamler
2. Univ.-Prof. Dr.-Ing. Uwe Sörgel, TU Darmstadt
3. Prof.dr.ir. Ramon Hanssen, TU Delft, Niederlande

Die Dissertation wurde am 07.10.2013 bei der Technischen Universität München eingereicht und durch die Ingenieurfakultät Bau Geo Umwelt am 27.01.2014 angenommen.

Abstract

Interferometric Synthetic Aperture Radar (InSAR) is a satellite remote sensing technique that provides information about the topography and deformation of the Earth's surface. In recent years, InSAR's capabilities have been considerably improved with the launch of high resolution SAR satellites such as TerraSAR-X, TanDEM-X and COSMO-SkyMed. Mapping of urban areas and even single buildings is now facilitated via multitemporal InSAR techniques, for instance, Persistent Scatterer Interferometry (PSI) and SAR Tomography (TomoSAR). These methods exploit long-time coherent scatterers, e.g. the so-called Persistent Scatterers (PSs), and provide elevation and surface displacement measurements with a high precision.

However, the density of PSs is low in non-urban areas and it is imperative to increase the spatial density of measured points. Here, high-resolution SAR sensors offer new opportunities. For this purpose, in addition to the PSs, partially coherent Distributed Scatterers (DSs) can be exploited. Various methods such as the Small Baseline Subset Algorithm (SBAS) and SqueeSAR have been proposed to extract information from DSs. However, SBAS is prone to phase unwrapping errors in rural areas and estimates deformation at only low resolution. The alternative technique SqueeSAR can be computationally expensive as it processes all possible interferogram combinations.

Accordingly, this thesis addresses the development of advanced stacking techniques in high resolution SAR interferometry, with a focus on complex areas that are difficult to process using conventional techniques. To this end, first, a new method has been developed for deformation monitoring of DSs at object resolution in non-urban areas. It applies adaptive spatial filtering to improve the differential interferometric phase, followed by deformation estimation using an L1-norm based SBAS approach that is more robust to phase unwrapping errors. Second, an alternative approach for mean deformation velocity mapping of DSs has been proposed for highly decorrelated areas, wherein, wrapped interferograms (with small baselines) are directly used and the deformation velocity is mapped at a suitable object resolution. It includes identification of homogenous patches, estimation of deformation velocity gradients for these patches and then, model-based deformation integration to obtain spatially dense deformation velocity estimates. Lastly, a fusion of TerraSAR-X and TanDEM-X data stacks has been presented for complex urban area monitoring exploiting both PSs and DSs. TerraSAR-X allows monostatic acquisitions and in conjunction with the TanDEM-X satellite, bistatic acquisitions are now also possible. Thus, stacks of monostatic repeat-pass and bistatic single-pass interferograms are available. The bistatic interferograms are of high quality and are free from deformation, atmosphere and temporal decorrelation. By properly integrating the data stacks, an improved estimation of topography and deformation is possible. However, the independent processing and subsequent simple combination of the bistatic and monostatic data is not beneficial. Standard TanDEM-X Digital Elevation Models (DEMs) are inaccurate in dense metropolitan areas because of phase unwrapping errors. These errors occur due to height discontinuities and geometrical limitations such as radar layover. Therefore, the joint processing of TerraSAR-X and TanDEM-X data has been investigated.

The developed techniques have been demonstrated using TerraSAR-X/TanDEM-X data from various test sites and a high performance has been proven. The results show an improved utilization of the information hidden in the data and an extension of the applicability of existing techniques for mapping displacement and topography in difficult test

areas. The proposed methods can benefit from future SAR systems with even higher resolution.

Index Terms- Earth Observation, Spaceborne Remote Sensing, Interferometric Synthetic Aperture Radar (InSAR), InSAR Stacking Techniques, Deformation Monitoring, Digital Elevation Model (DEM), Persistent Scatterer (PS), Distributed Scatterer (DS), TanDEM-X, TerraSAR-X.

Zusammenfassung

Interferometrisches Synthetisches Apertur Radar (InSAR) ist eine satellitengestützte Fernerkundungstechnik zur Bereitstellung von Informationen über die Topographie und Deformation der Erdoberfläche. In den letzten Jahren wurden durch den Start von hochauflösenden SAR-Sensoren wie TerraSAR-X, TanDEM-X und COSMO-SkyMed die InSAR-Anwendungen deutlich weiter entwickelt. Möglich ist nun das Kartieren von urbanen Gebieten und sogar von einzelnen Gebäuden durch multitemporale InSAR-Techniken wie zum Beispiel Persistent Scatterer Interferometrie (PSI) und SAR Tomographie (TomoSAR). Diese Methoden nutzen langzeit-kohärente Streuer, z.B. die sogenannten Persistent Scatterer (PSs) und stellen deren Höhe und Verschiebung mit sehr hoher Präzision zur Verfügung.

Außerhalb von urbanen Gebieten ist die PS-Dichte jedoch gering und es ist daher notwendig, die räumliche Dichte der gemessenen Punkte zu erhöhen. Hier bieten hochauflösende SAR-Sensoren neue Möglichkeiten. Dafür müssen zusätzlich zu den Persistent Scatterern auch die teilweise kohärenten Distributed Scatterer (DSs) genutzt werden. Um die in den DS enthaltenen Information zu nutzen, wurden bereits verschiedene Methoden, wie z.B. der Small Baseline Subset Algorithm (SBAS) und SqueeSAR vorgeschlagen. SBAS neigt jedoch in ländlichen Gebieten zu Fehlern beim Phase Unwrapping und liefert nur gering aufgelöste Deformationswerte. Die alternative Technik SqueeSAR ist extrem rechenaufwendig, da es alle möglichen Interferogram-Kombinationen berechnet.

Folglich ist die Entwicklung von neuartigen stapelbasierten Techniken in der hochauflösenden SAR-Interferometrie das Ziel dieser Arbeit. Der Fokus liegt auf schwierigen Gebieten, die mit herkömmlichen Methoden nur sehr schwer zu verarbeiten sind. Zu diesem Zweck wurde zuerst eine neue Methode zur Deformationsmessung mit variabler Auflösung in der Größenordnung der Objekte unter Nutzung von DSs in ländlichen Gebieten entwickelt. Diese beinhaltet ein adaptives räumliches Filtern zur Verbesserung der interferometrischen Phase, gefolgt von einer Deformationsschätzung mithilfe eines L1-Norm basierten SBAS-Verfahrens, welches robuster gegenüber Phase-Unwrapping-Fehlern ist. Weiterhin wurde ein alternatives Vorgehen zur Schätzung der mittleren Deformationsgeschwindigkeit der DSs in stark dekorrelierten Gebieten vorgeschlagen. Bei diesem werden gewrappte Interferogramme (mit kleinen Basislinien) direkt verwendet und die Deformationsgeschwindigkeit wird in einer passenden Objektauflösung kartiert. Es beinhaltet die Identifikation von homogenen Bereichen, die Schätzung des Deformationsgeschwindigkeitsgradienten für diese Bereiche und anschließend eine modelbasierte Integration der Werte, um räumlich dichtgelagerte Schätzungen für die Deformationsgeschwindigkeit zu erhalten. Abschließend wurde eine Fusion von TerraSAR-X und TanDEM-X Datenstapeln für das Monitoring von komplexen urbanen Gebieten unter Nutzung von beiden Steuertypen (d.h. PSs und DSs) vorgestellt. TerraSAR-X ermöglicht monostatische, und zusammen mit dem Satelliten TanDEM-X nun auch bistatische, SAR-Aufnahmen. Somit stehen Stapel von monostatischen repeat-pass und bistatischen single-pass Inteferogrammen zur Verfügung. Bistatische Interferogramme sind von sehr hoher Datenqualität und frei von Deformationssignalen, atmosphärischen Störungen und zeitlicher Dekorrelation. Durch geeignetes Zusammenführen der Datenstapel ist es möglich, die Schätzung der Topographie und der Deformation zu verbessern. Die unabhängige Verarbeitung und anschließende einfache Kombination der bi - bzw. monostatischen Daten ist aber nicht vorteilhaft. In dicht bebauten Stadtgebieten sind die digitalen Höhenmodelle der TanDEM-X Daten aufgrund von Fehlern beim Phase-Unwrapping ungenau. Diese Fehler sind durch Höhendiskontinuitäten und geometrische

Beschränkungen, wie z.B. Überlagerungen, verursacht. Deswegen wurde eine gemeinsame Verarbeitung von TerraSAR-X und TanDEM-X Daten entwickelt.

Die entwickelten Techniken wurden durch Nutzung von aktuellen TerraSAR-X/TanDEM-X Daten für verschiedene Testgebiete demonstriert und ihre Leistungsfähigkeit wurde nachgewiesen. Die Ergebnisse zeigen eine verbesserte Nutzung der in den Daten verborgenen Informationen und eine Erweiterung der Anwendbarkeit der existierenden Techniken zur Deformations- und Höhenmessung auch im schwierigen Testgebieten. Die vorgeschlagenen Auswertemethoden können stark von zukünftigen SAR Missionen mit noch höherer Auflösung profitieren.

Stichworte- Erdbeobachtung, Satellitenbasierte Fernerkundung, Interferometrisches Synthetisches Apertur Radar (InSAR), InSAR Stacking Techniken, Deformationsmessung, Digitales Höhenmodell, Persistent Scatterer (PS), Distributed Scatterer (DS), TanDEM-X, TerraSAR-X.

To my grandparents…

Acknowledgment

This work would not have been completed without the help and support of many individuals.

I would like to express my gratitude to Prof. Richard Bamler for his guidance, advice and mentorship. He has been a great teacher and I always look up to him for motivation and inspiration.

I am also indebted to Nico Adam for his invaluable supervision and research advice. I specially thank him for his infinite patience. The discussions I had with him were constructive and encouraging.

This thesis was co-funded by DLR and DAAD and I would like to thank both organizations for their generous support. Many thanks to Dr. Michael Eineder for providing me an opportunity to conduct my research in his department.

I would also like to thank all the lecturers at TUM under whom I learnt so much.

In addition, I am grateful to all the colleagues at DLR for their cooperation and for providing a nice working experience. Special thanks to Christian Minet and Ramon Brcic for help with the thesis.

I am also grateful to all my friends and family without whom I would not have been able to achieve so much. To my parents for their love and support, to my sister for all the fun we had, to my aunt and uncle for their encouragement and to my dogs for keeping me company, thank you. Last but not the least, to Hari, for being the love of my life, “ondu, nalku, mooru…”

Table of Contents

1 Introduction

Satellite remote sensing plays a significant role in Earth observation. In particular, Synthetic Aperture Radar (SAR) has unique capabilities for studying the Earth's surface at high resolution (Curlander and McDonough, 1991; Soumekh, 1999; Cumming and Wong, 2005). It emits electromagnetic radiation and then coherently records the amplitude and phase of the returned signal to produce complex-valued images of the ground reflectivity. It is an active microwave imaging system, and consequently possesses day and night operational and cloud-penetrating capabilities (which are highly advantageous as compared to optical or infrared sensors). It maps the scattering properties of the Earth's surface corresponding to the wavelength domain.

The Interferometric SAR (InSAR) technique produces maps of Earth's surface elevation using two SAR images (Bamler and Hartl, 1998; Massonnet and Feigl, 1998; Rosen et al., 2000). An extension of this basic technique, called Differential Interferometric SAR (DInSAR), allows highly precise measurements of land deformation in the radar's line-of-sight (LOS) direction. Multitemporal stacking interferometric techniques which make use of stacks of SAR images of the same area, for example, Persistent Scatterer Interferometry (PSI) (Ferretti et al., 2000; Ferretti et al., 2001), Small Baseline Subset Algorithm (SBAS) (Berardino et al., 2002) and SqueeSAR (Ferretti et al., 2011), are suited for monitoring long term dynamic processes such as urban subsidence/uplift, slope stability on landslides and seismic/volcanic deformation. The high resolution X-band SAR satellite TerraSAR-X (Buckreuss et al., 2009) allows millimeter accuracy in the High Resolution Spotlight mode (Adam et al., 2008; Eineder et al., 2009).

This thesis involves *the development and demonstration of advanced stacking techniques in high resolution SAR interferometry*. Algorithms have been developed which contribute to and extend the research field of InSAR. These algorithms are among the first to exploit meter resolution spaceborne SAR data. They have been applied to test cases which are challenging for conventional interferometric stacking techniques.

This chapter provides the scientific motivation for this thesis, the problem statement and objectives, and finally, the thesis outline.

1.1 Scientific Motivation

Monitoring of surface deformation is crucial for studying, understanding and forecasting geodynamical processes. Typical application areas include mines, oil/gas/water reservoirs, landslides, volcanoes and earthquakes. The deformation measurements provide invaluable information which can be used for further geological and risk analysis.

InSAR has been a powerful tool for remote sensing of the Earth's surface since the 1980s. The high quality and vast quantity of exciting results from this technique have demonstrated its potential for measuring topography and deformation. It has been used for acquiring information about urban subsidence and uplift, slope stability on landslides, seismic and volcanic deformation, coastlines and flood plains. However, it has limitations due to low temporal sampling rate, atmospheric propagation effects and temporal decorrelation.

In the last decade, InSAR's capabilities have been considerably improved. By using large stacks of SAR images acquired over the same area, long deformation time series can be analysed using multitemporal techniques. These coherent (i.e. phase-based) methods that have been developed include PSI, SAR Tomography (TomoSAR), SBAS and SqueeSAR, and exploit either permanently coherent phase-stable Persistent Scatterers (PSs) or partially coherent Distributed Scatterers (DSs). PSI provides a parametric estimate of the 3D location and displacement for PSs based on the assumption of one dominant scatterer in the resolution cell and utilizes long time span differential interferograms with respect to a single master image. In TomoSAR, a real 3D imaging of a scene is achieved by the formation of a synthetic aperture in elevation and estimation of the 3D radar reflectivity function (Reigber and Moreira, 2000; Lombardini, 2005; Fornaro et al., 2009; Zhu and Bamler, 2010a). In urban areas, PSI and TomoSAR allow analysis of even individual structures on the ground. Yet, there are drawbacks in rural areas due to temporal decorrelation, low density of PSs, their inhomogenous spatial distribution and phase ambiguities. To improve the spatial sampling of measured points, there is an increasing focus on utilizing DSs to extract geophysical parameters of interest (i.e. elevation and deformation) for surfaces characterized by fields, soil and rock surfaces. The distributed scattering mechanism involves a coherent sum of many independent small scatterers (no dominant scatterer) within a resolution cell (Goodman, 1976) and is modelled by a complex circular Gaussian radar return (Bamler and Hartl, 1998). Although, the phase quality of DSs is not on par with the PSs, it is possible to process DSs with good precision using algorithms such as SBAS and SqueeSAR. SBAS estimates the non-linear deformation time series using unwrapped small baseline differential interferograms. However, it is susceptible to phase unwrapping errors often encountered in non-urban areas. Also, the interferogram multi-looking employed to reduce phase noise (Zebker and Villasenor, 1992) results in a loss of resolution and the superposition of topography and deformation signals from different objects. SqueeSAR, on the other hand, also provides a modelled deformation utilizing all possible interferograms and processes statistically identical pixels as a single object, but can be computationally expensive.

To counter the limitations of the above-mentioned techniques, *advanced techniques in high resolution SAR interferometry* have been developed and implemented for topographic mapping and deformation monitoring as part of this thesis. In fact, since 2007, the new generation of high resolution SAR sensors such as TerraSAR-X and COSMO-SkyMed are providing imagery with unique characteristics enabling sophisticated interferometric applications. Figure 1 (a) shows a medium resolution ERS amplitude image of Lueneburg, Germany, whereas Figure 1 (b) shows the corresponding high resolution TerraSAR-X amplitude image. With shorter repeat cycles, smaller orbital tubes and higher bandwidth of the satellites, advanced monostatic repeat-pass stacking techniques are now supported by a practical data basis.

Additionally, with the TanDEM-X satellite which was launched in 2010 (Krieger et al., 2007), high resolution bistatic single-pass interferometry is now possible together with TerraSAR-X. The addition of a few TanDEM-X data pairs (that are free from displacement, atmosphere and temporal decorrelation) to the existing TerraSAR-X data stack can improve the results of stacking techniques such as PSI and SBAS. Essentially, the TerraSAR-X/TanDEM-X case represents a special sensor availability scenario in space, where, the two satellites in the mission were launched one after the other. There was a long monostatic acquisition period at the beginning of the mission, followed by a bistatic acquisition period which is going on currently and finally, there will be a monostatic acquisition period again. However, in dense metropolitan areas, spatial phase unwrapping is a challenge due to geometrical limitations such as radar layover and shadow (Schreier, 1993). Consequently,

fusion of bistatic and monostatic data has been explored and demonstrated in this dissertation for complex urban areas.

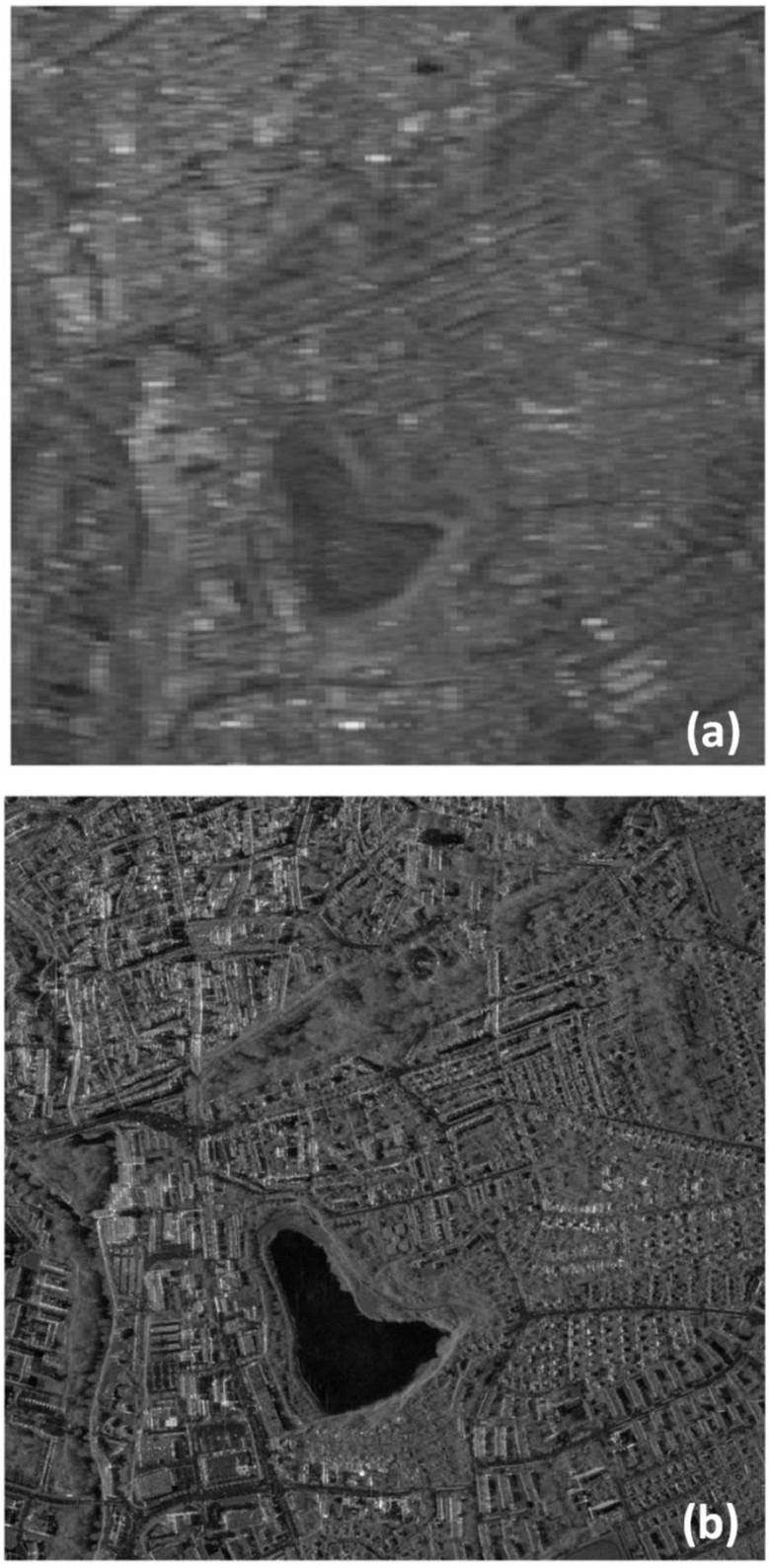

Figure 1: SAR amplitude images of Lueneburg, Germany. (a) ERS image with a spatial resolution of 25 m in slant range direction and 5 m in azimuth direction. (b) TerraSAR-X image with a spatial resolution of 0.6 m in slant range direction and 1.1 m in azimuth direction.

1.2 Problem Statement and Objectives

High resolution SAR missions, for example, TerraSAR-X and TanDEM-X, have opened up a new and exciting field of advanced interferometry for measuring elevation and displacement. Published multitemporal (i.e. monostatic repeat-pass) techniques such as PSI, TomoSAR and SBAS are however limited due to the unavailability of coherent scatterers, temporal decorrelation phenomenon and phase unwrapping errors in rural regions. In fact, phase unwrapping is also a major problem in dense urban areas. In this work, advanced stacking techniques and applications in high resolution SAR interferometry have been developed, with a focus on complex areas that are difficult to process using conventional techniques. This thesis was carried out with the following objectives:

- *Contribute* to the research field of DInSAR, i.e. displacement and topography estimation.
- *Extend* the application of recently developed techniques such as PSI, TomoSAR, SBAS and SqueeSAR.
- *Propose* new algorithms that improve the applicability of available techniques by:
    - Reducing computational efforts (e.g. exploiting only small baseline differential interferograms) and combining bistatic and monostatic data.
    - Improving the spatial resolution of the estimates as compared to the conventional algorithms.
    - Improving the precision of the estimates.
    - Increasing the robustness of the estimates with respect to phase unwrapping and resolution cell characteristics.
- *Implement*, *apply* and *assess* the algorithms on real data.
- *Illustrate* the measurement results of the developed techniques, *demonstrate* their potential and *identify* the typical use cases of these techniques.
- *Analyze* the properties (i.e. characteristics) of the techniques and the factors that affect their performance.
- *Encourage* the geo-user community in using these techniques.

Aiming at the above-mentioned goals, there are three main contributions of this dissertation:

- *First*, an advanced SBAS algorithm has been developed for deformation time series monitoring in non-urban areas. It involves an adaptive spatial filtering algorithm to improve the differential interferometric phase while preserving the object resolution. This is followed by deformation estimation using an L1-norm based SBAS approach that is more robust to the often-occuring phase unwrapping errors in rural areas.
- *Second*, an advanced algorithm for Distributed Scatterer Interferometry (DSI) has been proposed which copes with highly decorrelated areas. It provides spatially dense mean deformation velocity estimates without any phase unwrapping at a suitable object resolution. It identifies statistically homogenous patches and estimates gradients of deformation velocity for these patches. Afterwards, model-based deformation integration is performed to obtain the absolute deformation velocities.
- *Third*, a joint processing of monostatic repeat-pass and bistatic single-pass InSAR data exploiting PSs and DSs has been performed for monitoring metropolitan areas, where it is difficult to interpret the SAR images and interferometric phase due to phase discontinuities and complex scattering situations such as radar layover and shadow.

1.3 Thesis Outline

This is a *cumulative dissertation* comprising of 5 full paper peer-reviewed scientific publications, which are presented at the end (see Appendix A). The thesis is structured as follows.

Chapter 2 explains SAR and interferometry fundamentals, followed by an overview of state-of-the-art coherent PS and DS multitemporal techniques and their inherent limitations.

In Chapter 3, the advanced SBAS algorithm for non-linear deformation time series mapping of DSs at object resolution is described. Afterwards, practical demonstration is provided on two application test cases and a performance assessment of the deformation estimation is presented. This algorithm has been published in (Goel and Adam, 2012a):
A.1 Goel, K., Adam, N., 2012a. An advanced algorithm for deformation estimation in non-urban areas. ISPRS Journal of Photogrammetry and Remote Sensing 73, 100-110.

Chapter 4 explains the DSI algorithm for mean deformation velocity mapping of DSs at a suitable object resolution. Its application on a test case and a comparison with the advanced SBAS algorithm is described. Assessment of the quality of the obtained deformation products is also presented. This method has been published in (Goel and Adam, 2012b):
A.2 Goel, K., Adam, N., 2012b. High resolution deformation time series estimation for distributed scatterers using TerraSAR-X data. ISPRS Annals of the Photogrammetry, Remote Sensing and Spatial Information Sciences, XXII ISPRS Congress, Commission VII, Melbourne, Australia, 25 August-01 September 2012, I-7, 29-34, Copernicus Publications.
Besides, a paper describing this technology in detail has been published in (Goel and Adam, 2013a):
A.3 Goel, K., Adam, N., 2013a. A distributed scatterer interferometry approach for precision monitoring of known surface deformation phenomena. IEEE Transactions on Geoscience and Remote Sensing PP (99), 1-15, DOI: 10.1109/TGRS.2013.2289370.

The fusion of monostatic repeat-pass and bistatic single-pass InSAR stacks (i.e. TerraSAR-X and TanDEM-X data) for complex urban area monitoring via DSs is given in Chapter 5. A case study is presented and the precision of the elevation and deformation estimates is discussed. A paper describing this integration technique has been published in (Goel and Adam, 2013b):
A.4 Goel, K., Adam, N., 2013b. Fusion of monostatic/bistatic InSAR stacks for urban area analysis via distributed scatterers. IEEE Geoscience and Remote Sensing Letters PP (99), 1-5, DOI: 10.1109/LGRS.2013.2278204.

The advanced stacking of TerraSAR-X and TanDEM-X data for PSs is given in Chapter 6. The focus is on resolving single or double scattering mechanisms present in the same resolution cell in dense metropolitan regions. The technical details, first results and performance evaluation are presented using simulated and real data. This fusion technique has been published in (Goel and Adam, 2013c):
A.5 Goel, K., Adam, N., 2013c. Advanced stacking of TerraSAR-X and TanDEM-X data in complex urban areas. Proceedings of Joint Urban Remote Sensing Event, JURSE 2013, Sao Paulo, Brazil, 21-23 April, 115-118.

Finally, the thesis is summarized in Chapter 7 with a brief discussion and conclusion, followed by an outlook for future work.

2 Fundamentals and State-of-the-Art

It is important to study and get a detailed understanding of *Earth's deformation* impact on man-made and natural sites. Conventionally, geodetic leveling measurements and Global Positioning System (GPS) networks have been used to monitor the surface deformation. However, these provide information only about a few points. In comparison, spaceborne SAR interferometry provides a large number of measured points over long time periods, and this is suitable for analyzing the geodynamical processes. InSAR advantageously provides ground deformation rate estimates with millimeter per year accuracy over large contiguous areas (few hundred kilometers).

In this chapter, first, the relevant SAR and interferometry fundamentals are described briefly. Next, the state-of-the-art PS stacking techniques are introduced. These include the PSI and TomoSAR. Afterwards, the state-of-the-art DS stacking techniques, namely, the SBAS and SqueeSAR are presented. This chapter sets the basis for the new algorithms proposed in this thesis.

2.1 SAR Fundamentals

Spaceborne SAR enables the imaging and monitoring of Earth's surface at a global level with a short revisit time (Curlander and McDonough, 1991; Soumekh, 1999; Cumming and Wong, 2005). As a consequence, various areas can be studied regularly at low costs. It provides radiometric as well as the distance information about objects on ground. Thus, apart from studying scattering properties, it can also be used to study elevation, changes in the scene's radiometry and deformation of objects over time.

NASA launched the first civilian spaceborne SAR sensor, the SEASAT satellite, in 1978 for ocean studies. It was a short term mission (only 105 days), however, it proved the functioning of the instruments and paved the way for later systems. Since then, various SAR satellites, for instance, ERS-1/2, ENVISAT, RADARSAT-1/2, COSMO-SkyMed, TerraSAR-X and TanDEM-X have been launched and these have been used for various applications.

2.1.1 SAR Imaging Principle and Geometry

The Synthetic Aperture Radar (SAR) imaging geometry is shown in Figure 2. It is asymmetrical and characterized by a side looking sensor, so as to prevent range ambiguities and unwanted high level signals from vertical ground reflections. A cylindrical coordinate system is used to specify the 3D position of a scatterer on the ground:

- The *azimuth* axis x defines the position of the scatterer along the sensor path.
- The *slant range* axis r defines the distance of the scatterer from the SAR sensor.
- The *look angle* θ represents the angle between the sensor-to-scatterer line and nadir.

The range circle representing a constant range distance can be approximated to be a straight line due to large range distance and small angular diversities, and this straight line is the axis perpendicular to the azimuth - slant range plane and is called the *elevation* l (with origin in the center of the imaged pixel). The local incidence angle at the Earth's surface is the angle

between the sensor-to-scatterer line and the local normal to the Earth's tangent plane at that surface. In Cartesian coordinates, the 3D position of a scatterer is defined by the azimuth axis x, the ground range axis y and the height axis z. The sensor illuminates an area on the ground called the antenna footprint. The scene is mapped to the azimuth - slant range plane. In the standard imaging mode, called the Stripmap mode, the look angle and the squint angle of the sensor's LOS are kept stable.

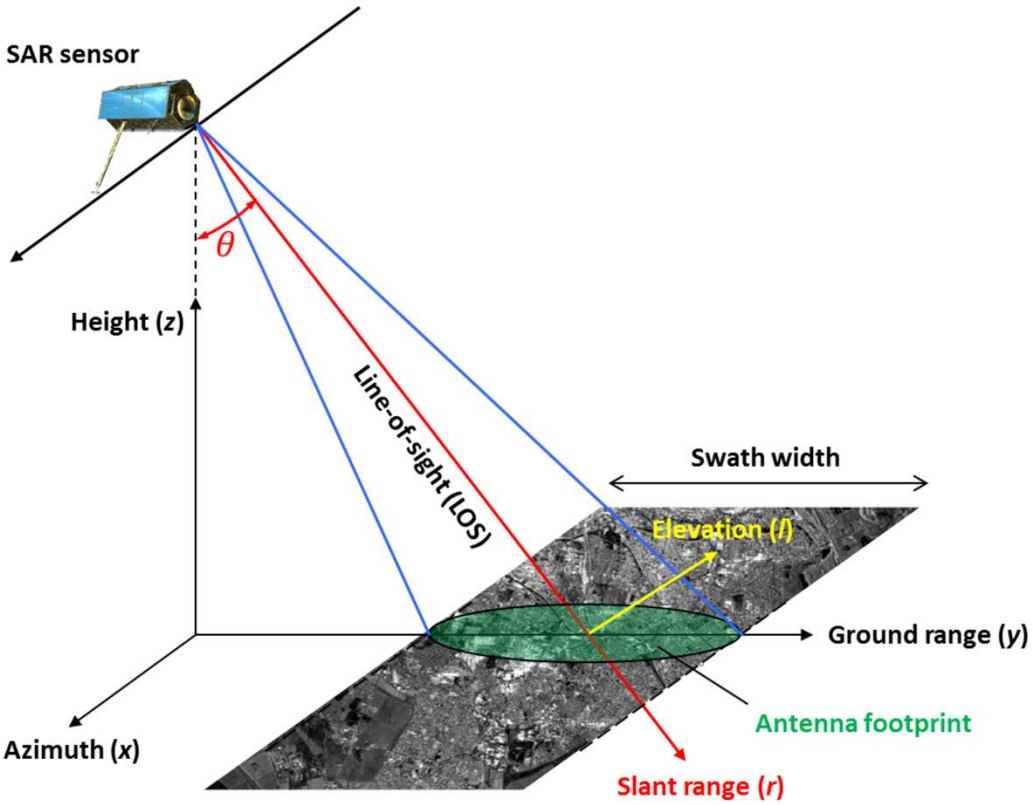

Figure 2: The side-looking acquisition geometry of SAR. In cylindrical coordinate system, the flight direction of the sensor is called the azimuth axis, the LOS direction is called the slant range axis, the angle between the LOS direction and the nadir is called the look angle θ. The range circle representing a constant range distance can be approximated to be a straight line, and this line is the axis perpendicular to the azimuth - slant range plane and is called the elevation. The Cartesian coordinate system is defined by the azimuth, the ground range and the height axes. The sensor, flying at a certain height, illuminates an area on the ground called the antenna footprint (which is limited in ground range by its swath width). The scene is mapped to the azimuth - slant range plane.

Radar is an acronym for RAdio Detection And Ranging. It was developed to detect targets such as ships or airplanes. Conventional radars were designed to achieve finer range resolution by the radiation of a short pulse and finer azimuth resolution by the radiation of a narrow beam. Pulse compression techniques (e.g. chirping) are available for achieving a range resolution significantly finer than that corresponding to the pulse width, provided a signal of sufficient bandwidth is transmitted.

SAR was developed to improve the azimuth resolution significantly than that achievable by making use of the radiated beam width. It enables imaging with a fine azimuth resolution with relatively small physical antenna using sophisticated signal processing techniques. SAR utilizes the flight path of the platform to simulate an extremely large aperture electronically. As it passes a given scatterer, many pulses are reflected in sequence. By coherently recording and combining these individual pulses, a "synthetic aperture" is created providing a high azimuth resolution that is independent of the slant range to the scatterer. Thus, SAR is an excellent tool for high resolution remote sensing of Earth's surface from space.

SAR does not provide imaging in elevation direction, i.e. scatterers having the same azimuth-range coordinates but at different elevation positions cannot be distinguished as they are summed up in the same pixel.

A SAR image is a 2D array of pixels in the slant range and azimuth directions, respectively. Each pixel corresponds to a small part of the Earth's surface called the resolution cell. It is represented by a complex number that carries amplitude and phase information about the microwave field backscattered by all the scatterers (e.g. rocks, vegetation, buildings) within the corresponding resolution cell projected on the ground. The amplitude of the SAR image is determined primarily by terrain slope, surface roughness and the dielectric constant (relative permittivity). In contrast, the phase of the SAR image is determined mainly by the distance between the satellite antenna and the ground scatterers and is represented as a fraction of a complete wavelength. In the standard monostatic imaging mode, where the antenna alternately transmits and receives its own echoes, the complex SAR signal s for a pixel depends on the two-way path distance between the sensor and target and is approximately given by the expression:

$$s = a \cdot e^{j\phi} = a \cdot e^{j\left(\frac{-2\pi}{\lambda} 2R + \phi_{scat}\right)} = a \cdot e^{j\left(\frac{-4\pi}{\lambda} R + \phi_{scat}\right)} \tag{1}$$

where a is the amplitude, ϕ is the phase, λ is the signal wavelength, R is the range distance determined by precisely measuring the time from transmission of a pulse to receiving the echo from the target and ϕ_{scat} is the phase contribution due to the scattering inside the resolution cell. The typically used wavelengths for spaceborne SAR sensors are 15-30 cm (L-band), 3.8-7.5 cm (C-band) and 2.4-3.8 cm (X-band).

The range resolution ρ_r of the SAR image is given by the bandwidth W of the transmitted chirp signal:

$$\rho_r = \frac{c}{2W} \tag{2}$$

where c is the speed of light. The azimuth resolution ρ_x depends on the physical length L of the SAR antenna:

$$\rho_x \approx \frac{L}{2} \tag{3}$$

The SAR sensors operating in Spotlight Mode have a finer azimuth resolution than that given by Equation (3), as the length of the synthetic aperture in azimuth is increased by squinting the radar beam in the direction of the area to be imaged.

2.1.2 Geometrical Effects Introduced by SAR

Since SAR is side looking, terrain elevation results in geometric effects in the SAR image (Schreier, 1993). These effects are demonstrated in Figure 3 where the SAR imaging along the range direction is shown.

The first effect is *foreshortening* and it occurs as long as the slope of the terrain is smaller than the local incidence angle. It leads to shortening of the distance between two points due to projection onto the slant range direction. As can be seen in Figure 3, the distance of the orange slope is much smaller in the SAR image than in reality.

When the terrain slope exceeds the radar local incidence angle, the scatterers are imaged in reverse order and superimposed on the contribution coming from other areas. This effect is called *layover*. Extended layover areas in urban areas cause scatterers on the ground and on buildings to be mapped into the same resolution cell. In Figure 3, the reflection coming from a part of the ground (in blue), the building façade (in red) and a part of the building roof (in green) are all superimposed on top of each other in the SAR image.

When an object in the scene blocks the radar wave from reaching other portions of the scene, *shadow* occurs in the SAR imagery, as shown in gray in Figure 3. These shadowed regions in the scene appear black.

Because of these geometrical limitations of SAR, interpretation of SAR data becomes difficult, especially for urban areas and buildings. The solutions are PSI and TomoSAR, and these would be described in Section 2.3. For PSI, parametric techniques were developed to resolve complex scattering mechanisms (Ferretti et al., 2005; Adam et al., 2005).

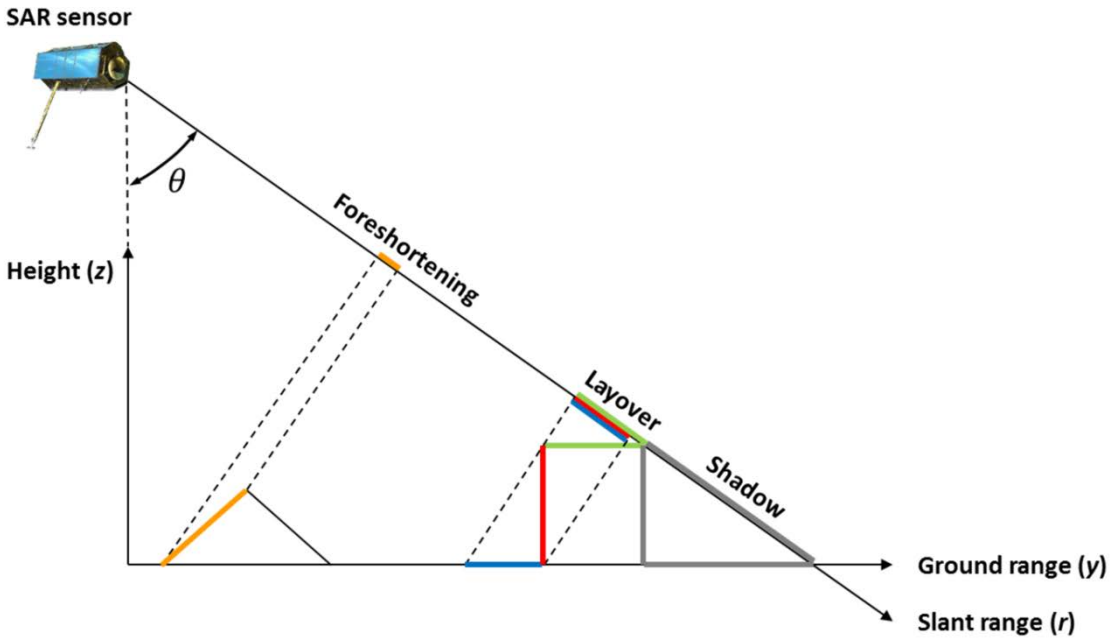

Figure 3: Geometrical effects in SAR images, namely, foreshortening, layover and shadow in the plane orthogonal to the flight (i.e. azimuth) direction. These effects depend on the look angle θ and the local slope of the terrain.

2.1.3 High Resolution SAR

X-band SAR satellites, namely, TerraSAR-X, TanDEM-X and COSMO-SkyMed are providing unique imagery with up to 1 m resolution for the last few years. SAR data with such a high resolution are available for the first time for civil applications. New techniques and applications in SAR and InSAR are now possible, that were previously difficult using medium and low resolution sensors such as the C-band ERS-1/2. Apart from supporting urban infrastructure monitoring by providing details of different man-made objects such as buildings, these data provide the opportunity to even study rural areas by providing a high spatial resolution, higher Signal to Noise Ratio (SNR), smaller orbital tubes and shorter revisit times.

TerraSAR-X is a high resolution German radar satellite launched in June, 2007 for scientific and commercial applications (Buckreuss et al., 2009). The orbit is 514 km high at an inclination of 97.44 degrees. TerraSAR-X has 11 days revisit time (orbit repeat cycle). Due to swath overlay, a 2.5 day revisit time can be achieved. The payload is a Synthetic Aperture Radar (SAR) with the following specifications:

- X-band radar frequency of 9.65 GHz.
- Right looking, but rolling to left looking possible.
- Incidence angle of 20-55 degrees.
- Transmit and receive in H or V polarization (single/dual).

TerraSAR-X has four imaging modes:

- ScanSAR Mode: Single polarization, scene size 100 km (ground range) by 150 km (azimuth), up to 18.5 m resolution.
- Stripmap Mode: Single or dual polarization, scene size 30 km (ground range) by 50 km (azimuth), up to 3 m resolution.
- Spotlight Mode: Single or dual polarization, scene size 10 km (ground range) by 10 km (azimuth), up to 2 m resolution.
- High Resolution Spotlight Mode: Single or dual polarization, scene size 5-10 km (ground range) by 5 km (azimuth), up to 1 m resolution. With 300 MHz bandwidth, a resolution of 0.6 meters in slant range and 1.1 meters in azimuth is achieved.

TerraSAR-X facilitates monostatic repeat-pass interferometry and allows analysis of individual structures on the ground with a high level of detail (Adam et al., 2008; Eineder et al., 2009).

TanDEM-X, launched in June, 2010, is TerraSAR-X's twin satellite and almost identical to it (Krieger et al., 2007). The two satellites fly in a closely controlled formation with typical distances between 250 and 500 m. TerraSAR-X and TanDEM-X together allow the acquisition of high resolution bistatic single-pass interferograms, which are very good in quality due to absence of deformation, atmosphere and temporal decorrelation. The main objective of this mission is the generation of a global Digital Elevation Model (DEM). Furthermore, it also provides a configurable SAR platform for demonstrating new interferometric techniques and applications.

TerraSAR-X and *TanDEM-X* data have been used to demonstrate the implemented algorithms in this dissertation.

2.2 SAR Interferometry Fundamentals

InSAR exploits the phase difference between two SAR images acquired from different orbit positions and/or at different times (Bamler and Hartl, 1998; Massonnet and Feigl, 1998; Rosen et al., 2000). This method provides information about geophysical quantitites such as *topography* (Zebker and Goldstein, 1986; Li and Goldstein, 2002) and *deformation* (Massonnet et al., 1993; Zebker et al., 1994). In fact, InSAR allows measurement of even millimetric surface displacements from space because it is coherent and utilizes short wavelengths. It is hence suited for monitoring long term dynamic processes such as volcanoes, crustal dynamics and land subsidence.

2.2.1 SAR Interferogram Generation

A single SAR image cannot uniquely determine a 3D scatterer's position, as it does not allow mapping in the third dimension, i.e. look angle θ (in the cylindrical coordinate system) or the elevation direction. This is illustrated in Figure 4 (a) which shows the SAR imaging geometry in the plane orthogonal to the azimuth direction. Here, all the scatterers located within the range beam and having the same distance R to the sensor are mapped into the same SAR image pixel. This drawback can be overcome by acquiring a second image of the same area from a slightly different position (but from a parallel track), as demonstrated in Figure 4 (b). Here, the distance between the two sensor positions is called the baseline B, its component perpendicular to some look direction is referred to as the perpendicular baseline $B_\perp$ and the angle between the line joining the two sensor positions and the horizontal direction is called the tilt angle β. The second acquisition resolves the ambiguity existing on the scatterer location completely, since only one point exists which is located at a distance R from the first sensor and $R+\delta R$ from the second one.

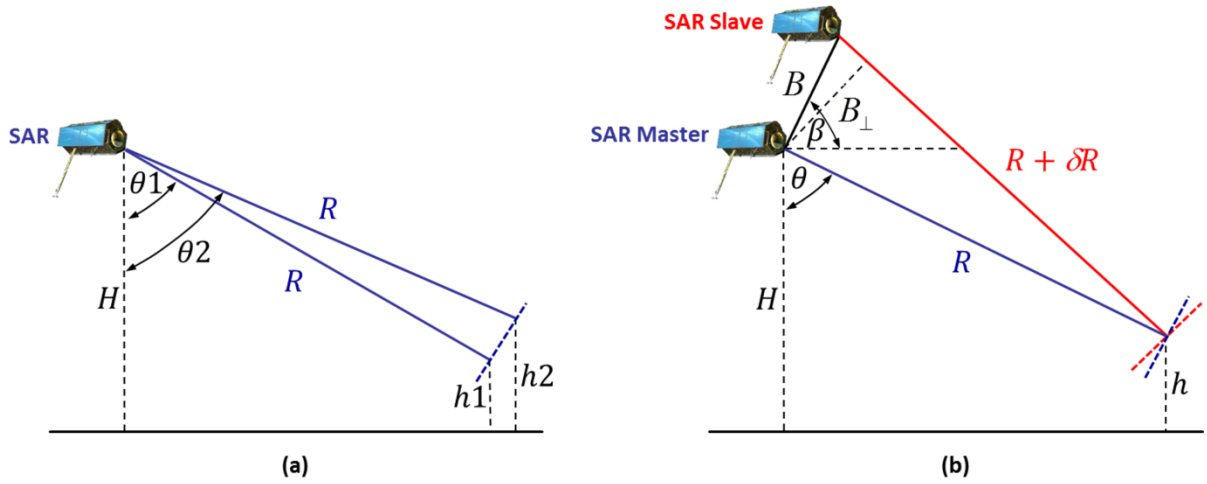

Figure 4: SAR imaging geometry in the plane orthogonal to the flight (i.e. azimuth) direction. (a) Single imaging. (b) Stereo imaging.

The information about the look angle θ comes from the path difference δR, since it can be observed from Figure 4 (b) that:

$$(R+\delta R)^2 = R^2 + B^2 - 2RB\sin(\theta-\beta) \tag{4}$$

From Equation (4) it can be deduced that:

$$\delta R = \sqrt{R^2 + B^2 - 2RB\sin(\theta-\beta)} - R \approx -B\sin(\theta-\beta) \tag{5}$$

The knowledge of the look angle θ gives the height h of the scatterer with respect to a reference plane as follows:

$$h = H - R\cos\theta \tag{6}$$

where H is the height of the first sensor. Accordingly, it can be said that the measurement of the path difference is the key to determining a scatterer's height via two SAR images in stereo-imaging geometry. The height measurement accuracy σ_h depends on the accuracy of measuring the path difference $\sigma_{\delta R}$ and can be obtained from Equation (5) and Equation (6) as follows:

$$\sigma_h = \frac{\partial h}{\partial(\delta R)}\sigma_{\delta R} = \frac{\partial h}{\partial\theta}\frac{\partial\theta}{\partial(\delta R)}\sigma_{\delta R} \approx \frac{R\sin\theta}{B\cos(\theta-\beta)}\sigma_{\delta R} = \frac{R\sin\theta}{B_\perp}\sigma_{\delta R} \tag{7}$$

One technique to calculate the path difference is SAR radargrammetry (Desai, 1997; Soergel et al., 2009; Raggam et al., 2010; Goel and Adam, 2012c). A point is considered in the first SAR image, henceforth called the master. The same point is then searched for in the second image, which is hereafter called the slave. Then, subtracting the range of the point in the master and slave images gives the path difference. However, this method is dependent on the range resolution and the path difference should be "large" (as compared to InSAR described below) for this technique to be applicable.

Another technique to measure a "small" path difference (and thus, height of a scatterer) is *across-track InSAR*, wherein, phase difference of the two SAR images is exploited. This technique provides a higher (sub-wavelength) accuracy in evaluating the scatterer's height. In practice, a complex SAR interferogram is generated by multiplying, pixel by pixel, the first SAR image with the complex conjugate of the second. For across-track interferometers, the standard mode of data collection is the *monostatic* mode (*repeat-pass*) where each antenna alternately transmits and receives its own echoes. For a monostatic interferometer, considering that the complex SAR signal for a pixel in the master and slave image is given by s_1 and s_2, respectively as follows:

$$s_1 = A_1 \cdot e^{j\phi_1} = A_1 \cdot e^{j\left(\frac{-4\pi}{\lambda}R + \phi_{scat\_1}\right)} \text{ and}$$
$$s_2 = A_2 \cdot e^{j\phi_2} = A_2 \cdot e^{j\left(\frac{-4\pi}{\lambda}(R+\delta R) + \phi_{scat\_2}\right)} \tag{8}$$

where A_1 and A_2 are the amplitude, ϕ_1 and ϕ_2 are the phase of the pixel in the master and slave image, respectively and ϕ_{scat_1} and ϕ_{scat_2} are the phase contributions due to the scattering inside the resolution cell in the master and slave image, respectively, the complex interferogram q for a generic pixel is given by:

$$q = s_1 \cdot s_2^* = A_1 \cdot A_2 \cdot e^{j(\phi_1 - \phi_2)} = A_1 \cdot A_2 \cdot e^{j\left(\frac{4\pi}{\lambda}\delta R + \left(\phi_{scat\_1} - \phi_{scat\_2}\right)\right)} \tag{9}$$

Here, the phase value of q is the wrapped interferometric phase, which is ambiguous as it is limited to the interval $(-\pi, \pi]$. Figure 5 (a) illustrates a TerraSAR-X amplitude image (Spotlight Mode) of an area close to Las Vegas, US. Figure 5 (b) depicts a corresponding interferogram. Phase unwrapping has to be performed to directly infer range differences (Goldstein et al., 1988; Ghiglia and Romero, 1994; Fornaro et al., 1996; Costantini, 1998; Eineder et al., 1998; Pepe and Lanari, 2006; Fornaro et al., 2011). After phase unwrapping, the true unwrapped interferometric phase ϕ_{InSAR} of a pixel is given by:

$$\phi_{InSAR} = \frac{4\pi}{\lambda}\delta R \tag{10}$$

Note that this is assuming that the phase contributions due to the scattering inside the resolution cell can be neglected. This is true in case of PSs, whereas phase stability is characterized by spatial coherence in case of DSs, as explained in the next subsection. So, it can be inferred that the interferogram contains the information about the path difference. The path difference measurement precision $\sigma_{\delta R}$ depends on the interferometric phase accuracy $\sigma_{\phi_{InSAR}}$ since:

$$\sigma_{\phi_{InSAR}} = \frac{4\pi}{\lambda}\sigma_{\delta R} \tag{11}$$

Substituting this in Equation (7) gives the height measurement accuracy:

$$\sigma_h \approx \frac{R\sin\theta}{B_\perp}\frac{\lambda}{4\pi}\sigma_{\phi_{InSAR}} \tag{12}$$

The simplified phase-topography relation is given by:

$$\phi_{InSAR} \approx \phi_{topo} = \frac{4\pi}{\lambda} \frac{B_{\perp}}{R \sin\theta} h \tag{13}$$

assuming that the flat Earth phase component has been removed and there are no deformation, atmospheric and noise phase components.

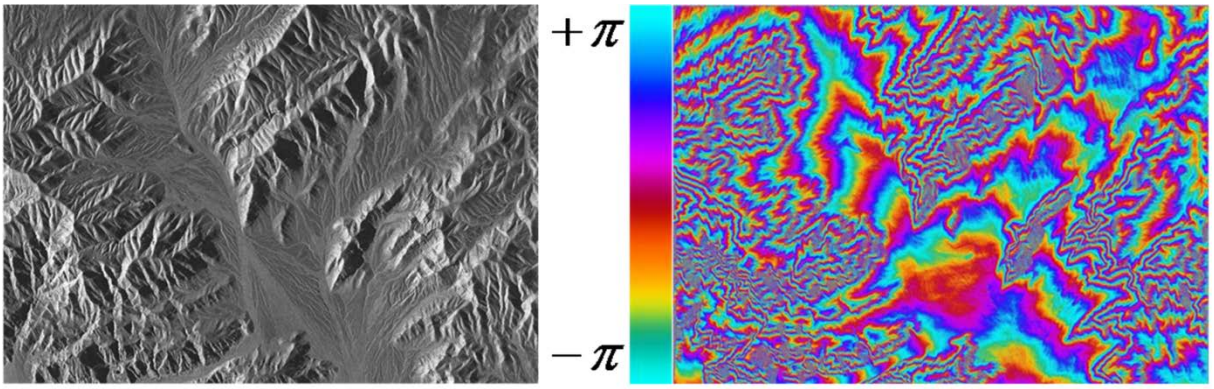

Figure 5: Depiction of a region close to Las Vegas, US. (a) TerraSAR-X amplitude image. (b) Corresponding TerraSAR-X interferogram with a perpendicular baseline of 309 m and temporal baseline of 11 days. (Adam et al., 2007)

The above-mentioned theory assumes that the imaged surface is stationary. If the two observations are separated in time, the phase difference might be caused not only by topography but also by ground movement. If the topography of the terrain is known beforehand (e.g. a DEM), this independent topography information can be subtracted from the interferogram to get the differential interferogram ϕ_{DInSAR}, indicating surface deformation:

$$\phi_{DInSAR} \approx \phi_{defo} = \frac{4\pi}{\lambda} B_t v \tag{14}$$

where B_t is the temporal separation (i.e. temporal baseline) for the interferogram and v is the displacement velocity of the scatterer in the LOS (assuming a constant velocity model). This technique to monitor deformation is called *Differential Interferometric SAR* (*DInSAR*). In reality, the differential interferometric phase for a pixel is composed of phase components due to deformation ϕ_{defo}, residual topography ϕ_{res_topo}, atmosphere ϕ_{atmo} and noise ϕ_{noise} as follows:

$$\phi_{DInSAR} = \phi_{defo} + \phi_{res\_topo} + \phi_{atmo} + \phi_{noise} = \frac{4\pi}{\lambda} B_t v + \frac{4\pi}{\lambda} \frac{B_{\perp}}{R \sin\theta} h_{res} + \phi_{atmo} + \phi_{noise} \tag{15}$$

where h_{res} is the residual height of the pixel due to errors in the DEM etc. The phase noise is due to temporal decorrelation, uncompensated spectral decorrelation, orbital errors and thermal noise. The interferogram is usually referenced with respect to a single pixel (typically a highly coherent point located in a non-deforming zone). The atmospheric phase is minimized if the reference pixel is in close spatial proximity, i.e. less than 1 km away (Hanssen, 1998; Hanssen, 2001). Similarly, the orbital errors also become negligible if the reference pixel is located nearby.

An example of a differential interferogram obtained from 2 TerraSAR-X images (Stripmap mode) of the area around the Italian town of L'Aquila is shown in Figure 6. The two images were acquired on 6th February, 2009 and 13th April, 2009, respectively. The differential fringes (i.e. colored rings) represent the ground movement caused by the magnitude 6.3 earthquake on 6th April, 2009.

For *bistatic* across-track interferometers (*single-pass*) where only one antenna transmits and both antennae receive the echoes (at the same time), the interferometric phase ϕ_{InSAR_Bi} for a pixel is given by:

$$\phi_{InSAR\_Bi} = \frac{2\pi}{\lambda}\left(\left(R+R\right)-\left(R+R'\right)\right) = \frac{2\pi}{\lambda}\delta R \tag{16}$$

where R is the distance of the target from the first sensor and R' from the second one. This effectively means that the phase-to-height sensitivity of a bistatic interferogram is half as compared to a monostatic interferogram:

$$\phi_{InSAR\_Bi} = \phi_{topo} + \phi_{noise} = \frac{2\pi}{\lambda}\frac{B_{\perp}}{R\sin\theta}h + \phi_{noise} \tag{17}$$

Note that a bistatic interferogram is composed of phase components due to topography and noise only. The phase noise here is due to possible uncompensated spectral decorrelation, orbital errors and thermal noise, there is no temporal decorrelation. The deformation and atmospheric phase components are also negligible since the two SAR acquisitions are taken at the same time.

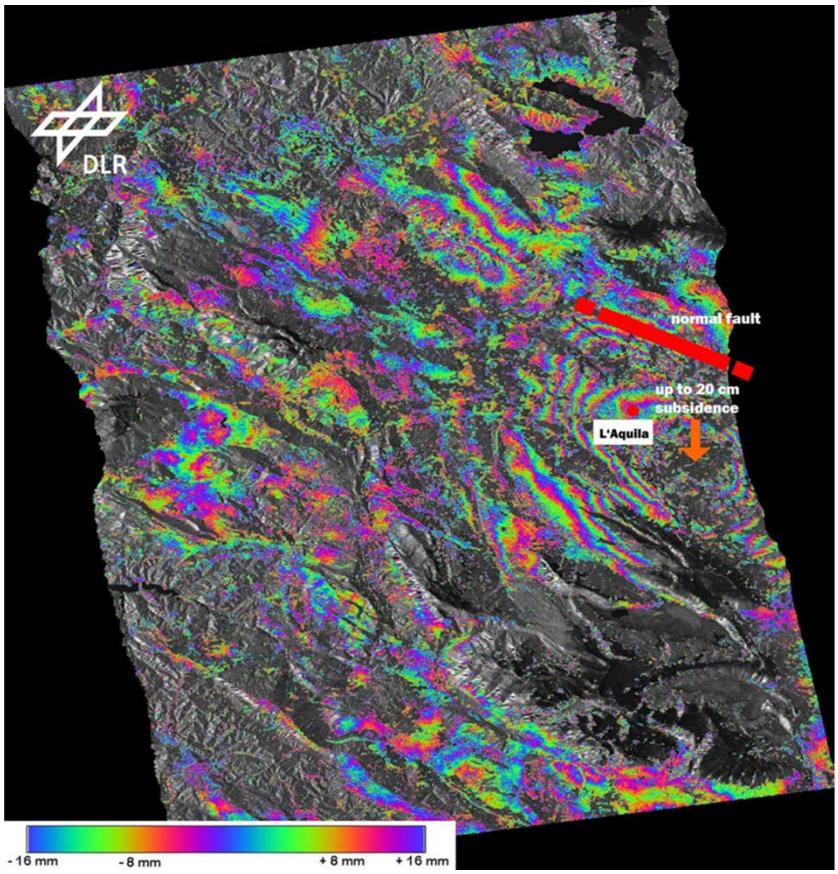

Figure 6: Differential interferogram formed from two TerraSAR-X images of the area around L'Aquila, Italy, showing the ground movement caused by the magnitude 6.3 earthquake on 6th April, 2009. The two images were acquired on 6th February, 2009 and 13th April, 2009, respectively. (Courtesy of Christian Minet, DLR)

Figure 7 shows a comparison between a bistatic interferogram ($B_t \approx 0$) and a monostatic interferogram (B_t = 693 days) of Las Vegas, US. The bistatic interferogram has been formed from two TerraSAR-X and TanDEM-X images (High Resolution Spotlight mode) taken at the same time. The monostatic interferogram has been formed from two TerraSAR-X images taken at different times. As can be seen, the bistatic interferogram is free from fringes due to deformation and atmosphere, as compared to the monostatic interferogram. Also, there is no temporal decorrelation in the bistatic interferogram.

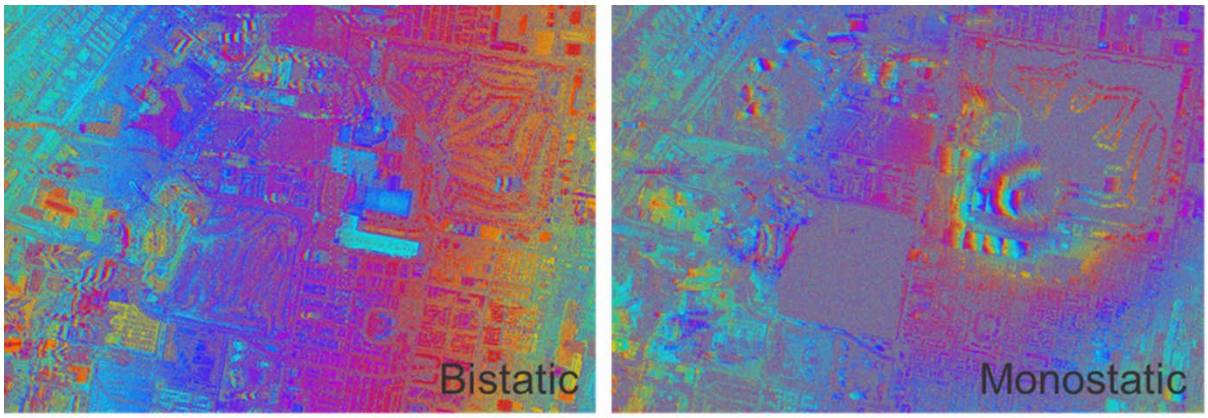

Figure 7: Comparison of a bistatic interferogram ($B_t \approx 0$) and a monostatic interferogram (B_t = 693 days) of Las Vegas, US, using TerraSAR-X/TanDEM-X data.

2.2.2 SAR Interferogram Statistics

The ideal case of interferometric return is due to a *point scatterer* (see Figure 8 (a)). If the resolution element contains a single point scatterer, the phase contributions due to the scattering inside the resolution cell, ϕ_{scat}, shows almost no variation with time. In such a case, the topography and deformation information can be estimated from the interferogram without any error. However, such scatterers rarely exist in reality.

Nevertheless, on man-made structures like roofs, building facades, metallic structures etc. in urban areas, there do exist PSs. A *PS* is characterized by one (or a few) dominating scatterer inside a resolution cell (see Figure 8 (b)). It exhibits a small variation of ϕ_{scat} with time and can also be used for topography and deformation mapping of the dominating scatterer. The phase stability of a PS is characterized by the Signal to Clutter Ratio (SCR) (clutter is the contribution of the echo from all the non-PS scattering elements within the cell). Such pixels form the basis of PSI for topography and deformation time series estimation. PSI exploits interferograms at the highest possible resolution (single-look data) to identify such scatterers.

On the other hand, in natural terrains, the scattering is generally the coherent sum of many subscatterers within a resolution cell (where no single subscatterer dominates the others) (Goodman, 1976). Such a scattering object is a Gaussian (or Rayleigh) scatterer, also called a *DS* (see Figure 8 (c)). It obeys circular Gaussian statistics (Bamler and Hartl, 1998). The variation of ϕ_{scat} with time is randomly distributed in the interval $(-\pi, \pi]$. InSAR stacking methods based on DSs include the SBAS and SqueeSAR. These methods exploit interferograms at a lower resolution (multi-look data). Essentially, the DSs are characterized by a low SNR, which has to be improved by a local spatial averaging (i.e. multi-looking). In other words, the statistics of interferograms characterized by DSs are governed by the complex covariance (Just and Bamler, 1994) and this has to be estimated by sample means as discussed below.

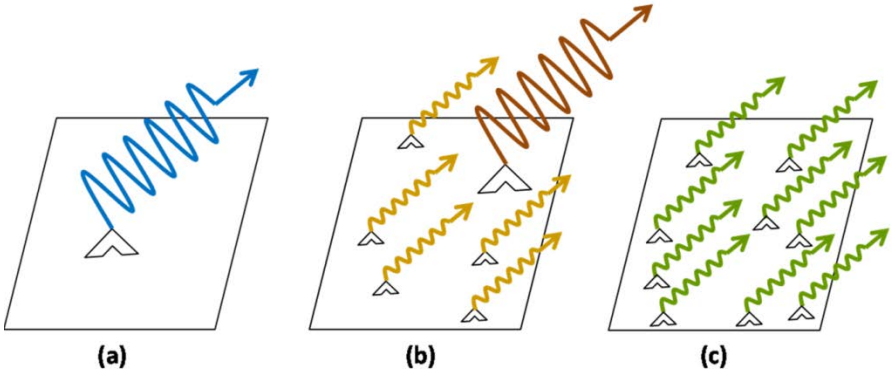

Figure 8: Modelling of scattering mechanism inside a SAR resolution cell. (a) Point scatterer. (b) PS with one (or more) dominating scatterer within a resolution element. (c) DS with multiple subscatterers within a resolution element (where no single subscatterer dominates the others).

The covariance between two complex SAR images s_1 and s_2 for a pixel is defined as the expectation of the product of the first with the complex conjugate of the second (Bamler and Hartl, 1998):

$$c = E\left(s_1 \cdot \left(s_2\right)^*\right) \tag{18}$$

The complex correlation coefficient (also referred to as the complex coherence) γ of the two SAR images for a pixel is obtained by normalizing the covariance by the standard deviation of the two images and is given by:

$$\gamma = \frac{E\left(s_1 \cdot \left(s_2\right)^*\right)}{\sqrt{E\left(\left|s_1\right|^2\right) \cdot E\left(\left|s_2\right|^2\right)}} \tag{19}$$

The Maximum Likelihood (ML) estimate $\hat{\gamma}$ of the correlation is obtained from L independent samples (i.e. looks):

$$\hat{\gamma} = \frac{\sum_{i=1}^{L} s_1^i \cdot \left(s_2^i\right)^*}{\sqrt{\sum_{i=1}^{L}\left|s_1^i\right|^2 \cdot \sum_{i=1}^{L}\left|s_2^i\right|^2}} \tag{20}$$

Usually, the samples are selected from a local spatial estimation window, for example, a rectangular patch around the pixel of interest (although, it is possible to do an ensemble average for a pixel by including spatial as well as temporal samples). The magnitude $\left|\hat{\gamma}\right|$ of the correlation, usually called coherence, is a measure of the phase noise of the pixel under consideration. It ranges from 0 to 1, 1 being the coherence for a noise-free interferometric pixel. The coherence describes the SNR:

$$SNR = \frac{\left|\hat{\gamma}\right|}{1-\left|\hat{\gamma}\right|} \tag{21}$$

The phase $\arg\{\hat{\gamma}\}$ of the correlation is the expected interferometric phase of the pixel. The phase standard deviation σ_ϕ of a pixel is a function of the coherence and the number of looks. It is worth mentioning that the estimator in Equation (20) is biased, it tends to overestimate low coherence. It becomes asymptotically unbiased for large number of looks, but this decreases the resolution. There are approaches available for unbiased coherence estimation (Touzi et al., 1999). The estimator also underestimates the coherence in case of interferometric fringes present due to residual digital elevation model (DEM), local slope etc.

(Zebker and Chen, 2005). Moreover, a rectangular estimation window can lead to averaging of pixels arising from different distributions leading to a wrong estimation of the correlation.

The *decorrelation* in SAR interferograms (i.e. decrease in coherence) occurs due to various factors such as geometric and Doppler decorrelation, temporal decorrelation and thermal noise.

The geometric decorrelation happens because the same ground resolution element is imaged from two slightly different look directions. It leads to a shift in the range spectra of the two SAR images. There exists a critical perpendicular baseline for every SAR system, above which there is a complete loss of coherence. The geometric decorrelation can be compensated in the Fourier transform domain via spectral shift filtering. The Doppler decorrelation occurs due to different Doppler centroids for the two images as they are taken with different squint angles. It can be mitigated in the Fourier transform domain by common band filtering.

When two SAR acquisitions are taken at different times, the reflectivity of the resolution cell might change. Since the backscattering depends on the terrain composition and roughness, any change in the terrain properties leads to a change in the reflectivity. This leads to temporal decorrelation. It is dependent on the wavelength used and the land coverage (e.g. water decorrelates in fractions of seconds, vegetation decorrelates in a few days, whereas buildings remain long-time coherent). Temporal decorrelation is difficult to model as it could occur due to changes in weather, anthropogenic activities or even natural hazards.

Thermal noise is mostly due to internal circuitry of the SAR instrument.

While InSAR is quite efficient in various applications of remote sensing, it has limitations due to decorrelation, atmospheric propagation effects and low temporal sampling rate. As a consequence, stacking techniques have been developed which overcome some of the limitations of conventional InSAR. These multitemporal techniques are either based on PSs or DSs and have been described in the next section.

2.3 Coherent Stacking Techniques

The coherent stacking methods involve the simultaneous processing of a stack of SAR images of the same area, which are taken at different times, for monitoring deformation time series and residual topography (after compensation of a DEM).

In *PSI*, PSs are exploited and differential interferograms with respect to a single master image are formed (Ferretti et al., 2000; Ferretti et al., 2001). The main idea behind PSI is that some of these interferograms might have a large perpendicular baseline or a large temporal baseline, and are hence affected by strong decorrelation noise. Thus, only points which do not change their scattering characteristics in time can preserve the interferometric phase information. It is thus implied that only the signal phases of permanently coherent PSs can be retrieved for interferometry in PSI. The interferograms are analysed at PSs to maximize the SCR. PSI uses a deformation model for the estimation.

TomoSAR is another technique which can be used for PSs and/or DSs and is an innovative evolution of classical interferometric stacking (Reigber and Moreira, 2000; Lombardini, 2005; Fornaro et al., 2009; Zhu and Bamler, 2010a). Instead of exploiting just the phase information of the acquired stack, the whole complex information is processed. TomoSAR extends the

principle of synthetic aperture onto the elevation direction for a real and unambiguous 3D imaging of a scene. It images multiple scatterers (present in the same resolution cell) along the elevation direction. Applications include retrieval of different persistent scattering mechanisms inside the same resolution cell and their corresponding reflectivity to counter radar layover. In fact, InSAR is actually the first step towards 3D imaging, however, it only allows mapping of the mean phase center of all scatterers present in a resolution cell. TomoSAR, on the other hand, provides a complete 3D representation of the scene. Differential TomoSAR (DTomoSAR) is a further extension which retrieves the elevation as well as the deformation information of multiple scatterers inside the same resolution cell and thus, provides a 4D imaging. PSI is a special case of DTomoSAR where only a single scatterer inside a pixel is assumed.

DS-based techniques include SBAS and SqueeSAR. The *SBAS* method exploits only small baseline (temporal and spatial) unwrapped differential interferograms, so as to limit the effects of uncompensated geometric decorrelation and temporal decorrelation on the DSs (Berardino et al., 2002). These interferograms are multi-looked to reduce the phase noise and improve the phase estimate. SBAS estimates the non-linear deformation time series via the Singular Value Decomposition (SVD) without using any deformation model (Golub and Loan, 1996).

The *SqueeSAR* technique uses all possible differential interferograms to get the best possible estimates of the phases associated with the deformation of each DS (Ferretti et al., 2011). It also employs an adaptive multi-looking of the interferograms to decrease the phase noise. A deformation model is assumed for the estimation. SqueeSAR increases the spatial density of measurement points over areas characterized by DSs, while preserving the high-quality information obtained using the PS technique over deterministic targets.

The methodologies of the above-mentioned techniques are described below.

2.3.1 Persistent Scatterer Interferometry

The PSI technique was developed by A. Ferretti, C. Prati and F. Rocca in the late 1990s for long-term *deformation monitoring, especially in urban environments* (Ferretti et al., 2000; Ferretti et al., 2001). Since then, similar approaches have been proposed by different scientists (Adam et al., 2003; Hooper et al., 2004; Kampes, 2006). The PSI processing consists of the following main steps:

- Given a stack of $N+1$ coregistered and calibrated SAR scenes, N differential interferograms are formed with respect to a chosen master scene. A reference DEM (which can be of moderate spatial resolution) is used to compensate for the topographic phase. The master scene is selected so as to maximize the coherence of the interferograms by limiting their baseline spread (usually, the master scene lies in the middle of the time series). The unwrapped phase for a generic pixel in the kth differential interferogram is given by Equation (15). Note that wrapped differential interferograms are used in PSI, since as can be seen later, the estimation is performed in the complex domain.
- Pixels are selected which contain a single PS, i.e. which exhibit a low phase dispersion with respect to time. There are two ways of doing this:

- For high SNR, the normalized amplitude dispersion index D_a is a good measure of the phase standard deviation σ_ϕ and is given by (Ferretti et al., 2001):

$$D_a = \frac{\sigma_a}{\mu_a} \approx \sigma_\phi \tag{22}$$

where σ_a and μ_a are the sample standard deviation and the mean, respectively of the amplitude time series a. Pixels with a normalized amplitude dispersion index below a certain threshold (ca. 0.25) are selected as initial PS candidates.

- Another method to detect PSs is to evaluate the SCR of the pixels in the temporal mean image. The clutter is estimated from the neighboring pixels using a certain spatial estimation window, assuming that the clutter surrounding the dominating scatterer within a resolution cell is comparable to clutter in the nearby pixels (which consist of clutter only). The phase standard deviation of the PS is given by (Adam et al., 2004):

$$\sigma_\phi \approx \frac{1}{\sqrt{2 \cdot SCR}} \tag{23}$$

Pixels with an SCR above a certain threshold (ca. 2) are selected as PSs.

- A preliminary estimation step is performed on the initial set of PS candidates to separate the atmospheric phase components from the interferograms. A reference network is established where neighboring PSs are linked by arcs and a reference point is assigned for the network. Typically, only points that are closer than a certain distance are linked. Phase differences between these points joined by the arcs are computed, since the error sources such as atmospheric propagation effects and orbital effects are not large enough to cause phase unwrapping problems if the arcs are typically limited to 2-3 km (Hanssen, 1998; Hanssen, 2001). The phase difference $\Delta\phi^k_{DInSAR\_model}$ between two generic pixels (connected by an arc in the reference network) in the k th differential interferogram can be computed from Equation (15) and is modelled as follows (assuming a constant velocity model):

$$\Delta\phi^k_{DInSAR\_model} = \Delta\phi^k_{defo} + \Delta\phi^k_{res\_topo} = \frac{4\pi}{\lambda} B^k_t \Delta v + \frac{4\pi}{\lambda} \frac{B^k_\perp}{R \sin\theta} \Delta h_{res} \tag{24}$$

where Δv and Δh_{res} are the differential displacement velocity in the LOS and the differential DEM error between the two points, respectively and $k = 1,...,N$. The following model coherence function (periodogram) ξ is maximized for differential velocity and differential DEM error estimation:

$$\xi(\Delta v, \Delta h_{res}) = \frac{1}{N} \left| \sum_{k=1}^{N} e^{j\left(\Delta\phi^k_{DInSAR\_obs} - \Delta\phi^k_{DInSAR\_model}\right)} \right| \tag{25}$$

where $\Delta\phi^k_{DInSAR\_obs}$ is the observed phase difference between the two pixels in the k th differential interferogram. The periodogram is a 2D function dependent on the differential velocity and differential DEM error. Its values are known over an irregular grid defined by the available temporal baselines B^k_t and spatial baselines $B^k_\perp$. The differential velocity and differential DEM error are estimated from the peak of this periodogram, i.e.

$$\left(\Delta\hat{v}, \Delta\hat{h}_{res}\right) = \underset{(\Delta v, \Delta h_{res})}{\arg\max}(\xi) \tag{26}$$

Note that in the literature, the maximum of the periodogram is misleadingly called the "temporal coherence" of the neighboring scatterers, although it has nothing to do with

the phenomenon of temporal decorrelation which was discussed in the previous section. It actually describes how well the interferometric phase observations fit the used interferometric phase model. Nonetheless, this terminology would be adopted and used later also in this dissertation as a measure of goodness-of-fit. After estimating the differential velocities and differential DEM errors for each arc, an integration is performed to estimate the velocities and DEM errors for each PS with respect to the reference pixel. A weighted least squares integration is used for this, wherein, arcs with a temporal coherence below a certain threshold are discarded and other arcs are weighted according to the temporal coherence values. The low-pass deformation and the DEM error phase components are then removed from the interferograms for the selected PSs. After this, a low-pass filtering is performed in the spatial domain, followed by a high-pass filtering in the time domain to estimate the atmospheric phase components for the initial PS candidates, since the atmospheric phase components exhibit a high spatial correlation but a low temporal correlation. Subsequently, an interpolation is performed to get the atmospheric phase components of the whole area for each interferogram, called the Atmospheric Phase Screen (APS). The estimated APS is then subtracted from the original data.

- Finally, all the remaining PS candidates are selected and for each of these points, the deformation velocity and the residual DEM are estimated relative to the closest PS of the reference network. This is comparable to the estimation of single arcs via Equation (26). Points exhibiting a temporal coherence below a certain threshold (ca. 0.75) are discarded. The PSs location is then geocoded and the deformation information provided to the end users.

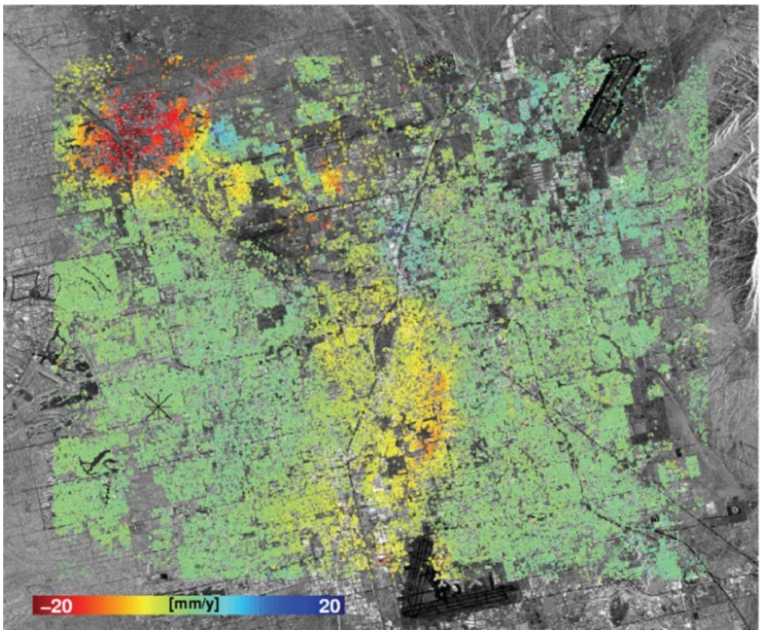

Figure 9: Linear deformation rates estimated for Las Vegas area in US via PSI exploiting 45 ERS-1/2 images from 1992-2000. The local subsidence has been mainly caused by groundwater extraction. (Bamler et al., 2006)

The quality of the PS analysis depends on the number of available images and the density of PSs. A minimum of about 25 images and a PS density of approximately 5-10 PS/km2 are needed (Colesanti et al., 2003). In addition, a deformation model has to be defined prior to deformation estimation. Typically, a linear model is assumed, although it is also possible to use seasonal or some other non-linear deformation models (Ferretti et al., 2000; Colesanti et al., 2003). Besides, if there are multiple dominant scatterers inside the same resolution cell, their separation is not possible using conventional PSI. PSI algorithms have been proposed to

resolve double scatterers (i.e. two dominant scatterers located at different elevations) inside a resolution cell (Ferretti et al., 2005; Adam et al., 2005).

PSI allows millimeter precision in deformation mapping. Figure 9 shows the estimated linear deformation rates for Las Vegas area in US after applying PSI on 45 ERS-1/2 acquisitions from 1992-2000 (Bamler et al., 2006). DLR's operational PSI module of the GENEric System for Interferometric SAR (PSI-GENESIS) has been employed for this (Adam et al., 2003; Adam et al., 2004; Kampes, 2006). It includes DInSAR processing. The coregistration module of the processor uses a geometry based algorithm which utilizes precise orbits and a DEM from SRTM. The PSI-GENESIS processing system is free from systematic errors and thus, has been chosen as the reference for the product validation of various PSI operational service providers (Adam et al., 2009).

2.3.2 SAR Tomography

The first concept for 3D imaging of continuous volumetric scatterers using TomoSAR was presented by A. Reigber and A. Moreira in 2000 (Reigber and Moreira, 2000). This can be used, for instance, in volumetric imaging of forests. In this chapter, instead of retrieving the reflectivity function along the elevation direction for a continuous volume scatterer, the case of several PSs inside one resolution cell is more of interest. This can be applied for *resolving layover in urban areas* (Lombardini, 2005; Fornaro et al., 2009; Zhu and Bamler, 2010a).

For large range distances and small angular diversities (which is true for spaceborne SAR), TomoSAR is a spectral estimation problem. Different parametric and non-parametric methods can be used for the spectral estimation using a stack of $N+1$ complex SAR acquisitions taken from slightly different viewing angles (distributed spatially and temporally). These methods exploit either single-look (for PSs) or multi-look data (for DSs). Parametric methods model the data and estimate the model parameters, whereas non-parametric methods make no assumptions about the statistical properties of the received signals. Generally, parametric methods may provide a better estimation if the data closely agrees with the assumed model, otherwise, non-parametric methods may be better. Parametric methods for single-look data include the Non-linear Least Squares (NLS) (Zhu and Bamler, 2010a). Non-parametric methods for single-look data include Beamforming (BF) (Fornaro et al., 2009) and SVD (Fornaro et al., 2009; Zhu and Bamler, 2010a). These non-parametric methods have limitations due to short length of the synthetic aperture in elevation, low number of samples and their irregular distribution. Compressive Sensing (CS), a sparse reconstruction technique, is a modern method which provides a good compromise between classical parametric and non-parametric spectral analysis methods. It is more robust to phase noise, requires lower computational efforts without any model selection and has super-resolution properties (Budillon et al., 2009; Zhu and Bamler, 2010b).

TomoSAR has been applied on Hotel Wynn in Las Vegas, US, exploiting 25 TerraSAR-X acquisitions (High Resolution Spotlight mode) from 2008-2009 (Zhu and Bamler, 2010a). The preprocessing, including the APS correction, has been performed using DLR's PSI-GENESIS system (Adam et al., 2003; Adam et al., 2004; Kampes, 2006). Figure 10 (a) visualizes the hotel in Google Earth and also shows the LOS of the SAR sensor. The top of the building (marked in red) and the ground (marked in red) are mapped onto the same resolution cell. Figure 10 (b) shows a corresponding TerraSAR-X amplitude image. Two points, P1 (single scatterer) and P2 (double scatterer), have been chosen for TomoSAR

analysis. Normalized reflectivity has been estimated along the elevation direction using the SVD method for these two points, as shown in Figure 11 (a) and Figure 11 (b), respectively. As expected, point P1 has a single peak and is proven to be a single scatterer on the ground, while point P_2 has two peaks and is proven to be a double scatterer.

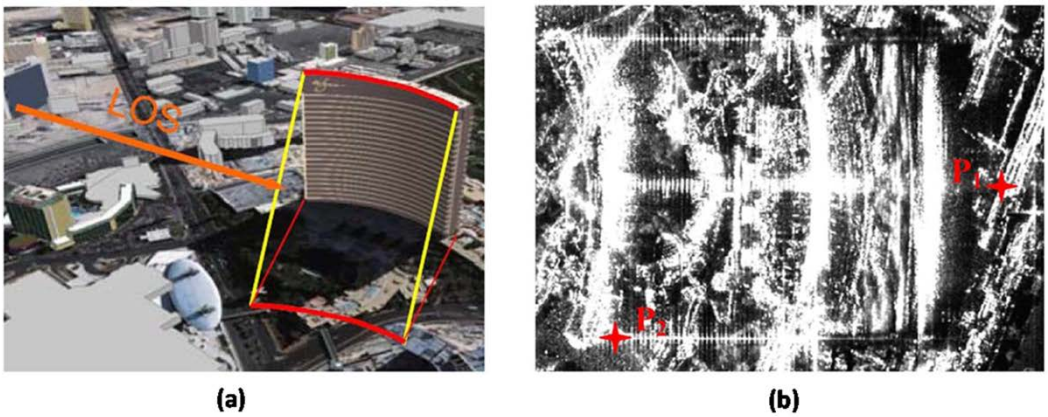

Figure 10: Hotel Wynn, Las Vegas, US. (a) Google Earth optical image with viewing direction of SAR (LOS). (b) TerraSAR-X amplitude image with analysis points P_1 and P_2. (Zhu and Bamler, 2010a)

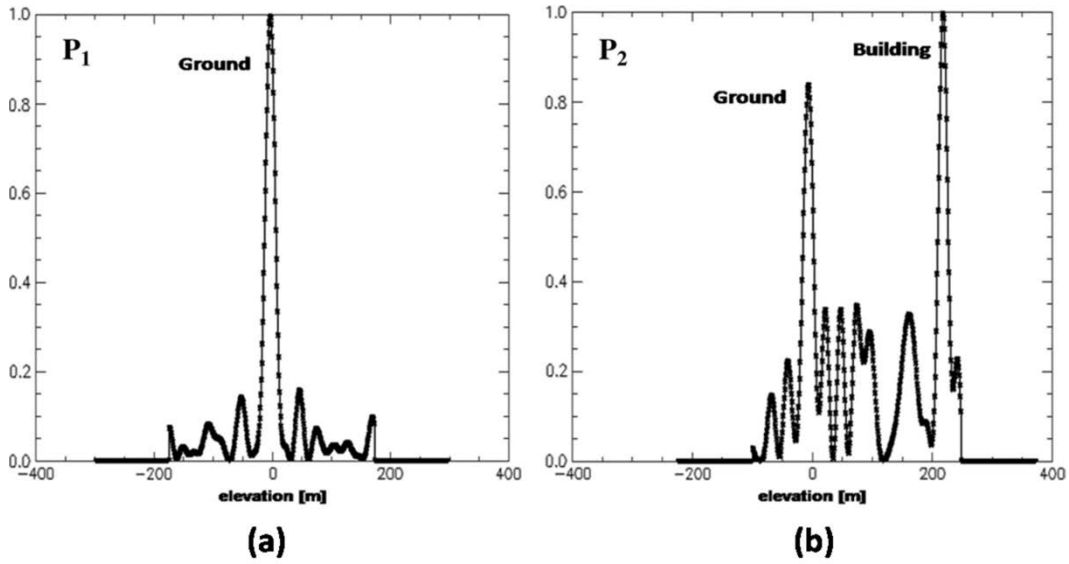

Figure 11: Normalized reflectivity estimates along the elevation direction for two points (marked in Figure 10) using TomoSAR exploiting 25 TerraSAR-X acquisitions from 2008-2009. (a) Analysis point P_1 is a single scatterer. (b) Analysis point P_2 is a double scatterer. (Zhu and Bamler, 2010a)

2.3.3 Small Baseline Subset Algorithm

The SBAS technique was developed by P. Berardino, G. Fornaro, R. Lanari and E. Sansosti in 2002 for *generating deformation time series, with a focus on non-urban areas* (Berardino et al., 2002). An extension of standard SBAS has been proposed too (Lanari et al., 2004). Additionally, similar techniques based on small baseline differential interferograms have been developed, for example, the Coherent Pixels Technique (Mora et al., 2003; Blanco-Sanchez et al., 2008). The basic processing steps in SBAS are as follows:

- Given a stack of $N+1$ coregistered and calibrated SAR scenes acquired at times t^n where $n = 0,...,N$; M multi-look small baseline (temporal and spatial) differential

interferograms are generated. A reference DEM (which can be of moderate spatial resolution) is used to compensate for the topographic phase. The use of small baselines limits temporal decorrelation and uncompensated spatial decorrelation, thus, providing spatially dense deformation maps. However, it could result in separation of the interferograms into different subsets in the baseline-time domain. SBAS can link the independent subsets using SVD provided that the subsets overlap in time, as described later in this subsection. This increases the temporal sampling rate.

- Next, pixels (i.e. DSs) are identified that exhibit an average spatial coherence greater than a certain threshold (ca. 0.3) and SBAS is applied only to those pixels.
- The differential interferograms are then spatially unwrapped. The unwrapped phase for a generic pixel in the k th differential interferogram is given by Equation (15). All coherent pixels are then referenced to one non-deforming pixel with high coherence.
- After the phase unwrapping step, the low-pass component of the deformation signal and topographic error are estimated for each coherent pixel via the Least Squares (LS) solution of the following system of equations:

$$[BM, c]p_c = \phi_{DInSAR} \tag{27}$$

where B is the matrix defining the small baseline combinations used, M is the matrix corresponding to a displacement model, c is the vector corresponding to the DEM error, ϕ_{DInSAR} is the vector of unwrapped differential interferometric phase values and p_c is the vector of unknown parameters, namely, the low-pass component of the deformation signal and topographic error. It is important to note that the displacement model is only used in this step and does not restrict the estimation of unmodelled deformation later on. After this, the estimated residual topography and low-pass deformation are subtracted modulo-2π from each interferogram, resulting in a fringe rate reduction. Accordingly, a new unwrapping step is then applied to the residual wrapped phase, the phase unwrapping being considerably simplified. By adding back the subtracted low-pass deformation, refined unwrapped differential interferograms are obtained.

- These resulting small baseline interferograms form the following linear model for every coherent pixel:

$$Bv = \phi'_{DInSAR} \tag{28}$$

where ϕ'_{DInSAR} is the vector of unwrapped differential interferometric phase values after the removal of topographic error and v is the vector of unknown mean phase velocities between time-adjacent acquisitions, i.e.:

$$v^T = \left[v^1 = \frac{\phi^1}{t^1 - t^0}, ..., v^N = \frac{\phi^N}{t^N - t^{N-1}} \right] \tag{29}$$

where $\phi^T = \left[\phi^1, ..., \phi^N\right]$ is the vector of the N unknown phase values associated with the deformation of the considered pixel. Because of the separation of interferograms into different subsets, the rank of B is $N - L + 1$, where $N + 1$ is the number of images and L is the number of subsets and thus, Equation (28) would have infinite solutions. A minimum-norm LS solution (L2-norm minimization) of Equation (28) is obtained by using the SVD method (Golub and Loan, 1996). The matrix B is decomposed into matrices U, S and V as follows:

$$B = USV^T \tag{30}$$

where S is composed of the singular values and is given by $S = diag\left(\sigma^1, ..., \sigma^{N-L+1}, 0, ..., 0\right)$. The estimate $\hat{v}$ is then given by:

$$\hat{v} = VS^+U^T\phi'_{DInSAR} \tag{31}$$

where $S^{+} = diag\left(1/\sigma^{1},...,1/\sigma^{N-L+1},0,...,0\right)$. An additional integration step gives the solution ϕ.

- Later, for estimating the atmospheric propagation effects, a low-pass filtering is performed in the spatial domain (after removing the estimated low-pass deformation). This is followed by a high-pass filtering in the time domain because the atmospheric phase components exhibit a high spatial correlation but a low temporal correlation. This is similar to the PS approach for removing the APS (Ferretti et al., 2000; Ferretti et al., 2001).

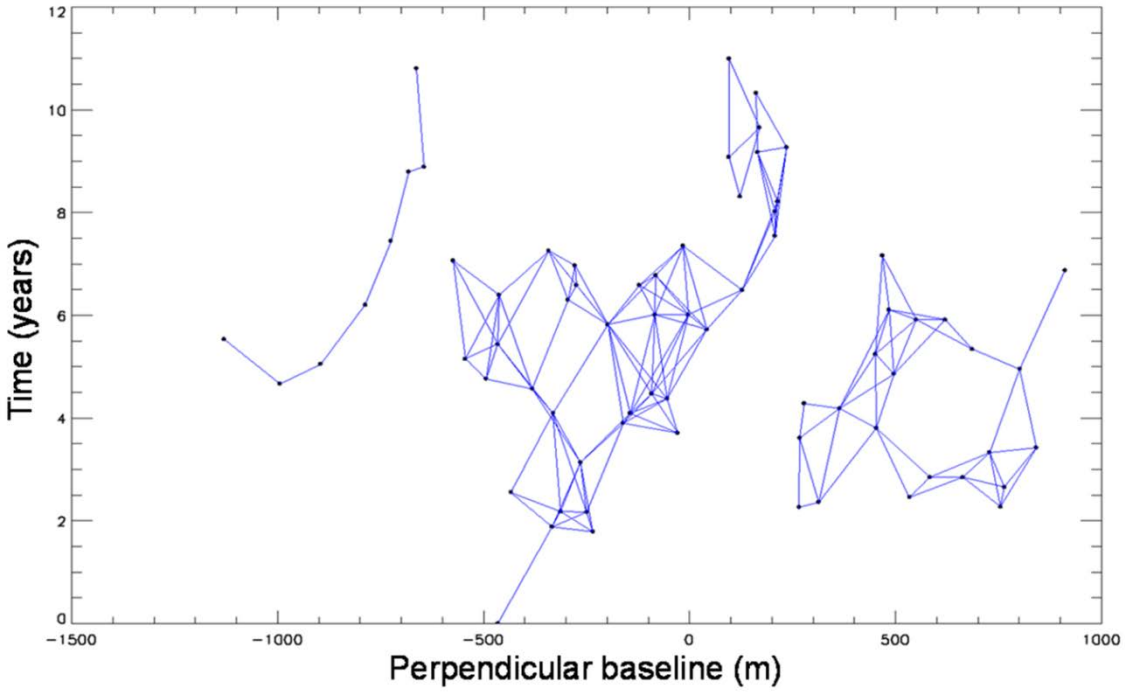

Figure 12: Baseline-time plot for Gardanne coal mine, France. Each dot corresponds to a SAR image and each line corresponds to an interferogram. 72 ERS images from 1993-2004 were used to generate 165 small baseline differential interferograms. (Goel et al., 2011)

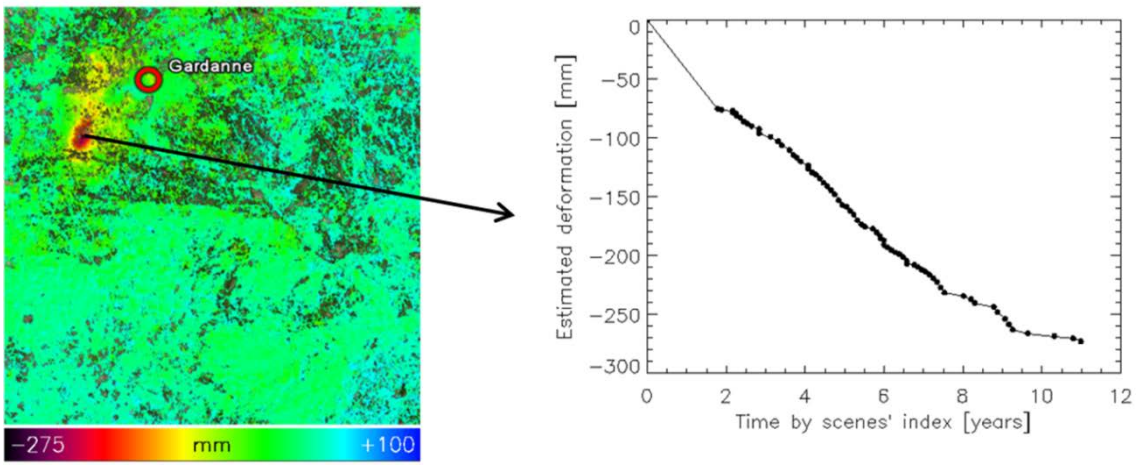

Figure 13: Cumulative deformation estimated for Gardanne coal mine, France, via SBAS exploiting 72 ERS images from 1993-2004. Two subsidence bowls are visible (one having a larger deformation than the other and also covering a larger area). The cumulative deformation is largest in the center of the bowls and gradually decreases going away from the center. A maximum of 273.5 mm of cumulative deformation has been measured, as shown in the deformation time series for the most deforming pixel. (Goel et al., 2011)

Advantageously, SBAS provides complete non-linear deformation time series of the scatterers using the SVD method which does not require any modelling. SBAS has been applied on Gardanne coal mine, which is located in Southern France between Aix-en-Provence and Marseille, close to the town of Gardanne (Goel et al., 2011). 72 ERS images from 1993-2004 have been used to generate 165 differential interferograms based on spatial baseline threshold of 150 m and temporal baseline threshold of 700 days. A rectangular multi-looking with 4 looks in the range direction and 20 looks in the azimuth direction has been performed, so as to reduce phase noise and obtain square pixels of about 80 meters in both directions. DLR's PSI-GENESIS processor has been used for DInSAR processing (Adam et al., 2003; Adam et al., 2004; Kampes, 2006). The phase unwrapping is based on the Minimum Cost Flow (MCF) algorithm (Costantini, 1998; Eineder et al., 1998). Figure 12 shows the baseline-time plot for Gardanne, where, each dot corresponds to a SAR image and each line corresponds to an interferogram. The interferograms are separated into 3 subsets. The deformation estimates are shown in Figure 13.

2.3.4 SqueeSAR

SqueeSAR, recently developed by A. Ferretti, A. Fumagalli, F. Novali, C. Prati, F. Rocca and A. Rucci in 2011, is a technique that *extracts information from DSs making use of all possible interferograms* (Ferretti et al., 2011). Following the basic concept of SqueeSAR, another similar approach has been proposed (Wang et al., 2012). The basic steps in SqueeSAR are as follows:

- Given a stack of $N+1$ coregistered and calibrated SAR acquisitions, SqueeSAR, first, employs the Kolmogorov-Smirnov statistical test (Papoulis and Pillai, 2002) on each pixel to identify its statistically homogenous "brother" pixels, exploiting the amplitude data stack.
- Next, DSs are identified based on a minimum number of "brother" pixels (ca. 20) and a minimum average spatial coherence (ca. 0.3).
- For each DS, the sample covariance matrix is estimated utilizing its "brother" pixels (Zan, 2008). The covariance matrix corresponds to the complex covariance between all image pairs for a DS. The covariance values can be arranged in a square matrix having the number of rows and columns equal to the number of images in the dataset. Instead of using covariance matrix, complex coherence (i.e. correlation) matrix can instead be used too. As mentioned before in Subsection 2.2.2, for an image pair, the amplitude of the complex coherence is the coherence of the pixel, whereas the phase of the complex coherence is the filtered (adaptive multi-looked) interferometric phase of the pixel. Since SqueeSAR is based on the analysis of the covariance or complex coherence matrix, all possible interferograms are generated and the associated coherence values are computed, regardless of the temporal or geometrical baseline. In (Wang et al., 2012), a phase defringing (i.e. flattening) is performed prior to the coherence estimation in order to correct for estimation biases in the presence of interferometric fringes due to topography, motion etc. It involves an adaptive multi-resolution fringe frequency estimation by searching for the maximum coefficient in the Fourier transform of local patches (Zebker and Chen, 2005; Davidson and Bamler, 1999).
- Afterwards, a phase triangulation algorithm is applied to the covariance matrix of each DS to retrieve the N optimized phase values associated with the deformation of each DS. In other words, a ML estimation is performed to yield the best possible estimates

of the phase values fitting all interferograms (i.e. the covariance matrix elements) for each DS. The name SqueeSAR indeed comes from the fact that the information needs to be "squeezed" out from the covariance matrix of each DS.

- The DSs are then processed jointly with the PSs for deformation monitoring, using the traditional PS interferometric chain. Note that a deformation model has to be defined prior to deformation estimation.

SqueeSAR provides motion parameter estimates for DSs with significantly enhanced SNR. A demonstration of the estimation of deformation histories of DSs in urban areas via SqueeSAR is provided in Figure 14 (Wang et al., 2012). It shows the estimated seasonal deformation amplitudes for the area around Paris Las Vegas Hotel in Las Vegas, US. 50 TerraSAR-X acquisitions from 2008-2010 have been utilized. The pre-processing, including amplitude calibration and APS correction, has been performed using the PSI-GENESIS system from DLR (Adam et al., 2003; Adam et al., 2004; Kampes, 2006). The PSs have been processed using the standard PSI technique, while DSs have been processed using SqueeSAR. As can be seen, the PSs provide a good coverage over most parts of the building façades, except for the upper half of the tower due to its complex motion. The DSs give extra information over the rest of the image. Therefore, it can be concluded that SqueeSAR increases the density of measurement points for which deformation and residual DEM can be estimated.

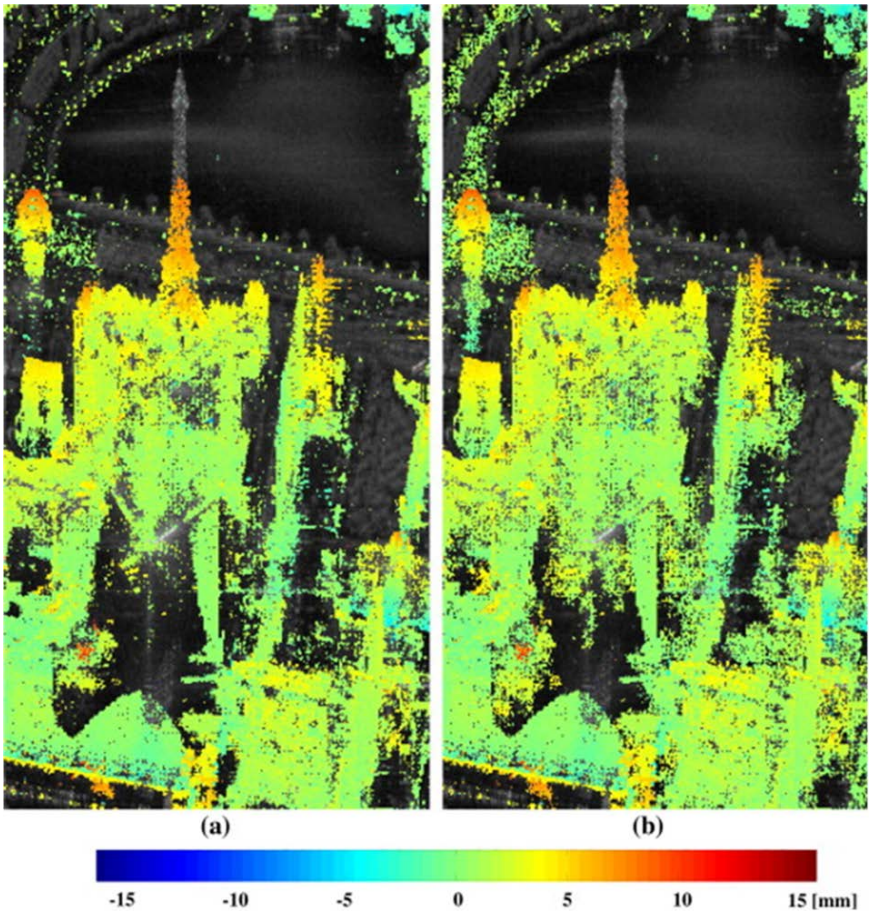

Figure 14: Seasonal deformation amplitudes estimated for area around Paris Las Vegas Hotel in Las Vegas, US, via PSI (for PSs) and SqueeSAR (for DSs) exploiting 50 TerraSAR-X acquisitions from 2008-2010. (a) Only PSs. (b) Both PSs and DSs. (Wang et al., 2012)

2.4 Discussion and Conclusion

The potential advantages of the coherent stacking techniques, discussed previously in this chapter, are evident. The SAR satellites such as TerraSAR-X, TanDEM-X and COSMO-SkyMed are providing data with higher resolution, shorter revisit times and better orbit control, thus, facilitating cutting-edge interferometric applications. For the first time, the availability of these high resolution data has given the opportunity to map deformation for a large number of scatterers with good precision and also relate the scatterers to real world objects. However, *there are still limitations in this field that need to be overcome* as discussed below.

PSI and TomoSAR are most powerful in urban areas because there are a lot of man-made structures, and consequently a large number of PSs. The high resolution SAR sensors have made it possible to retrieve millimetric ground displacements and structural stress of individual buildings from space. Nevertheless, the density of PSs is low in non-urban areas which are characterized by vegetated or low reflectivity homogenous regions. Another key drawback is the difficulty to apply these methods in case of strong non-linear motion and fast deformation. Furthermore, geometrical limitations such as radar layover lead to wrong estimation using PSI. TomoSAR provides a solution for the layover problem, but it is an advanced technique and the computational efficiency is restricted by the dimension of the spectral estimation (3D, 4D or higher dimensions in case of multi-component motion), search range in each dimension and the applied spectral estimation algorithm (e.g. compressive sensing is computationally very expensive).

SBAS and SqueeSAR exploit DSs, which have a higher density in rural areas. In conventional SBAS, the interferograms are spatially filtered before the stacking to enhance the SNR. However, the straightforward rectangular estimation window (i.e. boxcar multi-looking) results not only in a reduction of resolution and a superposition of different objects on ground but also in a loss of deformation information contained in isolated pixels. Additionally, abrupt changes in deformation are smoothed out. A technique has been presented to extend standard SBAS (Lanari et al., 2004). It uses both single-look and multi-look data and provides deformation at two spatial scales, regional and local. Yet, there is still a need for fully exploiting the high resolution SAR data available from sensors such as TerraSAR-X and extracting deformation at a high resolution. Additionally, phase unwrapping is an important step in SBAS and local phase unwrapping errors often occur and are difficult to detect in data with a lot of fringe discontinuities, which is especially the case in natural terrains. Several decorrelated areas such as forests, water etc. might separate the coherent areas and the relative values in the different coherent patches can have unknown integer multiples of 2π phase offsets, thus making phase unwrapping time consuming and error prone. Although some endeavours have been made to limit the impact of severe phase unwrapping errors on the estimated deformation time series, for example, techniques have been proposed to exploit both the temporal and the spatial structure of the data by a 3D phase unwrapping and further extend the MCF algorithm (Pepe and Lanari, 2006; Fornaro et al., 2011), nonetheless, phase unwrapping still remains a major source of error in spotted coherent areas and is time consuming too. SqueeSAR, on the other hand, can be computationally expensive as it utilizes all possible interferograms. Also, it usually assumes a model for the deformation and is not suitable for phenomena characterized by highly non-linear deformation.

With respect to the above mentioned techniques, new/alternative multitemporal approaches for high resolution deformation estimation have been developed as part of this dissertation. The next chapters are dedicated to presenting these novel techniques and application test cases using TerraSAR-X/TanDEM-X data. In fact, the developed estimation principles are among the first ones which utilize this new class of meter resolution SAR data and improve the robustness and precision of the estimates. It has been successfully demonstrated that these techniques provide spatially dense deformation maps for areas characterized either by high temporal decorrelation or by layover problems, and counteract some of the limitations of conventional coherent SAR techniques.

3 Advanced Small Baseline Subset Algorithm

An advanced differential SAR interferometry stacking algorithm is presented in this chapter for *high resolution deformation monitoring in non-urban areas* exploiting DSs. The following paper is summarized (Goel and Adam, 2012a):

A.1 Goel, K., Adam, N., 2012a. An advanced algorithm for deformation estimation in non-urban areas. ISPRS Journal of Photogrammetry and Remote Sensing 73, 100-110.

Two case studies of a gas storage reservoir and the town of Lueneburg in Germany, using high resolution TerraSAR-X data, are presented to demonstrate this new technique.

3.1 Introduction

A major limitation in SAR's ability to map deformation in non-urban areas is the decorrelation of signals with time over large areas, leading to a high phase noise. As reviewed in the previous chapter, SBAS and SqueeSAR are two options which are suitable for deformation mapping in such regions, but they have some limitations. Conventional SBAS estimates deformation at a low spatial resolution and is prone to phase unwrapping errors. SqueeSAR makes use of all possible interferograms leading to a high computational burden and assumes a temporal model (e.g. a constant velocity model) for the deformation.

An advanced SBAS approach has been developed for high resolution deformation monitoring with a focus on natural terrains characterized by typical temporal decorrelation and phase ambiguities. It is based on an *object-adaptive parameter estimation*, exploiting only the *small baseline differential interferograms* so as to reduce the effects of topography on the DSs. The practical implementation starts with an accurate phase and coherence estimation and residual topography removal for the small baseline interferograms using an adaptive spatial phase filtering algorithm (Ferretti et al., 2011; Parizzi and Brcic, 2011; Goel and Adam, 2011). It reduces the phase noise while maintaining the high geometric resolution provided by new satellites such as TerraSAR-X (meter resolution). Subsequently, the phase estimates are used to retrieve the non-linear deformation time series using an L1-norm based SBAS technique (Lauknes et al., 2011). This results in a more robust solution with respect to the often-occurring and difficult-to-detect phase unwrapping errors found in non-urban areas.

3.2 Methodology

Assuming that *N SAR images* and *M single-look small baseline differential interferograms* are available, the implemented methodology for deformation estimation in rural regions consists of the following two steps:

3.2.1 Adaptive Spatial Phase Filtering

The first step involves an *improved estimation of the differential interferometric phase and coherence* even in the presence of high phase noise and error sources (e.g. temporal

decorrelation, topographic errors and atmospheric propagation effects). The accurate phase estimation supports deformation monitoring techniques such as SBAS and improves the phase unwrapping. The accurate coherence estimation helps in selection of pixels for deformation monitoring as it provides information about temporal decorrelation and also for guiding phase unwrapping algorithms. As mentioned in the previous chapter, this can be achieved by a local spatial multi-looking. Considering the sample amplitude values of images as 1 (i.e. the pixels are not weighted according to their brightness, no assumption is made about a pixel's quality from its brightness) and compensating the deterministic phase components due to topography (for a better estimation of the complex correlation), Equation (20) can be reduced to:

$$\hat{\gamma} = \frac{1}{L}\left(\sum_{i=1}^{L} e^{j\phi_1^i} \cdot e^{-j\phi_2^i}\right) \cdot e^{-j\phi_{topo}} \tag{32}$$

where ϕ_1^i and ϕ_2^i are the phase values of the SAR image pair for the i th pixel of the L neighboring pixels in the estimation window, L being the effective number of looks.

The high resolution of satellites such as TerraSAR-X leads to many resolution cells covering a homogenous object in non-urban areas, i.e. a DS object usually spans several image pixels where the backscattered energy is lower, but statistically homogeneous within the area. The implemented method for an improved high resolution interferometric stacking is based on the assumption that a single "deformation time series" can describe or characterize this object. The object area (i.e. pixels) thus needs to be identified and interferometric phase can be improved by an adaptive spatial filter, which involves a robust local slope estimation for adaptive phase flattening to remove topographic errors and then averaging of the homogenous pixels to reduce phase noise (while preserving object resolution) (Goel and Adam, 2011). The sub-steps involved are shown in Figure 15 and described below:

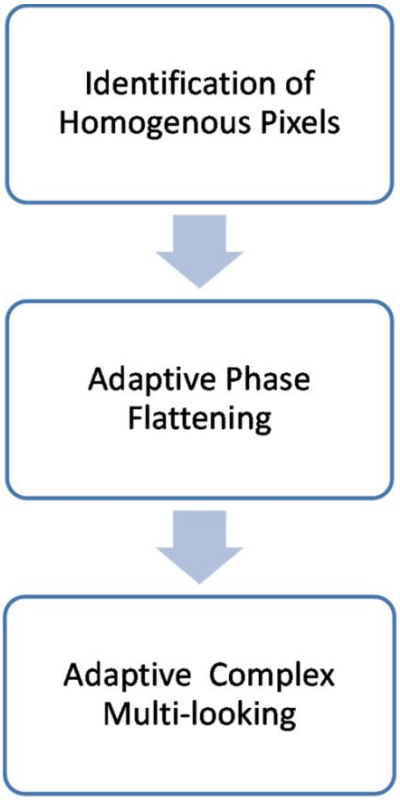

Figure 15: Adaptive spatial phase filtering algorithm for high resolution differential interferometric stacking.

- *Identification of Homogenous Pixels:* The amplitudes of the complex returns are a good indicator for distinguishing between different backscatterer characteristics. Statistically similar pixels can thus be selected for multi-looking based on their amplitude distributions using various statistical tests. Usually, it is assumed that homogenous pixels can be found in a local neighborhood such as a rectangular window. However, they can be far apart depending upon reflectivity and boundaries of objects (fields, trees, roads etc.). The idea is thus to average a given pixel only with neighbors that present similar scattering properties instead of a conventional rectangular (i.e. boxcar) averaging (which results in a loss of resolution and usually biases the estimates).

  Using the stack of N coregistered (up to sub-pixel accuracy) and calibrated SAR amplitude images, the statistically homogenous pixels surrounding each pixel are identified via a statistical test. Different statistical tests have been proposed in recent years, including the Kullback-Leibler Divergence test (Bishop, 2006), the Kolmogorov-Smirnov test (Papoulis and Pillai, 2002; Ferretti et al., 2011) (used in the SqueeSAR approach) and the Anderson-Darling test (Pettitt, 1976). The Anderson-Darling test has been proven to be the most effective test to identify if two pixels arise from the same distribution (Parizzi and Brcic, 2011). It gives the best detection rate at a constant false alarm rate. This test performs reasonably well even for a stack of acquisitions containing as few as 10 images. It is a non-parametric test, i.e. it does not assume that the samples belong to a defined probability distribution. Instead, using the amplitudes of the stack of SAR images, the empirical cumulative distribution functions of amplitudes are obtained for the two pixels (i.e. points) under consideration. The distance between the distributions, with more weighting given to tails, tells if the two points statistically arise from the same distribution. For a set of points a and b, the Anderson-Darling statistic A^2 is:

$$A^2 = \frac{N}{2} \sum_{F_{a,b}(x)} \frac{\left[F_a(x) - F_b(x)\right]^2}{\left[F_{a,b}(x) \cdot \left(1 - F_{a,b}(x)\right)\right]} \tag{33}$$

  where N is the number of SAR amplitude images, $F_a(x)$ and $F_b(x)$ are empirical cumulative distribution functions of amplitudes for points a and b, $F_{a,b}(x)$ is the empirical distribution function of the pooled distribution $[a,b]$. If the Anderson-Darling statistic is less than a threshold value, the two pixels are assumed homogenous.

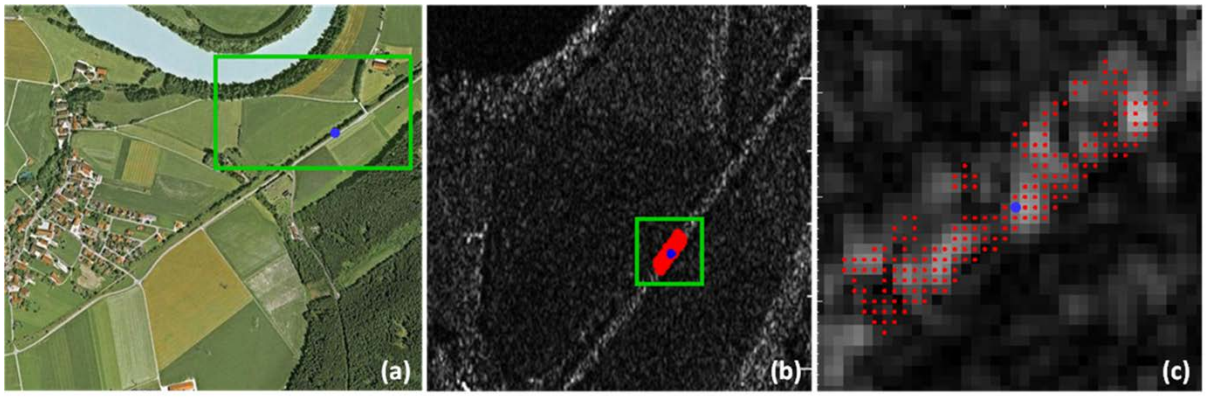

Figure 16: Identification of homogenous pixels (in red) for the blue pixel by Anderson-Darling test. (a) is a Google Earth optical image. (b) is the TerraSAR-X image of the region enclosed in the green rectangle in (a). (c) is a zoom-in of the green rectangle in (b).

Figure 16 shows an example of the Anderson-Darling test. 55 TerraSAR-X images (January, 2008 to May, 2010) of a gas storage reservoir located in Germany were used for the processing. The Anderson-Darling test was performed for the blue pixel (which lies on a road) with each of its neighbors. The homogenous pixels were identified and marked in red. It can be seen that the homogenous pixels identified lie on the same road.

- *Adaptive Phase Flattening:* The homogenous pixels identified are then used for adaptive phase flattening of M single-look small baseline differential interferograms to compensate for topographic residuals (due to errors in the DEM). The phase flattening is important because the topographic errors affect subsequent estimation of an improved phase and coherence (Zebker and Chen, 2005).

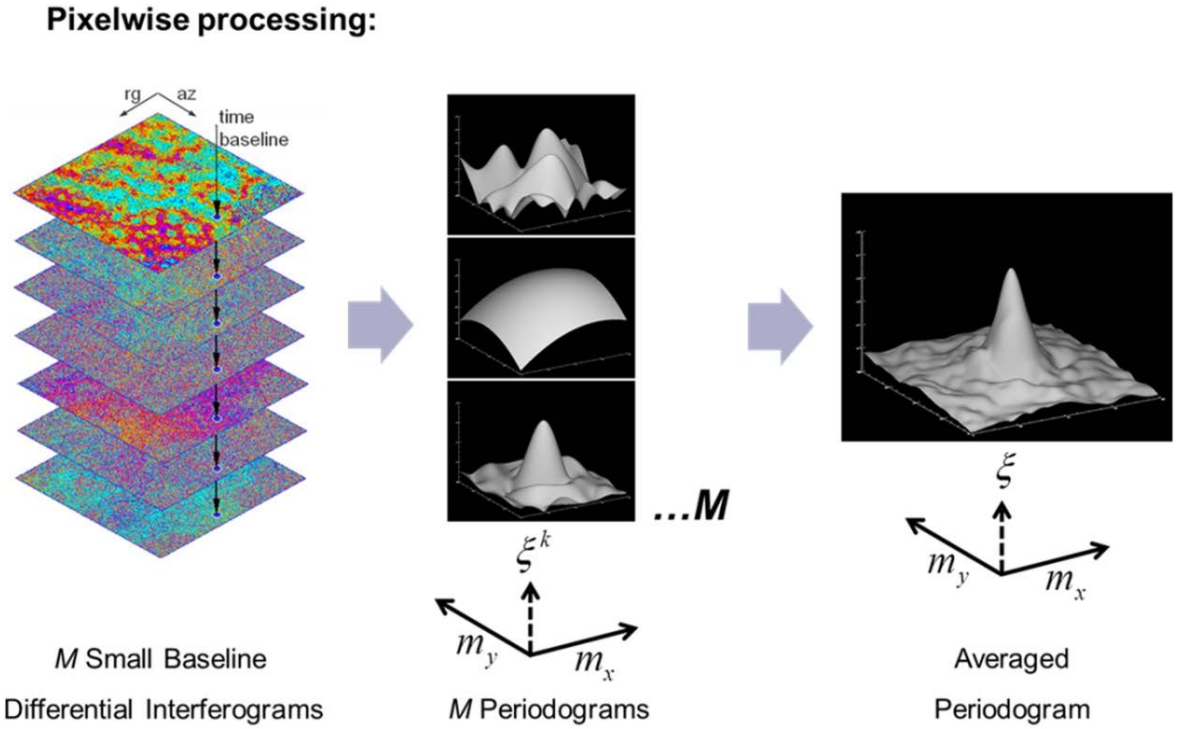

Figure 17: Pictorial representation of adaptive phase flattening for a pixel.

For a robust estimation of the local gradients (i.e. slopes) m_{h_x} and m_{h_y} of the residual DEM in range x and azimuth y directions, respectively for each pixel, a search algorithm in the solution space is applied. M periodograms are generated corresponding to each interferogram using the L homogenous pixels identified in the previous step. A periodogram $\xi^k, k = 1,...,M$, is a function of the local gradients of the residual DEM in range and azimuth directions for the adaptive neighborhood:

$$\xi^k(m_{h_x}, m_{h_y}) = \frac{1}{L}\left|\sum_{i=1}^{L} e^{j\left(\phi_{DInSAR}^{i,k} - \phi_{DInSAR\_ref}^{k} - \frac{4\pi}{\lambda}\frac{B_{\perp}^{k}}{R\sin\theta}\left(m_{h_x} p_x^i + m_{h_y} p_y^i\right)\right)}\right| \tag{34}$$

where $\phi_{DInSAR}^{i,k}$ is the single-look differential interferometric phase for homogenous pixel i and interferogram k, $\phi_{DInSAR\_ref}^{k}$ is the single-look differential interferometric phase for the reference pixel (the pixel for which the correlation and the local gradients of the residual topography are being estimated) and interferogram k and

finally, p_x^i and p_y^i are pixel indices (relative to the reference pixel) in range and azimuth directions resp. for homogenous pixel i. Further on, the slope estimation is made robust by averaging all the periodograms for a pixel to reduce sidelobes, since each periodogram's values are known over an irregular grid defined by the corresponding interferogram's spatial baseline ($B_\perp^k$). An averaged periodogram ξ is obtained as follows:

$$\xi(m_{h_x}, m_{h_y}) = \frac{1}{M}\sum_{k=1}^{M}\xi^k \tag{35}$$

The local gradients of the residual topography $\hat{m}_{h_x}$ and $\hat{m}_{h_y}$ for each pixel are estimated from the peak of the averaged periodogram (which is the ML estimate), i.e.:

$$(\hat{m}_{h_x}, \hat{m}_{h_y}) = \underset{m_{h_x}, m_{h_y}}{\arg\max}(\xi) \tag{36}$$

The estimated gradients of the residual DEM for each pixel are then removed from each interferogram to get the flattened interferograms $\phi_{flat}^k, k = 1,...,M$. Adaptive phase flattening is depicted pictorially in Figure 17.

It is worth mentioning that the computational complexity can be reduced by generating fewer periodograms using some highly coherent interferograms with a suitable variation of baselines. The variation in baselines is needed for reducing the sidelobes. In other words, some interferograms with relatively large baselines are also needed for a better precision. Practically, this simplified computation using fewer interferograms can also reasonably estimate the local gradients of the residual DEM. Of course, a rough estimate of the coherence is required, which is possible by a normal rectangular multi-looking of the interferograms.

- *Adaptive Complex Multi-looking:* Finally, estimation of the M filtered small baseline differential interferograms and their coherence is performed. This is done pixelwise for each interferogram, wherein, an adaptive complex multi-looking of the flattened interferometric phase of the adaptive neighborhood is performed for an accurate phase and coherence estimation, i.e.:

$$\hat{\gamma}^{i,k} = \frac{1}{L}\sum_{i=1}^{L} e^{j\left(\phi_{flat}^{i,k}\right)} \tag{37}$$

where $\phi_{flat}^{i,k}$ is the flattened differential interferometric phase for homogenous pixel i and interferogram k and $\hat{\gamma}^{i,k}$ is the correlation. Phase value of $\hat{\gamma}^{i,k}$ is the filtered differential interferometric phase estimate and absolute value of $\hat{\gamma}^{i,k}$ is the coherence estimate, respectively for homogenous pixel i and interferogram k.

Figure 18 illustrates the adaptive spatial filtering algorithm in comparison with the conventional rectangular multi-looking, as applied on the TerraSAR-X data of the gas storage site. Figure 18 (a) is a Google Earth image of a part of the test site and its single-look interferogram. Figure 18 (b) shows the coherence and interferogram estimate after boxcar (rectangular) multi-looking. Figure 18 (c) shows the coherence and interferogram estimate after adaptive spatial phase filtering. Features such as fields and roads can be clearly distinguished after applying adaptive spatial phase filtering as compared to the typical boxcar (rectangular) multi-looking. It can be seen that the object resolution is preserved. Note that this figure is also in (Goel and Adam, 2012a) and the color bar has been corrected here.

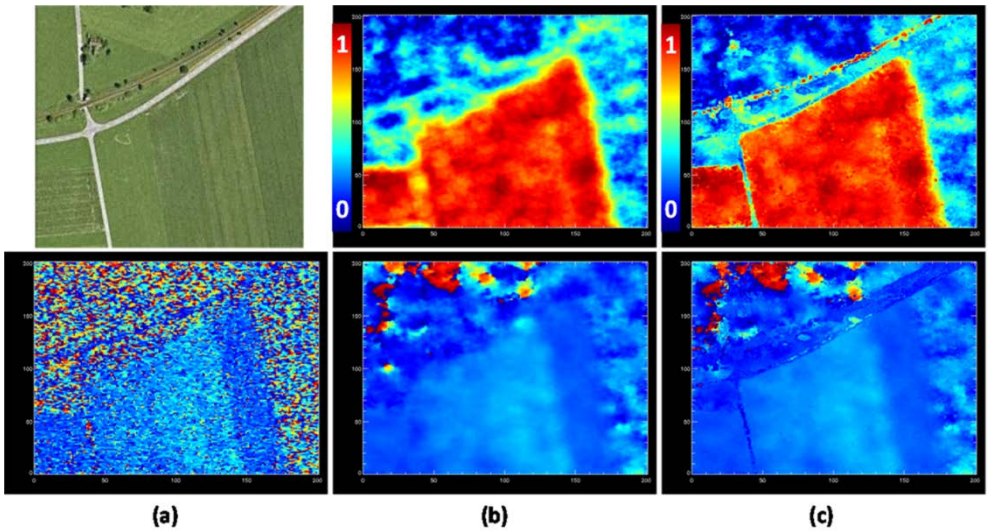

Figure 18: (a) is a Google Earth image and its single-look interferogram. (b) is coherence and interferogram estimate after boxcar multi-looking. (c) is coherence and interferogram estimate after adaptive spatial filtering.

3.2.2 Deformation Retrieval

When a traveler reaches a fork in the road,
the L1-norm tells him to take either one way or the other,
but the L2-norm instructs him to head off into the bushes.

John F. Claerbout and Francis Muir, 1973.

In this second step, the improved small baseline differential interferograms are used to estimate the LOS deformation and residual topography using an *L1-norm based SBAS technique*. SBAS has been described in the previous chapter (Berardino et al., 2002). Importantly, the interferograms are spatially unwrapped and all coherent pixels, i.e. DSs are calibrated with respect to a reference pixel. Note that in the new algorithm, in addition to the spatial coherence, DSs selection is also done based on a minimum number of looks (i.e. homogenous pixels) in order to exclude PSs. Next, the residual DEM and mean deformation velocity are estimated for the DSs via the LS solution of the computed sequence of DInSAR interferograms (see Equation (27)). After this operation, the estimated residual topography and mean deformation velocity are subtracted modulo-2π from each interferogram, resulting in a fringe rate reduction. Accordingly, a new unwrapping step is then applied to the residual wrapped phase, the phase unwrapping being considerably simplified. By adding back the subtracted mean deformation velocity, refined unwrapped differential interferograms are obtained (see Equation (28)). The interferogram subsets are afterwards linked using the SVD method and a minimum-norm LS solution (i.e. L2-norm minimization) is obtained. Advantageously, SBAS provides complete non-linear deformation time series of the scatterers without using any model. Finally, the atmospheric propagation effects are estimated and removed via a spatial low pass and a temporal high pass filtering.

However, in rural areas, there might be several decorrelated areas (e.g. trees, soil, water etc.) separating the coherent patches. This often introduces phase unwrapping errors and the relative values in the different coherent patches can have unknown integer multiples of 2π phase jumps and no method can retrieve them, as discussed in the previous chapter. These phase jumps in the unwrapped data are outliers (spike noise) and inversion using L2-norm

minimization often performs poorly. Instead, a more robust phase inversion solution, with respect to the phase unwrapping errors found in non-urban areas, can be obtained by using an L1-norm minimization (Lauknes et al., 2011).

A generic L_p-norm solution is given by:

$$\hat{v} = \arg\min_{v} \left(\sum_{i=0}^{M-1} \left| \phi'_{DInSAR} - Bv \right|_i^p \right)^{\frac{1}{p}} \tag{38}$$

The L2-norm minimizes the sum of squared residuals, whereas the L1-norm minimizes the sum of the absolute values of the residuals. The L2-norm inversion is optimal when Gaussian noise is present in the data. But if L2-norm minimization is used in the presence of a spike, the estimated fit tends to deviate towards the outlier thereby resulting in a wrong estimation. In (Rodriguez-Gonzalez et al., 2011), L1-norm network inversion was demonstrated for robust outlier rejection in PSI. The L1-norm cost function has been applied to solve Equation (28) in this thesis. The algorithm proposed by Barrodale and Roberts (Barrodale and Roberts, 1973) is used for L1-norm minimization. It is a modification of the simplex method of linear programming and is computationally efficient.

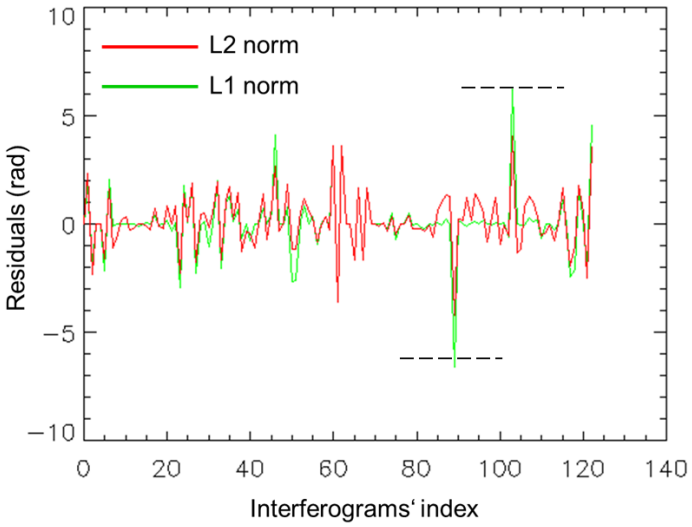

Figure 19: Residuals obtained after L2 and L1-norm inversion for a pixel during SBAS processing. The phase unwrapping errors (i.e. outliers) are shown by black dotted lines.

The performance of L2 and L1-norm inversion has been compared for the SBAS technique. Figure 19 shows the L2 and L1-norm residuals for a pixel belonging to the TerraSAR-X dataset of the gas storage site. It can be seen that in case of phase unwrapping errors, i.e. outliers (shown by black dotted lines), the residuals are high for L2-norm, but even higher for L1-norm. Thus, L1-norm minimization can be used for outlier detection and correction (by providing a phase unwrapping error map). Misdetections are avoided because of the higher residual peaks. Figure 20 shows the baseline-time plot for the TerraSAR-X dataset. Each dot corresponds to a SAR image and each line corresponds to an interferogram. The lines are color coded according to the L2-norm and L1-norm residuals for the pixel in the two plots, respectively. It can be seen that in the presence of outliers (encircled in black), L2-norm spreads the phase unwrapping errors to the neighboring interferograms. On the other hand, L1-norm provides a robust solution, a small disturbance in the data leads to only a small disturbance in the signal reconstruction.

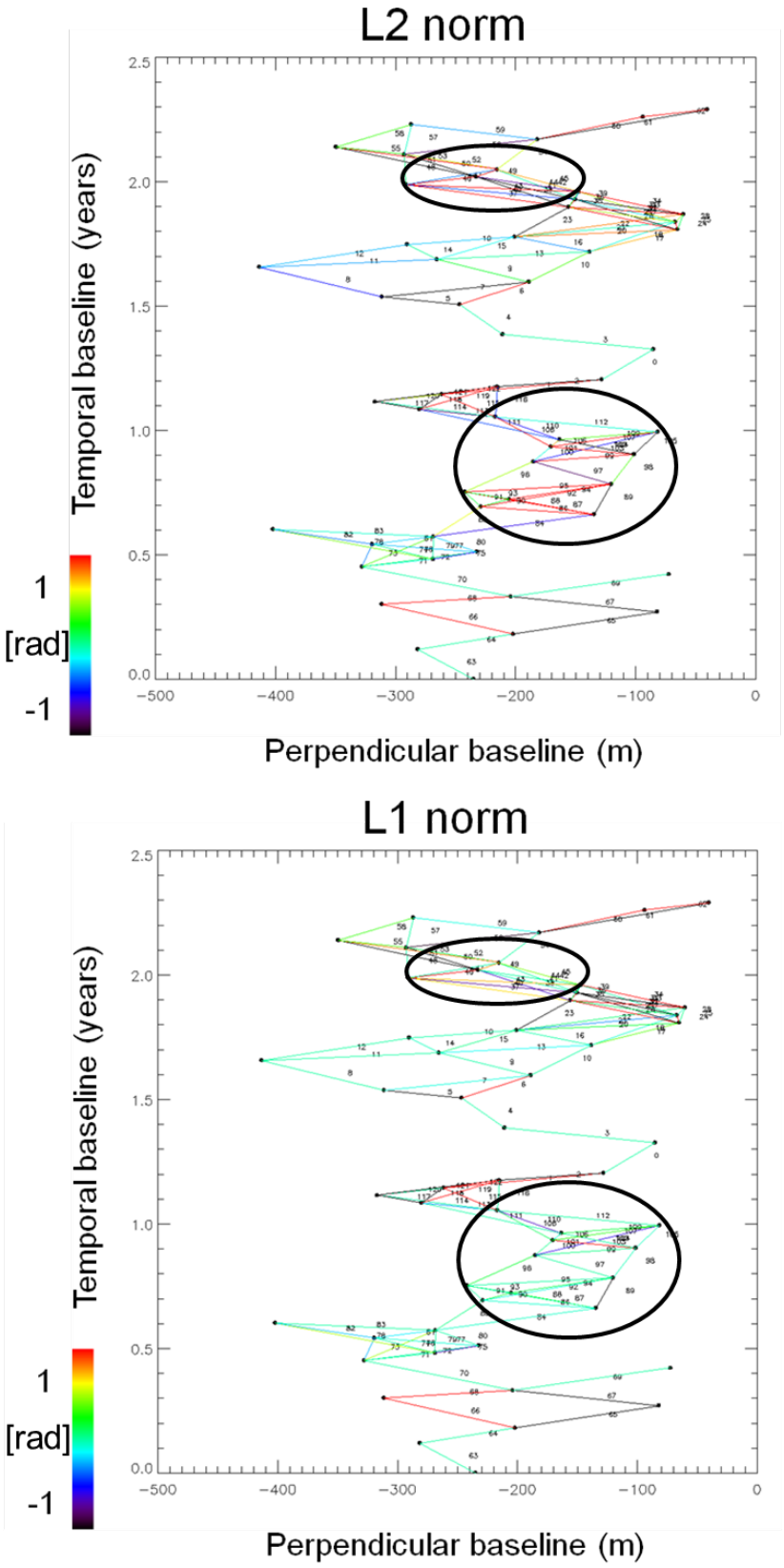

Figure 20: Baseline-time plot of the TerraSAR-X dataset of the gas storage site located in Germany. Each dot represents a SAR image and each line represents an interferogram. The lines (i.e. interferograms) are color coded according to the L2-norm and L1-norm residuals for a pixel in the two plots, respectively. The phase unwrapping errors (i.e. outliers) are encircled in black. While L2-norm spreads the phase unwrapping errors to the neighboring interferograms in the presence of outliers, L1-norm provides a robust solution.

3.3 Application Test Cases and Results

Practical demonstration for this newly developed technique for deformation estimation in non-urban areas is provided via *two case studies using high resolution TerraSAR-X data*. A performance assessment has been done as well.

3.3.1 Case Study 1

The first test site is a *natural gas storage reservoir in Germany*. The test site is visualized in Google Earth in Figure 21 (a), the approximate area of the gas storage is enclosed in red. As can be seen, this is a rural region covered mostly by vegetation and agricultural fields, thus making it ideal for testing this algorithm. Underground gas storage causes subsidence and uplift of terrain depending on the reservoir pressure. The annual storage cycle generally comprises of gas injection in summer and extraction in winter, leading to a cyclic deformation pattern. Mapping this surface movement is important for reservoir monitoring and hazard analysis.

For measuring the ground displacement, 55 Stripmap mode TerraSAR-X scenes of the reservoir from January, 2008 to May, 2010 with a look angle of 41.05 degrees and HH polarization have been used. Figure 21 (b) shows the mean SAR amplitude image of the test site. An area of approximately 7 km (ground range) by 14 km (azimuth) has been processed. The pixel dimensions in range and azimuth directions are 1.27 meters and 1.35 meters, respectively. This non-urban site covered by vegetation and fields has a low density of PSs in comparison to the DSs, as shown in Figure 22. Improving the spatial density and the quality of deformation estimates in non-urban areas is the main objective of this technique.

The dataset has been processed using the new technique. Based on a maximum spatial baseline of 150 meters and a maximum temporal baseline of 100 days, 123 single-look small baseline differential interferograms have been generated. For DInSAR processing, DLR's operational PSI-GENESIS processor has been employed (Adam et al., 2003, Adam et al., 2004; Kampes, 2006). Figure 20 shows the SBAS configuration for the test site, i.e. the baseline-time plot for the scenes and the interferograms. The coherence matrix of the dataset is illustrated in Figure 23. It shows the combinations of acquisitions used (i.e. the interferograms), each of which is color coded according to its average coherence. It can be seen that only small baseline combinations have been used for the processing. Moreover, the average coherence of this rural region can be observed as low, typical for areas affected by temporal decorrelation.

Then, the adaptive spatial filtering algorithm is applied on the single-look interferograms, as demonstrated in the two examples in Figure 24. Figure 24 (a) shows the single-look small baseline differential interferogram of the test site, Figure 24 (b) shows the interferogram estimate after adaptive spatial filtering and Figure 24 (c) shows the coherence estimate after adaptive spatial filtering. A big improvement is clearly seen in the quality of the interferometric phase. Also, it can be visualized that the area is mostly noisy and few points retain their coherence in the two examples (possibly due to vegetation growth, agriculture or snow cover), thus, making this test site especially difficult.

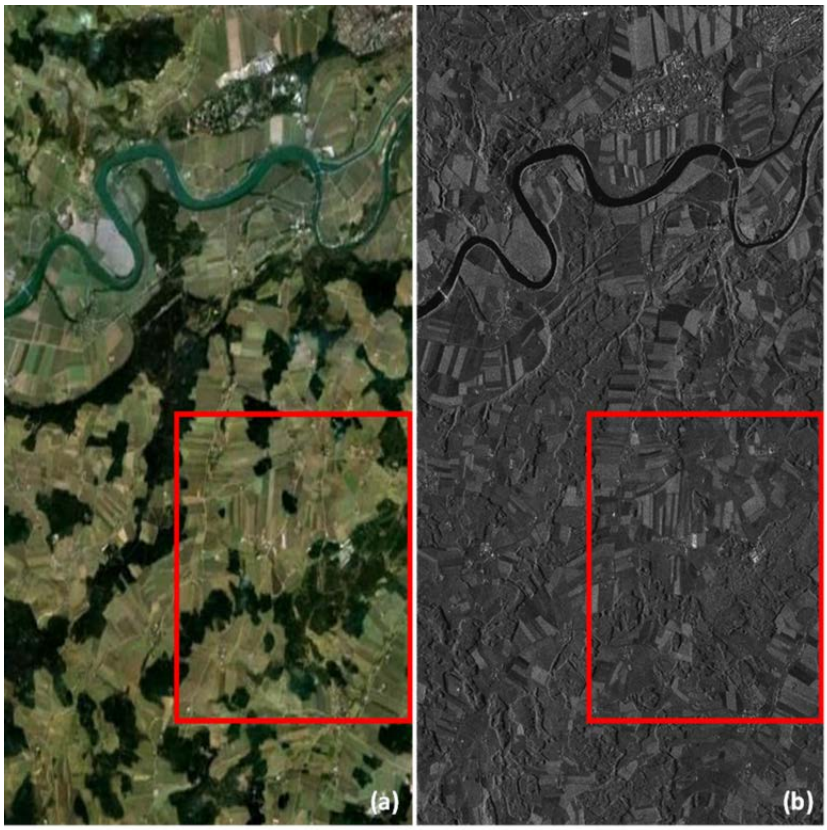

Figure 21: (a) is the Google Earth optical image of the test site in Germany. (b) is the TerraSAR-X mean amplitude image of the test site. The underground gas storage reservoir is located inside the red rectangle.

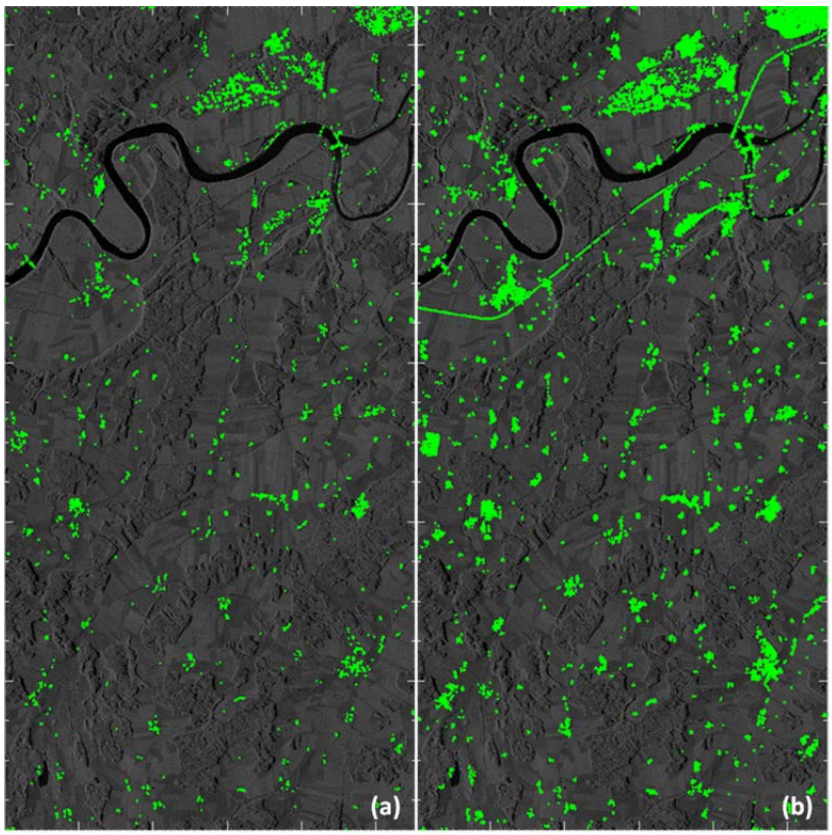

Figure 22: TerraSAR-X image of the gas storage site in Germany. (a) shows the PSs in green (54,258 points), whereas (b) shows the PSs and DSs in green (284,081 points). The density of PSs is very low compared to the DSs in this non-urban area.

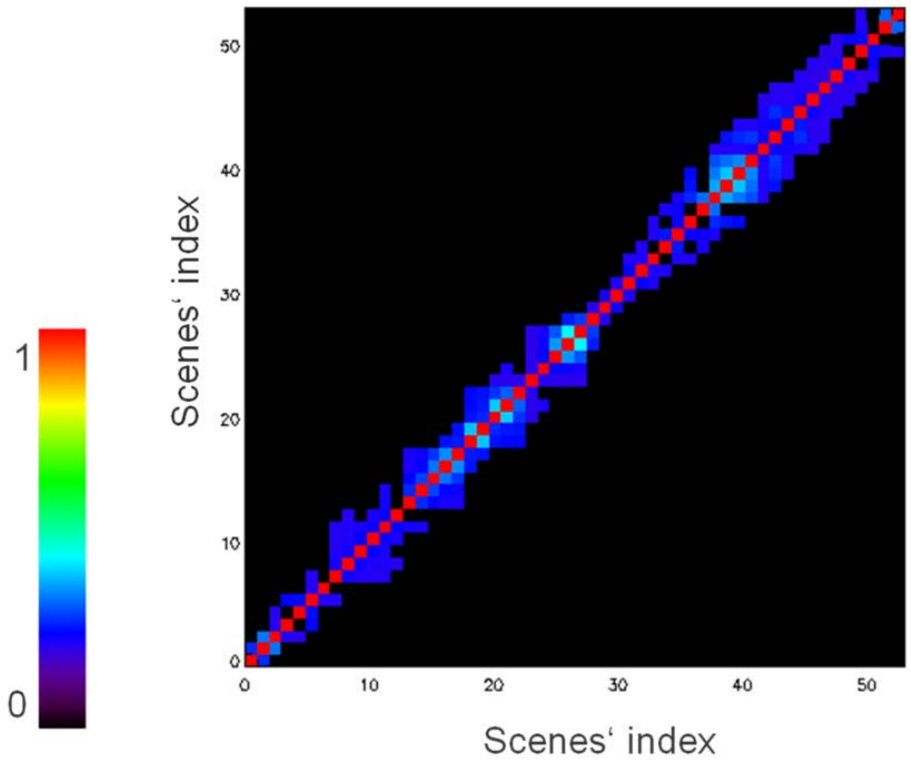

Figure 23: Coherence matrix of the TerraSAR-X dataset of the gas storage reservoir situated in Germany. It depicts the average coherence of the small baseline differential interferograms used in the processing (black color depicts the interferograms not used).

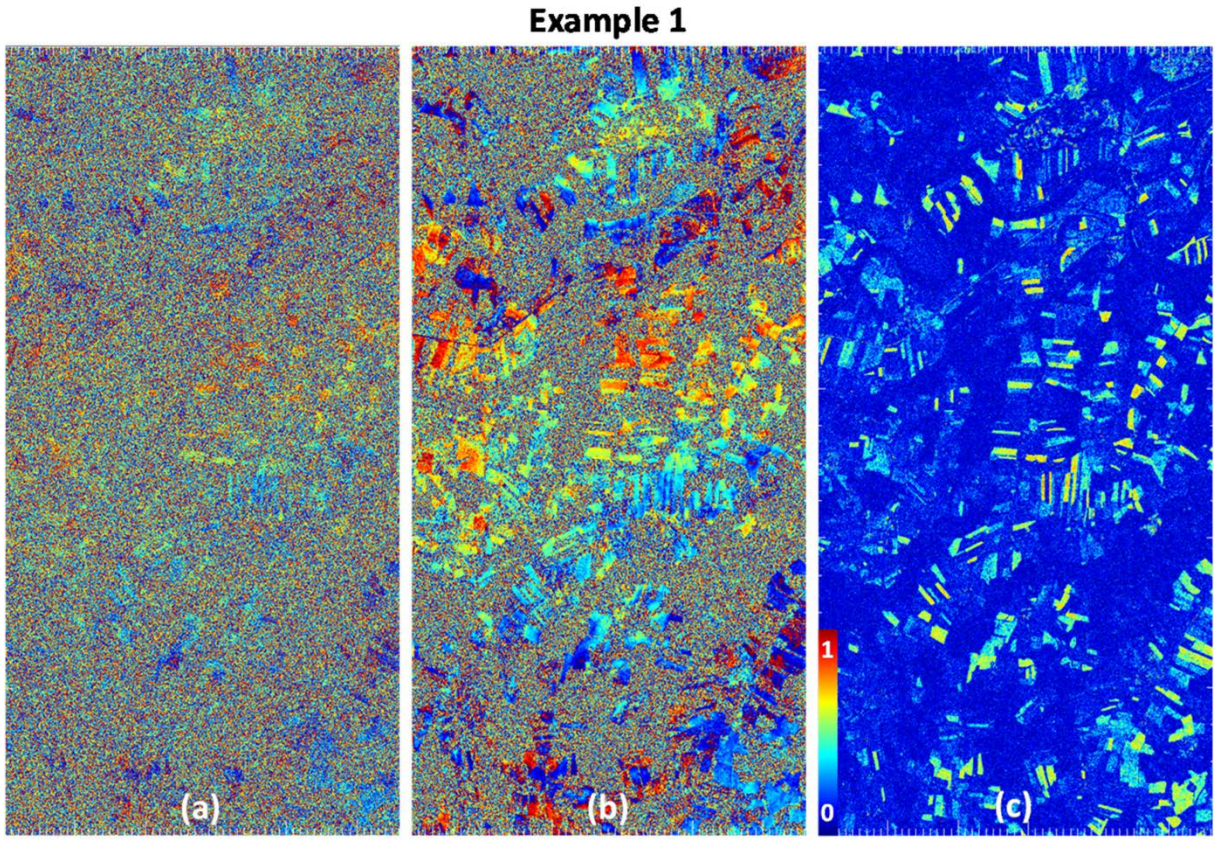

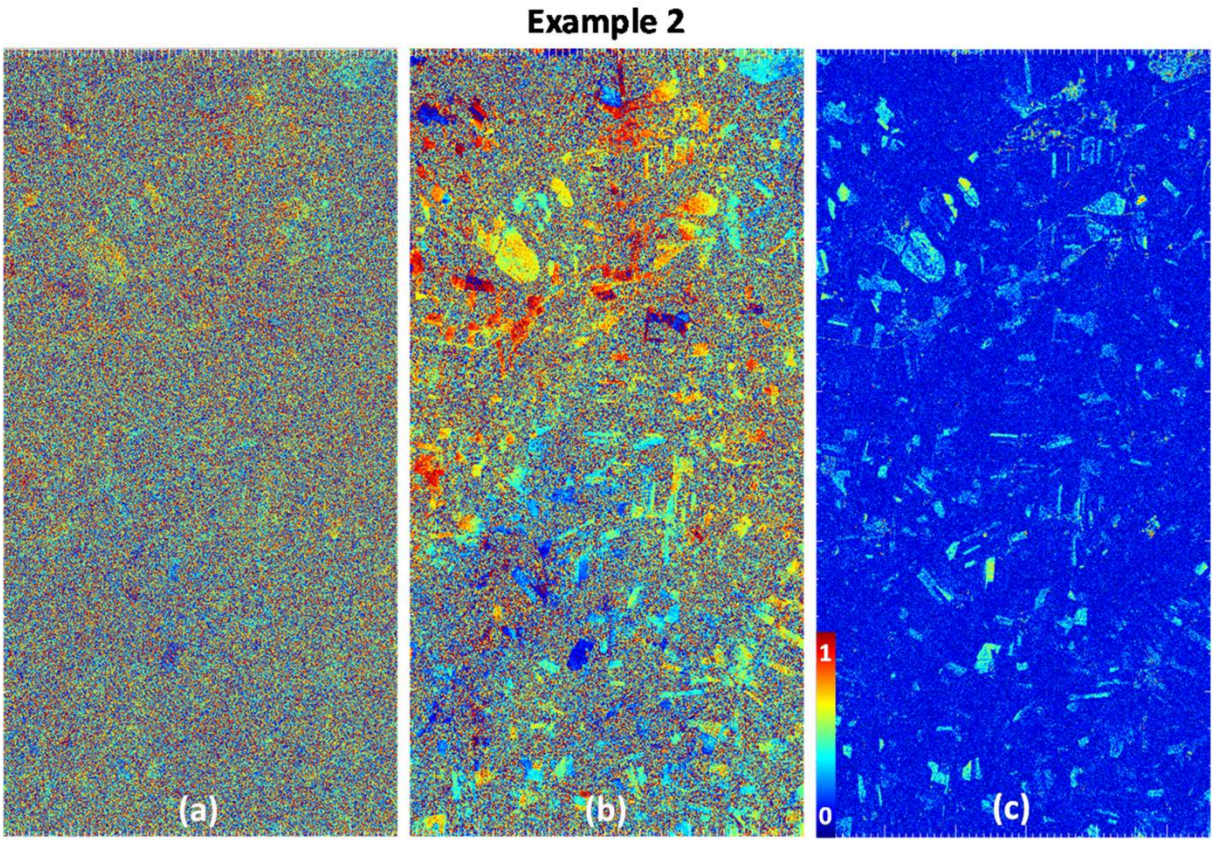

Figure 24: Two demonstrations of the adaptive spatial phase filtering algorithm. (a) is the single-look interferogram of the gas storage site located in Germany. (b) is the interferogram estimate after adaptive spatial filtering. (c) is the coherence estimate after adaptive spatial filtering.

Later on, the MCF algorithm is used for phase unwrapping (Costantini, 1998; Eineder et al., 1998). The unwrapped interferograms are subsequently used for deformation monitoring using the SBAS approach via the L1-norm minimization. Pixels that have an average coherence of at least 0.4 are used and a minimum of 20 looks are used, as shown in Figure 22 (b). The deformation estimation results are presented in Figure 25 and are compared with the results obtained from the typical L2-norm based SBAS approach. The Root-Mean-Square (RMS) deformation has been used for visualizing the results as it is visually effective and provides an integral information about the displacement with respect to time. It can be observed that the coherent points of the test case are not well connected, leading to phase unwrapping errors. The L2-norm inversion propagates these errors spatially, as can be seen in Figure 25, as compared to the L1-norm based solution.

Deformation time series are visualized in Figure 26 for some of the pixels marked in Figure 25. The L2-norm inversion fails to estimate the cyclic non-linear deformation occurring in the area of the gas storage (points A and B), although it performs reasonably well for point C which is located far away from the reservoir. L1-norm solution, on the other hand, corresponds well to the cyclic nature of operation of the gas storage reservoir (i.e. injection during summer, production during winter) and the related reservoir pressure. Minima during winter and maxima during summer can be observed. Also to be noticed is the fact that small displacement in the order of a few millimeters can be observed using the X-band TerraSAR-X sensor. The standard deviation of the deformation estimates using the L1-norm inversion is shown in Figure 27.

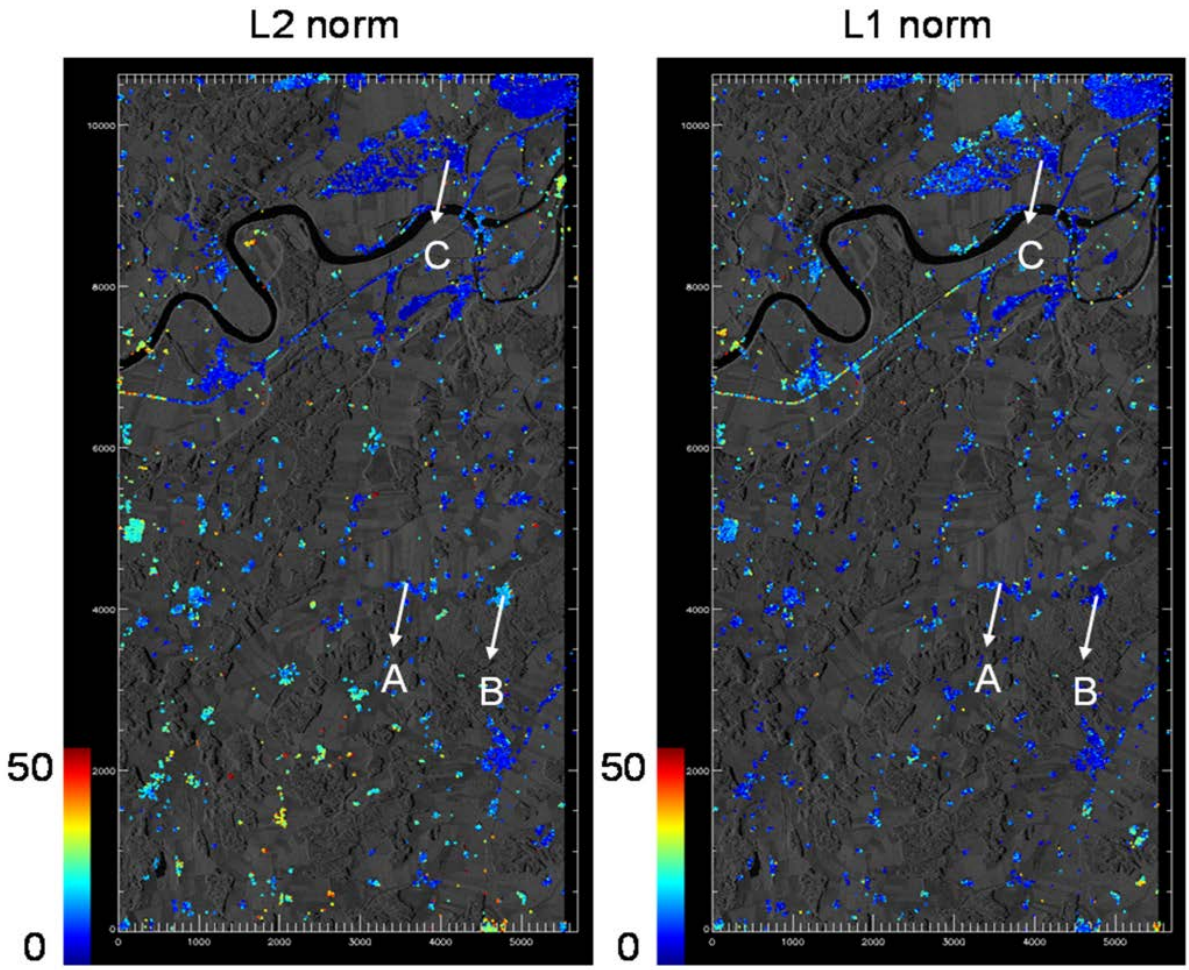

Figure 25: RMS deformation [mm] for the gas storage site in Germany using L2-norm and L1-norm based SBAS. Processed points are overplotted on the mean amplitude image and color coded according to RMS deformation values. Deformation time series of points A, B and C are shown in Figure 26.

The results demonstrate the potential of this new technique for providing accurate deformation in natural terrains. The increased quality and density of the deformation estimates of DSs in non-urban areas can also be seen in Figure 28, where a comparison with the normal SBAS approach has been provided. Here, a small area surrounding point A (of Figure 25) is shown. Figure 28 (a) shows the TerraSAR-X image of this area. Figure 28 (b) shows the RMS deformation using conventional SBAS, wherein, a small number of points have been estimated due to conventional rectangular multi-looking which reduces the resolution. Also, the L2-norm used in conventional SBAS has propagated the phase unwrapping errors (see points in red). Figure 28 (c) shows the RMS deformation using the new method and the improvement in resolution and quality is clearly visible.

Besides, one of the main advantages of the technique with respect to other coherent methods, for instance, PSI and SqueeSAR, is the capability to estimate non-linear deformation without any modelling and prior knowledge, as has been demonstrated for the application test case. It is thus well suited for monitoring strong non-linear deformations and similar applications in rural areas where PS density is low and temporal decorrelation is faster.

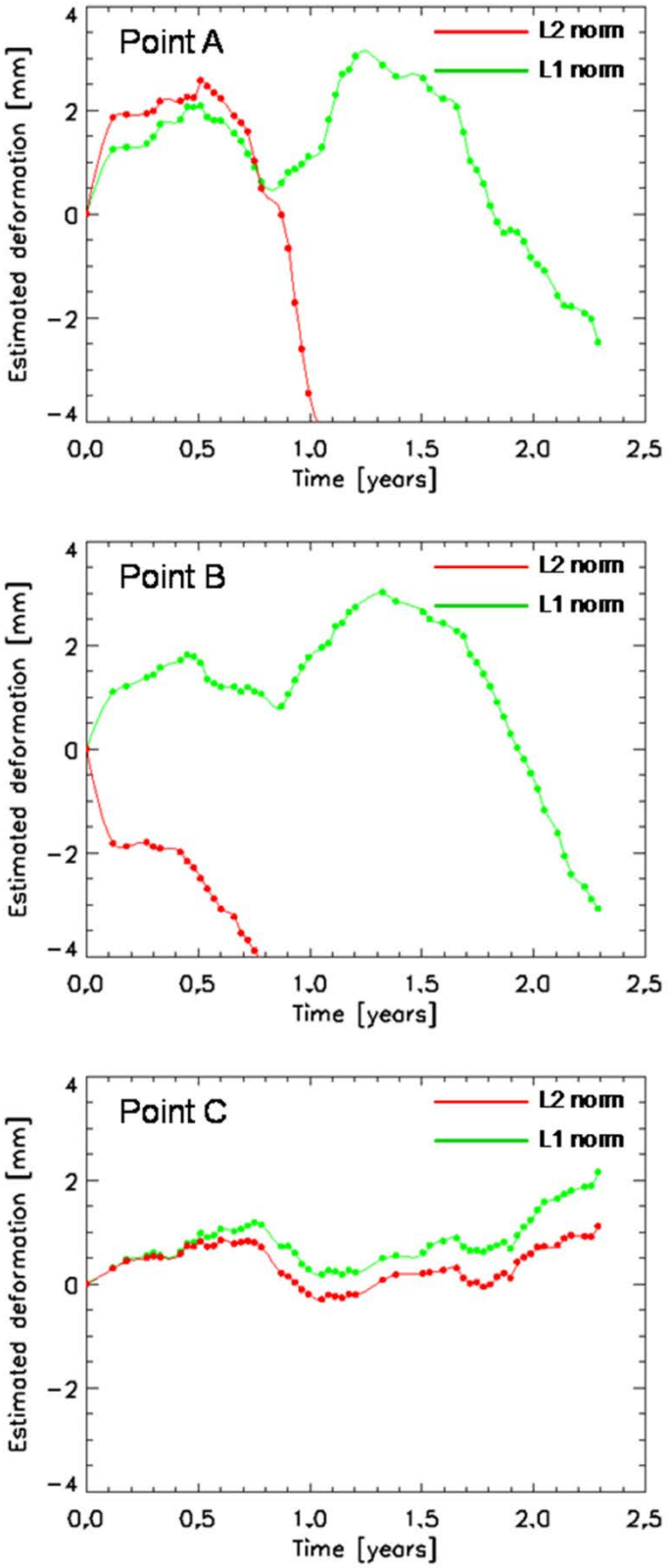

Figure 26: Deformation time series using L2-norm and L1-norm based SBAS for points A, B and C (marked in Figure 25).

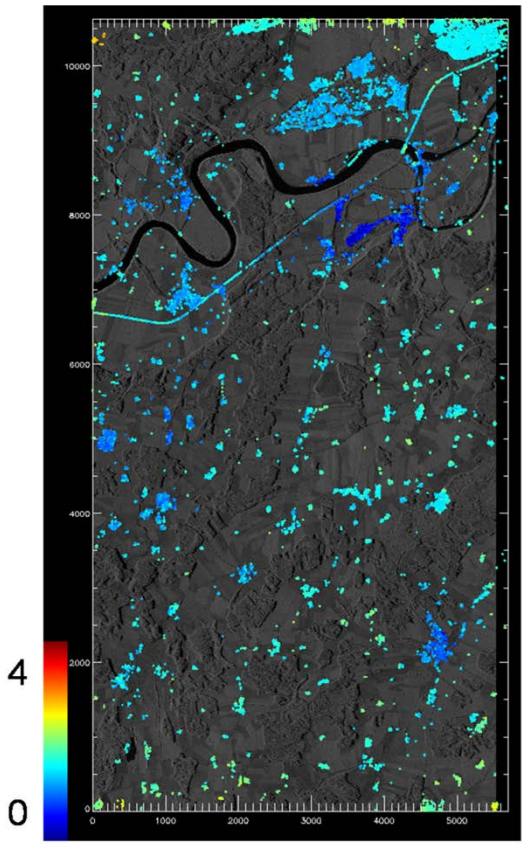

Figure 27: Standard deviation [mm] of deformation estimates of the gas storage site in Germany using L1-norm based SBAS.

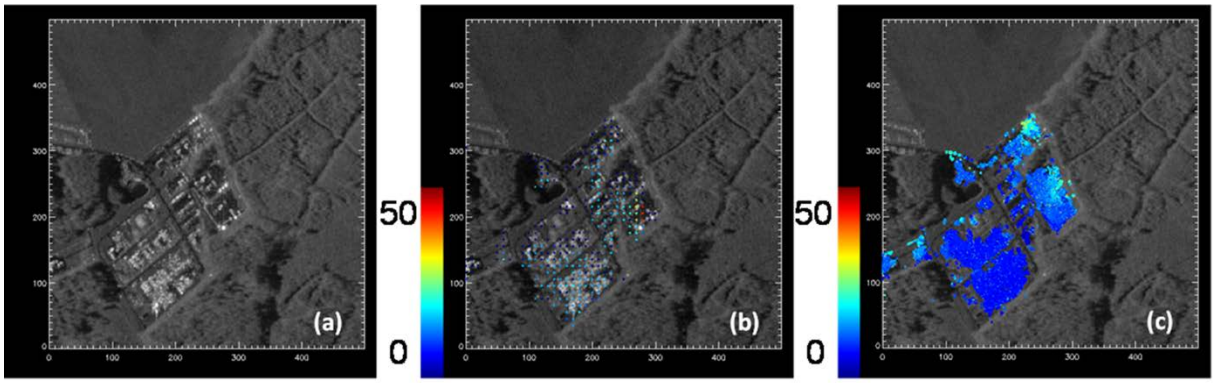

Figure 28: Comparison of quality and density of deformation estimates in rural areas via standard SBAS and the new technique. (a) is the TerraSAR-X image of the area surrounding point A (marked in Figure 25). (b) shows the RMS deformation [mm] via standard SBAS. (c) shows the RMS deformation [mm] via the new approach.

3.3.2. Case Study 2

The second test site is the town of *Lueneburg in Germany*. For deformation mapping using the proposed technique, 17 TerraSAR-X High Resolution Spotlight mode images of the test site from 2010-2011 have been used. Lueneburg is a town situated in the German state of Lower Saxony. Due to constant salt mining dating back to the 19th century and continuing till 1980, various areas of the town experienced a gradual or high subsidence, became unstable and had to be demolished. The sinking still continues even today. Many ground stations have been established since 1946 to monitor the deformation, but due to the changing subsidence

patterns and locations, spaceborne differential SAR interferometric technique has been applied for deformation mapping of Lueneburg. Since October 2010, TerraSAR-X data have been ordered to monitor the subsidence at high resolution.

The dataset has been processed using the proposed technique (Goel and Adam, 2012d). For the non-linear deformation monitoring, 89 small baseline differential interferograms have been generated based on a maximum spatial baseline of 150 m and a maximum temporal baseline of 150 days. DLR's PSI-GENESIS processor has been employed for DInSAR processing (Adam et al., 2003, Adam et al., 2004; Kampes, 2006). The baseline-time plot is shown in Figure 29, where, each dot corresponds to a SAR image and each line corresponds to an interferogram. The coherence matrix of the dataset is illustrated in Figure 30. It shows the combinations of acquisitions used (i.e. the interferograms), each of which is color coded according to its average coherence.

Then, the object-adaptive spatial phase filtering is applied. Figure 31 shows an example of the identification of the homogenous pixels for a pixel which lies on a building. It can be observed that the homogenous pixels identified lie on the building as well. Figure 32 compares boxcar multi-looking with object-adaptive spatial filtering for the test site. It can be seen that the adaptive spatial filtering greatly improves the interferometric phase estimate. Building features are clearly distinguishable and noise is better reduced.

Subsequently, the MCF algorithm is used for phase unwrapping (Costantini, 1998; Eineder et al., 1998) and the deformation is measured using the L1-norm based SBAS technique. Pixels that have an average coherence of at least 0.3 are used. Total displacement measured in mm is shown in Figure 33. Also, an example of the deformation time series for point A (marked in Figure 33) which has deformed highly in the considered time period is shown in Figure 34. As can be seen, the method is able to retrieve the deformation at high resolution. The standard deviation of the deformation estimates is between 0 and 3.7 mm.

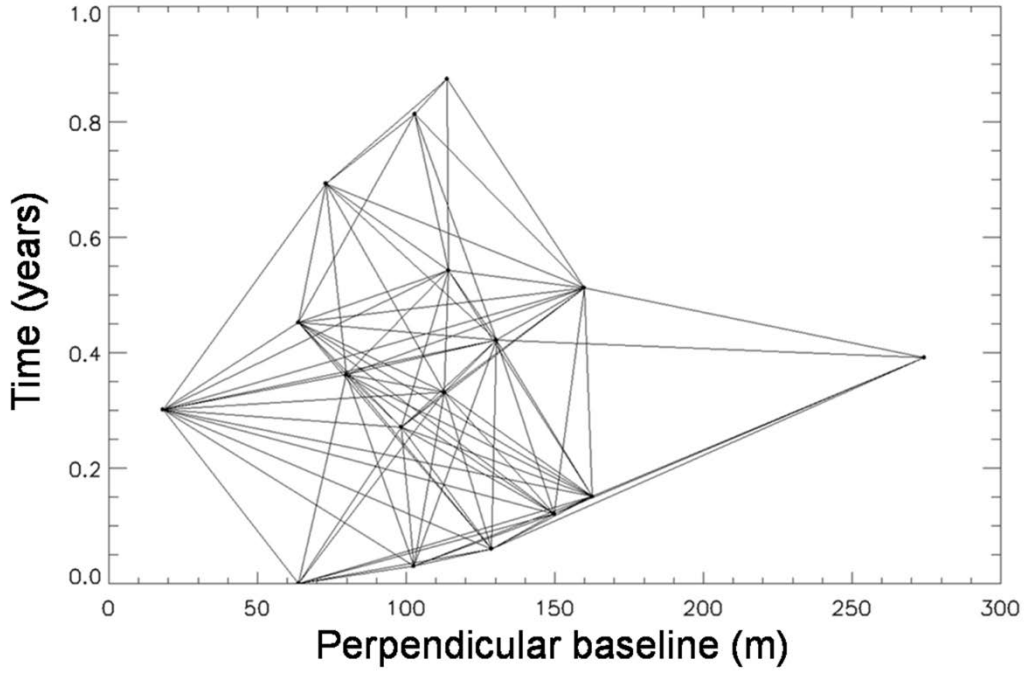

Figure 29: Baseline-time plot of the TerraSAR-X dataset of Lueneburg, Germany. Each dot represents a SAR image and each line represents an interferogram.

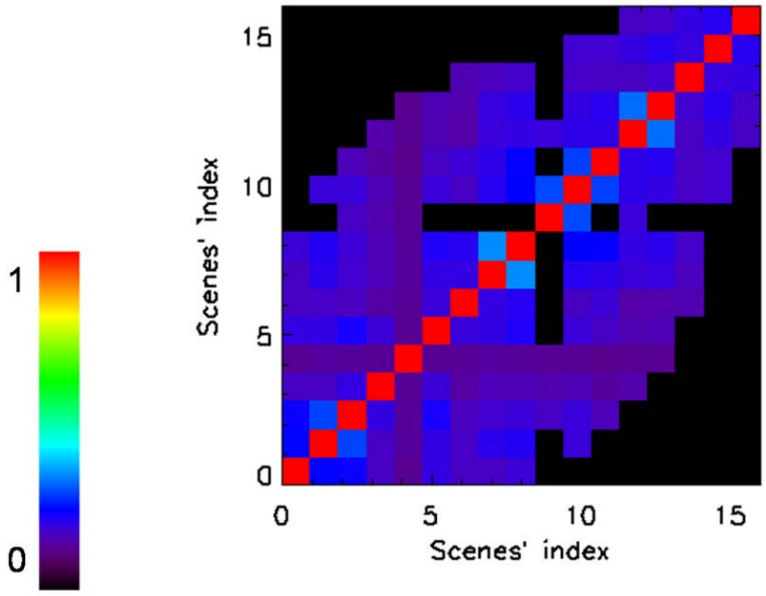

Figure 30: Coherence matrix of the TerraSAR-X dataset of Lueneburg, Germany. It depicts the average coherence of the small baseline differential interferograms used in the processing (black color depicts the interferograms not used).

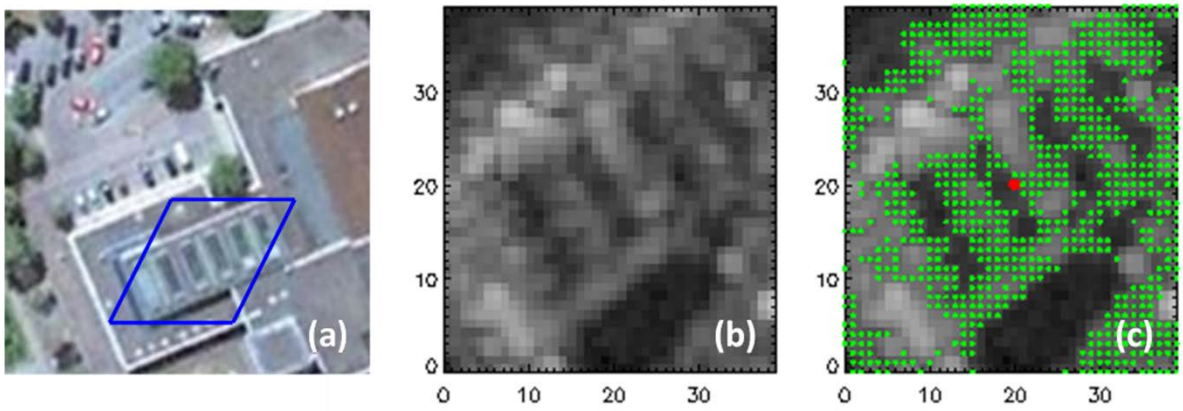

Figure 31: (a) is a Google Earth optical image of an area in Lueneburg, Germany. (b) is the TerraSAR-X image of the region enclosed in blue in (a). (c) shows the statistically homogenous pixels (in green) identified for the red pixel by Anderson-Darling test.

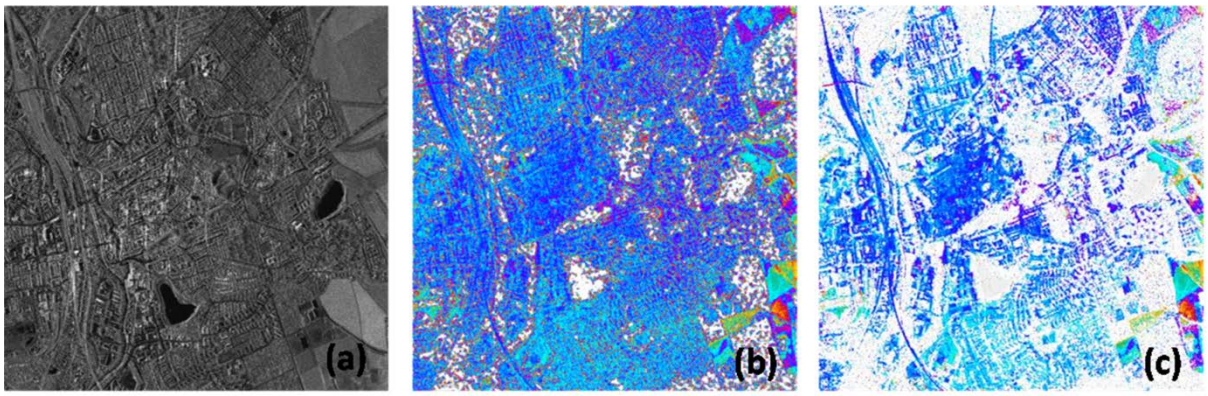

Figure 32: (a) is the SAR mean amplitude image of Lueneburg, Germany. (b) is the interferogram estimate after boxcar multi-looking. (c) is the interferogram estimate after adaptive spatial filtering. Coherence threshold of 0.2 has been applied for the visualization of both the interferogram estimates.

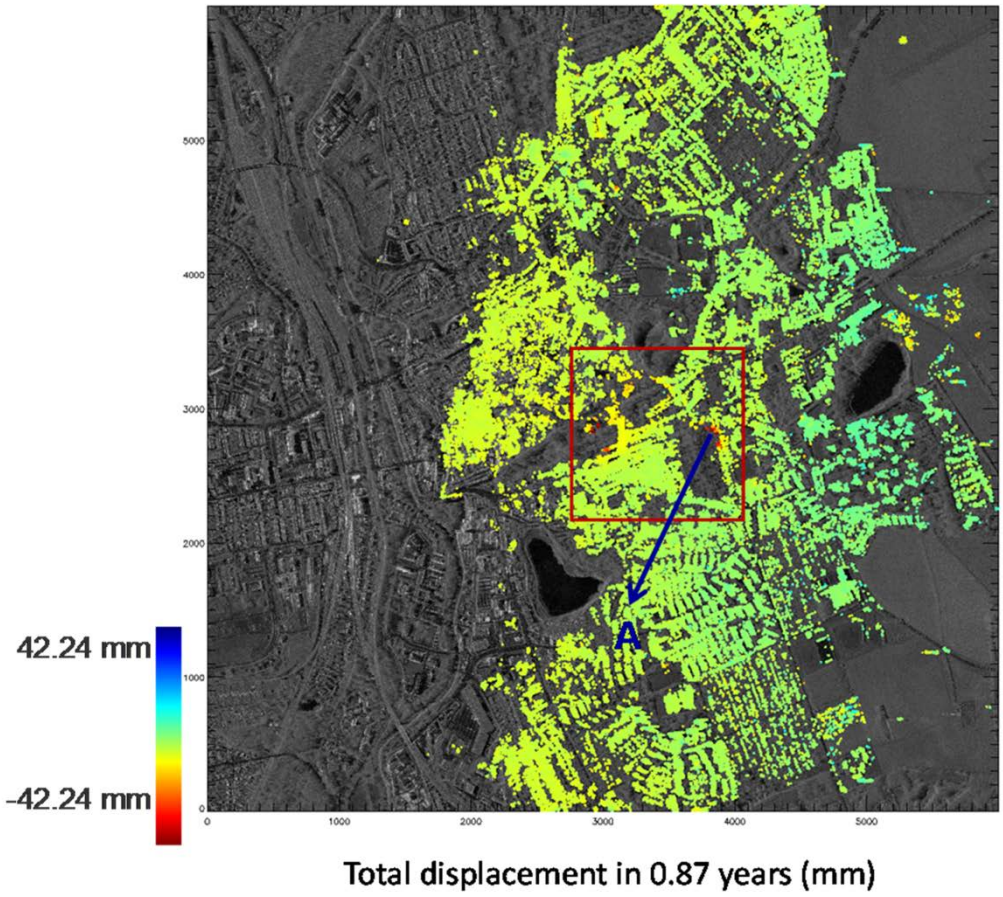

Figure 33: Total deformation estimated for Lueneburg, Germany, for a period of 0.87 years from 2010-2011. Deformation time series is visualized for point A (which has deformed highly in this time period) in Figure 34. The area enclosed in red is used as a test site in the next chapter.

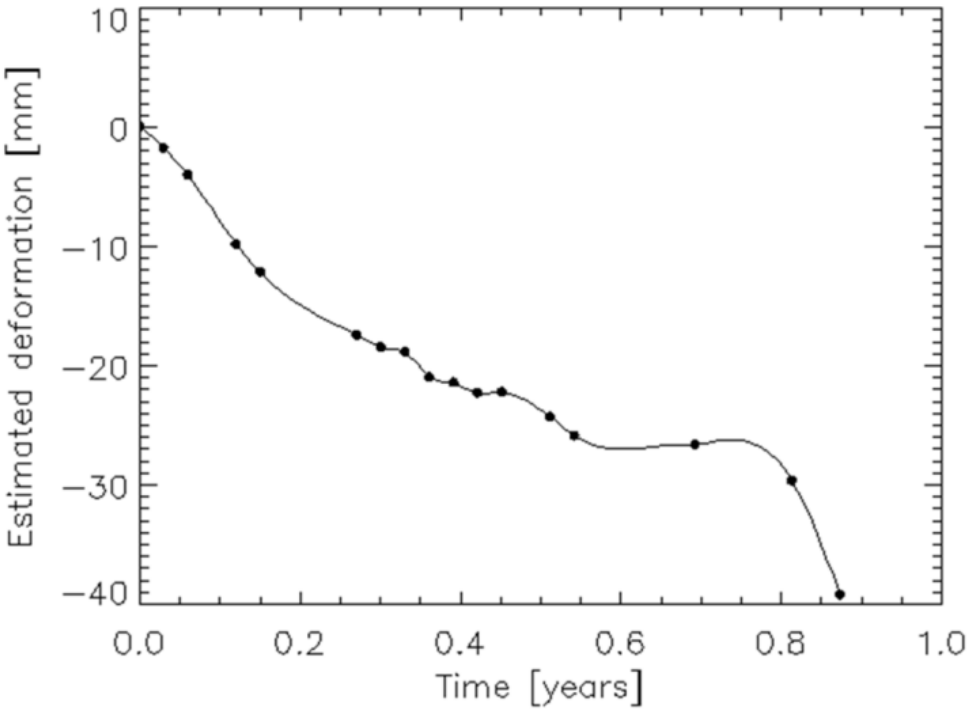

Figure 34: Deformation time series for point A (marked in Figure 33).

It is to be noted that the area enclosed in red in Figure 33 consists of points which are highly deforming. However, there are still many points which are decorrelated and have not been estimated and these might be undergoing deformation as well. In fact, this area enclosed in red is used as a test site in the next chapter and analysed further. The ground truth for Lueneburg is also presented there.

3.4 Discussion and Conclusion

An innovative technique has been developed to improve the robustness and precision of the parameter estimation in areas characterized by DSs. Demonstration and performance assessment have been provided using TerraSAR-X data of a gas storage reservoir located in Germany and the town of Lueneburg in Germany. The results show the potential of this advanced SBAS algorithm in providing high resolution non-linear deformation times series in natural terrains. The adaptive multi-looking *preserves the object resolution*. In fact, this technique is more suitable for high resolution sensors. For conventional sensors, e.g. ERS, the homogenous objects need a large dimension and thus the applicability of the technique is test site dependent. It is to be noted that a minimum number of scenes are required for the detection of homogenous objects and the estimation of complex correlation. The deformation retrieval via the L1-norm based SBAS approach is *more robust with respect to the phase unwrapping errors* which often occur in rural areas.

In terms of the computational complexity, the amount of data to be processed is increased and more processing time is needed. However, this technique is straightforward to implement with only little changes with respect to the existing algorithms.

This approach is applicable for monitoring such phenomena as gas storage induced surface deformation and similar non-linear geophysical effects. In practice, the subsidence maps can be used for further geological analysis and risk mitigation.

However, as shown in the second case study, highly decorrelated regions still pose a challenge in displacement monitoring. New algorithms are required for measuring such difficult areas characterized by high temporal decorrelation and for providing spatially dense deformation maps. This is the basis for the new model-based technique developed and presented in the next chapter of this thesis.

4 Advanced Distributed Scatterer Interferometry Algorithm

This chapter presents a *new DSI technique* for mapping mean deformation velocity in highly decorrelated areas with known deformation patterns, exploiting high resolution SAR data. These two papers have been recapped here:
A.2 Goel, K., Adam, N., 2012b. High resolution deformation time series estimation for distributed scatterers using TerraSAR-X data. ISPRS Annals of the Photogrammetry, Remote Sensing and Spatial Information Sciences, XXII ISPRS Congress, Commission VII, Melbourne, Australia, 25 August-01 September 2012, I-7, 29-34, Copernicus Publications.
A.3 Goel, K., Adam, N., 2013a. A distributed scatterer interferometry approach for precision monitoring of known surface deformation phenomena. IEEE Transactions on Geoscience and Remote Sensing PP (99), 1-15, DOI: 10.1109/TGRS.2013.2289370.
High resolution TerraSAR-X dataset of Lueneburg in Germany is used as a processing example of this technique.

4.1 Introduction

As summarized in the previous chapters, state-of-the-art interferometric stacking techniques, for instance, PSI, SBAS and SqueeSAR, have limitations in natural terrains due to temporal decorrelation and the unavailability of coherent scatterers. As a consequence, phase unwrapping is difficult and only a few points can be measured in highly decorrelated areas.

With respect to the above-mentioned techniques, an alternative DSI method has been developed and implemented for *deformation velocity monitoring in difficult decorrelated regions whose deformation velocity can be described by a suitable model*, exploiting high resolution SAR data. Typical application examples include sub-surface mining areas, sub-surface construction sites and oil/gas/water reservoirs. The proposed method utilizes DSs and consists of three main steps. First, an identification of DSs, i.e. homogenous object patches of pixels, is done by a similarity test algorithm using a stack of SAR amplitude images as described in the previous chapter (Parizzi and Brcic, 2011; Goel and Adam, 2012a). Then, a robust object-adaptive parameter estimation is performed to estimate the local *gradients* of deformation velocity and the local *gradients* of residual DEM in range and azimuth directions for these patches, utilizing small baseline differential interferograms. Finally, since the independent estimated neighboring patches are close and deformation is assumed to be smooth, a 2D model-based deformation integration is performed to get the LOS deformation velocity. To implement this inversion, a Bayesian estimation framework (Papoulis and Pillai, 2002; Sivia and Skilling, 2006) is applied which makes use of directed graphs (Bishop, 2006) and particle filters (Isard and Blake, 1998; Arulampalam et al., 2002). The new concept with respect to the existing DS algorithms is that:

- There is *no need for conventional spatial phase unwrapping* (based on estimation of phase gradients, followed by their integration) and the mean deformation velocity is estimated at a suitable resolution in the order of the dimension of objects.
- The computational complexity is reduced, as compared to SqueeSAR, by making use of only small baseline differential interferograms.

- Even in the presence of high phase noise, the algorithm compensates DEM errors and atmospheric artifacts.
- Due to model-based deformation integration, a spatially dense deformation velocity map is estimated, instead of just a few measured points.

4.2 Methodology

Assuming that *N SAR images* and *M single-look small baseline differential interferograms* are available, the implemented methodology for deformation estimation of DSs involves the following steps:

4.2.1 Identification of Homogenous Patches

In this step, independent homogenous patches, i.e. *DS objects are identified* using the stack of coregistered and calibrated SAR amplitude images. A DS object covers several pixels in high resolution SAR images and these pixels exhibit similar scattering properties and belong to the same distribution. These statistically homogenous patches are dependent on the reflectivity, have typically a constant local slope and clear boundaries (e.g. fields, roads etc.). The Anderson-Darling statistical test is used to identify homogenous pixels based on the SAR amplitude images (Parizzi and Brcic, 2011; Goel and Adam, 2012a).

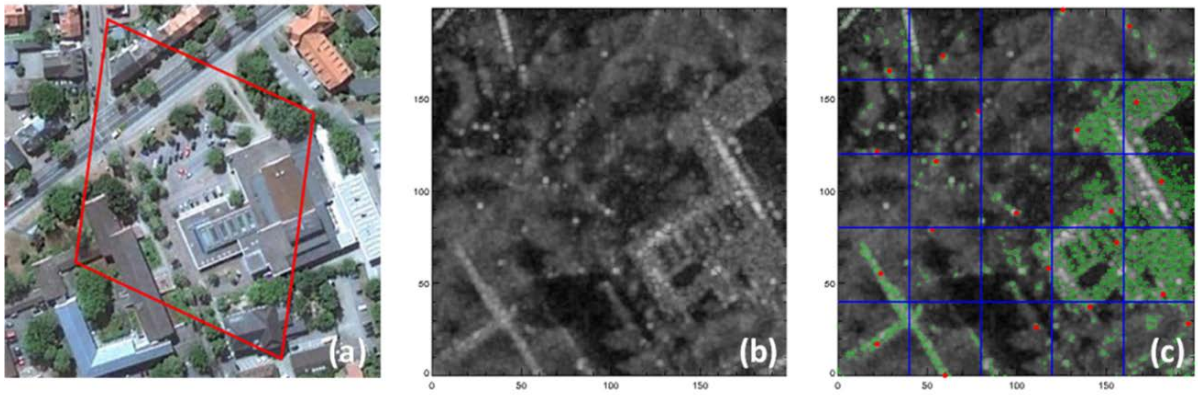

Figure 35: Identification of homogenous patches. (a) Google Earth image of a small part of Lueneburg in Germany, the region of interest is enclosed in red. (b) Mean amplitude TerraSAR-X image of the region of interest. (c) The division of the region into blocks by the blue lines, wherein, the points in green represent the homogenous pixels and the points in red represent the reference pixels.

Basically, the area is divided into non-overlapping rectangular blocks. Then, within each rectangular block, a homogenous patch of pixels is identified. The patch should have a minimum size, since the estimation takes advantage of large homogenous areas. Also, the average spatial coherence of the patch should be larger than a certain threshold to counter phase noise. For each detected patch, a reference pixel is selected. Any pixel in the homogenous patch can be assigned as the reference pixel (since ideally, all the pixels in the homogenous patch have the same coherence). The block size is chosen in such a way that the atmosphere is mitigated if the phase of the reference pixel is subtracted from the phases of the other pixels in the block, and also considering that the patch size should be large enough to

provide with a reliable estimation. Figure 35 shows an example of the identification of homogenous patches for a small region in the town of Lueneburg in Germany. 17 TerraSAR-X High Resolution Spotlight mode images of the test site from 2010-2011 were used. The region is divided into blocks of 40 pixels by 40 pixels, i.e. 24 m by 24 m approximately. A minimum patch size of 20 pixels and a coherence threshold of 0.3 have been applied. Note that the small patch size is only used here for a demonstration of the Anderson-Darling statistical test. For the final processing as mentioned later in this chapter, a bigger patch size of 400 pixels is used in order to make the estimation more precise.

4.2.2 Gradient Estimation for Deformation Velocity and Residual DEM

The single-look differential interferograms are now exploited for the *parameter estimation of DS objects*. Only interferograms with small spatial and temporal baselines are used in order to decrease the effects of residual topography and temporal decorrelation on the DS objects. Additionally, the computational complexity is reduced. The single-look differential interferometric phase $\phi_{DInSAR}^{i,k}$ of a pixel i for interferogram k, with respect to a reference pixel, is given by Equation (15). Accordingly, a homogenous patch can be described by the model parameters: LOS deformation velocity and residual DEM. However, the same deformation velocity or residual DEM value is not assigned to all the homogenous pixels in a patch. In fact, the deformation velocities and residual DEMs of the homogenous pixels in a patch can be, to the first order, well approximated by a linear spatial behaviour in range and azimuth directions, respectively with respect to the reference pixel. Given the differential phase data, the local gradients (i.e. tilts) of deformation velocity m_{v_x}, m_{v_y} (in mm/year/pixel) and the local gradients (i.e. slopes) of residual DEM m_{h_x}, m_{h_y} (in m/pixel) in range x and azimuth y directions, respectively are estimated for the homogenous patches at sub-object resolution. Then, the local gradients of deformation velocity are integrated to obtain the deformation velocity for each DS pixel, as explained in the next subsection.

First, the phase values of each patch for every differential interferogram are corrected with respect to the patch's reference pixel so that the atmospheric effects and orbital errors are mitigated. Second, these are then used for parameter estimation by adjusting to the data a phase model $\phi_{DInSAR\_model}^{i,k}$, which is composed of deformation and residual topography phase components as follows:

$$\begin{aligned}\phi_{DInSAR\_model}^{i,k} &= \phi_{defo}^{i,k} + \phi_{res\_topo}^{i,k} \\ &= \left(\frac{4\pi}{\lambda} B_t^k m_{v_x} p_x^i + \frac{4\pi}{\lambda} B_t^k m_{v_y} p_y^i\right) + \left(\frac{4\pi}{\lambda}\frac{B_\perp^k}{R\sin\theta} m_{h_x} p_x^i + \frac{4\pi}{\lambda}\frac{B_\perp^k}{R\sin\theta} m_{h_y} p_y^i\right)\end{aligned} \tag{39}$$

where $i = 1,...,L$ (L being the number of homogenous pixels in the patch), $k = 1,...,M$ and p_x^i and p_y^i are pixel indices (related to the reference pixel indices) in range and azimuth directions respectively for homogenous pixel i. Since a DS pixel's phase quality is not on par with a PS, the phase model is not adjusted to the data pixelwise. Instead, all the homogenous pixels inside the DS object patch are simultaneously used for the model fitting by maximizing the following model coherence function (periodogram) ξ:

$$\xi(m_{v_x}, m_{v_y}, m_{h_x}, m_{h_y}) = \frac{1}{M}\sum_{k=1}^{M}\left(\frac{1}{L}\left|\sum_{i=1}^{L} e^{j\left(\phi_{DInSAR\_obs}^{i,k} - \phi_{DInSAR\_model}^{i,k}\right)}\right|\right) \tag{40}$$

where $\phi_{DInSAR\_obs}^{i,k}$ is the observed single-look interferometric phase for homogenous pixel i and interferogram k calibrated with respect to the respective reference pixel. Obviously, the gradients of deformation velocity and the residual topography for each patch are estimated from the peak of this periodogram, i.e.:

$$(\hat{m}_{v_x}, \hat{m}_{v_y}, \hat{m}_{h_x}, \hat{m}_{h_y}) = \underset{m_{v_x}, m_{v_y}, m_{h_x}, m_{h_y}}{\arg\max} \left(\xi\right) \tag{41}$$

The maximum of ξ is the temporal coherence of the DS object. Usually it is not as good as the temporal coherence of a PS, due to temporal decorrelation. The range of the gradients of linear deformation and residual DEM, over which the maximum is searched, is based on prior knowledge of the displacement and topographic fields. Usually, $m_v = [-1,1]$ (mm/yr/pixel) and $m_h = [-1,1]$ (m/pixel) is a suitable search range in case no prior knowledge is available. The precision of the estimation depends upon the number of homogenous pixels and spatial extension of the patch, in addition to the average spatial coherence of the patch. Further on, the more the number of interferograms, the better is the estimation as the sidelobes (i.e. ambiguous solutions) are reduced and a clear peak is obtained. An illustration of the periodogram is provided in Figure 36 using Lueneburg dataset for a highly deforming patch. 89 small baseline differential interferograms were utilized for the processing. A minimum patch size of 400 and an average spatial coherence threshold of 0.3 was set. A distinct peak is clearly noticeable. At this point, the algorithm has compensated residual DEM as well as the atmospheric phase screen. The gradients of deformation velocity have been estimated at sub-object resolution using only small baseline differential interferograms.

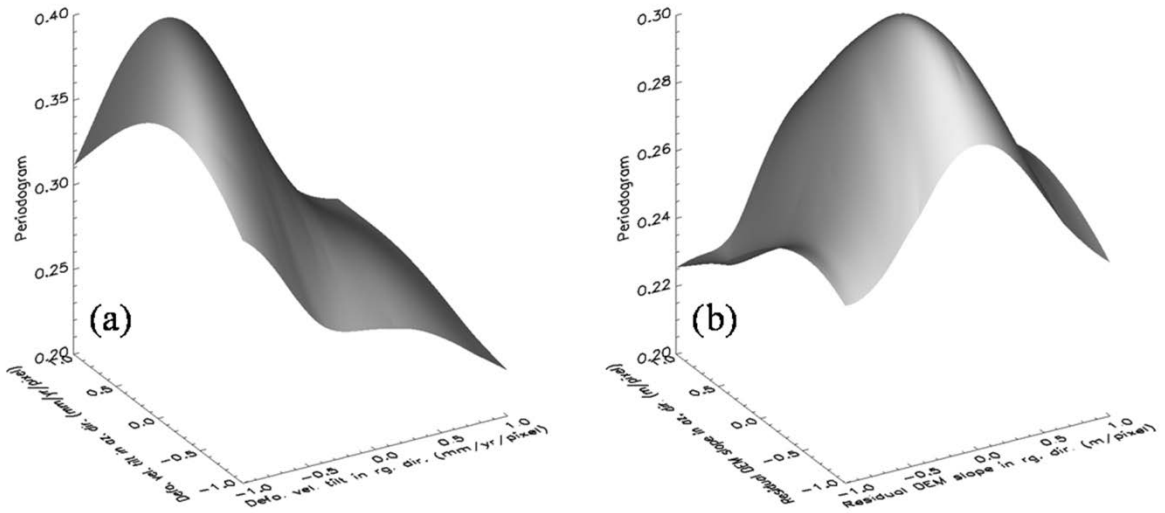

Figure 36: Periodogram demonstration using Lueneburg dataset for a highly deforming patch. (a) Periodogram ξ for $m_{v_x} = [-1,1]$ (mm/yr/pixel), $m_{v_y} = [-1,1]$ (mm/yr/pixel), $m_{h_x} = 0$ (m/pixel) and $m_{h_y} = 0$ (m/pixel). (b) Periodogram ξ for $m_{v_x} = 0$ (mm/yr/pixel), $m_{v_y} = 0$ (mm/yr/pixel), $m_{h_x} = [-1,1]$ (m/pixel) and $m_{h_y} = [-1,1]$ (m/pixel).

4.2.3 Deformation Velocity Integration

Finally, a *2D deformation velocity integration* can be performed to get the deformation velocity. A simple 1D case is shown in Figure 37. For a 2D deformation integration, it is

assumed that the independent estimated neighboring patches are close and the deformation velocity field varies smoothly in space. Note that there are certain deformation fields which are non-smooth and this method is not valid for such cases. For the 2D deformation integration, a model-based approach has been implemented. Depending on the source of the subsidence, e.g. mining, oil/gas extraction, volcano, earthquake etc., a suitable model can be adopted and its parameters estimated. The advantage here is that the estimated model parameters can be further used to assess and analyze the impacts of such geophysical phenomena. It is also straightforward and easy to apply. Due to model-based deformation retrieval, the final resolution of deformation velocity is in the order of the dimensions of objects (and not at sub-object resolution as in the previous subsection).

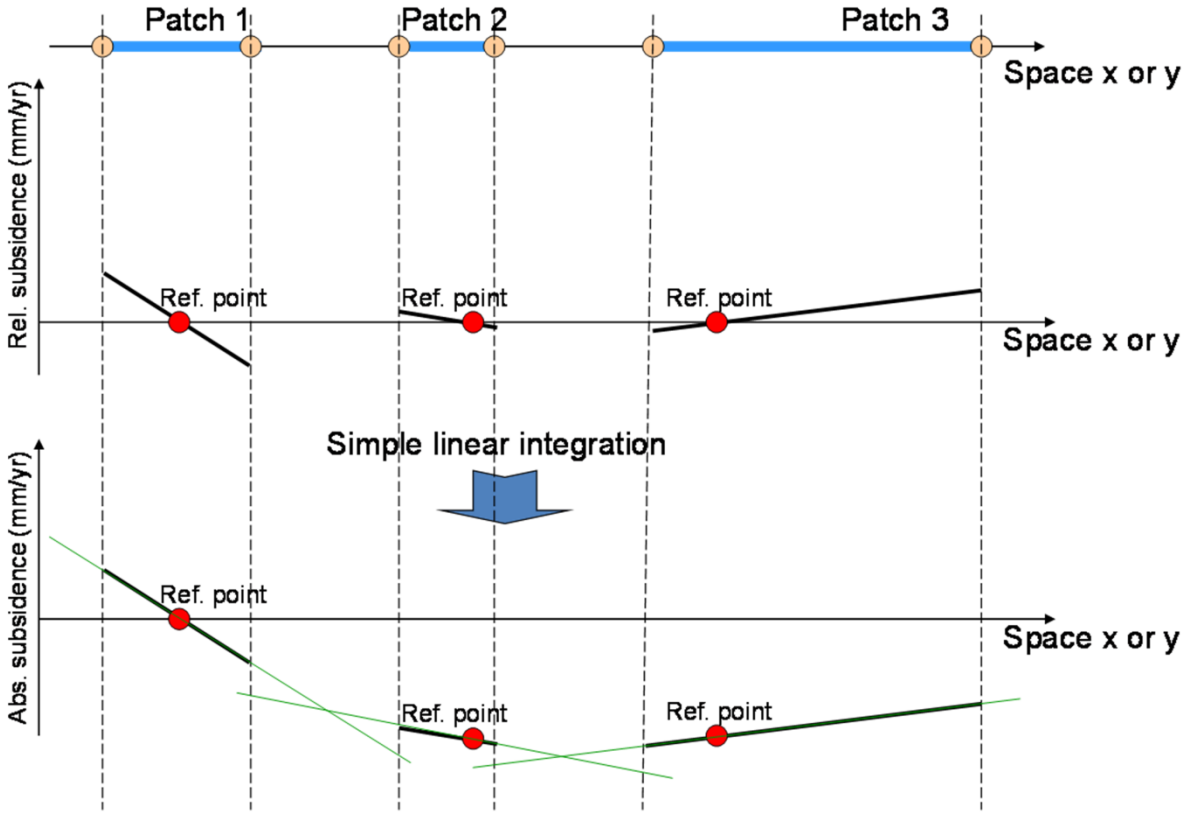

Figure 37: A simple 1D example of integrating the relative deformation of the various patches to get the absolute values.

In the practical implementation, an elliptical subsidence bowl has been assumed for the test site Lueneburg, which has undergone salt mining induced subsidence. This is because the most common shape of surface deformation due to mining is a circular or elliptical sag (Spreckels, 2000; Raucoules et al., 2003; Leijen and Hanssen, 2007; Perski et al., 2009). A 2D elliptical Gaussian deformation velocity field $g(x, y)$ (in mm/year) along the x and y directions is given by:

$$g(x, y) = p \cdot e^{-\left(a(x-x_0)^2 + 2b(x-x_0)(y-y_0) + c(y-y_0)^2\right)} \tag{42}$$

where p is the height/depth of the peak/valley and (x_0, y_0) is the center of the deformation trough. The coefficients a, b and c are given as follows:

$$a = \frac{\cos^2\theta}{2\sigma_x^2} + \frac{\sin^2\theta}{2\sigma_y^2} \tag{43}$$

$$b = -\frac{\sin 2\theta}{4\sigma_x^2} + \frac{\sin 2\theta}{4\sigma_y^2} \tag{44}$$

$$c = \frac{\sin^2 \theta}{2\sigma_x^2} + \frac{\cos^2 \theta}{2\sigma_y^2} \tag{45}$$

where θ is the rotation of the ellipse from x axis in clockwise direction and σ_x and σ_y are the spreads in x and y directions, respectively The deformation model is shown in Figure 38. For simplicity, it has been assumed that the vertical deformation derived from the model expresses surface subsidence along the satellite's LOS. Equation (42) allows the possibility to model an elliptical (or circular) subsidence bowl or even a non-deforming zone. The deformation integration is thus a model parameter estimation problem, wherein, the 2D Gaussian deformation field parameters p, x_0, y_0, θ, σ_x, σ_y have to be estimated given the gradients of the deformation velocity $m_{v_x}^j$ and $m_{v_y}^j$ for the reference points x_{ref}^j and y_{ref}^j, respectively corresponding to the P patches $j = 1,...,P$.

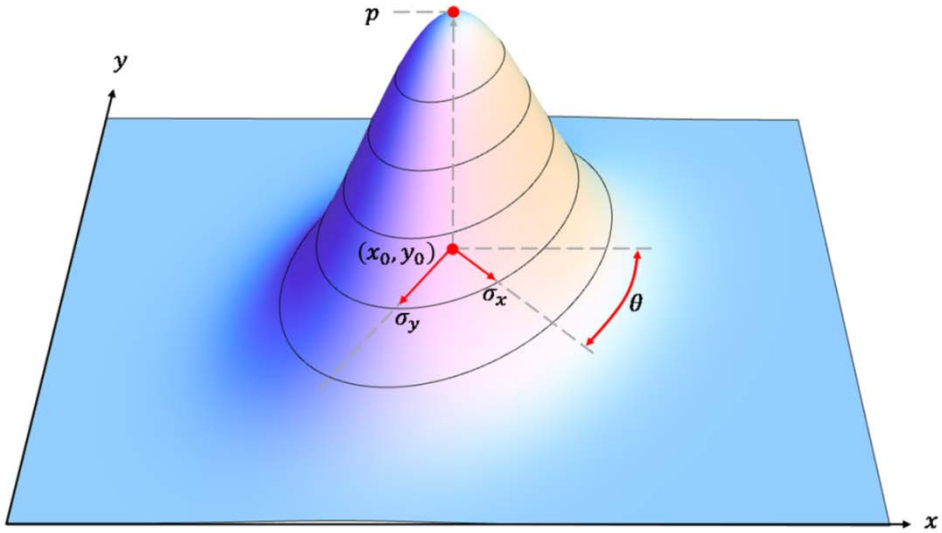

Figure 38: A 2D elliptical Gaussian deformation velocity model along the range (x) and azimuth (y) directions. It is defined by the parameters p, x_0, y_0, θ, σ_x, σ_y. p is the height/depth of the peak/valley, (x_0, y_0) is the center of the deformation, θ is the rotation of the ellipse from x axis in clockwise direction, and σ_x and σ_y are the spreads in x and y directions, respectively.

It is important to note that a non-linear least squares curve fitting cannot be directly performed as the observations are the "gradients" of the deformation velocity in range and azimuth directions. In fact, the model parameter estimation can be expressed as a multidimensional non-linear optimization problem, where, the sum of the absolute errors between the observed gradients of deformation velocity and the modelled gradients of deformation velocity has to be minimized. Conventional methods for multidimensional non-linear minimization include Powell's conjugate gradient descent method (Powell, 1964), the downhill simplex method of Nelder and Mead (1965) and the truncated-Newton method by Nash (1982). However, most of these iterative methods need an initial starting point and find a local minimum of the function to be minimized and thus, may not be robust for the deformation integration. In addition, many of these optimization algorithms require derivatives' evaluations, but the function to be minimized is not totally differentiable.

Instead, Bayesian inference has been applied for the multidimensional non-linear regression (Papoulis and Pillai, 2002; Sivia and Skilling, 2006) by means of directed graphs and particle filters. It is a statistical approach in which all forms of uncertainty are expressed in terms of probability and parameter estimation is performed based on measured or empirical data. Bayesian inference has been demonstrated successfully for 3D positioning of PSs based on radargrammetry (Goel and Adam, 2012c).

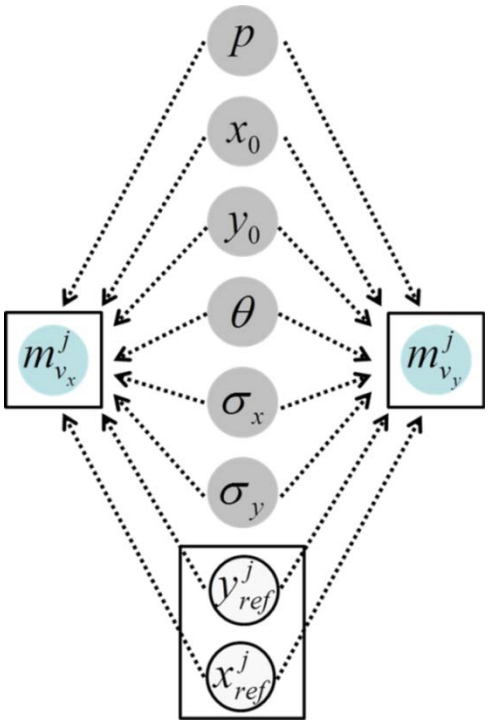

Figure 39: DGM for the estimation of 2D Gaussian deformation velocity field parameters. For each patch j, $j = 1,...,P$, the gradients of deformation velocity $m_{v_x}^j$ and $m_{v_y}^j$ in range (x) and azimuth (y) directions, respectively (known RVs, blue nodes) depend on the Gaussian deformation velocity field parameters p, x_0, y_0, θ, σ_x, σ_y (RVs to be estimated, grey nodes) and also on the location x_{ref}^j and y_{ref}^j of the reference point (known RVs, white nodes), and hence the direction of the arrows (i.e. arcs). The RVs $m_{v_x}^j$, $m_{v_y}^j$, x_{ref}^j and y_{ref}^j are enclosed in boxes, representing the multiple nodes for the P patches.

The Directed Graphical Model (DGM) for deformation estimation is constructed as shown in Figure 39 (Bishop, 2006). DGMs reduce complex Bayesian inference computations into simple graph manipulations. The parameters which are either observed, known or need to be estimated are considered as Random Variables (RVs) and represented by nodes. Here, $m_{v_x}^j$ and $m_{v_y}^j$ are observed RVs and are consequently represented by blue nodes in Figure 39. x_{ref}^j and y_{ref}^j are white nodes because they are known parameters, whereas p, x_0, y_0, θ, σ_x, σ_y are grey nodes because they have to be estimated. $m_{v_x}^j$, $m_{v_y}^j$ and x_{ref}^j, y_{ref}^j are enclosed in a box which represents multiple nodes (i.e. a sequential estimation) for the P patches $j = 1,...,P$. The directions of the arrows (i.e. arcs) describe the dependencies between the RVs. For the patch j, the gradients of the deformation velocity $m_{v_x}^j$ and $m_{v_y}^j$ in range and azimuth directions, respectively depend on the 2D Gaussian deformation velocity field parameters p, x_0, y_0, θ, σ_x, σ_y and also on the location x_{ref}^j and y_{ref}^j of the reference point. The probabilistic relation between the RVs can be evaluated using the DGM as follows (obtainable also from Bayes' theorem):

$$f(p, x_0, y_0, \theta, \sigma_x, \sigma_y \mid m_{v_x}^{1,\ldots,P}, m_{v_y}^{1,\ldots,P}, x_{ref}^{1,\ldots,P}, y_{ref}^{1,\ldots,P}) = \frac{l \cdot f(p) \cdot f(x_0) \cdot f(y_0) \cdot f(\theta) \cdot f(\sigma_x) \cdot f(\sigma_y)}{\int_{\sigma_y}\int_{\sigma_x}\int_{\theta}\int_{y_0}\int_{x_0}\int_{p} l \cdot f(p) \cdot f(x_0) \cdot f(y_0) \cdot f(\theta) \cdot f(\sigma_x) \cdot f(\sigma_y) \cdot dp \cdot dx_0 \cdot dy_0 \cdot d\theta \cdot d\sigma_x \cdot d\sigma_y} \tag{46}$$

where l is the likelihood function given by:

$$l = \prod_{j=1}^{P} f(m_{v_x}^j \mid p, x_0, y_0, \theta, \sigma_x, \sigma_y, x_{ref}^j, y_{ref}^j) \cdot \prod_{j=1}^{P} f(m_{v_y}^j \mid p, x_0, y_0, \theta, \sigma_x, \sigma_y, x_{ref}^j, y_{ref}^j) \tag{47}$$

In Equation (46) above, the term on the left hand side of the equation is the joint posterior Probability Density Function (PDF) of the elliptical Gaussian model parameters p, x_0, y_0, θ, σ_x, σ_y. The numerator on the right hand side of Equation (46) is comprised of the likelihoods $f(m_v^j \mid p, x_0, y_0, \theta, \sigma_x, \sigma_y, x_{ref}^j, y_{ref}^j)$ of the measured (i.e. observed) gradients of the deformation velocity for the different patches and the prior PDFs $f(p)$, $f(x_0)$, $f(y_0)$, $f(\theta)$, $f(\sigma_x)$, $f(\sigma_y)$ of the Gaussian model parameters. The likelihood of an observed gradient m_v^j (in range or azimuth direction) of deformation velocity for a patch j is computed using the absolute error between the observed gradient of deformation velocity and the modelled gradient of deformation velocity as follows:

$$f(m_v^j \mid p, x_0, y_0, \theta, \sigma_x, \sigma_y, x_{ref}^j, y_{ref}^j) = \frac{1}{2b} \cdot e^{-\left(\frac{\left|m_v^j - m\_gauss_v^j\right|}{b}\right)} \tag{48}$$

Here, $m\_gauss_v^j$ is the modelled gradient (in range or azimuth direction) of deformation velocity for patch j, that is to say, it is calculated from the Gaussian model parameters p, x_0, y_0, θ, σ_x, σ_y and b is a scale parameter. An L1-norm minimization has been used for the likelihood function, assuming Laplacian noise in the estimated gradients. This is because outliers might be present in the gradient estimates due to low spatial coherence of DS pixels. The L2-norm minimization results in a more stable solution when Gaussian noise is present in the estimated gradients, however, it is not robust when outliers are present. In contrast, the Laplacian density has larger tails than the Gaussian and thus, a greater number of large residuals are expected. Note that b is an additional parameter to be estimated. The prior PDFs of the Gaussian model parameters depend upon the prior knowledge (e.g. they can be taken as a uniform distribution in a suitable range). The denominator on the right side of Equation (46) is the evidence and can be neglected for the parameter estimation. It is only important if model selection has to be performed, as explained later in Chapter 6.

For the deformation estimation, the joint posterior PDF is computed and maximized to get the parameter estimates p^{MAP}, x_0^{MAP}, y_0^{MAP}, θ^{MAP}, σ_x^{MAP}, σ_y^{MAP}. This estimator is the MAP estimator:

$$\left(p^{MAP}, x_0^{MAP}, y_0^{MAP}, \theta^{MAP}, \sigma_x^{MAP}, \sigma_y^{MAP}\right) = \underset{p, x_0, y_0, \theta, \sigma_x, \sigma_y}{\arg\max} \left(f(p, x_0, y_0, \theta, \sigma_x, \sigma_y \mid m_{v_x}^{1,\ldots,P}, m_{v_y}^{1,\ldots,P}, x_{ref}^{1,\ldots,P}, y_{ref}^{1,\ldots,P})\right) \tag{49}$$

The applied framework employs bootstrap particle filtering (i.e. condensation algorithm) for the MAP parameter estimation (Isard and Blake, 1998; Arulampalam et al., 2002). Particle filter is a sequential Monte Carlo technique for implementing recursive Bayesian filter using the concepts of importance sampling (and resampling). The basic idea is to represent the

required distribution by a set of discrete N_P random particles (i.e. samples and weights associated to each sample), thus, inherently dealing with complex, multimodal non-Gaussian PDFs which are difficult to represent analytically. The MAP estimation via Equation (49) is performed based on these particles. The assessment of the estimation quality is performed by computing the standard deviation of the estimated parameters by means of the posterior PDF. It is also possible to estimate more than one deformation bowls by dividing the SAR scene into smaller areas and performing the parameter estimation for these individually.

Note that in case a model has to be optimally chosen from different spatial models of deformation, it can be easily done via Bayesian inference. A good model balances goodness-of-fit with simplicity. The model which best describes the Bayesian problem is the one with the highest evidence. Following the basic concept of Monte Carlo integration, the practical implementation of Bayesian inference using particle filters can easily calculate the evidence by converting the integral into some kind of average of the discrete random particles.

To end with, the algorithm provides the deformation velocity at a resolution approximately in the scale of the homogenous objects in typically decorrelated areas. Due to model-based deformation integration, the deformation velocity for the whole subsidence bowl is estimated, including its center, as compared to conventional techniques such as PSI, SBAS and SqueeSAR which have a lesser number of estimated points.

4.3 Application Test Case and Results

The practical demonstration of this technique is provided using High Resolution Spotlight mode TerraSAR-X data of the town of *Lueneburg in Germany*, which was used in the previous chapter and has undergone salt mining induced subsidence. The area enclosed in red in Figure 33 is used as the test site. Figure 40 shows the Google Earth image of this test site. Figure 41 shows its corresponding SAR mean amplitude image. Important to note is the presence of vegetated and low reflectivity homogenous areas, leading to low density of PSs.

Figure 40: Google Earth image of the test site Lueneburg in Germany (enclosed in red).

Figure 41: TerraSAR-X mean amplitude image of the test site Lueneburg in Germany.

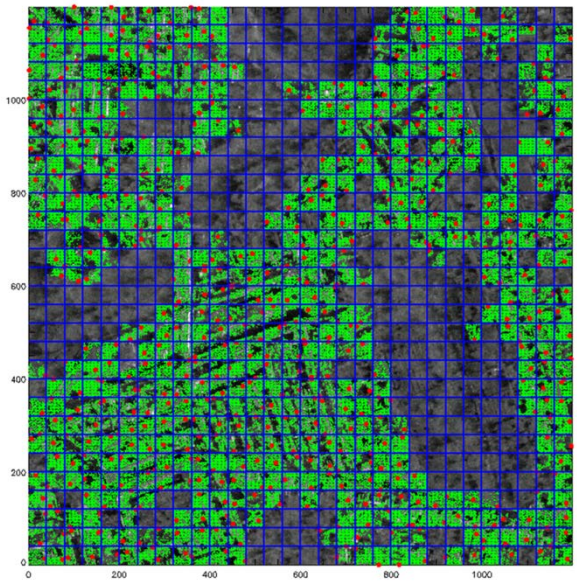

Figure 42: Identification of homogenous patches for Lueneburg in Germany using 17 TerraSAR-X amplitude images via Anderson-Darling statistical test. The region is divided into blocks by the blue lines, where, the points in green represent the homogenous pixels and the points in red represent the reference pixels.

The dataset has been processed using the new DSI technique. As mentioned in the previous chapter, 89 small baseline differential interferograms have been generated based on a maximum spatial baseline of 150 m and a maximum temporal baseline of 150 days. DLR's PSI-GENESIS processor has been employed for DInSAR processing (Adam et al., 2003, Adam et al., 2004; Kampes, 2006). The baseline-time plot is shown in Figure 29. As can be noticed, it is a well-connected network of interferograms because of the short repeat cycle of TerraSAR-X and highly reproducible scene repetition of the spotlight acquisitions, consequently ensuring the temporal continuity of the deformation measurements. The coherence matrix of the dataset is illustrated in Figure 30. It can be seen that only small baseline combinations have been used for the processing. Moreover, the average coherence of this region can be observed as low, typical for rural areas, thus advocating the need for DSI.

The identification of homogenous patches for Lueneburg using the 17 TerraSAR-X amplitude images is shown in Figure 42. The region was divided into rectangular blocks of 40 pixels by 40 pixels, i.e. 24 m by 24 m approximately. Within each block, homogenous pixels were identified by means of the Anderson-Darling statistical test based on a minimum patch size of 400 pixels and a coherence threshold of 0.3.

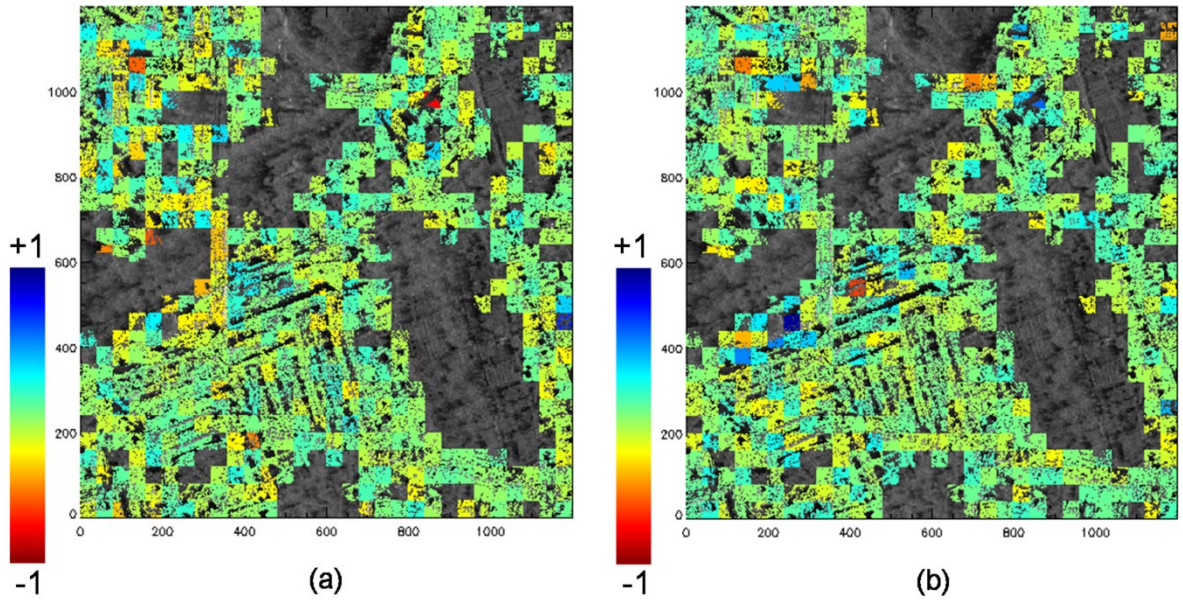

Figure 43: Residual DEM gradient estimation results for Lueneburg, Germany, using 89 small baseline differential interferograms. (a) Local gradients of residual DEM in range (x) direction in m/pixel. (b) Local gradients of residual DEM in azimuth (y) direction in m/pixel.

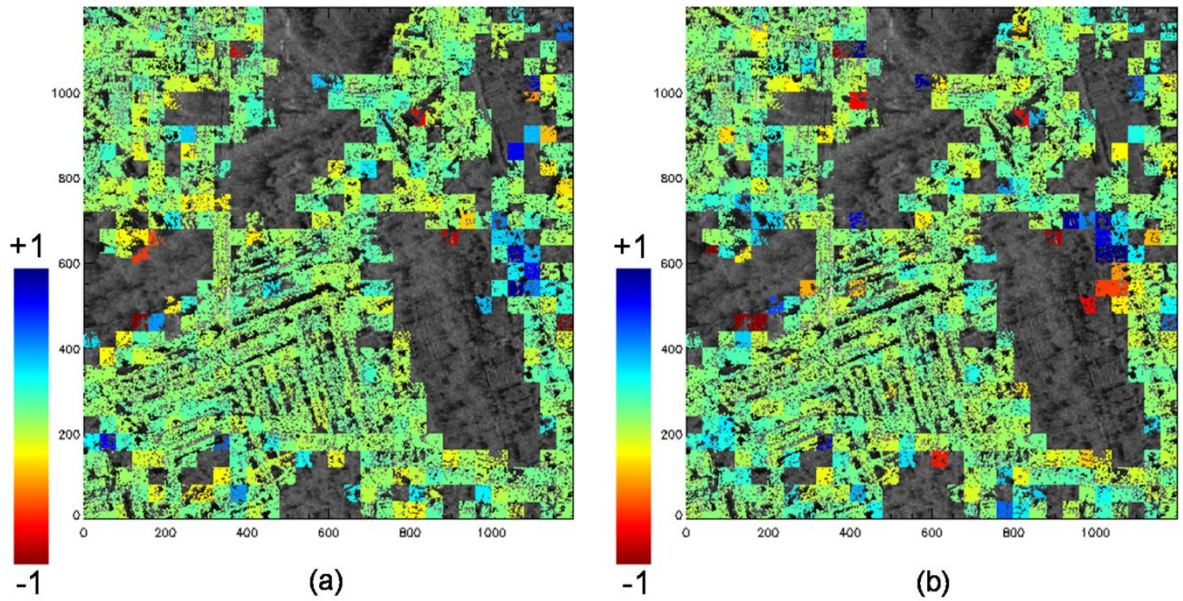

Figure 44: Deformation gradient estimation results for Lueneburg, Germany, using 89 small baseline differential interferograms. (a) Local gradients of deformation velocity in range (x) direction in mm/year/pixel. (b) Local gradients of deformation velocity in azimuth (y) direction in mm/year/pixel.

Figure 43 visualizes the gradient estimation results for the residual DEM in range and azimuth directions in m/pixel for the test site. Estimation of residual DEM gradients is essential for an accurate estimation of deformation velocity gradients. Figure 44 visualizes the

gradient estimation results for the deformation velocity in range and azimuth directions in mm/year/pixel. The number of homogenous pixels and temporal coherence (i.e. peaks of the periodograms) for the patches are illustrated in Figure 45. The gradients have been estimated for a total of 536,456 points in an area of 1200 pixels by 1200 pixels.

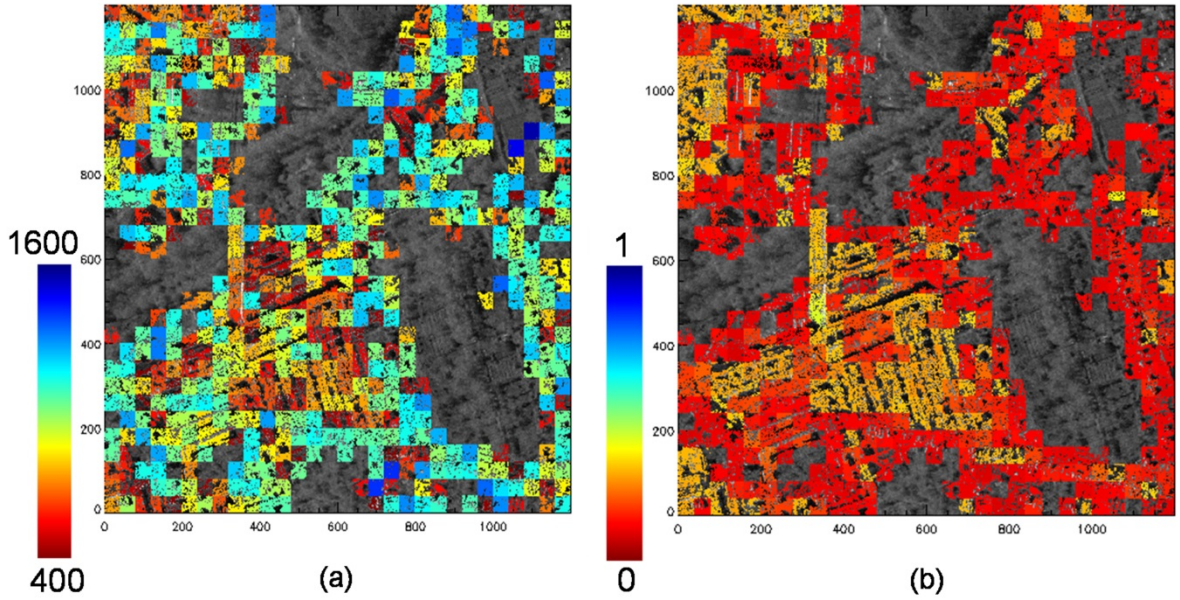

Figure 45: (a) The number of homogenous pixels for the patches of Lueneburg, Germany. (b) The temporal coherence (i.e. peaks of the periodograms) for the patches.

The deformation integration results using the DSI technique are presented in Figure 46. The scene was divided into nine equal areas of 400 pixels by 400 pixels each and deformation integration was performed independently for these, wherein, 10 million particles were used for representing the posterior distribution in Equation (46). The results obtained for surface deformation velocity show two Gaussian subsidence bowls, one having a larger deformation than the other and also covering a larger area. The Gaussian subsidence bowls with spreads smaller than a certain threshold were not taken into account. This is because, practically, at least three patches need to be fed into the integration model for an elliptical Gaussian subsidence (it has 6 parameters). Other types of deformation, e.g. structural stress of buildings, can spatially be fully described by 2 parameters only, i.e. a single homogeneous patch is sufficient for the deformation estimation. Keeping in mind that the minimum patch size used for this test case was 400 pixels (large enough to provide a reliable estimate of the deformation and topographic gradients as mentioned in Subsections 4.2.1 and 4.2.2), a threshold of 20 pixels was applied for the spreads of the Gaussian deformation bowl (assuming that the patch is a square of 20 pixels by 20 pixels).

The dataset was also processed using another technique, namely, the high resolution advanced SBAS technique which was explained in the previous chapter (Goel and Adam, 2012a). It makes use of small baseline differential interferograms and incorporates an object-adaptive spatial phase filtering and residual topography removal for an accurate phase and coherence estimation, while preserving the object resolution. This is followed by retrieval of deformation via the SBAS approach, wherein, the phase inversion is performed using an L1-norm minimization which is more robust to the typical phase unwrapping errors encountered in non-urban areas, cf. Chapter 3. Again, the 17 TerraSAR-X images and the 89 small baseline differential interferograms were utilized to obtain the deformation time series for Lueneburg. Pixels that have an average spatial coherence of at least 0.3 were used (i.e.

121,024 points in an area of 1200 pixels by 1200 pixels). The mean deformation velocities estimated using this SBAS technique are presented in Figure 47. The high density of information which can be extracted using the DSI technique can be seen by comparing Figure 47 with Figure 44 (which has 536,456 estimated points).

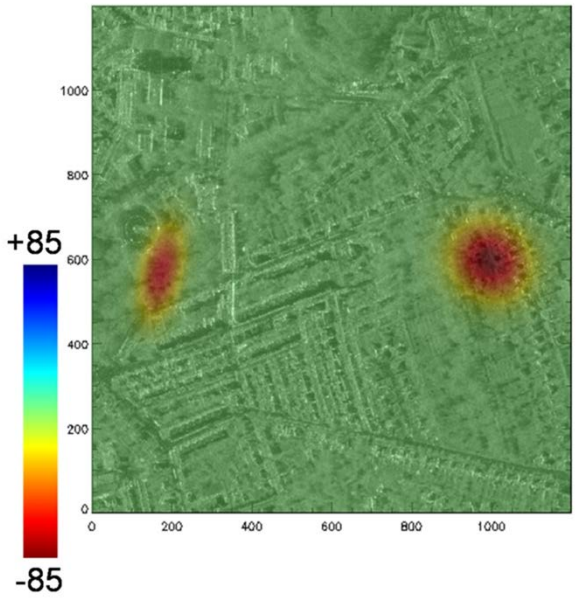

Figure 46: Deformation velocity in mm/year estimated for Lueneburg in Germany using the new DSI technique.

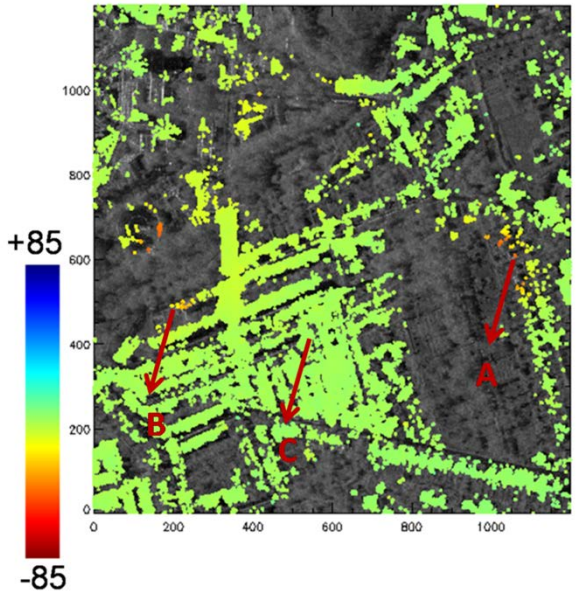

Figure 47: Deformation velocity in mm/year estimated for Lueneburg in Germany using the high resolution advanced SBAS technique (Goel and Adam, 2012a). Deformation time series comparison for points A, B and C using advanced SBAS and DSI are shown in Figure 48.

The features which have been identified as deforming in Figure 47 are also deforming in Figure 46. The DSI approach, significantly, provides spatially dense deformation velocity estimates instead of just a few measured points using advanced SBAS. The main reason is that the model-based gradient inversion is advantageous as compared to standard phase unwrapping in such areas as the deformation model is known. It is thus possible to better

define the areas which are subsiding and even identify new ones not previously detected using conventional techniques in non-urban terrains.

Deformation time series are visualized in Figure 48 for some of the pixels marked in Figure 47. The time series using advanced SBAS and DSI (assuming a constant velocity model) have been compared. The estimated mean deformation velocities using DSI show a good fit to the non-linear deformation time series measured using SBAS.

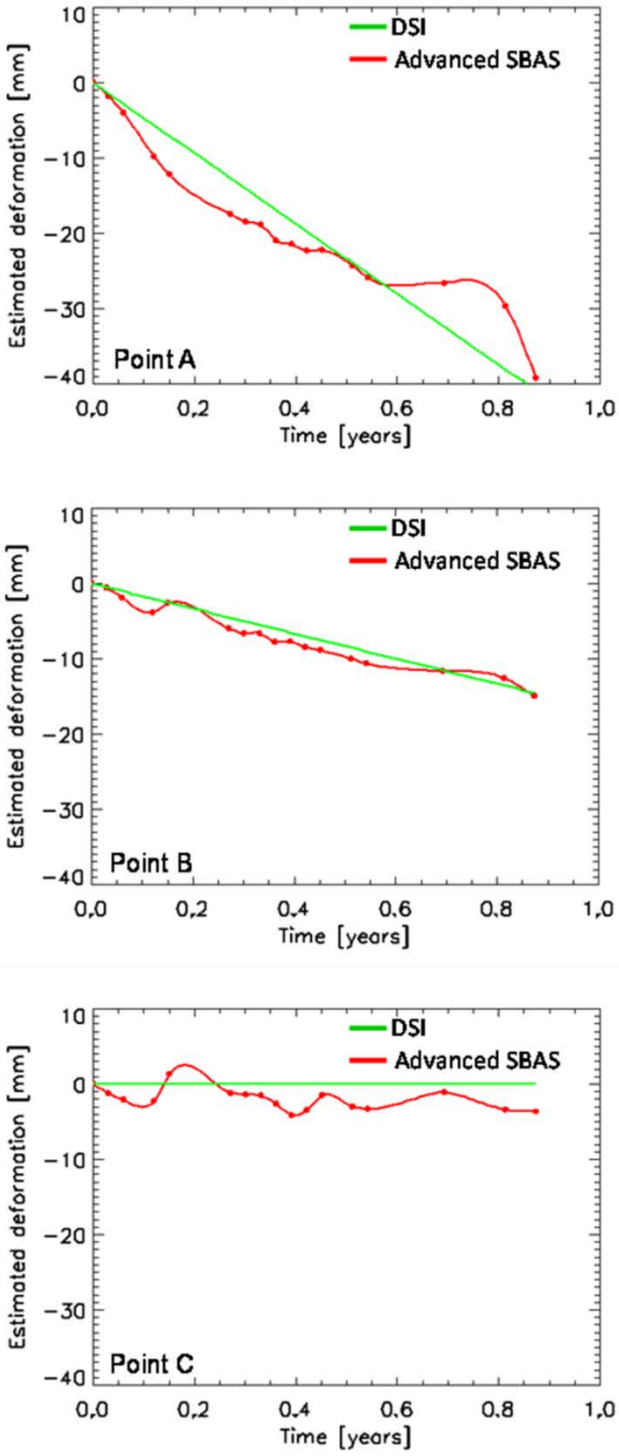

Figure 48: Deformation time series comparison for points A, B and C in Lueneburg, Germany, marked in Figure 47, using DSI (assuming a constant velocity model) and advanced SBAS.

The density histograms of the mean deformation velocity estimates utilizing the two techniques are shown in Figure 49. What can be seen is the advantage provided by DSI, which measures even the points with highest subsidence (i.e. centers of subsidence bowls), that are not measured by advanced SBAS due to high temporal decorrleation. It also shows that the points, where the subsidence has not been detected using DSI, have zero deformation velocities. This, of course, does not mean that there is no deformation outside the identified subsidence bowls. It just shows the absence of motion patterns that follow the Gaussian elliptical deformation velocity model.

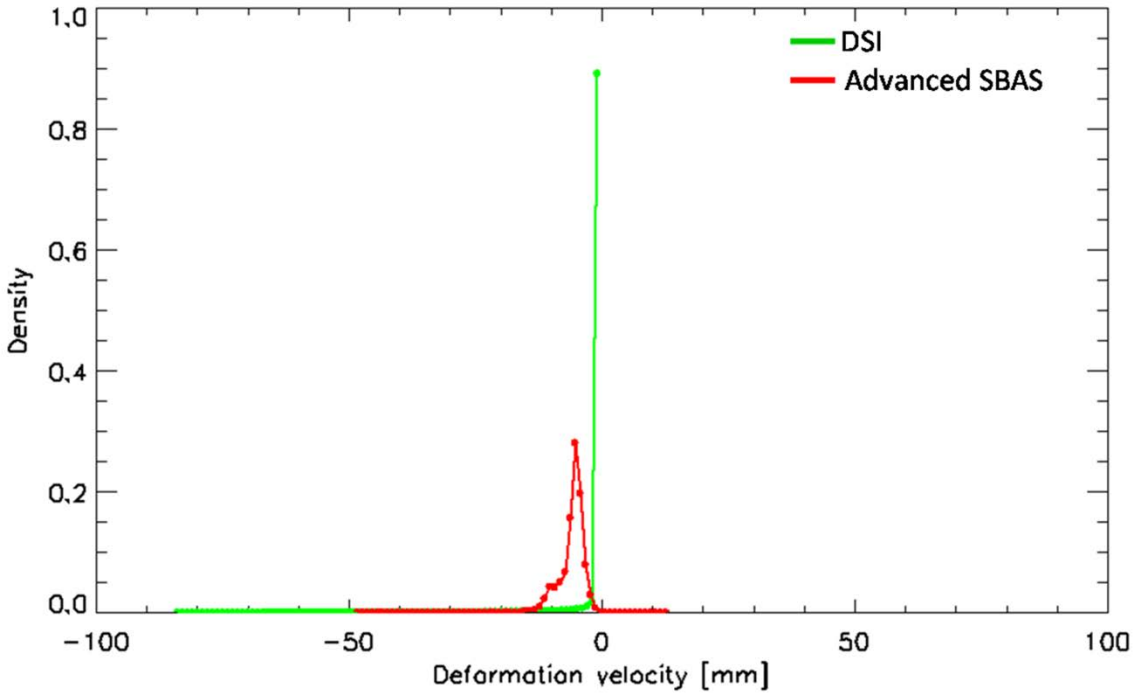

Figure 49: Density histograms of the mean deformation velocity estimates for Lueneburg, Germany, utilizing DSI and advanced SBAS.

Additionally, the ground truth for Lueneburg has been collected. Figure 50 shows the pictures of the area of the bigger subsidence bowl in Lueneburg, 'Ochtmisser Kirchsteig', which has been detected using the DSI technique (i.e. region surrounding point A marked in Figure 47). The effects of subsidence are encircled in yellow. Figure 51 shows the picture of the area of the smaller subsidence bowl in Lueneburg, 'Frommestrasse', which has been detected (i.e. region surrounding point B marked in Figure 47). It can be seen that both these regions have undergone high subsidence (and have suffered considerable damage), as measured by the DSI technique too.

The standard deviations of the estimated parameters have also been calculated from the posterior PDF. These provide information about the precision of estimation. The standard deviation values for p^{MAP}, x_0^{MAP}, y_0^{MAP}, θ^{MAP}, σ_x^{MAP}, σ_y^{MAP} are in the order of 0.37 mm/year, 5.96 pixels, 5.96 pixels, 0.01 radians, 1.28 pixels, 1.28 pixels, respectively. Evidently, the precision of this technique is good for high resolution sensors such as TerraSAR-X. The results demonstrate the potential of this new technique for deformation mapping in highly decorrelated areas utilizing DSs.

Figure 50: Pictures of the area of the bigger subsidence bowl in Lueneburg, ‘Ochtmisser Kirchsteig’, which has been detected using DSI (i.e. region surrounding point A marked in Figure 47).

Figure 51: Picture of the area of the smaller subsidence bowl in Lueneburg, ‘Frommestrasse’, which has been detected using DSI (i.e. region surrounding point B marked in Figure 47).

4.4 Discussion and Conclusion

A novel concept has been developed for a robust deformation velocity mapping and parametric modelling in highly decorrelated regions, at a suitable object resolution. The

increased density and quality of the deformation estimates is the clear advantage. This new DSI technique is based on an object-adaptive parameter estimation which makes use of the high resolution provided by modern sensors. Only the small baseline differential interferograms are utilized in order to reduce the computational burden. The algorithm compensates the DEM errors and atmosphere.

Note that a first order approximation is made that the deformation velocities and residual topographies of the homogenous pixels in a patch show a linear spatial behaviour in range and azimuth directions, respectively with respect to the reference pixel.

Essentially, this assumption is true for deformation as long as it is not varying spatially faster in comparison to the pixel size (otherwise, a higher SAR resolution would be beneficial), and moreover, it is also based on the sensor characteristics. In other words, the maximum deformation gradient which is measurable in an interferogram is determined by the signal wavelength and pixel spacing (Massonnet and Feigl, 1998). However, this is only valid under an ideal condition that there is no noise in the SAR observations. Phase noise due to uncompensated geometrical decorrelation, temporal decorrelation, thermal noise, atmospheric effects etc. can significantly affect the detectable deformation gradients. As a result, very small and large deformation gradients become undetectable if the level of noise is too high. In Baran et al. (2005), a new functional model has been proposed for the maximum and also the minimum detectable deformation gradients in an interferogram, taking into account the interferometric coherence which is a measure of the interferometric SNR, thus making the models more realistic. This way of modelling the spatial behaviour of surface deformation (assuming that it changes linearly over short distances) is especially valid for natural terrain, where, most surface deformation signals are smooth.

With regards to topography, the above-mentioned assumption is a typical attribute of statistically homogenous pixels, since radar brightness is strongly dependent on orientation and slope of a resolution cell. Explicitly, only those pixels would be selected as homogenous, which exhibit a smoothly varying topography. Thus, the identification of homogenous patches is crucial. Again, in natural areas, the topography is mostly smooth.

Given that the above conditions are satisfied, this technique estimates the deformation velocity at a suitable object resolution. This is advantageous in contrast to conventional SBAS which estimates the deformation at a low resolution, and moreover, does not provide the deformation at points which have undergone high temporal decorrelation. There are various advantages of deformation and topographic gradient estimation using the wrapped phase via a periodogram. It ensures that more points (even with low coherence i.e. high phase noise) are estimated and even high gradients are measured. The conventional phase unwrapping algorithms are prone to errors due to spatial decorrelation, surface discontinuities, spatial fringe rates etc. The deformation and topographic components are separately estimated and can be used directly for integration, instead of the need for deformation estimation after phase unwrapping which is susceptible to errors (e.g. SBAS). There is no error propagation from one patch to the next (based on some quality map) as compared to local (path-following) phase unwrapping. Different interferograms acquired from different baselines (3D) are used for the estimation and this is the reason that this method is more accurate. However, it is worth mentioning that SBAS estimates the non-linear deformation times series, whereas the DSI technique is concentrated on providing the mean deformation velocity. This is the reason that SBAS requires conventional phase unwrapping operations, which might be difficult in such sparsely urbanized areas. The DSI method is computationally costly in identification of homogenous patches and the gradient estimation, whereas SBAS is computationally

expensive in phase unwrapping. With respect to SqueeSAR, the computational complexity is greatly reduced since only the small baseline differential interferograms are used.

The following aspects need to be taken into consideration.

Single-look differential interferograms have been used for the processing. Multi-looked interferograms generally should not be used, since the basis of this technique is using homogenous pixels for the estimation. Anyhow, conventional rectangular multi-looking can work if homogenous areas are larger and the multi-looking and subsequent estimation is restricted to small fixed averaging areas. Adaptive multi-looking (Goel and Adam, 2012a) is better as larger patches are possible (if the test site allows) and it leads to a better precision. But the multi-looking can lead to a smoothing of the deformation estimates. Also, non-overlapping blocks have been used for the identification of homogenous patches. Overlapping blocks can be considered too in the future to increase the resolution.

The units used for the local gradients of deformation velocity m_v are mm/year/pixel and for the local gradients of residual DEM m_h are m/pixel. This allows a generic estimation for different sensors. Needless to say, it is also possible to use “meters” instead of “pixels”, wherein, the sensor’s pixel spacing information is then required.

The smallest deformation pattern which can be measured depends on the type of subsidence effect and the resolution of the sensor. For example, as mentioned before in the previous section, if an elliptical Gaussian subsidence occurs, the minimum size of the bowl should be at least 3 patches. Anyhow, usually such a bowl has a larger dimension than this. In case of deformation due to structural stress of buildings or thermal dilation of bridges, even a single patch is enough.

For the test site, Lueneburg, which had been a salt mine, an elliptical subsidence has occurred. Subsidence bowls over mines usually occur when the overburden sags downwards due to failure of mine pillars. It results in a depression in the ground which is usually elliptical or circular in shape. The subsidence is nearly temporally linear and is normally greatest at the center of the bowl and decreases progressively till the boundaries of the impacted surface area are reached. Note that any appropriate model can be assumed and its parameters estimated in the same way using Bayesian inference, as described for the elliptical trough (just the number of unknowns should be less than or equal to the number of observations). For instance, sinkhole subsidence can instead occur in areas lying above underground mines which are located very close to the ground surface. This type of subsidence is pretty localized in extent and causes an abrupt depression of the ground surface as overburden material collapses into the mine. In addition, Bayesian inference also facilitates model selection for choosing the best model from different deformation models. The DSI approach is suitable to be applied to such phenomena as mining induced surface deformation and similar geological effects, which can be described by an appropriate model.

This chapter, in fact, is a “principle demonstration” of a new technique which provides measurements in highly noisy areas, which are often an issue with DInSAR time series analysis. The problem with standard phase unwrapping is that the involved distribution to be maximized is periodic and multi-modal. Hence, besides the standard errors, occasionally wrong results are obtained due to getting trapped in a wrong maximum/minimum. If many measurements are combined, a periodogram can be computed which may have side-lobes (multi-modal). However, using more data to estimate only a few parameters makes the solution less ambiguous in highly noisy areas (in general). The current limitation of this DSI technique is the model-based implementation, which requires the surface deformation pattern

to be known before starting the data analysis. In the future, it would be beneficial to research about more advanced integration methods which are model-free, thus, making this DSI approach more general.

This technique can benefit from better prior information, e.g. the suitable deformation integration model to be applied and from future SAR systems with 600 MHz chirp bandwidth. Future work can concentrate on integrating the topography gradients and correcting the exploited DEM. This requires a model-free approach since usually, the residual DEM cannot be modelled. Afterwards, non-linear surface displacements, as well as the atmosphere, can be estimated from the residual phase by taking into account their different frequency characteristics in space and time. More importantly, model-free deformation velocity integration would be the upcoming focus.

5 Fusion of Monostatic and Bistatic Interferometric Data Stacks for Distributed Scatterers

In the previous chapters, the stacking algorithms based on monostatic repeat-pass interferometry have been presented for elevation mapping and deformation monitoring. The TerraSAR-X and TanDEM-X satellites now together allow bistatic single-pass (motion-free and atmosphere-free) interferometry too. This chapter describes the potential of joint monostatic and bistatic SAR interferometric stacking for *complex urban area monitoring exploiting DSs*. The aim is an improved scene elevation and surface deformation estimation. The following paper is summed up:

A.4 Goel, K., Adam, N., 2013b. Fusion of monostatic/bistatic InSAR stacks for urban area analysis via distributed scatterers. IEEE Geoscience and Remote Sensing Letters PP (99), 1-5, DOI: 10.1109/LGRS.2013.2278204.

An application test case is presented using high resolution mixed TerraSAR-X/TanDEM-X data stacks of Las Vegas, US.

5.1 Introduction

In dense urban areas, interpretation of the SAR images and interferometric phase is problematic due to phase discontinuities (e.g. due to height discontinuities, noise etc.) and complex scattering situations such as radar layover and shadow. Spatial phase unwrapping proves to be a challenge and ambiguities in layover areas cannot be solved. Therefore, *the standard SRTM/TanDEM-X DEMs are erroneous or even useless in urban areas*, and advanced multi-baseline phase unwrapping algorithms are needed (Lachaise et al., 2007). Hence, there is a need to by-pass geometrical limitations (such as layover) of radar, and thus enhance the precision and quality of TanDEM-X height models.

PS-based multitemporal techniques allow analysis of individual structures in metropolitan areas with a high level of detail (Adam et al., 2008; Eineder et al., 2009). On buildings, there can be many such PS points. However, availability of such scatterers is opportunistic. To improve the spatial sampling of the measured points, partially coherent DSs can be exploited, since DSs also make up a significant percentage in X-band. On man-made structures like roofs, building walls, asphalt roads and concrete surfaces, the DSs also provide a long-time coherent radar return, although, the phase quality is not on par with the PSs. There is an increasing focus on an optimal processing of DSs for urban area monitoring.

The fusion of monostatic and bistatic high resolution InSAR stacks has been demonstrated exploiting DSs for complex urban area monitoring and by-passing scattering scenarios, for instance, radar layover. The bistatic and monostatic (small baseline) interferograms are first spatially adaptive multi-looked and DSs are selected (Parizzi and Brcic, 2011; Goel and Adam, 2012a). The bistatic interferograms with no deformation and atmospheric phase components are then exploited for topography estimation of each DS (no external DEM is used). These topographic phases are removed from the monostatic interferograms and the L1-norm based SBAS technique is applied to retrieve the residual topography and deformation time series of each DS (Berardino et al., 2002; Goel and Adam, 2012a).

5.2 Methodology

Based on *N SAR images* (including both bistatic and monostatic data), *M single-look bistatic interferograms* and *M′ single-look small baseline monostatic interferograms* are generated. The various steps involved in the fusion algorithm are:

5.2.1 Adaptive Spatial Phase Multi-looking and Distributed Scatterers Selection

The fusion algorithm first involves *the identification of DSs* which are basically, image pixels (i.e. resolution cells) with distributed scattering mechanism. As mentioned in the previous chapters, for extracting information from DSs, the SNR has to be improved by a local spatial averaging. Spatially adaptive filters which average statistically homogenous pixels can be used to enhance the amplitude, interferometric phase and coherence. Rectangular windows can be used too, however, they result in a loss of resolution and usually bias the estimates, for example, when there is a PS present in the rectangular window (which is usually the case in high resolution images of urban areas). Statistically identical pixels can be selected for multi-looking based on their amplitude distributions using statistical tests such as the Anderson-Darling test (Parizzi and Brcic, 2011; Goel and Adam, 2012a).

The Anderson-Darling test is performed for each image pixel and the homogenous pixels surrounding it are identified (i.e. a spatially adaptive estimation window which can have any size and shape) via Equation (33). A pixel can be included in different estimation windows, as compared to segmentation where each pixel is assigned to a single class. Note that in case of complex topography in urban areas (for example, presence of a building façade, roof and ground in neighboring pixels), the similarity test algorithm ensures that the homogenous pixels which are identified for a certain image pixel (e.g. a point on a building façade) belong to the same class (i.e. points on the façade as well). This is because the different classes have different backscattering characteristics. The estimation window for each pixel is then used for complex phase multi-looking of the interferograms (bistatic and monostatic) for an improved phase and coherence estimation. The object resolution is preserved in this adaptive multi-looking. Then, DSs are selected for further processing based on a minimum average spatial coherence and a minimum number of looks (so as to exclude PSs). Additionally, in the next subsection, a further selection of DSs is done based on the temporal coherence.

5.2.2 Bistatic Stacking Interferometry

The bistatic interferograms which are free from motion, atmospheric disturbances and temporal decorrelation are now exploited for height estimation of DSs. An external DEM is not used, since it has artifacts in urban areas and is of low resolution (e.g. SRTM DEM). Also, the standard TanDEM-X DEM suffers from the side-looking geometry of SAR, due to which issues like radar layover and shadow remain unsolved, unless multi-aspect data or a stack of acquisitions are used. For more details about layover geometry and modeling, see Wilkinson (1999) and Thiele et al. (2007). The interferometric phase $\phi^{k}_{InSAR\_Bi\_model}$ for a generic pixel in

the kth bistatic interferogram can be modelled using Equation (17) and is composed of the phase components due to topography only:

$$\phi^k_{InSAR\_Bi\_model} = \phi^k_{topo} = \frac{2\pi}{\lambda}\frac{B^k_\perp}{R\sin\theta}h \tag{50}$$

where h is the height of the pixel (relative to a reference pixel).

Given a few spatially adaptive multi-looked bistatic interferograms with different perpendicular baselines (and thus, different height of ambiguities) and referenced with respect to a single pixel, it is possible to retrieve the height information for each DS by using its wrapped interferometric phase vector. The height h of a DS here refers to the average height of the DS area which has been multi-looked. Since a pixelwise adaptive multi-looking has been performed, as described in the previous subsection, areas with sloping or complex topography are appropriately handled. The following model coherence function (periodogram) ξ is maximized for height estimation:

$$\xi(h) = \frac{1}{M}\left|\sum_{k=1}^{M} e^{j\left(\phi^k_{InSAR\_Bi\_obs} - \phi^k_{InSAR\_Bi\_model}\right)}\right| \tag{51}$$

where $\phi^k_{InSAR\_Bi\_obs}$ is the observed (spatially adaptive multi-looked) interferometric phase for a generic pixel in the kth bistatic interferogram. Since there is no deformation phase in the bistatic interferograms, the periodogram is a 1D function dependent just on the DS's height (and not on its velocity) and its values are known over an irregular grid defined by the available spatial baselines ($B^k_\perp$). The topography estimate for each DS is estimated from the peak of this periodogram, i.e.:

$$(\hat{h}) = \arg\max_h(\xi) \tag{52}$$

The maximum of the periodogram is the temporal coherence of the DS. The reference pixel is usually a highly coherent point located in a non-deforming zone (note that the same reference point is used later on for the monostatic interferograms in the next subsection). The precision of the estimation depends on the number of bistatic interferograms and the baseline distribution, since the sidelobes of the periodogram reduce by using more bistatic interferograms with varying perpendicular baselines (Rocca, 2004). It also depends on the phase stability of the DS and the sensor characteristics. The variance σ_h^2 of the height estimate of a DS is approximately given as follows (Bevington and Robinson, 1969):

$$\sigma_h^2 \cong \frac{\sum_{k=1}^{M}\left(\frac{1}{\sigma^k_\phi}\right)^2}{\sum_{k=1}^{M}\left(\frac{1}{\sigma^k_\phi}\right)^2 \sum_{k=1}^{M}\left(\frac{x^k}{\sigma^k_\phi}\right)^2 - \left(\sum_{k=1}^{M}\frac{x^k}{\left(\sigma^k_\phi\right)^2}\right)^2} \tag{53}$$

where $x^k = \frac{2\pi}{\lambda}\frac{B^k_\perp}{R\sin\theta}$ is the height-to-phase conversion factor and σ^k_ϕ is the phase standard deviation of the DS for interferogram k, respectively. The latter is a function of the spatial coherence and number of looks (Bamler and Hartl, 1998). Assuming $\sigma_\phi = 20^\circ$ and the height of ambiguities of the TerraSAR-X dataset described in the next section, $\sigma_h \cong 1.5m$. Then, DSs based on a minimum temporal coherence are selected for subsequent processing.

It is to be noted that, first, since the DS pixel has been multi-looked using its statistically homogenous pixels, the possibility of a layover (e.g. building and ground) inside a resolution

cell is quite low and usually a clear periodogram peak is obtained. This is because the radar amplitude is strongly dependent on orientation and slope of a resolution cell. Explicitly, only those pixels would be selected as homogenous which exhibit a smoothly varying topography. Second, since wrapped phase data is used for height estimation of DSs and no phase unwrapping is required, radar layover is by-passed and does not affect the algorithm.

5.2.3 Monostatic Stacking Interferometry

The DEM phase components estimated via the bistatic interferograms are used to compute the differential monostatic interferograms. *These monostatic interferograms are then exploited for residual topography and deformation time series mapping*. There might still be residual topography present in the flattened monostatic interferograms, since the baseline spread of bistatic interferograms is restricted by the number of data pairs and their perpendicular baseline separation. Only small baseline monostatic interferograms are used, so as to reduce the effects of residual topography and decorrelation on the DSs.

The SBAS technique is used to estimate the residual topography and complete non-linear deformation time series of the scatterers, incorporating the linear as well as the seasonal motion (e.g. for buildings), without using any model (Berardino et al., 2002). The conventional L2-norm minimization performs poorly in case of difficult-to-detect phase unwrapping errors. These errors might be present in urban areas due to tall and closely-located buildings, which result in radar layover and shadow. Thus, the more robust L1-norm cost function is applied to estimate the deformation time series for each DS at object resolution (Goel and Adam, 2012a).

5.3 Application Test Case and Results

The proposed algorithm has been applied on a test site approximately 4 km by 2.5 km centered at the Las Vegas Convention Center in *Las Vegas, US*. 84 High Resolution Spotlight mode TerraSAR-X/TanDEM-X images from February, 2008 to December, 2011 with a look angle of 36.04 degrees and VV polarization have been used. The mean amplitude image of the test site and its corresponding Google Earth optical image are shown in Figure 52. The pixel spacing is approximately 0.38 m in range direction and 0.42 m in azimuth direction (adapted to oversampling). A comparison between a bistatic and a monostatic interferogram of the test site Las Vegas can be seen in Figure 7.

The SAR images have been used to generate 5 bistatic interferograms with height of ambiguities -33.4, -44.7, -54.3, 53.9 and -53.8 m/cycle, respectively. Next, 174 monostatic interferograms have been generated. These include, first, small baseline interferograms based on a maximum perpendicular baseline of 150 m and a maximum temporal baseline of 30 days. Second, these also include a few long time span (approximately 750 days) interferograms with very small perpendicular baselines (approximately 5 m) so as to include the full cycles of seasonal motion on buildings in these interferograms, the very small perpendicular baseline ensures that the effect of topographic phase on the interferograms is minimal. InSAR processing has been done using DLR's PSI-GENESIS processor (Adam et al., 2003, Adam et al., 2004; Kampes, 2006). Figure 53 shows the baseline-time plot for the

scenes and interferograms, wherein, each dot represents a SAR image and each line represents an interferogram used in the processing.

Figure 52: Mean SAR amplitude image and its corresponding Google Earth optical image of the test site Las Vegas, US.

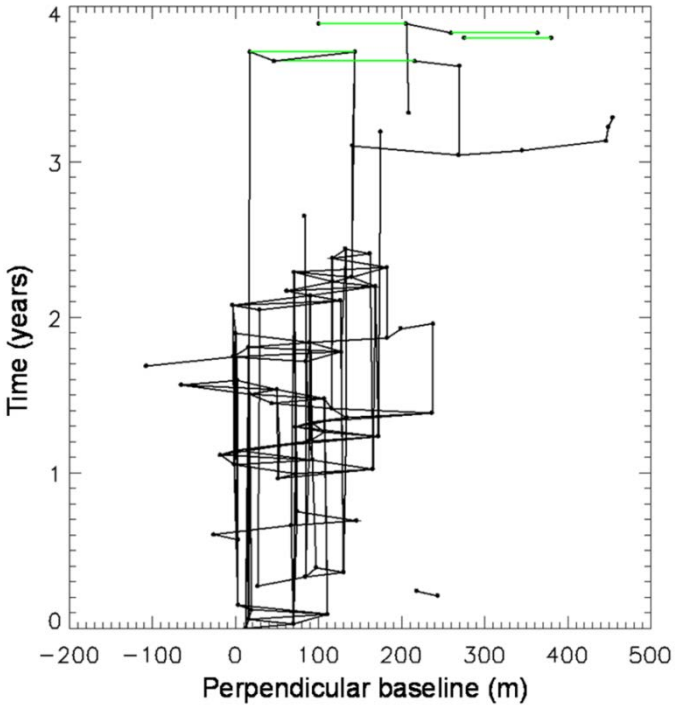

Figure 53: Baseline-time plot of the TerraSAR-X/TanDEM-X data of Las Vegas, US. Each dot represents a SAR image and each line represents an interferogram. The monostatic interferograms are shown in black, whereas the bistatic interferograms are shown in green.

Then, the adaptive spatial filtering algorithm is applied on the single-look interferograms, as demonstrated in Figure 54. The minimum and maximum size of the homogenous patch is set to 20 and 200 pixels, respectively. The reduction in the phase noise and the improvement in interferometric phase can be clearly seen.

This is followed by height estimation of the DSs for the test site by means of 1D periodogram approach using only the 5 bistatic single-pass interferograms, as presented in Figure 55. DSs have been selected which have an average spatial coherence of at least 0.7 and temporal coherence of at least 0.5, so as to exclude decorrelated areas. A total of 6,361,670 points have been processed (approximately 600,000 DSs per square km). Assuming a best case scenario of 100,000 PSs per square km, this is a 6 times increase in the density of

measured points. The subsequent flattening of the monostatic repeat-pass interferograms is illustrated in Figure 56. Evidently, the fringes due to very high buildings in Las Vegas have been removed. It is worth mentioning that the residual topography is still present in the monostatic interferograms (due to possible errors in the height estimation using the bistatic interferograms) and has to be removed. The better the precision of the height estimation (as given by Equation (53)), the lower is the magnitude of the residual topography.

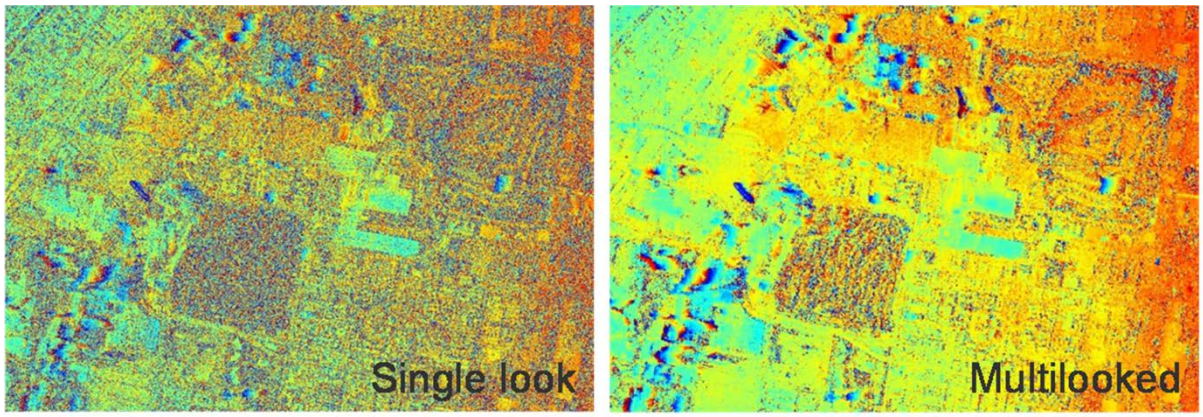

Figure 54: A single-look monostatic interferogram of Las Vegas, US and its spatially adaptive multi-looked version.

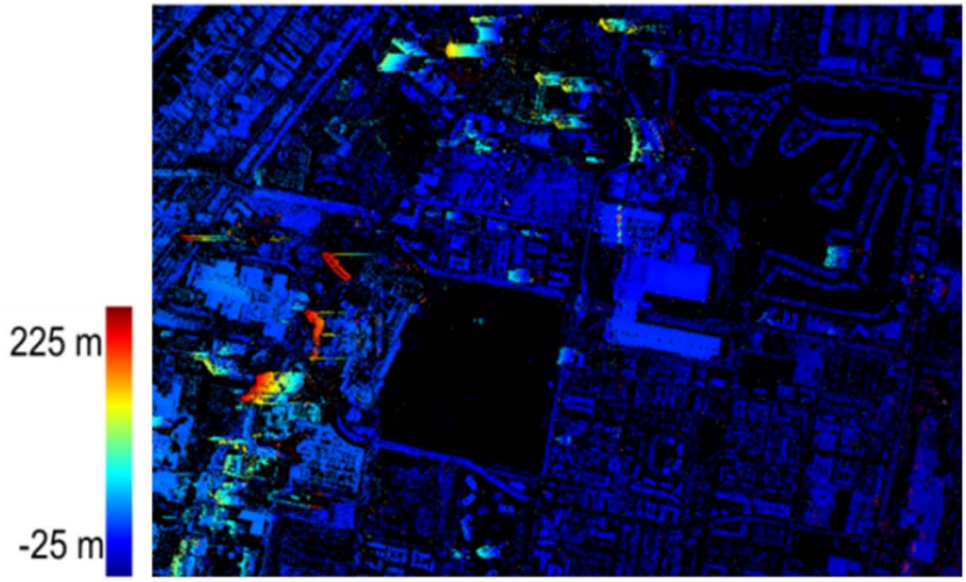

Figure 55: DS height estimates for Las Vegas, US, using bistatic interferograms via 1D periodogram.

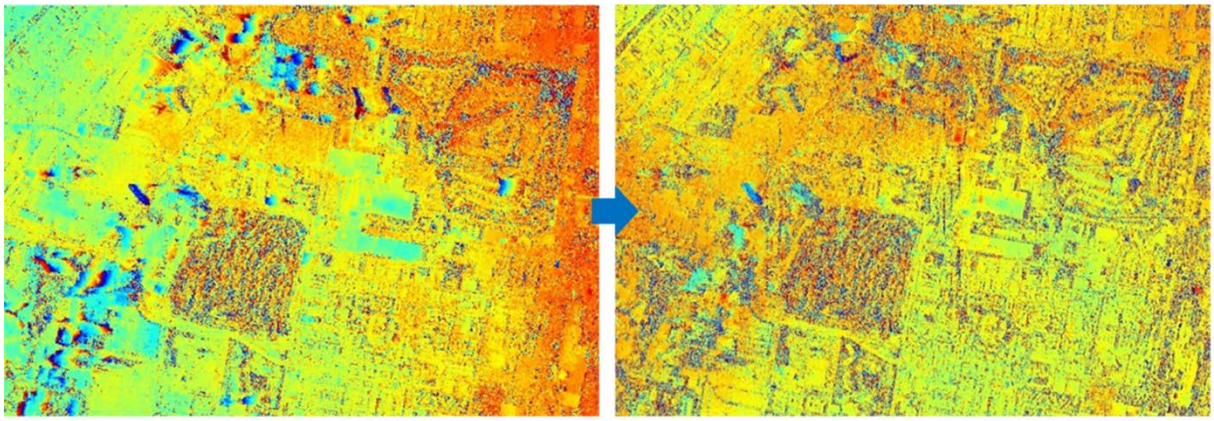

Figure 56: Illustration of removal of topographic phase from a monostatic interferogram of Las Vegas, US.

The flattened monostatic interferograms are now unwrapped using the MCF algorithm (Costantini, 1998; Eineder et al., 1998). These are subsequently used for residual topography and deformation monitoring using the SBAS approach via the L1-norm minimization. The estimated residual topography for the DSs of Las Vegas is in the order of a few meters, although there are some DSs which have a significantly high DEM error which is greater than 10 m (approximately 2.8% of the selected DSs). The estimated RMS deformation and an example of a deformation time series for a DS are shown in Figure 57. The RMS deformation is visually effective and provides integral information about the displacement with respect to time. As can be seen, even non-linear deformation time series can be estimated, which include the linear as well as seasonal deformation on buildings due to thermal dilation (Zhu and Bamler, 2011). The standard deviation of the deformation estimates using the L1 norm inversion is between 0 and 3.1 mm and thus, this method provides millimeter precision. The standard deviation is higher for DS points in layover regions or having a seasonal motion.

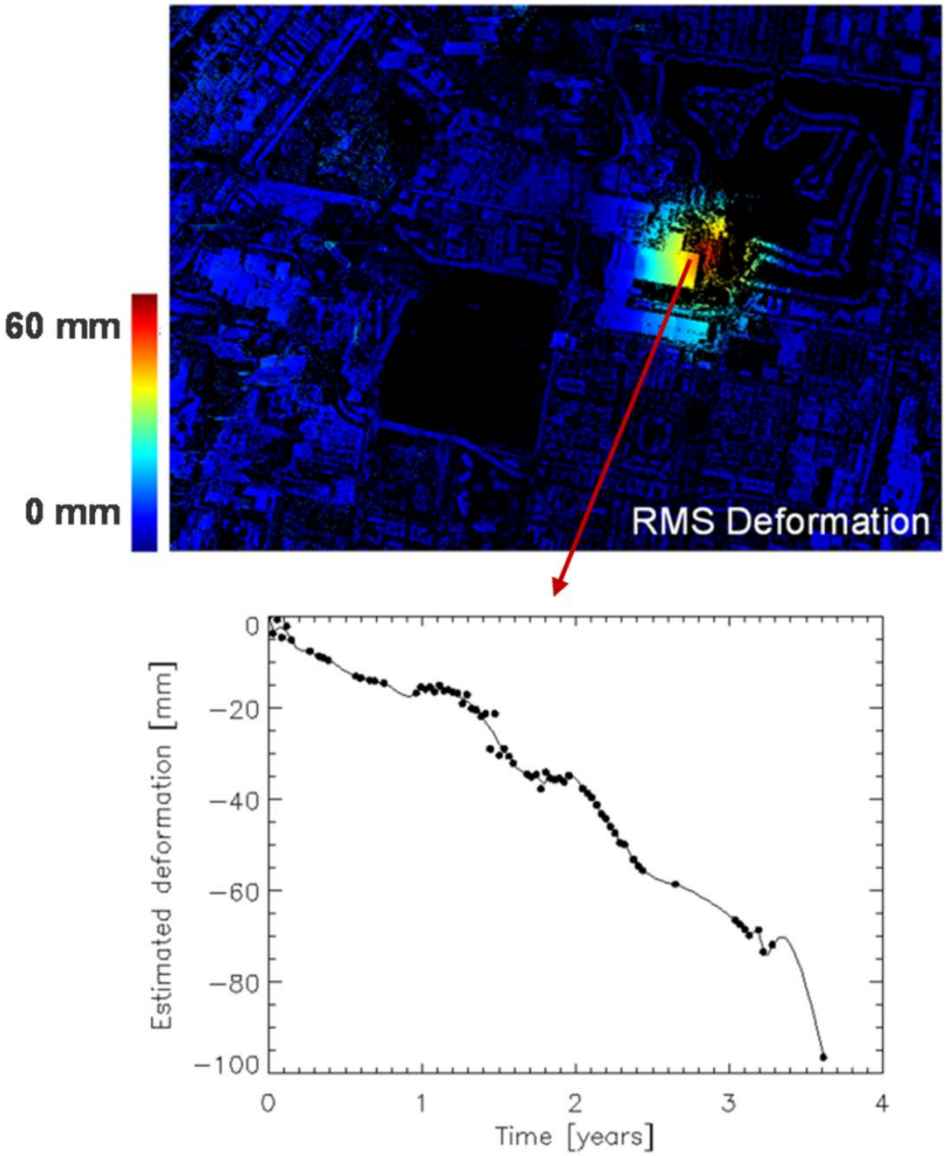

Figure 57: DS deformation estimates for Las Vegas using flattened monostatic interferograms via L1-norm based SBAS. Deformation time series is visualized for a DS, where, the dots represent the estimated deformation at the time of SAR acquisitions and the solid line is a line fitting using cubic spline interpolation.

5.4 Discussion and Conclusion

High resolution SAR sensors TerraSAR-X and TanDEM-X enable bistatic and monostatic interferometry. Especially, the bistatic interferograms have a high data quality and are free from deformation, atmosphere and temporal decorrelation. By properly integrating the data stacks, an improved estimation of topography and deformation time series at object resolution is possible. In particular, an advanced integration of TerraSAR-X and TanDEM-X InSAR data has been investigated utilizing DSs in dense metropolitan areas, where the standard TanDEM-X elevation models are inaccurate. The DSs also have a high density in urban areas. The developed method complements coherent stacking techniques such as PSI and TomoSAR. The results of processing a TerraSAR-X/TanDEM-X dataset of Las Vegas in US show the millimeter precision which can be obtained. No standard TanDEM-X / external DEM was used in the processing. Since the same multi-looking window is used for topography and deformation estimation of DSs, error propagation is minimal. The fusion algorithm is easy to implement without much add-ons to the existing techniques and is computationally efficient.

Note that there might be bright pixel patterns along azimuth and range directions, especially in urban areas. These are caused by high power side lobes due to discontinuities at the margins of the signal spectrum for strong signal returns. Side lobe suppression can be performed to reduce this effect (Breit et al., 2008).

Additionally, the periodogram approach for estimating heights using the bistatic interferograms works well for single PSs too, however, it must be stressed that the periodogram can lead to a wrong estimation in case of PSs which are characterized by two (or few) dominant scatterers inside a resolution cell. In fact, the next chapter presents the potential of jointly processing TerraSAR-X/TanDEM-X data using PSs.

6 Fusion of Monostatic and Bistatic Interferometric Data Stacks for Persistent Scatterers

This chapter presents the integration of monostatic repeat-pass and bistatic single-pass SAR interferometric stacks for *complex urban area monitoring exploiting PSs*. The aim is to resolve single or double scattering mechanism present in the same resolution cell. The following paper is recapitulated:

A.5 Goel, K., Adam, N., 2013c. Advanced stacking of TerraSAR-X and TanDEM-X data in complex urban areas. Proceedings of Joint Urban Remote Sensing Event, JURSE 2013, Sao Paulo, Brazil, 21-23 April, 115-118.

Additionally, simulations based on realistic acquisition and noise scenarios have been presented to evaluate the potential and limits of this fusion technique. Afterwards, a demonstration is provided using high resolution mixed TerraSAR-X/TanDEM-X data of Las Vegas, US which was used in the previous chapter.

6.1 Introduction

PSI is a well-established interferometric stacking technique for measuring Earth's topography and deformation (Ferretti et al., 2000; Ferretti et al., 2001). High resolution satellite TerraSAR-X allows millimeter accuracy with the standard monostatic mode (Adam et al., 2008; Eineder et al., 2009). Its twin satellite TanDEM-X, together with TerraSAR-X, now facilitates bistatic mode also. Addition of a few motion-free and atmosphere-free bistatic TanDEM-X data pairs to the existing monostatic TerraSAR-X data stack can improve the 3D positioning and deformation monitoring of objects. However, the combination of bistatic and monostatic data can be challenging in dense metropolitan areas, where, the standard TanDEM-X elevation models are inaccurate because of geometrical limitations such as radar layover. Also, complex urban structures and the side-looking radar observation geometry make it likely that more than one scatterer are inside a resolution cell (Ferretti et al., 2005). Typical example is a layover of building and ground. In urban areas, around 15-30% of the PSs are double scatterers characterized by two dominant scatterers inside the same azimuth - slant range resolution cell but located at different elevations (Adam et al., 2005; Zhu, 2011). The elevation here refers to the axis perpendicular to the azimuth - slant range plane, as described in Subsection 2.1.1.

An approach has been developed that jointly processes monostatic and bistatic data for *resolving single or double scatterer in a resolution cell*. The typical solution to this problem is TomoSAR (Lombardini, 2005; Fornaro et al., 2009; Zhu and Bamler, 2010a), which provides the radar reflectivity along the elevation direction (see Subsection 2.3.2). However, a classical spectral estimation is limited in resolution and needs exact information on different interferometric phase contributions. A parametric tomography approach performs better but needs the scatterer configuration beforehand. Thus, the full tomography (utilizing the amplitude and phase data) requires information which basically comes from the PSI or TomoSAR estimation itself and needs an iterative processing. Instead, the proposed algorithm extends conventional PSI and solves the model selection problem about the number of scatterers (one or two) inside the resolution cell using bistatic interferometric phase data and monostatic amplitude data only. The use of only the monostatic amplitudes (and not the phases) is to avoid deformation and atmospheric interference. The technique utilizes the

baseline-dependency of the amplitudes. The quality and precision of TanDEM-X elevation models can be enhanced and subsequently, monostatic differential interferometric phase data can be used for displacement monitoring.

6.2 Methodology

Standard PSI is developed to cope with a single dominant scatterer inside a resolution cell (Ferretti et al., 2000; Ferretti et al., 2001). The periodogram based on a common master image is the optimal estimator in case of a single scatterer surrounded by incoherent clutter (see Equation (26)). Of course, the estimation is performed on arcs (linking neighboring PSs) to mitigate atmospheric propagation effects and the periodogram is a 2D function which estimates the differential velocity between the neighboring PSs, besides estimating the differential DEM error between them.

The TanDEM-X data pairs acquired simultaneously result in bistatic interferograms which have a high phase quality. There are no phase components due to motion and atmosphere and in addition, there is no temporal decorrelation (see Figure 7 for a comparison between a bistatic and a monostatic interferogram). Given a few bistatic interferograms with different height of ambiguities and calibrated with respect to a single pixel, it is possible to retrieve the height information in case of a single scatterer inside a resolution cell using the periodogram approach (similar to conventional PSI, without the need of a common master image). In this case, the periodogram is a 1D function which estimates the height (but not the velocity) of each PS. The topography estimation is performed akin to Subsection 5.2.2 based on *M single-look bistatic interferograms*, except that the observed interferometric phase is single-look, there is no need to multi-look the data for PSs. Referencing to a single pixel works fine since the atmospheric phase components are negligible. The precision of the height estimate of a PS is given by Equation (53), wherein, the phase standard deviation of the PS is given either by Equation (22) or Equation (23), depending on the method used for selecting the PS.

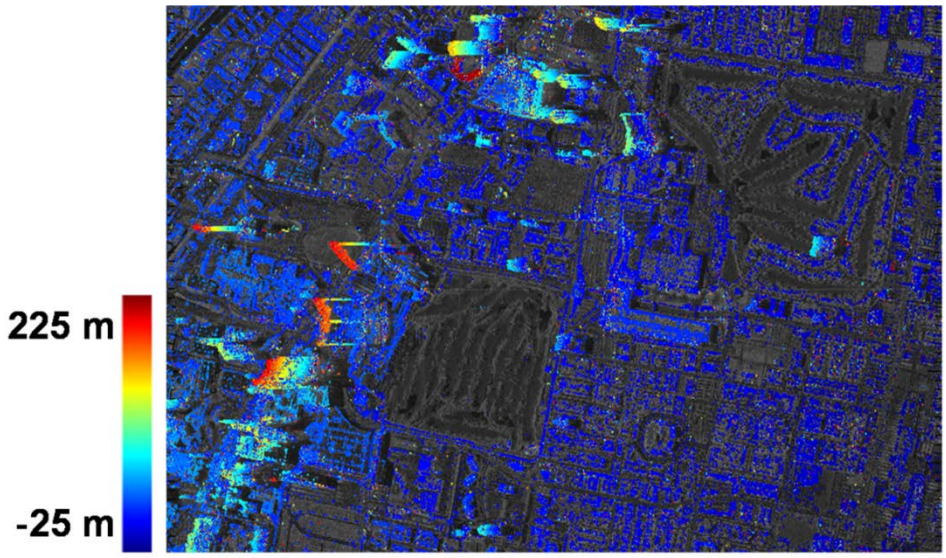

Figure 58: PS height estimates for Las Vegas, US, using bistatic interferograms via 1D periodogram. Processed points are overplotted on the mean amplitude image and color coded according to height values.

Figure 58 presents the PS height estimates via 1D periodogram for the test site Las Vegas using 5 bistatic interferograms with height of ambiguities -33.4, -44.7, -54.3, 53.9 and -53.8

m/cycle, respectively. The height estimates can be used later on for the removal of topographic phase from the monostatic interferograms. Afterwards, the flattened monostatic interferograms can be used for deformation mapping using standard PSI.

However, it can be seen in Figure 58 that there are many outliers in the results. This is because of the presence of double scatterers inside a resolution cell. An example of a periodogram for a single scatterer is shown in Figure 59 (a). What can be seen is the presence of strong sidelobes in the periodogram due to the use of only 5 TanDEM-X interferograms. Obviously, an ideal situation would be many bistatic interferograms with varying height of ambiguities to reduce the sidelobes of the periodogram and get a clear peak. Practically, this is not always possible. The periodogram estimates the height accurately only when a single scatterer is present in a resolution cell. The case of double scatterers in a resolution cell leads to biased or even a wrong estimation as demonstrated in Figure 59 (b).

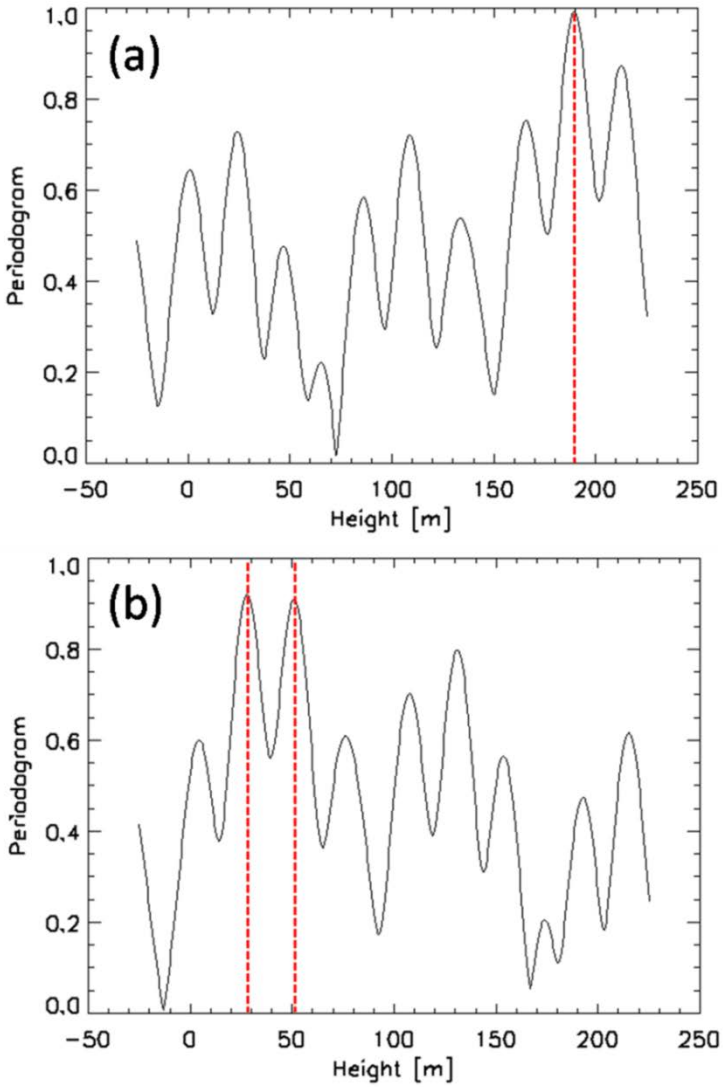

Figure 59: (a) Example of a periodogram for a single scatterer of the test site Las Vegas, US. (b) Example of a periodogram for a double scatterer of the test site Las Vegas, US (biased or wrong estimation of height).

To detect the scatterer configuration, the proposed algorithm increases the number of observations by making use of monostatic amplitude data (which is baseline-dependent as described later in Subsection 6.2.1 and Subsection 6.2.2), in addition to the bistatic interferometric phase data. It provides the number of dominant scatterers inside a resolution

cell and consequently solves the model selection problem. This allows resolving complicated scattering situations such as layover in urban areas, which is a problem for SAR. The scatterer configuration detection and height estimation support PSI and TomoSAR, which include the phase information and thus require the correction of displacement and atmospheric phase beforehand.

Given N *SAR monostatic amplitude images*, the model selection is based on the following two mechanisms.

6.2.1 Single Scattering Mechanism

A single scatterer, i.e. a panel made of metal can be described by a "*Sinc fit*", i.e. the following amplitude $a^j, j = 1,...,N$ (Adam et al., 2005; Bamler and Hartl, 1998; Ferretti et al., 2005):

$$a^j\left(x^j, r, \Delta, \phi\right) = r \cdot \left(\left|\frac{\sin\left(x^j\Delta + \phi\right)}{\left(x^j\Delta + \phi\right)}\right|\right) \tag{54}$$

where $x^j = \frac{4\pi}{\lambda}\frac{B_\perp^j}{R\sin\theta}$ is the phase-to-height conversion factor for image j, respectively, r is the reflectivity of the scatterer, Δ is the extension of the panel and ϕ is the orientation of the panel (i.e. orientation of the panel plane with respect to the azimuth - slant range plane).

6.2.2 Double Scattering Mechanism

The alternative model describing the amplitude $a^j, j = 1,...,N$ of a double scatterer is a "*Cos fit*" and results from the amplitude of the sum of two complex sinusoids and describes a fading (Adam et al., 2005). It is given by:

$$a^j\left(x^j, r_1, r_2, \Delta h, \phi\right) = sqrt\left(r_1^2 + r_2^2 + 2 \cdot r_1 \cdot r_2 \cdot \cos\left(x^j\Delta h + \phi\right)\right) \tag{55}$$

It models the reflectivities r_1 and r_2 of the two scatterers, their height difference Δh and the phase shift ϕ of the cosine. Here, the assumption is that the two scatterers inside the resolution cell are ideal point scatterers. A more complicated model is given by assuming that the two scatterers are panels of metals with certain extensions and orientations. In this case, the amplitude can be modelled by a "*Cos fit with sinc envelope*" as follows:

$$\begin{aligned} a^j\left(x^j, r_1, r_2, \Delta h, \phi, \Delta', \phi'\right) = &\left(\left|\frac{\sin\left(x^j\Delta' + \phi'\right)}{\left(x^j\Delta' + \phi'\right)}\right|\right) \cdot \\ &sqrt\left(r_1^2 + r_2^2 + 2 \cdot r_1 \cdot r_2 \cdot \cos\left(x^j\Delta h + \phi\right)\right) \end{aligned} \tag{56}$$

where Δ' is the extension and ϕ' is the phase shift of the sinc envelope, respectively.

Based on the above two scattering mechanisms, a robust joint MAP estimation of the unknown parameters and model selection is performed exploiting the coregistered and calibrated monostatic amplitude images. This is done via Bayesian inference (Papoulis and Pillai, 2002; Sivia and Skilling, 2006) making use of directed graphs (Bishop, 2006) and particle filters (Isard and Blake, 1998; Arulampalam et al., 2002), similar to Chapter 4. The

model which has the higher evidence (i.e. marginal likelihood) is chosen as the scatterer configuration as explained below.

Given the data D, assumed to have arisen from one of the two models M_1 or M_2 according to a probability density $f(D \mid M_1)$ or $f(D \mid M_2)$, respectively, the Bayes factor K is given by (Kass and Raftery, 1995):

$$K = \frac{f(D \mid M_1)}{f(D \mid M_2)} \tag{57}$$

The probability density $f(D \mid M_k)$, where $(k = 1,2)$, is called the evidence or marginal likelihood of the data and is obtained by integrating over the parameter space θ_k:

$$f(D \mid M_k) = \int f(D \mid \theta_k, M_k) \cdot f(\theta_k \mid M_k) \cdot d\theta_k \tag{58}$$

A value of $K > 1$ means that the model M_1 is supported more by the data under consideration than model M_2. Usually, it is difficult to calculate the evidence integral given by Equation (58) for high-dimensional and non-analytical cases. Instead, the likelihood corresponding to the ML estimate of the parameters for each model is used, and then, the test becomes a classical likelihood-ratio test. However, using particle filters, the evidence can be easily computed based on Monte Carlo integration. An advantage of the use of Bayes factors is that it includes a penalty for including too much model structure and guards against overfitting.

Then, depending upon the model selected, a suitable height estimation can later be performed using the bistatic interferograms (referenced with respect to a single pixel). For a single scatterer, this is done via the periodogram method described previously. In case of a double scatterer, the actual heights of the two dominant scatterers can be determined similarly to (Ferretti et al., 2005), wherein, the computation is greatly reduced since the velocity parameter can be neglected (as only the bistatic interferograms are being used) and the height difference and the reflectivities of the two dominant scatterers have been already estimated using the amplitude data. The Rayleigh elevation resolution ρ_l is given by:

$$\rho_l = \frac{\lambda R}{2\Delta B_\perp} \tag{59}$$

where $\Delta B_\perp$ is the elevation aperture size, i.e. the spread of the orbits perpendicular to the LOS.

6.3 Application Test Case and Preliminary Results

This fusion technique has been first applied on *simulated data* for performance assessment. Then, high resolution TerraSAR-X/TanDEM-X data of *Las Vegas, US*, have been used and first results are presented.

6.3.1 Simulated Data

The amplitudes of a single scatterer and a double scatterer are simulated based on real phase-to-height conversion factors of the high resolution TerraSAR-X dataset of Las Vegas,

US, consisting of 74 monostatic acquisitions. The single scatterer is simulated by assuming a panel of metal with $r = 1.0$, $\Delta = 1.0m$, $\phi = 36^\circ$. The double scatterer is simulated by assuming two panels of metal with $r = 1.0$, $\Delta = 1.0m$, $\phi = 36^\circ$ and $r = 0.5$, $\Delta = 1.0m$, $\phi = -54^\circ$, respectively and a height difference of $\Delta h = 50m$. Gaussian noise with different SNR is added to the simulated scatterers.

Figure 60 shows the probability of detection P_D and the probability of false alarm P_{fa} of a double scatterer for different SNR using different models for the double scatterer, namely, "Cos fit" and "Cos fit with sinc envelope". For each SNR value, 1000 realizations were performed to evaluate the detection and false alarm rates. 100,000 particles were used for computing the particle PDFs for Bayesian inference for each realization. It can be seen that "Cos fit" has a higher P_D and P_{fa}. In comparison, "Cos fit with sinc envelope" has a lower P_D and P_{fa}. This is because it has a larger number of unknowns and more particles are needed to get the same detection rate. For example, if the number of particles used for each realization are increased to 1 million, the detection rate of a double scatterer using "Cos fit with sinc envelope" increases from 0.63 to 0.8 (for SNR=2dB) and from 0.83 to 0.9 (for SNR=4dB), although the computation time is more. Of course, the false alarm rate of a double scatterer using "Cos fit with sinc envelope" is better because it does not assume that the two dominant scatterers are ideal point scatterers and thus, this model fits the data better. Anyhow, for a typical SNR of 2 dB (which is often used as a threshold to identify PSs), the double scatterer detection rate is more than 60% for both the double scatterer models using 100,000 particles per realization.

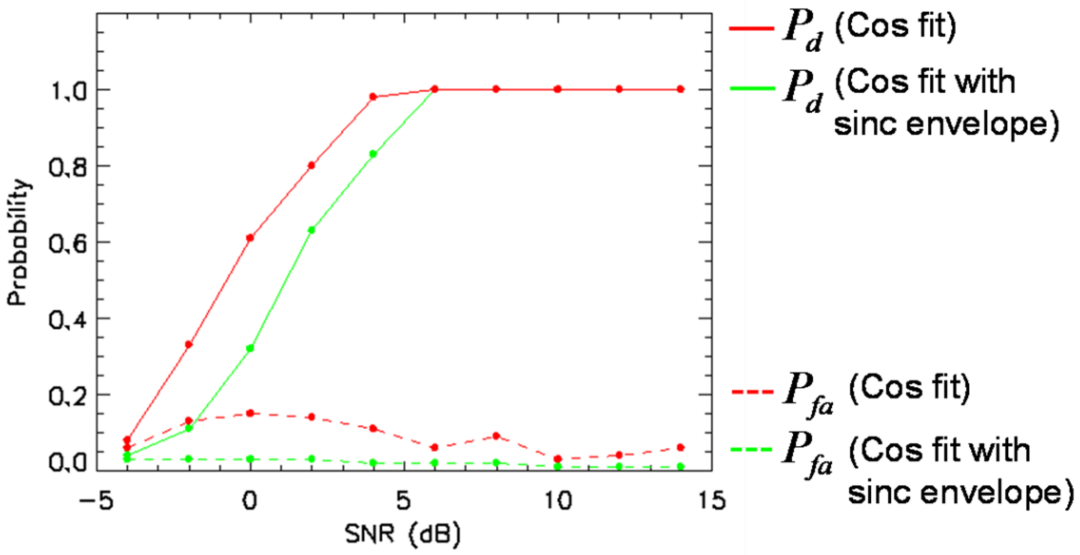

Figure 60: Probability of detection P_D and probability of false alarm P_{fa} of a double scatterer for different SNR using different models for the double scatterer, namely, "Cos fit" and "Cos fit with sinc envelope".

Additionally, a building wall and ground layover scenario (i.e. 100 double scatterers) has been simulated, wherein, the building has a height of 100 m and the ground is at 0 m. A model selection and parameter estimation is performed based on 100,000 particles for each simulated scatterer. Figure 61 shows the estimated heights of the simulated double scatterers for SNR=2dB and SNR=10dB. Red dots show the detected double scatterers and green dots show the detected single scatterers (i.e. a wrong model selection). The true heights are depicted by the black line. The elevation resolution for the simulated data with $\lambda = 0.031m$,

$R = 620km$ and $\Delta B_{\perp} = 561.67m$ is $\rho_l = 17.11m$. This implies a height resolution of $\rho_z = 10.07m$ for an incidence angle of $\theta = 36.04^{\circ}$, as depicted by the blue lines in Figure 61. At low SNR, the resolution limit of this algorithm is clearly visible. However, for high SNR, the algorithm is able to achieve super-resolution for a few double scatterers (although this is limited since a sinc and a cosine tend to be similar when Δh is small).

It is worth mentioning that the parameter estimation for "Cos fit with sinc envelope" model is more precise for the parameters r_1, r_2, Δh and ϕ. The standard deviation of the parameters Δ' and ϕ' is high since the sinc envelope passes through a few observations only.

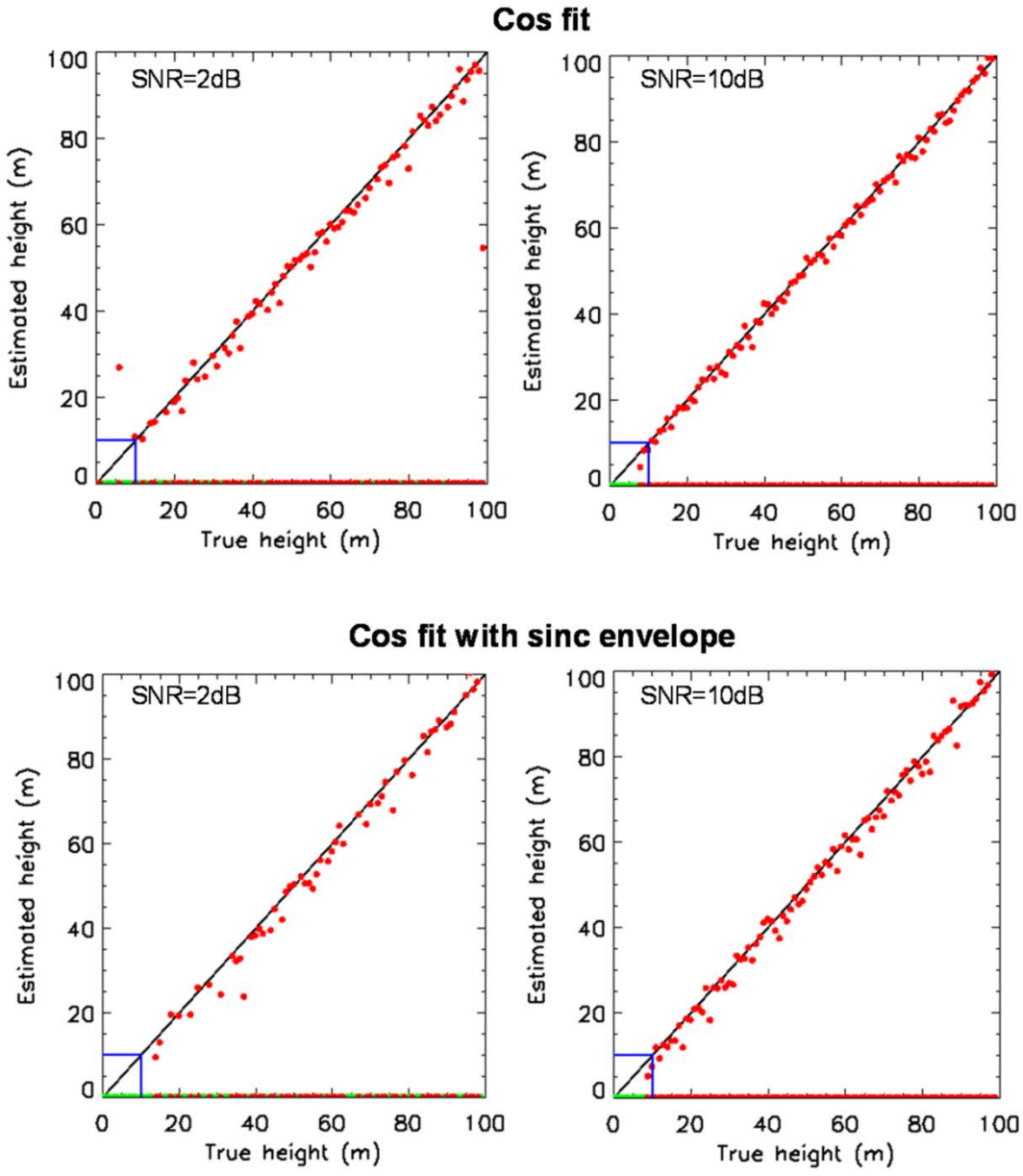

Figure 61: Estimated heights of simulated double scatterers for SNR=2dB and SNR=10dB. Red dots show the detected double scatterers and green dots show the detected single scatterers (i.e. a wrong model selection). For the upper plots, "Cos fit" model is used for double scatterers, whereas for the lower plots, "Cos fit with sinc envelope" model is used for double scatterers. "Sinc fit" model is used for single scatterers. The true heights are depicted by the black line. Blue lines show the height resolution.

6.3.2 Real Data

The real data is that of the city of *Las Vegas in US*. The same data stack used in the previous chapter, comprising of 84 High Resolution Spotlight acquisitions from 2008-2011 and 5 bistatic interferograms with height of ambiguities -33.3927, -44.6864, -54.2698, 53.9007 and -53.7940 m/cycle, respectively, has been exploited here. The pre-processing, including amplitude calibration and PS detection, has been done using DLR's PSI-GENESIS system (Adam et al., 2003; Adam et al., 2004; Kampes, 2006). For simplicity, only the "Cos fit" has been used to model a double scatterer here. 1 million particles have been used for computing the particle PDFs for Bayesian inference.

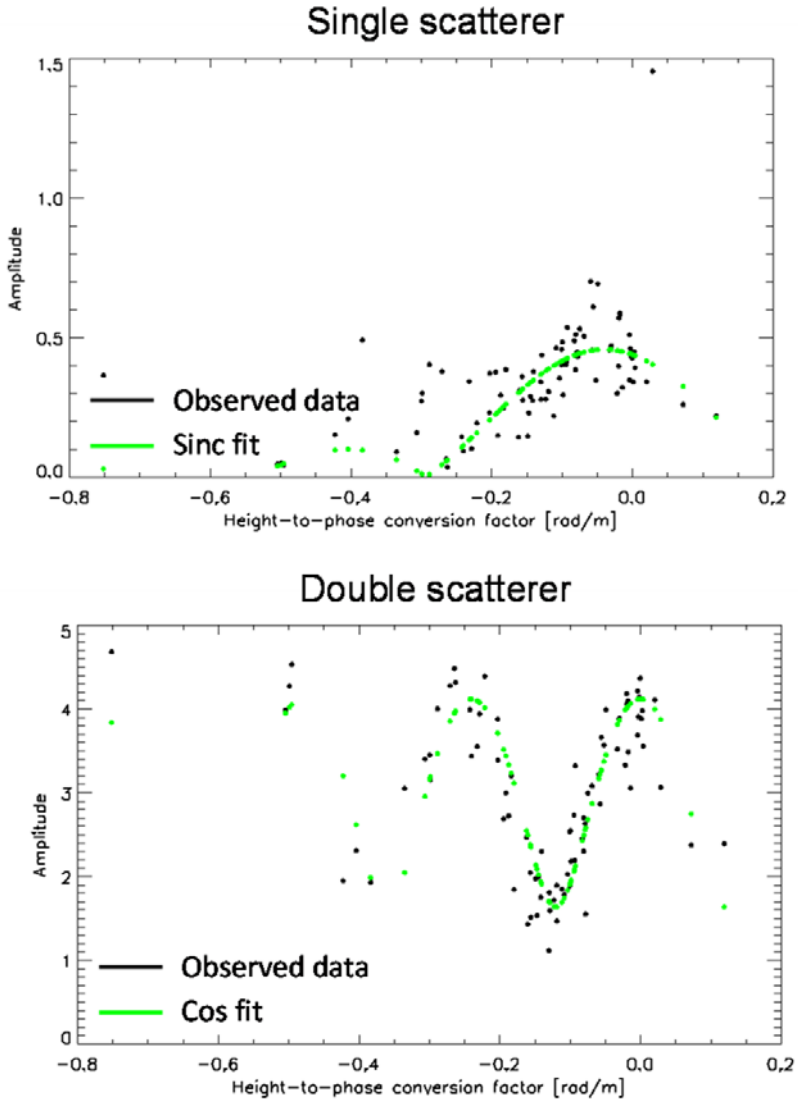

Figure 62: Demonstration of parametric "Sinc fit" (single scatterer) and "Cos fit" (double scatterer) for two PSs of the test site Las Vegas, US, respectively.

Figure 62 compares the parameter fits for the two resolution cell configuration models for two PSs of the test site. A "Sinc fit" corresponds well to the observed data for a single scatterer, whereas a "Cos fit" is an appropriate fit to the observed data for a double scatterer. As can be seen, the parametric modelling and robust fit allows the optimal estimation of the resolution cell configuration.

Figure 63 shows the detected single scatterer and double scatterer resolution cells in green for a part of the test site (i.e. a building and its surroundings). The layover areas where double scatterers exist can be visualized in Figure 63 (a), which is the amplitude image of the test area. Figure 63 (c) is plausible, it shows the double scattering resolution cells in areas where they are expected (for example, layover of building and ground), thus, validating the algorithm.

Based on the number of scatterers inside a resolution cell, the optimal estimation and subsequent removal of topographic residuals from the monostatic interferograms can finally be implemented, followed by improved deformation monitoring using standard PSI.

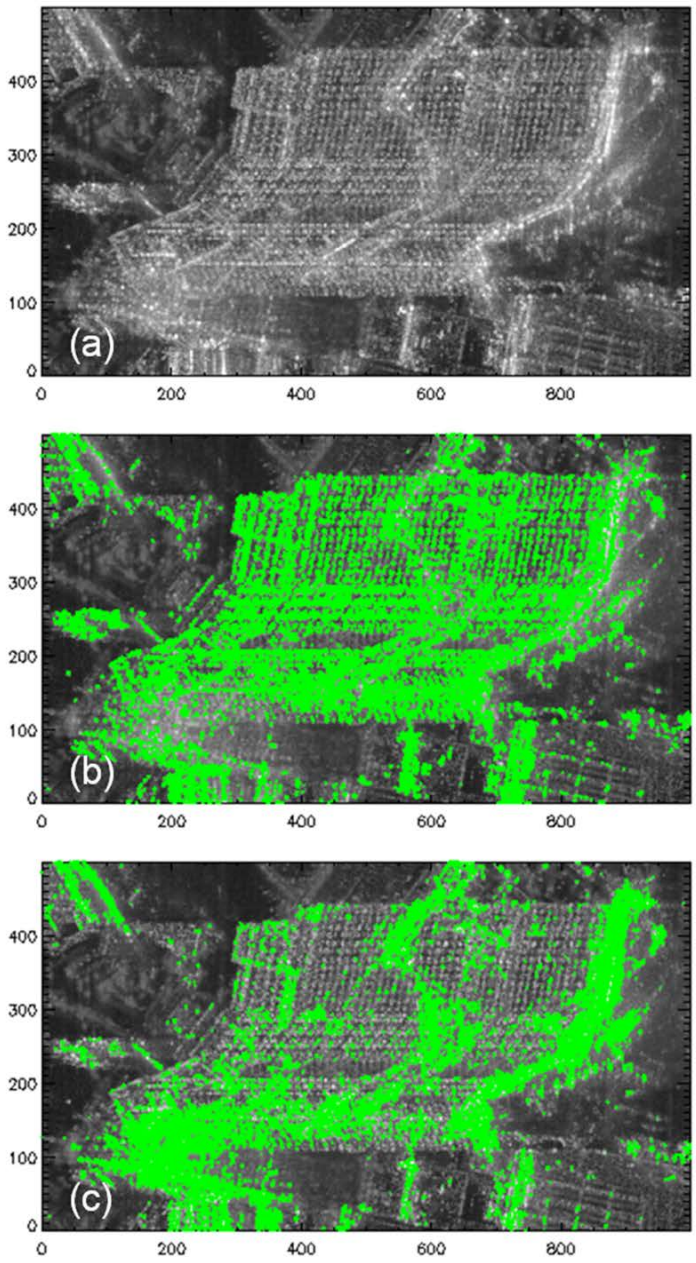

Figure 63: (a) Amplitude image of a part of the test site, Las Vegas, US. (b) Detected single scatterers are overplotted and shown in green. (c) Detected double scatterers are overplotted and shown in green.

6.4 Discussion and Conclusion

A new concept has been developed for the fusion of repeat-pass monostatic and single-pass bistatic SAR data. It makes use of bistatic interferograms and monostatic SAR amplitude images to cope with the typical PS resolution cell configurations and detects one or two scatterers inside a SAR resolution cell. *It is insensitive to deformation and atmospheric disturbances as compared to PSI and TomoSAR*. It can be applied in the early stages of interferometric processing. A preliminary demonstration has been provided using TerraSAR-X and TanDEM-X data of Las Vegas in US. Future work can concentrate on providing processing examples for this technique.

7 Summary

This thesis *broadens the scope of SAR interferometry* for deformation and topographic mapping in difficult areas by exploiting high resolution SAR data with new algorithms. This summary chapter first starts with a discussion about the work done in the thesis and the conclusion, followed by an outlook about the potential improvements and future topics.

7.1 Discussion and Conclusion

This dissertation was set out to explore new contributions which can be made to the research field of DInSAR, with the advent of high resolution SAR missions such as TerraSAR-X and TanDEM-X. Applicability of conventional InSAR stacking techniques (e.g. PSI, TomoSAR, SBAS and SqueeSAR) for deformation studies is limited by various factors. For instance, temporal decorrelation is a major problem in rural areas. In contrast, highly urbanized areas face the problem of radar layover and shadow. Taking into account these issues, this thesis aimed at development, test and analysis of advanced stacking techniques and applications in high resolution SAR interferometry, with a focus on deformation and topographic measurements in challenging regions. Furthermore, the intention was also to improve the precision, robustness and spatial resolution of the estimates, while reducing the computational efforts. In order to realize these objectives, the following techniques based on meter resolution SAR data have been implemented.

An *advanced SBAS technique* has been developed for deformation monitoring in non-urban areas. The following conclusions can be drawn about it:

- It extends the applicability of conventional SBAS in rural areas and also, takes advantage of high resolution SAR data.
- It estimates the deformation time series for DSs at a higher spatial resolution (i.e. object resolution, e.g. in the order of a meter for High Resolution Spotlight mode TerraSAR-X data) compared to conventional SBAS.
- It is also more robust with respect to phase unwrapping errors in areas where decorrelated patches separate the coherent patches. This is because an L1-norm minimization is used to retrieve the deformation leading to a more robust solution in case of outliers.
- The algorithm has been applied on high resolution TerraSAR-X data of a natural gas storage reservoir and the town of Lueneburg in Germany. The results obtained show that this method is capable of reconstructing the non-linear deformation time series in regions where there are a few coherent scatterers only.
- Additionally, the adaptive spatial phase filtering algorithm developed as part of this technique can be used as the estimator of the complex correlation of any interferogram generated from the available SAR data.
- This advanced SBAS method is, however, computationally more demanding than normal SBAS because the multilooked interferometric data is at a higher resolution.
- Also, highly decorrelated areas (e.g. vegetated and low reflectivity homogenous regions with spatial coherence less than 0.3) still cannot be monitored using this technique.

For precision monitoring of such difficult decorrelated areas whose deformation velocity can be described by a suitable model, another *advanced DSI technique* has been realized. The following can be inferred about it:

- It contributes to the research field of DInSAR by a "principle demonstration" of providing measurements in highly noisy areas, which are often an issue with DInSAR time series analysis. This method is based on the assumption of smoothly varying displacement fields which can be modelled. It uses a periodogram approach and combines 3D wrapped phase data to provide deformation gradients for each coherent DS patch. These gradients are subsequently integrated using a model.
- It provides spatially dense deformation velocity maps in contrast to conventional coherent methods. Provided that the assumption mentioned in the previous point is fulfilled, more points are estimated because no standard phase unwrapping is required and the deformation model is known.
- It maps the mean deformation velocity of DSs at a suitable object resolution. This is advantageous in contrast to conventional SBAS which estimates the deformation at a low resolution.
- With respect to SqueeSAR, it is computationally inexpensive as it exploits only small baseline differential interferograms.
- The technique's application using high resolution TerraSAR-X data of the town of Lueneburg in Germany demonstrates the high potential of this new technique in deformation mapping of areas undergoing high temporal decorrelation.
- For implementing the deformation integration, a Bayesian inference estimation framework has been applied. Firstly, directed graphs are used to represent dependencies of RVs. And secondly, PDFs are modelled by particle representations. The implemented estimation framework allows a Bayesian model selection and provides an estimation based upon a well-established theory. As a matter of fact, this Bayesian inference tool can be used for solving general multidimensional non-linear optimization problems.
- The current drawback of this technique is the model-based deformation velocity integration, which requires the surface deformation pattern to be known beforehand. Research is needed on more advanced model-free integration methods in the future.
- In addition, this DSI technique provides only the mean deformation velocity estimates, as compared to non-linear deformation time series provides by SBAS.

Next, *a fusion of monostatic repeat-pass and bistatic single-pass InSAR data stacks exploiting DSs* has been performed for dense urban area monitoring. It can be concluded that:

- This integration technique complements coherent stacking techniques such as PSI and TomoSAR.
- It also complements standard SRTM/TanDEM-X DEMs which are inaccurate in urban areas due to spatial phase unwrapping problems caused by radar layover and shadow.
- It combines monostatic and bistatic data to fully exploit the potential of TerraSAR-X/TanDEM-X missions.
- It provides an improved estimation of topography and deformation, since the bistatic interferograms have a high data quality and are free from deformation, atmosphere and temporal decorrelation.
- More importantly, this technique demonstrates that DSs also, and not only PSs, have a high density in urban areas and can be optimally exploited for deformation studies.
- The results of processing a TerraSAR-X/TanDEM-X dataset of Las Vegas, US, demonstrate the millimeter precision which can be obtained.
- However, as compared to PSI, the deformation is mapped at object resolution.

Last, *a fusion of monostatic repeat-pass and bistatic single-pass InSAR data stacks exploiting PSs* has been done for complex urban area monitoring. It can be implied that:

- This technique extends standard PSI.
- It increases the robustness of the estimates with respect to resolution cell characteristics by resolving single and double scattering (i.e. layover) mechanisms, based on bistatic phase data and monostatic amplitude data only and this is the reason that this technique is insensitive to temporal decorrelation, atmospheric propagation effects and displacement.
- First results using TerraSAR-X/TanDEM-X dataset of Las Vegas in US show its high potential.

The vision of this thesis is to encourage the geo-user community in using these techniques and to fully exploit the potential of meter resolution SAR data.

7.2 Outlook

Based on the current status of advanced SAR interferometry, *the recommendations for future research* are:

- Fusion of PSs and DSs would considerably increase the information content. In fact, SqueeSAR is the first step towards such a combination. The DS-based techniques developed as part of this thesis can be improved further to optimally process information from PSs too.
- The implemented techniques can also be enhanced for a wide area processing in order to take advantage of future SAR missions such as ESA's Sentinel-1 operating in C-band.
- The advanced DSI technique can take benefit from a model-free approach for deformation velocity integration. This would also be useful for estimating the non-linear deformation time series later.
- Another key limitation of InSAR is that it estimates the deformation in the LOS. InSAR data stacks from different imaging geometries can be combined to retrieve the 3D displacement vector.
- An efficient 3D phase unwrapping algorithm exploiting both the spatial and temporal structure of the interferometric data would enhance the multitemporal techniques realized here.
- The techniques can also use L-band SAR data in the future from JAXA's ALOS-2-PALSAR system. The advantage here would be a significant coherence improvement, although there would a reduced sensitivity in deformation detection due to the wavelength increase.

In the end, the advanced stacking techniques and applications presented in this dissertation have contributed to more precise surface displacement measurements of various areas for an effective Earth observation.

A Relevant Publications as Part of the Thesis

A.1 Goel, K., Adam, N., 2012a. An advanced algorithm for deformation estimation in non-urban areas. ISPRS Journal of Photogrammetry and Remote Sensing 73, 100-110.

ISPRS Journal of Photogrammetry and Remote Sensing 73 (2012) 100–110

Contents lists available at SciVerse ScienceDirect

ISPRS Journal of Photogrammetry and Remote Sensing

journal homepage: www.elsevier.com/locate/isprsjprs

An advanced algorithm for deformation estimation in non-urban areas

Kanika Goel *, Nico Adam

German Aerospace Center (DLR), Remote Sensing Technology Institute (IMF), Oberpfaffenhofen, 82234 Wessling, Germany

ARTICLE INFO

Article history:
Available online 30 June 2012

Keywords:
Adaptive spatial phase filtering
Distributed scatterer (DS)
L1 norm minimization
Small Baseline Subset Algorithm (SBAS)
TerraSAR-X

ABSTRACT

This paper presents an advanced differential SAR interferometry stacking algorithm for high resolution deformation monitoring in non-urban areas with a focus on distributed scatterers (DSs). Techniques such as the Small Baseline Subset Algorithm (SBAS) have been proposed for processing DSs. SBAS makes use of small baseline differential interferogram subsets. Singular value decomposition (SVD), i.e. L2 norm minimization is applied to link independent subsets separated by large baselines. However, the interferograms used in SBAS are multilooked using a rectangular window to reduce phase noise caused for instance by temporal decorrelation, resulting in a loss of resolution and the superposition of topography and deformation signals from different objects. Moreover, these have to be individually phase unwrapped and this can be especially difficult in natural terrains. An improved deformation estimation technique is presented here which exploits high resolution SAR data and is suitable for rural areas. The implemented method makes use of small baseline differential interferograms and incorporates an object adaptive spatial phase filtering and residual topography removal for an accurate phase and coherence estimation, while preserving the high resolution provided by modern satellites. This is followed by retrieval of deformation via the SBAS approach, wherein, the phase inversion is performed using an L1 norm minimization which is more robust to the typical phase unwrapping errors encountered in non-urban areas. Meter resolution TerraSAR-X data of an underground gas storage reservoir in Germany is used for demonstrating the effectiveness of this newly developed technique in rural areas.

1. Introduction

Differential Interferometric SAR (D-InSAR) is a powerful tool for displacement mapping in radar's line of sight (Bamler and Hartl, 1998; Rosen et al., 2000). By using large stacks of SAR images acquired over one and the same area and analyzing long time series, temporal evolution of ground deformation can be extracted using advanced techniques such as Persistent Scatterer Interferometry (PSI) (Ferretti et al., 2000, 2001; Kampes, 2006; Adam et al., 2008). In PSI, differential interferograms with respect to a single master image are processed at single look resolution and point scatterers that are coherent over long time intervals and for wide look-angle variations are utilized. These phase stable points are called persistent scatterers (PSs) and correspond to one or two dominant scatterers in a resolution cell. PSI is most powerful in urban areas because there are lots of man-made structures, and consequently there is a high number of such PSs. Besides, the new generation of high resolution SAR sensors such as the X-band TerraSAR-X and COSMO-SkyMed have helped in obtaining a large PS density, which has made it possible to retrieve millimetric ground displacement and structural stress of individual buildings from space. However, PSI is difficult to apply in case of strong non-linear motion and fast deformation. Another key limitation of PSI is the low density of PSs in non-urban (rural) areas which are characterized by vegetated or low reflectivity homogenous regions (see Fig. 1a). Application examples include mines, volcanoes, oil/gas/water reservoirs and seismic zones. In fact, there is an increasing focus on increasing the spatial sampling of deformation exploiting also the distributed scatterers (DSs) (see Fig. 1b) and improving the quality of deformation estimates. Distributing scattering mechanism involves a coherent sum of many independent small scatterers (no dominant scatterer) within a resolution cell (Goodman, 1976) and is modelled by a complex circular Gaussian radar return (Bamler and Hartl, 1998). Stacking techniques such as the Small Baseline Subset Algorithm (SBAS) (Berardino et al., 2002; Mora et al., 2003) and SqueeSAR (Ferretti et al., 2011; Zan, 2008) have been developed to process DSs (Gaussian scatterers).

Essentially, SBAS retrieves the deformation by making use of spatially unwrapped small baseline differential interferograms. These are linked using the singular value decomposition (SVD) method and a minimum-norm least squares (LS) solution is obtained (Golub and Loan, 1996). It is worth pointing out that even non-linear deformation can be estimated using SBAS. There are

* Corresponding author. Tel.: +49 8153 28 1233; fax: +49 8153 28 1420.
E-mail address: kanika.goel@dlr.de (K. Goel).

0924-2716/$ - see front matter © 2012 International Society for Photogrammetry and Remote Sensing, Inc. (ISPRS) Published by Elsevier B.V. All rights reserved.
http://dx.doi.org/10.1016/j.isprsjprs.2012.06.001

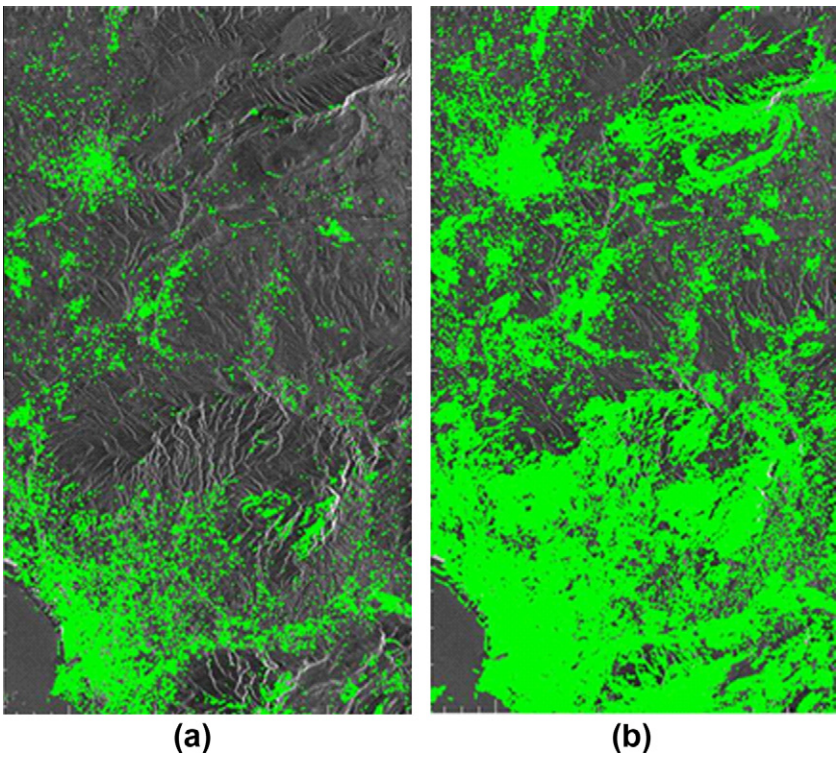

Fig. 1. ERS image of Gardanne coal mine located in France. (a) Shows the PSs in green, whereas, (b) shows the PSs and DSs in green. We can clearly see that in this rural region, the density of PSs is low compared to the DSs.

certain drawbacks however as follows. First, the interferograms are spatially filtered before the stacking to enhance the Signal to Noise Ratio (SNR) (Zebker and Villasenor, 1992). This results not only in a reduction of resolution and a superposition of different objects on ground, but also, in a loss of deformation information contained in isolated pixels. Additionally, abrupt changes in deformation are smoothed out. There is a need for fully exploiting the high resolution SAR data available from sensors such as TerraSAR-X and extracting deformation at a high resolution. Second, phase unwrapping (Constantini, 1998; Eineder et al., 1998) is an important step in SBAS and phase unwrapping errors often occur in data with a lot of fringe discontinuities, which is especially the case in non-urban areas. Several decorrelated areas such as forests, soil, water etc. might separate the coherent areas and the relative values in the different coherent patches can have unknown integer multiples of 2π phase offsets, thus making phase unwrapping time consuming and error prone. In contrast, SqueeSAR uses amplitude statistics to detect the DSs and carries out an accurate estimation of covariance matrices for the DSs, i.e. it exploits all possible interferograms to "squeeze" the deformation. Afterwards, a phase triangulation algorithm is applied to each DS to retrieve the optimized phase values for the SAR images. The DSs are then processed jointly with the PSs using the conventional PSI chain. However, this technique can be computationally expensive. Moreover, it usually makes a linear model assumption and is not suitable for phenomena characterized by highly non-linear deformation.

With respect to the above mentioned techniques, we introduce an alternative approach for high resolution deformation monitoring with a focus on natural terrains characterized by typical temporal decorrelation and phase ambiguities. It is based on an object adaptive parameter estimation, exploiting only the small baseline differential interferograms so as to reduce the effects of topography on the DSs. The practical implementation starts with an accurate phase and coherence estimation and residual topography removal for the small baseline interferograms using an adaptive spatial phase filtering algorithm (Parizzi and Brcic, 2011; Goel and Adam, 2011). It reduces the phase noise while maintaining the high geometric resolution provided by new satellites such as TerraSAR-X (meter resolution). Subsequently, the phase estimates are used to retrieve the line-of-sight deformation using the SBAS technique. Here, phase inversion is performed using an L1 norm minimization instead of the standard least squares (L2 norm minimization). This results in a more robust solution with respect to the often occurring and difficult to detect phase unwrapping errors found in non-urban areas (Lauknes et al., 2011). Subject of this paper is to present the developed technique and an application test case using high resolution TerraSAR-X data of an underground gas storage field located in Germany.

2. Methodology

Assuming that we have N SAR images and M single look small baseline differential interferograms available, the implemented methodology for deformation estimation in rural regions involves the following two steps:

2.1. Adaptive spatial phase filtering

In the first step, we start with an improved estimation of the differential interferometric phase and coherence even in the presence of high phase noise and error sources (e.g. temporal decorrelation, topographic errors and atmospheric effects). The accurate phase estimation supports deformation monitoring techniques such as SBAS and also improves the phase unwrapping. The accurate coherence estimation helps in selection of pixels for deformation monitoring as it provides information about temporal decorrelation and also, for guiding phase unwrapping algorithms.

For extracting the geophysical parameters of interest in natural terrains affected by decorrelation phenomena, the SNR of the

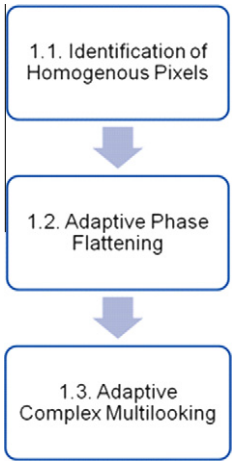

Fig. 2. Adaptive spatial phase filtering algorithm for high resolution differential interferometric stacking.

differential interferograms has to be improved by a local spatial averaging (multilooking). In other words, the statistics of interferograms characterized by DSs are governed by the covariance (Bamler and Hartl, 1998) and this has to be estimated correctly. The local complex covariance is the cross-correlation coefficient of a SAR image pair estimated over a small window, once all the deterministic phase components (mainly due to the topography) have been compensated for. For a pixel, the complex covariance (correlation) γ for a SAR image pair is estimated as follows:

$$\gamma = \frac{\sum_{i=1}^{L} s_{1,i} \cdot s_{2,i}^{*} \cdot e^{-j\varphi_{topo}}}{\sqrt{\sum_{i=1}^{L} |s_{1,i}|^2 \cdot \sum_{i=1}^{L} |s_{2,i}|^2}} \quad (1)$$

where $s_{1,i}$ and $s_{2,i}$ are the complex signal values of the SAR image pair for the i th pixel of the L neighboring pixels in the estimation window and ϕ_{topo} is the topographic phase of the window. Considering the amplitudes of images as one (i.e. we do not weigh the pixels according to their brightness, no assumption is made about a pixel's quality from its brightness), Eq. (1) can be reduced to:

$$\gamma = \frac{1}{L} \sum_{i=1}^{L} e^{j\varphi_{1,i}} \cdot e^{-j\varphi_{2,i}} \cdot e^{-j\varphi_{topo}} \quad (2)$$

where $\phi_{1,i}$ and $\phi_{2,i}$ are the phase values of the SAR image pair for the ith pixel of the L neighboring pixels in the window. The amplitude of the complex covariance is the coherence estimate of the pixel (a measure of phase noise), whereas, its phase is the expected interferometric phase of the pixel. Unfortunately, this estimator is biased and underestimates the covariance in case of interferometric fringes present due to residual digital elevation model (DEM), local slope and motion (Zebker and Chen, 2005). Besides, usually, a rectangular patch around the pixel of interest is used for multilooking. This might lead to averaging of pixels arising from different distributions leading to a wrong estimation of the covariance.

Keeping this in mind, we have implemented an object adaptive spatial phase filtering algorithm for generating high resolution coherent differential interferometric stacks (Goel and Adam, 2011). It is based on two principles. First, the high resolution of satellites such as TerraSAR-X leads to many resolution cells covering a homogenous object (DS) in non-urban areas. This object can be described by a single deformation parameter. The object area (pixels) thus needs to be identified and interferometric phase can be improved by an adaptive spatial filter, which also incorporates phase flattening. Second, we just concentrate on small baseline differential interferograms to limit the effects of topographic errors on the DSs. Practically, the algorithm involves three sub-steps which are shown in Fig. 2 and described below:

1. Using a stack of N coregistered (up to sub-pixel accuracy) and calibrated SAR amplitude images, we identify for each pixel the statistically homogenous pixels surrounding it. Usually, it is assumed that homogenous pixels can be found in a local neighborhood such as a rectangular window. However, they can be far apart depending upon reflectivity and boundaries of objects (fields, trees, roads, etc.). The idea is thus to average a given pixel only with neighbors that present similar scattering properties instead of a rectangular (boxcar) averaging.

Various statistical tests have been proposed in recent years to identify homogenous pixels based on the amplitude of coregistered and calibrated stack of SAR images. These include the Kullback–Leibler Divergence test (Bishop, 2006), the Kolmogorov–Smirnov (KS) test (Papoulis and Pillai, 1984) (used in the SqueeSAR approach) and the Anderson–Darling (AD) test (Pettitt, 1976). The AD test has been proven to be the most effective statistical test to identify if two pixels arise from the same distribution (Parizzi and Brcic, 2011). This test performs reasonably well even for a stack of acquisitions containing as small as 10 images. It is a non-parametric test, i.e. we do not assume that the samples belong to a defined probability distribution. Instead, using the amplitude of the stack of SAR images, we obtain the empirical cumulative distribution functions of amplitudes for the two pixels (points) under consideration. The distance between the distributions, with weighting given to tails (higher order moments of the distribution are taken into consideration), tells us if the two points statistically

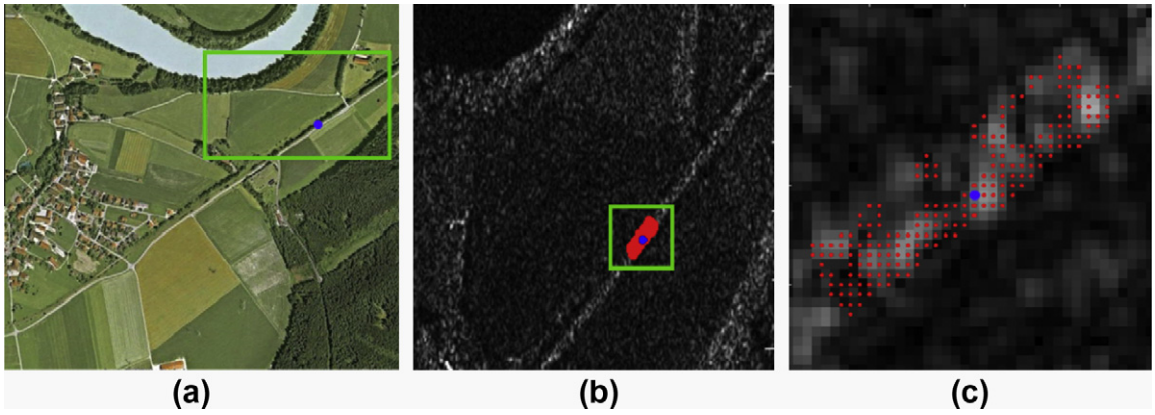

Fig. 3. Identification of homogenous pixels (in red) for the blue pixel by Anderson–Darling (AD) test. (a) is a Google Earth image, (b) is the TerraSAR-X image of the region enclosed in green rectangle in (a), (c) is a zoom-in of the green rectangle in (b).

arise from the same distribution. For a set of points a and b, the AD statistic A^2 is:

$$A^2 = \frac{N}{2}\sum_{F_{a,b}(x)} \frac{[F_a(x) - F_b(x)]^2}{[F_{a,b}(x)\cdot(1-F_{a,b}(x))]} \tag{3}$$

where N is the number of SAR amplitude images, $F_a(x)$ and $F_b(x)$ are empirical cumulative distribution functions of amplitudes for points a and b, $F_{a,b}(x)$ is empirical distribution function of the pooled distribution $[a, b]$. If the AD statistic is less than a threshold value, the two pixels are homogenous.

Fig. 3 shows an example of the AD test. 55 TerraSAR-X images (January, 2008 to May, 2010) of a gas storage reservoir located in Germany were used for the processing. We performed the AD test for the blue pixel (which lies on a road) with each of its neighbors. The homogenous pixels were identified and marked in red. We see that using the AD test, the homogenous pixels identified lie on the same road as well.

2. The homogenous pixels identified are then used for adaptive phase flattening of M single look small baseline differential interferograms to compensate for topographic residuals (due to errors in DEM). The phase flattening or debiasing is important because the topographic errors affect subsequent estimation of an improved phase and coherence (Zebker and Chen, 2005).

For a robust estimation of the local slopes m_x and m_y of the residual DEM in range and azimuth directions resp. for each pixel, a search algorithm in the solution space is applied. M periodograms are generated corresponding to each interferogram using the L homogenous pixels identified. A periodogram ξ^k, $k = 1, ..., M$, is a function of the local slopes in range and azimuth directions for the adaptive neighborhood:

$$\xi^k(m_x, m_y) = \frac{1}{L}\left|\sum_{i=1}^{L} e^{j(\varphi^{i,k} - \varphi^k_{ref} - \frac{4\pi}{\lambda}\frac{B^k_\perp}{R\sin\theta}(m_x p^i_x + m_y p^i_y))}\right| \tag{4}$$

where λ is the transmitted wavelength, $B^k_\perp$ is the perpendicular baseline for interferogram k, R is the sensor-scatterer distance, θ is the local incidence angle (for flat terrain), $\phi^{i,k}$ is the single look differential interferometric phase for homogenous pixel i and interferogram k, φ^k_{ref} is the single look differential interferometric phase for the reference pixel (the pixel for which we are estimating the covariance and the local slopes) and interferogram k, and finally, p^i_x and p^i_y are pixel indices in range and azimuth directions resp. for homogenous pixel i. Further on, we make the slope estimation robust by averaging all the periodograms for a pixel to reduce side lobes. We finally get an averaged periodogram ξ as follows:

$$\xi(m_x, m_y) = \frac{1}{M}\sum_{k=1}^{M}\xi^k \tag{5}$$

The local slopes $\hat{m}_x$ and $\hat{m}_y$ for each pixel are estimated from the peak of the averaged periodogram (which is the maximum likelihood estimate), i.e.:

$$(\hat{m}_x, \hat{m}_y) = \arg\max_{m_x, m_y}(\xi) \tag{6}$$

The estimated slopes for each pixel are then removed from each interferogram to get the flattened interferograms φ^k_{flat}, $k = 1, \ldots, M$. It is worth mentioning that computational complexity can be reduced by generating fewer periodograms using some highly coherent interferograms with a suitable variation of baselines. The variation in baselines is needed for reducing the side lobes. In other words, some interferograms with relatively large baselines are also needed for a better precision. Practically, this simplified computation can also reasonably estimate the local slopes. But, of course, a rough estimate of the coherence is required, which is possible by a normal rectangular multilooking of the interferograms.

Adaptive phase flattening is depicted pictorially in Fig. 4.

3. Finally, estimation of the M filtered *small baseline* interferograms and their coherence is performed. This is done pixelwise for each interferogram, wherein, an adaptive complex averaging (multilooking) of the flattened interferometric phase of the adaptive neighborhood is performed for an accurate phase and coherence estimation, as derived in Eq. (2), i.e.:

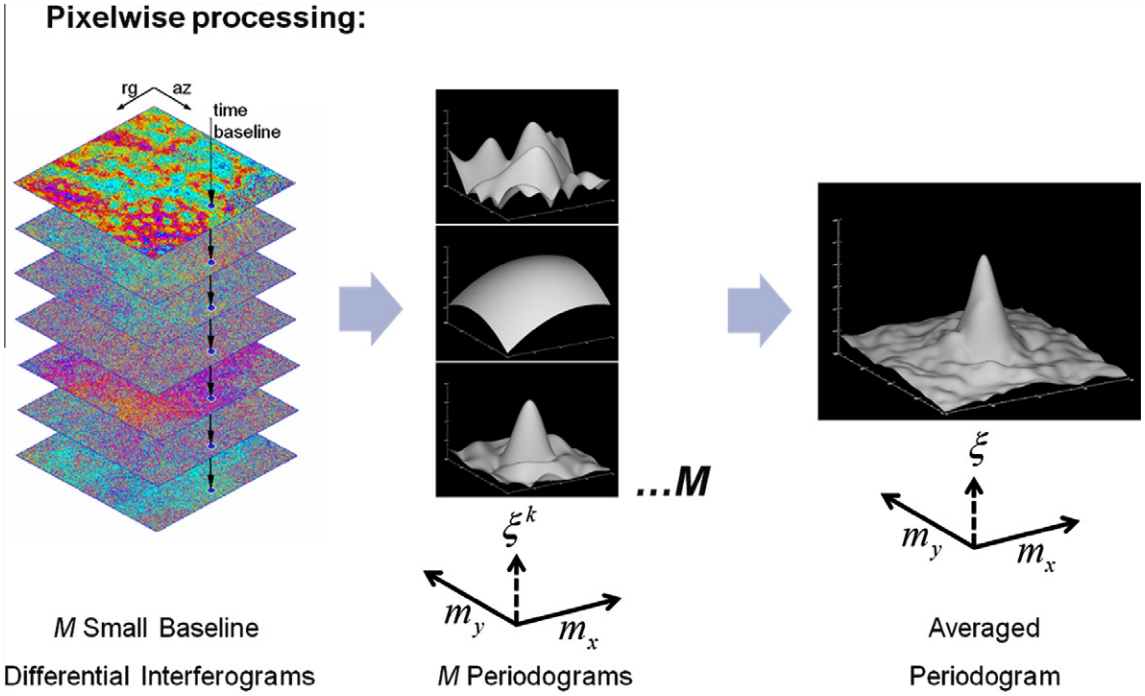

Fig. 4. Pictorial representation of adaptive phase flattening for a pixel.

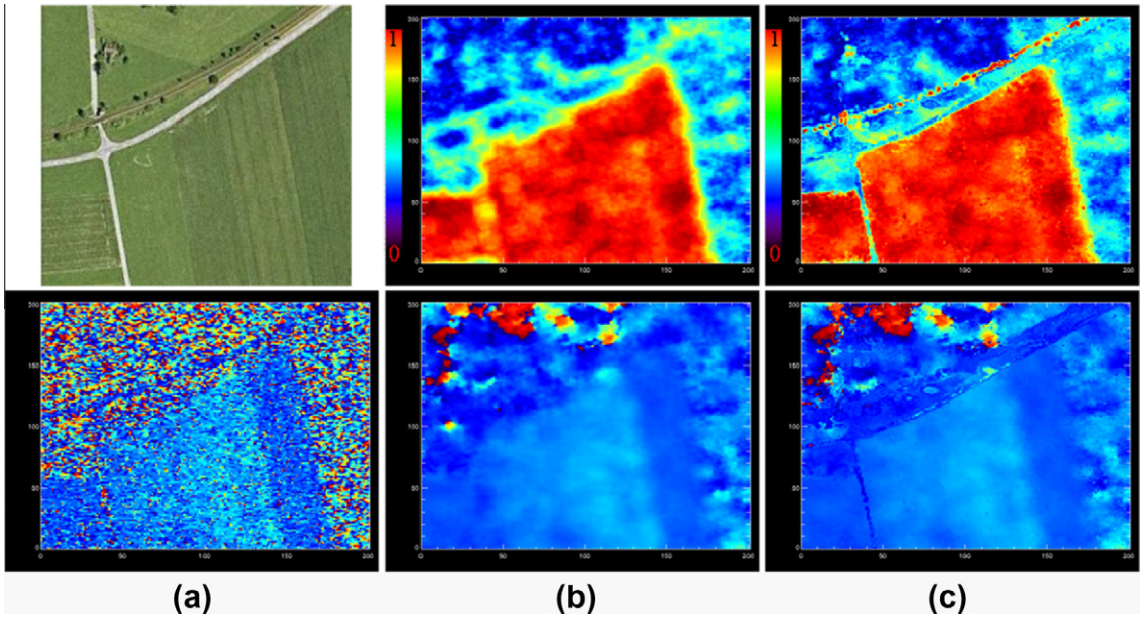

Fig. 5. (a) is a Google Earth image and its single look interferogram , (b) is coherence and interferogram estimate after boxcar multilooking, (c) is coherence and interferogram estimate after adaptive spatial filtering.

$$c^{i,k} = \frac{1}{L}\sum_{i=1}^{L} e^{j(\varphi_{flat}^{i,k})} \tag{7}$$

where $\varphi_{flat}^{i,k}$ is the flattened differential interferometric phase for homogenous pixel i and interferogram k and $c^{i,k}$ is the complex correlation statistically describing the DS. Phase value of $c^{i,k}$ is the filtered interferometric phase estimate and absolute value of $c^{i,k}$ is the coherence estimate resp. for homogenous pixel i and interferogram k. Coherence tells us about the SNR and therefore the reliability of the interferometric phase and varies from 0 to 1.

Fig. 5 illustrates the adaptive spatial filtering algorithm in comparison with the conventional rectangular multilooking, as applied on the TerraSAR-X data of the gas storage site. Fig. 5a is a Google Earth image of a part of the test site and its single look interferogram. Fig. 5b shows the coherence and interferogram estimate after boxcar (rectangular) multilooking. Fig. 5c shows the coherence and interferogram estimate after adaptive spatial phase filtering. We can clearly distinguish features such as fields and roads after applying adaptive spatial phase filtering as compared to the typical boxcar (rectangular) multilooking. We can see that the object resolution is preserved.

2.2. Deformation retrieval

In this second step, we use the improved full resolution small baseline differential interferograms to retrieve the LOS deformation and residual topography using an L1 norm based SBAS technique. SBAS is described in detail in (Berardino et al., 2002). Each of the differential interferograms is unwrapped and all coherent pixels are referenced to one pixel which has a high coherence and a known deformation. Subsequently, the low pass (LP) component of the deformation signal and topographic (DEM) residuals are estimated for each coherent pixel using a displacement model. In practice, this displacement model is only used in this step and does not restrict the estimation of non-linear deformation later on. After the removal of residual topography, the resulting small baseline interferograms form the following system of equations for every coherent pixel:

$$B\upsilon = \delta\varphi' \tag{8}$$

where B is the matrix defining the small baseline combinations used, $\delta\varphi'$ is the vector of unwrapped differential interferometric phase values after the removal of topographic error and υ is the vector of unknown mean phase velocities between time-adjacent acquisitions. A minimum-norm least squares (LS) solution (L2 norm minimization) of Eq. (8) is obtained by using the SVD method (Golub and Loan, 1996). An additional integration step gives the deformation solution. Even non-linear deformation can be estimated using SBAS. Finally, the atmospheric effects are estimated and removed by carrying out a spatial low pass (after removing the low pass deformation estimated previously) and a temporal high pass filtering operation.

However, in rural areas, there might be several decorrelated areas (e.g. trees, soil, water, etc.) separating the coherent patches. This often introduces phase unwrapping errors and the relative values in the different coherent patches can have unknown integer multiples of 2π phase jumps. These phase jumps in the unwrapped

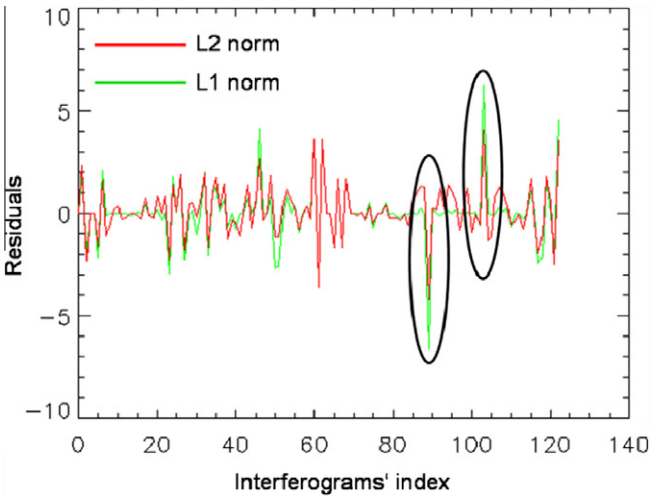

Fig. 6. Residuals obtained after L2 and L1 norm inversion for a pixel during SBAS processing. The phase unwrapping errors (outliers) are encircled in black.

data are outliers (spike noise) and inversion using L2 norm minimization often performs poorly. Instead, a more robust phase inversion solution, with respect to the often occurring and difficult to detect phase unwrapping errors found in non-urban areas, can be obtained by using an L1 norm minimization (Lauknes et al., 2011).

A generic L_p norm solution is given by:

$$\hat{v} = \arg\min_{v} \left(\sum_{i=0}^{M-1} |\delta\varphi' - Bv|_i^p \right)^{\frac{1}{p}} \tag{9}$$

The L2 norm minimizes the sum of squared residuals, whereas, the L1 norm minimizes the sum of the absolute values of the residuals. The L2 norm inversion is optimal when Gaussian noise is present in the data. But if L2 norm minimization is used in the presence of a spike, the estimated fit tends to deviate towards the outlier thereby resulting in a wrong estimation. In (Rodriguez-Gonzalez et al., 2011), L1 network inversion was demonstrated for robust outlier rejection in PSI. In this paper, we apply the L1 norm cost function to solve Eq. (8). The algorithm proposed by Barrodale and Roberts

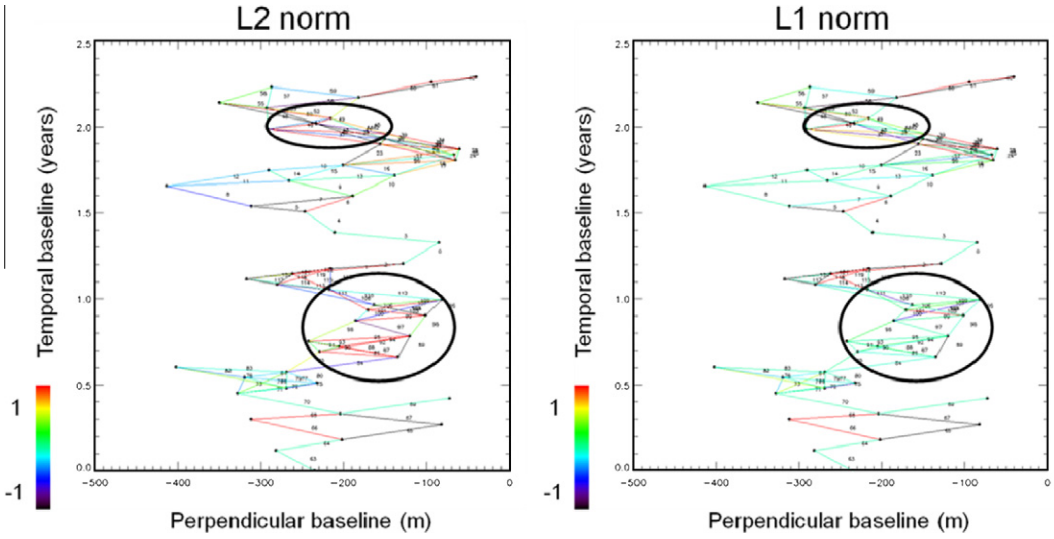

Fig. 7. Baseline-time plot of the TerraSAR-X dataset of the gas storage site, each dot represents a SAR image and each line represents an interferogram. The lines (interferograms) are color coded according to the L2 norm and L1 norm residuals for a pixel in the two plots respectively. The phase unwrapping errors (outliers) are encircled in black.

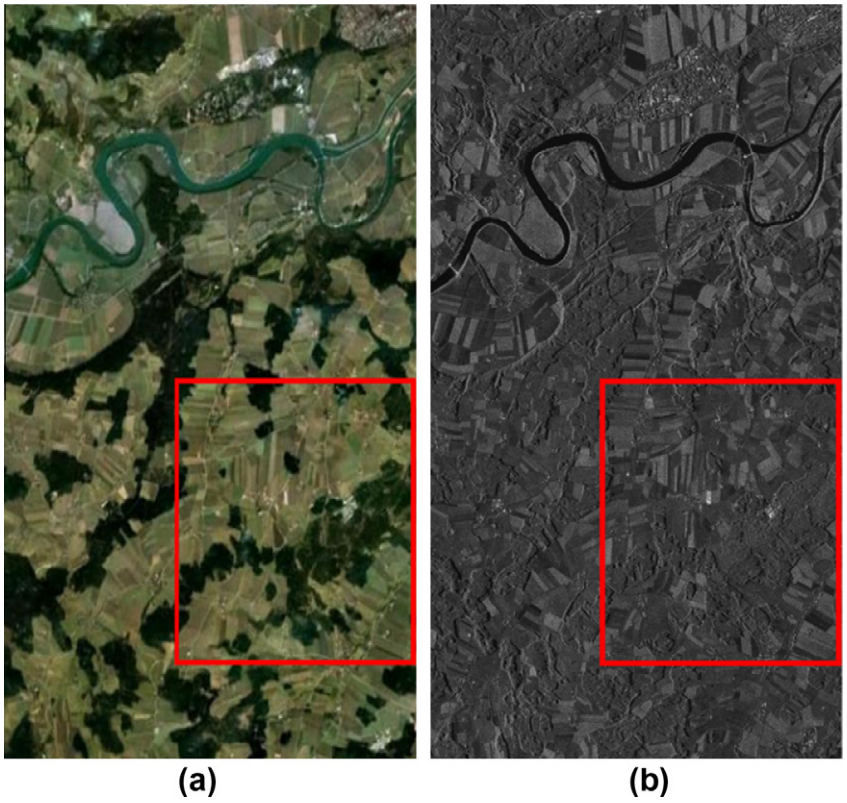

Fig. 8. (a) Is the Google Earth image of the test site in Germany, (b) is the TerraSAR-X mean amplitude image of the test site. The underground gas storage reservoir is located inside the red rectangle.

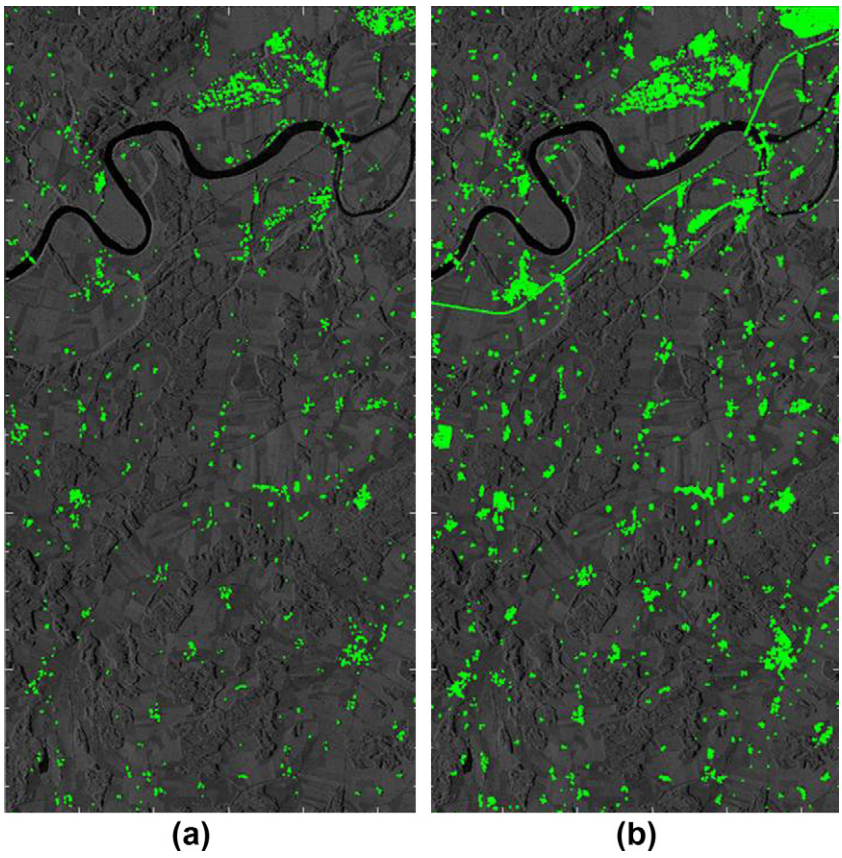

Fig. 9. TerraSAR-X image of the gas storage site in Germany. (a) shows the PSs in green (54,258 points), whereas, (b) shows the PSs and DSs in green (284,081 points). The density of PSs is very low compared to the DSs in this non-urban area.

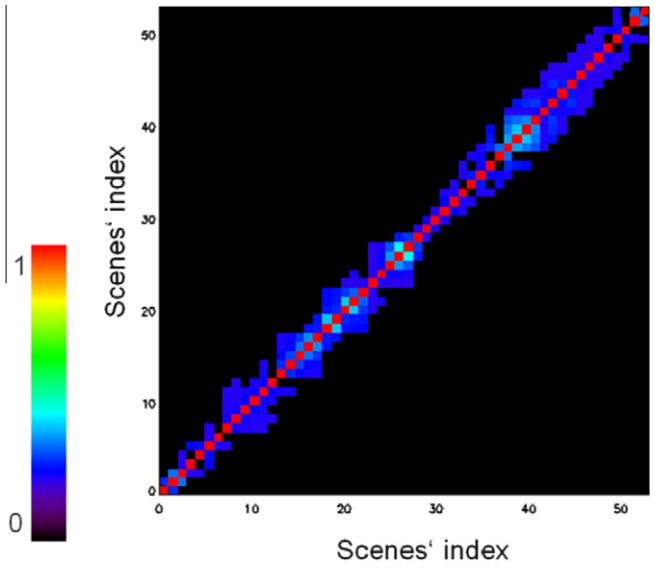

Fig. 10. Covariance matrix of the TerraSAR-X dataset of the gas storage reservoir situated in Germany. It depicts the average coherence of the small baseline differential interferograms used in the processing.

(Barrodale and Roberts, 1973) is used for L1 norm minimization. It is a modification of the simplex method of linear programming and is computationally efficient.

We have compared the performance of L2 and L1 norm inversion for the SBAS technique. Fig. 6 shows the L2 and L1 norm residuals for a pixel belonging to the TerraSAR-X dataset of the gas storage site. We see that in case of phase unwrapping errors, i.e. outliers (encircled in black), the residuals are high for L2 norm, but even higher for L1 norm. Thus, L1 norm minimization can be used for outlier detection and correction (phase unwrapping error map). Misdetections are avoided because of the higher residual peaks. Fig. 7 shows the baseline-time plot for the TerraSAR-X dataset. Each dot corresponds to a SAR image and each line corresponds to an interferogram. The lines (representing the interferograms) are color coded according to the L2 norm and L1 norm residuals for the pixel in the two plots respectively. We can see that in the presence of outliers (encircled in black), L2 norm spreads the phase unwrapping errors to the neighboring interferograms. On the other hand, L1 norm provides a robust solution, a small disturbance in the data leads to only a small disturbance in the signal reconstruction.

3. Results and discussion

The newly developed technique for deformation estimation in non-urban areas is applied and demonstrated on a natural gas storage reservoir in Germany. The test site is visualized in Google Earth in Fig. 8a, the approximate area of the gas storage is enclosed in red. As we can see, this is a rural region covered mostly by vegetation and agricultural fields, thus making it ideal for testing our algorithm. Underground gas storage causes subsidence and uplift of terrain depending on the reservoir pressure. The annual storage cycle generally comprises of gas injection in summer and extraction in winter, leading to a cyclic deformation pattern. Mapping this surface movement is important for reservoir monitoring and hazard analysis.

For measuring the ground displacement, we have used 55 Stripmap TerraSAR-X scenes of the reservoir from January, 2008 to May, 2010 with a look angle of 41.05° and 'HH' polarization. The TerraSAR-X satellite with its high resolution of up to 1 m and a short revisit time of 11 days allows high precision mapping of wide areas in a cost-effective way. The short X-band wavelength of 31.3 mm allows monitoring of even small surface deformation, as compared to the C-band sensors such as ERS operating at 56.6 mm. Fig. 8b shows the mean SAR amplitude image of the test site. An area of approximately 7 km × 14 km. has been processed. The pixel dimensions in range and azimuth directions are 1.27 m and 1.35 m resp. This non-urban site covered by vegetation and fields

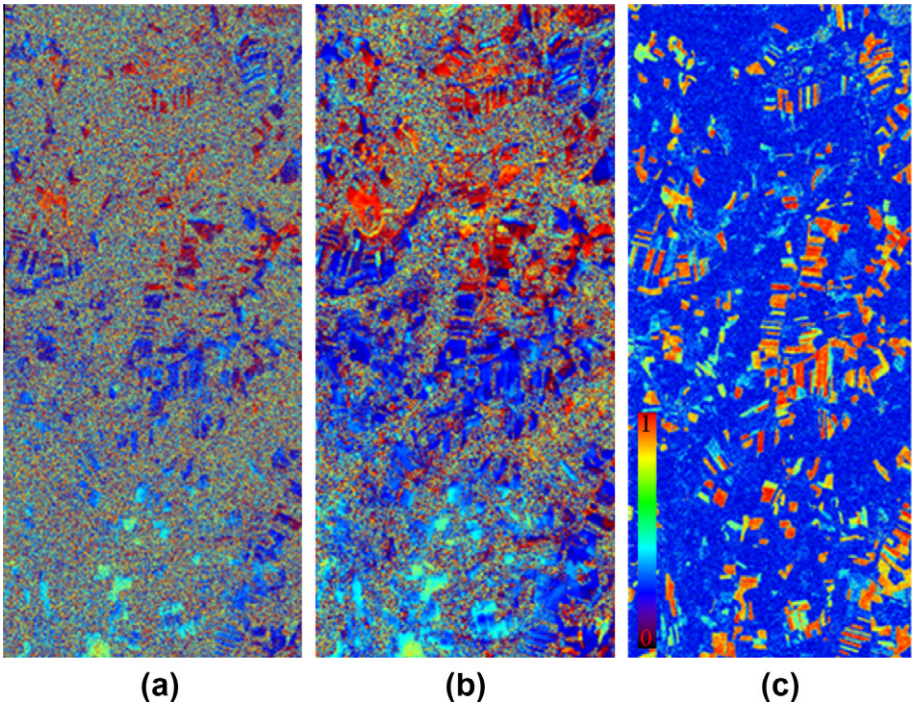

Fig. 11. (a) is a single look interferogram of the gas storage site, (b) is the interferogram estimate after adaptive spatial filtering, (c) is the coherence estimate after adaptive spatial filtering.

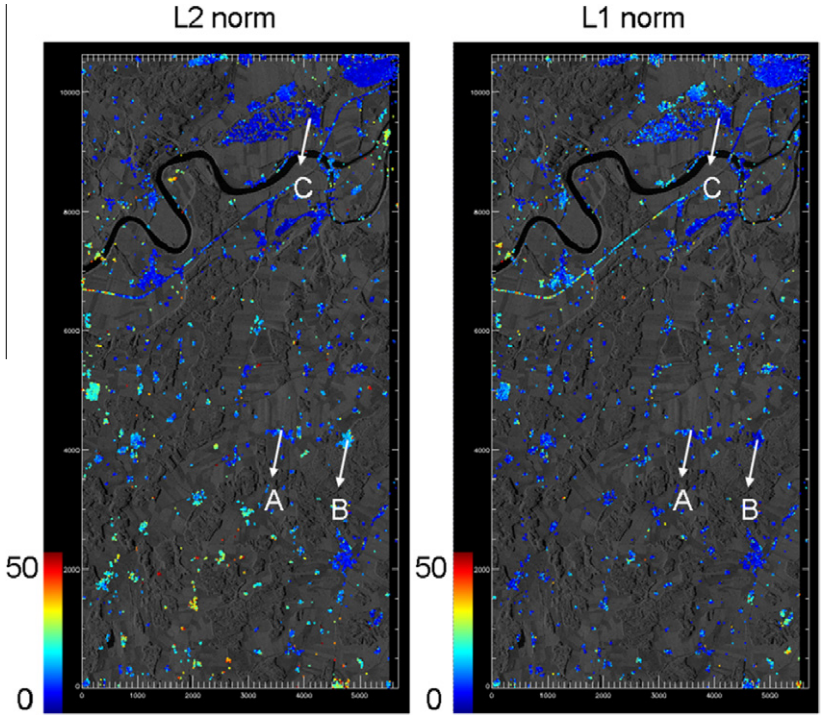

Fig. 12. RMS deformation [mm] for the gas storage site using L2 norm and L1 norm based SBAS. Processed points are overplotted on the mean amplitude image and color coded according to RMS deformation values. Deformation time series of points A, B and C are shown in Fig. 13.

has a low density of PSs in comparison with the DSs, as shown in Fig. 9. Fig. 9a visualizes the PSs in green (54,258 points), whereas, Fig. 9b visualizes the PSs and DSs in green (284,081 points). Improving the spatial density and the quality of deformation estimates in non-urban areas is the main objective of this paper.

The dataset has been processed using our new technique. We generated 123 single look small baseline differential interferograms based on a maximum spatial baseline of 150 m and a maximum temporal baseline of 100 days. For coregistration and D-InSAR processing, DLR's operational PSI-GENESIS processor has been employed (Adam et al., 2003, 2004). The coregistration module of the processor uses a geometry based algorithm which utilizes precise orbits and a DEM from SRTM. Fig. 7 shows the SBAS configuration for the test site, i.e. the baseline time plot for the scenes and the interferograms. The covariance matrix of the dataset is illustrated in Fig. 10. It shows the combinations of acquisitions used (i.e. the interferograms), each of which is color coded according to its average coherence. We can see that only small baseline combinations have been used for the processing. Moreover, the average coherence of this rural region can be observed as low, typical for areas affected by temporal decorrelation.

We then apply our adaptive spatial filtering algorithm on the single look interferograms, as demonstrated in Fig. 11. Fig. 11a shows a single look *small baseline* differential interferogram of the test site, Fig. 11b shows the interferogram estimate after adaptive spatial filtering and Fig. 11c shows the coherence estimate after adaptive spatial filtering. We clearly see a big improvement in the quality of the interferometric phase. Later on, we use the minimum cost flow (MCF) algorithm for phase unwrapping (Constantini, 1998; Eineder et al., 1998).

The unwrapped interferograms are subsequently used for deformation monitoring using the SBAS approach via the L1 norm minimization. We use pixels that have an average coherence of at least 0.4, as shown in Fig. 9b. The deformation estimation results have been presented in Fig. 12 and compared with the results obtained from the typical L2 norm based SBAS approach. We have used the root-mean-square (RMS) deformation for visualizing the results as it is visually effective and provides an integral information about the displacement with respect to time. We can observe that the coherent points of the test case are not well connected, leading to phase unwrapping errors. The L2 norm inversion propagates these errors spatially, as can be seen in Fig. 12, as compared to the L1 norm based solution.

Deformation time series are visualized in Fig. 13 for some of the pixels marked in Fig. 12. The L2 norm inversion fails to estimate the cyclic non-linear deformation occurring in the area of the gas storage (points A and B), although it performs reasonably well for point C which is located far away from the reservoir. L1 norm solution, on the other hand, corresponds well to the cyclic nature

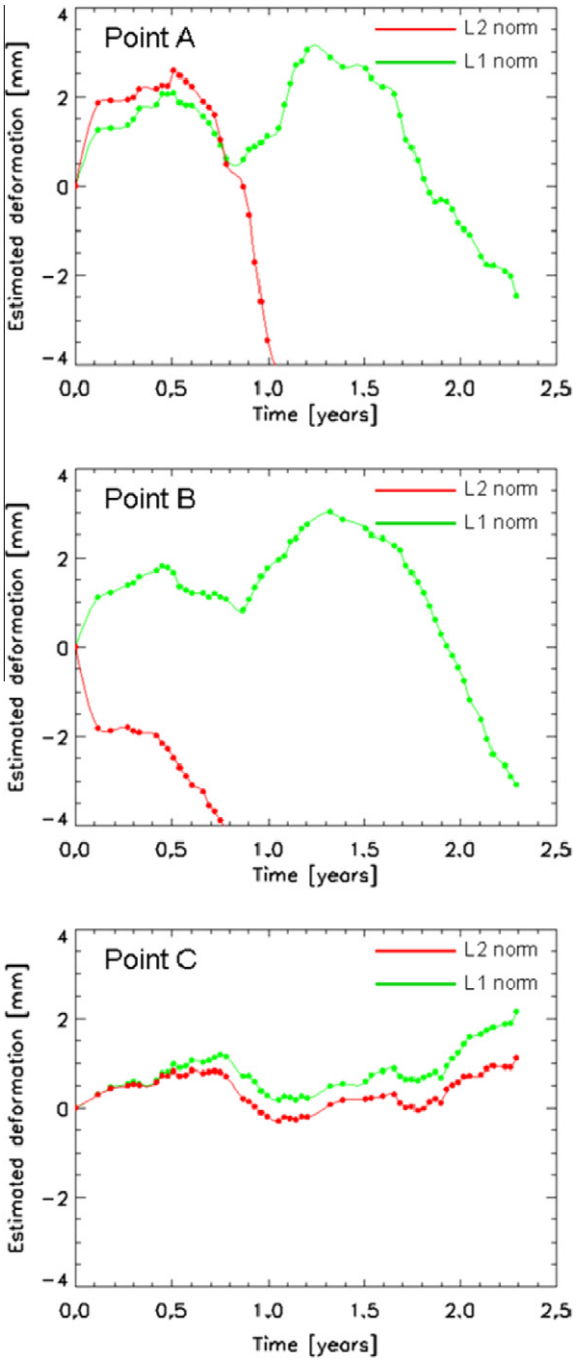

Fig. 13. Deformation time series using L2 norm and L1 norm based SBAS for points A, B and C marked in Fig. 12.

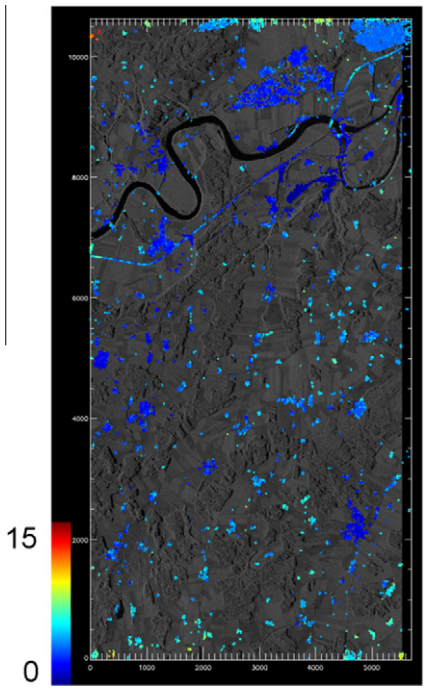

Fig. 14. Variance [mm ∗ mm] of deformation estimates using L1 norm based SBAS.

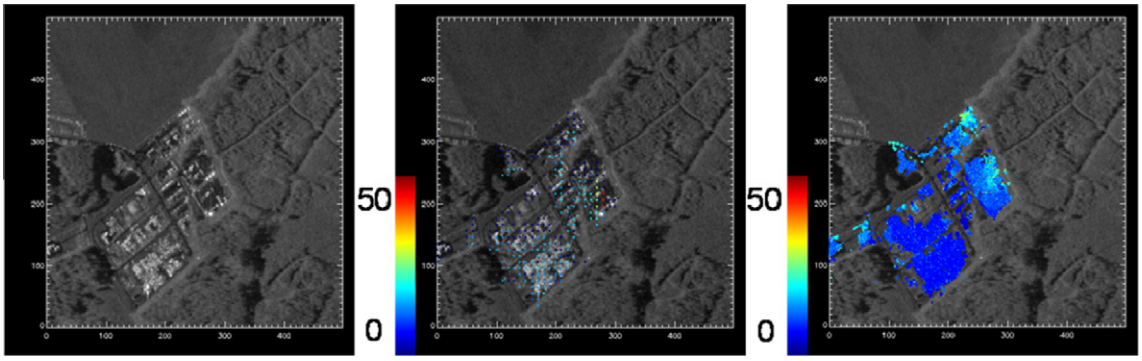

Fig. 15. Comparison of quality and density of deformation estimates in non-urban areas using standard SBAS and our technique. (a) is the TerraSAR-X image of the area surrounding point A (marked in Fig. 12), (b) shows the RMS deformation (mm) using standard SBAS, (c) shows the RMS deformation (mm) using our new approach.

of operation of the gas storage reservoir (injection during summer, production during winter) and the related reservoir pressure. We can observe minima during winter and maxima during summer. Also to be noticed is the fact that small displacement in the order of a few millimeters can be observed using the TerraSAR-X sensor. The variance of the deformation estimates using the L1 norm inversion is shown in Fig. 14.

The results demonstrate the potential of this new technique for providing accurate deformation in natural terrains. The increased quality and density of the deformation estimates of DSs in non-urban areas can also be seen in Fig. 15, where, a comparison with the normal SBAS approach has been provided. Here, a small area surrounding point A (of Fig. 12) is shown. Fig. 15a shows the TerraSAR-X image of this area. Fig. 15b shows the RMS deformation using conventional SBAS. Fig. 15c shows the RMS deformation using our new method and the improvement is clearly visible. Besides, one of the main advantages of the technique is the capability to estimate even non-linear deformation, as has been demonstrated for the application test case.

Of course, there is a slight reduction of resolution due to the adaptive multilooking, but, the object resolution is preserved. In fact, this technique is more suitable for high resolution sensors. For conventional sensors, the homogenous objects need a large dimension and thus the applicability of the technique is test site dependent. It is to be noted that a minimum number of scenes are required for the detection of homogenous objects and the estimation of covariance.

In terms of the computational complexity, the amount of data to be processed is increased and more processing time is needed. However, this technique is straightforward to implement with only little changes with respect to the existing algorithms.

Finally, we would like to remark the applicability of our approach for monitoring such phenomena as gas storage induced surface deformation and similar non-linear geophysical effects. In practice, the subsidence maps can be used for further geological analysis and risk mitigation.

4. Conclusion

A new technique has been developed for high resolution non-linear deformation monitoring in rural areas. The aim is to improve the robustness and precision of the parameter estimation in areas characterized by DSs. The technique first makes use of an adaptive spatial filtering algorithm to improve the differential interferometric phase, wherein, phase flattening and multilooking are incorporated using a statistically homogenous adaptive neighborhood. Then, deformation estimation is performed using an L1 norm based SBAS approach. A demonstration has been provided using TerraSAR-X data of a gas storage reservoir located in Germany.

Future work can concentrate on deformation estimation of DSs using a 4D periodogram approach, without any need of phase unwrapping.

Acknowledgement

We would like to thank Infoterra for providing the TerraSAR-X data for the gas storage site. We are also thankful to the anonymous reviewers for the constructive suggestions which greatly helped to improve this paper.

References

Adam, N., Kampes, B., Eineder, M., Worawattanamateekul, J., Kircher, M., 2003. The development of a scientific permanent scatterer system. In: ISPRS Hannover Workshop High Resolution Mapping from Space, Institute of Photogrammetry and Geoinformation, Hannover, Germany, 6–8 October, pp. 1–6 (on CD-ROM).

Adam, N., Kampes, B., Eineder, M., 2004. Development of a scientific permanent scatterer system: modifications for mixed ERS/ENVISAT time series. In: ENVISAT/ERS Symposium, Salzburg, Austria, 6–10 September, (on CD-ROM).

Adam, N., Eineder, M., Yague-Martinez, N., Bamler, R., 2008. High resolution interferometric stacking with TerraSAR-X. In: Proceedings of IEEE International Conference on Geoscience and Remote Sensing Symposium, IGARSS 2008, Boston, US, 7–11 July, pp. II-117–II-120.

Bamler, R., Hartl, P., 1998. Synthetic aperture radar interferometry topical review. Inverse problems 14, R1–R54, IOP Publishing Limited (UK).

Barrodale, I., Roberts, F.D.K., 1973. An improved algorithm for discrete L1 linear approximation. SIAM Journal on Numerical Analysis 10, 839–848.

Berardino, P., Fornaro, G., Lanari, R., Sansosti, E., 2002. A new algorithm for surface deformation monitoring based on small baseline differential SAR interferograms. IEEE Transactions on Geoscience and Remote Sensing 40 (11), 2375–2383.

Bishop, C.M., 2006. Pattern Recognition and Machine Learning. Springer, New York.

Constantini, M., 1998. A novel phase unwrapping method based on network programming. IEEE Transactions on Geoscience and Remote Sensing 36 (3), 813–821.

Eineder, M., Hubig, M., Milcke, B., 1998. Unwrapping large interferograms using the minimum cost flow algorithm. In: Proceedings of IEEE International Conference on Geoscience and Remote Sensing Symposium, IGARSS 1998, Seattle, US, 6–10 July, pp. 83–87.

Ferretti, A., Prati, C., Rocca, F., 2000. Nonlinear subsidence rate estimation using permanent scatterers in differential SAR interferometry. IEEE Transactions on Geoscience and Remote Sensing 38 (5), 2202–2212.

Ferretti, A., Prati, C., Rocca, F., 2001. Permanent scatterers in SAR interferometry. IEEE Transactions on Geoscience and Remote Sensing 39 (1), 8–20.

Ferretti, A., Fumagalli, A., Novali, F., Prati, C., Rocca, F., Rucci, A., 2011. A New Algorithm for Processing Interferometric Data-Stacks: SqueeSAR. IEEE Transactions on Geoscience and Remote Sensing 49 (9), 3460–3470.

Goel, K., Adam, N., 2011. High resolution differential interferometric stacking via adaptive spatial phase filtering. In: Proceedings of IEEE International Conference on Geoscience and Remote Sensing Symposium, IGARSS 2011, Vancouver, Canada, 24–29 July, pp. 1341–1344.

Golub, G., Loan, C., 1996. Matrix Computations, third ed. John Hopkins University Press, Baltimore.

Goodman, J.W., 1976. Some fundamental properties of speckle. Journal of the Optical Society of America A 66 (11), 1145–1150.

Kampes, B.M., 2006. Radar Interferometry – Persistent Scatterer Technique. Springer.

Lauknes, T., Zebker, H., Larsen, Y., 2011. InSAR deformation time series using an L1-norm small-baseline approach. IEEE Transactions on Geoscience and Remote Sensing 49 (1), 536–546.

Mora, O., Mallorqui, J.J., Broquetas, A., 2003. Linear and nonlinear terrain deformation maps from a reduced set of interferometric SAR images. IEEE Transactions on Geoscience and Remote Sensing 41 (10), 2243–2253.

Papoulis, A., Pillai, S.U., 1984. Probability, Random Variables, and Stochastic Processes, second ed. McGraw-Hill, New York.

Parizzi, A., Brcic, R., 2011. Adaptive InSAR stacks multilooking exploiting amplitude statistics: a comparison between different techniques and practical results. IEEE Geoscience and Remote Sensing Letters 8 (3), 441–445.

Pettitt, A.N., 1976. A two-sample Anderson–Darling rank statistic. Biometrika 63 (1), 161–168.

Rodriguez-Gonzalez, F., Bhutani, A., Adam, N., 2011. L1 network inversion for robust outlier rejection in persistent scatterer interferometry. In: Proceedings of IEEE International Conference on Geoscience and Remote Sensing Symposium, IGARSS 2011, Vancouver, Canada, 24–29 July, pp. 75–78.

Rosen, P.A., Hensley, S., Joughin, I.R., Li, F.K., Madsen, S.N., Rodriguez, E., Goldstein, R.M., 2000. Synthetic Aperture Radar Interferometry. Proceedings of the IEEE 88 (3), 333–382.

Zan, F. D., 2008. Optimizing SAR interferometry for decorrelating scatterers. Doctoral dissertation, Politecnico di Milano, Italy.

Zebker, H., Chen, K., 2005. Accurate estimation of correlation in InSAR observations. IEEE Geoscience and Remote Sensing Letters 2 (2), 124–127.

Zebker, H.A., Villasenor, J., 1992. Decorrelation in interferometric radar echoes. IEEE Transactions on Geoscience and Remote Sensing 30 (5), 950–959.

A.2 Goel, K., Adam, N., 2012b. High resolution deformation time series estimation for distributed scatterers using TerraSAR-X data. ISPRS Annals of the Photogrammetry, Remote Sensing and Spatial Information Sciences, XXII ISPRS Congress, Commission VII, Melbourne, Australia, 25 August-01 September 2012, I-7, 29-34, Copernicus Publications.

HIGH RESOLUTION DEFORMATION TIME SERIES ESTIMATION FOR DISTRIBUTED SCATTERERS USING TERRASAR-X DATA

Kanika Goel, Nico Adam

Remote Sensing Technology Institute (IMF), Germany German Aerospace Center (DLR), Oberpfaffenhofen, 82234-Wessling, Germany. Email: kanika.goel@dlr.de, Phone: +49-8153-28-1233, Fax: +49-8153-28-1420.

Commission VII, WG VII/2

KEY WORDS: Deformation Time Series, Differential SAR Interferometry, Distributed Scatterer (DS), High Resolution SAR, TerraSAR-X.

ABSTRACT:

In recent years, several SAR satellites such as TerraSAR-X, COSMO-SkyMed and Radarsat-2 have been launched. These satellites provide high resolution data suitable for sophisticated interferometric applications. With shorter repeat cycles, smaller orbital tubes and higher bandwidth of the satellites; deformation time series analysis of distributed scatterers (DSs) is now supported by a practical data basis. Techniques for exploiting DSs in non-urban (rural) areas include the Small Baseline Subset Algorithm (SBAS). However, it involves spatial phase unwrapping, and phase unwrapping errors are typically encountered in rural areas and are difficult to detect. In addition, the SBAS technique involves a rectangular multilooking of the differential interferograms to reduce phase noise, resulting in a loss of resolution and superposition of different objects on ground. In this paper, we introduce a new approach for deformation monitoring with a focus on DSs, wherein, there is no need to unwrap the differential interferograms and the deformation is mapped at object resolution. It is based on a robust object adaptive parameter estimation using single look differential interferograms, where, the local tilts of deformation velocity and local slopes of residual DEM in range and azimuth directions are estimated. We present here the technical details and a processing example of this newly developed algorithm.

1. INTRODUCTION

Various differential SAR interferometric stacking techniques have been developed that exploit phase stable i.e. persistent scatterers (PSs). PS interferometry provides a parametric estimation of the displacement and 3D location based on the assumption of one or two dominant scatterers in the resolution cell (Ferretti et al., 2000, Ferretti et al., 2001, Kampes, 2006, Adam et al., 2008). However, it has some limitations in non-urban (rural) areas due to low density of PSs, their inhomogenous spatial distribution, phase ambiguities and atmospheric effects. There is an increasing focus on utilizing distributed scatterers (DSs) to extract geophysical parameters of interest (i.e. LOS deformation and DEM error) for surfaces characterized by fields, forests, soil and rock surfaces. Application examples include mines, volcanoes, oil/gas/water reservoirs and seismic zones. Distributing scattering mechanism involves a coherent sum of many independent small scatterers (no dominant scatterer) within a resolution cell (Goodman, 1976). Techniques such as the Small Baseline Subset Algorithm (SBAS) and SqueeSAR have been proposed to process DSs.

SBAS makes use of spatially unwrapped small baseline differential interferograms (Berardino et al., 2002, Mora et al., 2003). These are linked using the Singular Value Decomposition (SVD) method and a minimum-norm least squares (LS) solution is obtained (Golub and Loan, 1996). Essentially, the phase is averaged in an estimation window to reduce the phase noise (Zebker and Villasenor, 1992). However, the drawback of the straightforward rectangular estimation window is a loss of resolution and a superposition of different objects on ground. In addition, phase unwrapping (Constantini, 1998, Eineder et al., 1998) is an important step in SBAS and phase unwrapping errors are often encountered in natural terrains. There might be several decorrelated areas (e.g. trees, soil, water etc.) separating the coherent patches and the relative values in the different coherent patches can have unknown integer multiples of 2π phase offsets.

SqueeSAR, on the other hand, makes use of all possible interferograms and employs an adaptive spatial multilooking to reduce the phase noise and estimate the covariance matrix for each DS (Ferretti et al., 2011, Zan et al., 2008). Afterwards, a phase triangulation algorithm is applied to each DS to retrieve the optimized phase values for the SAR images. The DSs are then processed jointly with the PSs using the traditional PS interferometric chain. However, this technique can be computationally expensive.

With respect to the above-mentioned techniques, we have developed and implemented an alternative method for high resolution deformation monitoring of DSs. The proposed method performs an object adaptive parameter estimation which is based on two principles. First, the high resolution of satellites such as TerraSAR-X leads to many resolution cells covering a homogenous object in non-urban areas. This object can be described by a single deformation parameter. The object's area (pixels) thus needs to be identified for an optimal estimation of the model parameter, namely, the LOS deformation velocity. Second, we just concentrate on small baseline differential interferograms to reduce the effects of topography on the DSs, and mainly to reduce the computational complexity.

Practically, the algorithm involves the identification of the object's area (pixels) by a similarity test algorithm using a stack of SAR amplitude images (Parizzi and Brcic, 2011). The differential interferometric phase values of the object's pixels (calibrated with respect to a reference pixel which lies within the object boundary, so that, the atmospheric effects and orbital

errors are cancelled out) are then exploited for parameter estimation using a search algorithm in the solution space. For each object patch, a periodogram approach is applied in the spatial domain (object area) and time domain (small baseline differential interferometric stack) for a robust estimation of the local tilts of displacement velocity and local slopes of residual DEM in range and azimuth directions with respect to the reference pixel. Finally, since the independent estimated neighboring patches are close and deformation is assumed to be smooth, a 2D-model-deformation integration can be performed to get the absolute deformation. The new concept with respect to the existing algorithms is that there is no need for spatial phase unwrapping and the deformation time series is estimated at full resolution. Even in the presence of high phase noise, the algorithm compensates DEM errors and additionally, atmospheric artifacts are removed automatically for each patch as the phase values are referred to one pixel within the patch. Objective of this paper is to present the developed algorithm and demonstrate it using TerraSAR-X high resolution spotlight data of Lueneburg in Germany.

2. METHODOLOGY

Assuming that we have N SAR images and M single look small baseline differential interferograms available, the implemented methodology for deformation estimation of DSs involves the following steps:

2.1 Identification of Homogenous Patches

We start with the identification of independent homogenous patches using a stack of coregistered and calibrated SAR amplitude images. These statistically homogenous patches are dependent on the reflectivity, have typically a constant local slope and clear boundaries (e.g. fields, roads etc.).

Various statistical tests have been proposed in recent years to identify homogenous pixels based on the amplitude of coregistered and calibrated stack of SAR images. These include the Kullback-Leibler Divergence test (Bishop, 2006), the Kolmogorov-Smirnov (KS) test (Papoulis and Pillai, 1984) (used in the SqueeSAR approach (Ferretti et al., 2011)) and the Anderson-Darling (AD) test (Pettitt, 1976). The AD test has been proven to be the most effective statistical test to identify if two pixels arise from the same distribution (Parizzi and Brcic, 2011). It is a non-parametric test i.e. we do not assume that the samples belong to a defined probability distribution. Instead, using the amplitude of the stack of SAR images, we obtain the empirical cumulative distribution functions of amplitudes for the two pixels (points) under consideration. The distance between the distributions, with weighting given to tails (higher order moments of the distribution are taken into consideration), tells us if the two points statistically arise from the same distribution. For a set of points a and b, the AD statistic A^2 is:

$$A^2 = \frac{N}{2} \sum_{F_{a,b}(x)} \frac{\left[F_a(x) - F_b(x)\right]^2}{\left[F_{a,b}(x) \cdot \left(1 - F_{a,b}(x)\right)\right]} \qquad (1)$$

where, N is the number of SAR amplitude images, $F_a(x)$ and $F_b(x)$ are empirical cumulative distribution functions of amplitudes x for points a and b, $F_{a,b}(x)$ is empirical distribution function of the pooled distribution $[a,b]$. If the AD statistic is less than a threshold value, the two pixels are assumed to belong to the same homogenous area.

In this step, we divide the area into rectangular blocks. The block size is chosen in such a way that the atmosphere is mitigated if we subtract the phase of the reference pixel from the phases of the other pixels in the block, and also considering that the patch size should be large enough to provide us with a reliable estimation. Then, within each rectangular block, homogenous patch pixels are identified based on a certain criterion which gives us the best possible estimate of the DS inside the block. In practice, the estimation takes advantage of large homogenous areas. It is based on the fact that the large number of samples improves the precision and the large spatial extension increases the sensitivity of the estimation. This is the reason that we consider a minimum patch size. Also, the average coherence of the patch should be larger than a certain threshold. The coherence of the pixels can be calculated using an adaptive multilooking algorithm (Parizzi and Brcic, 2011, Goel and Adam, 2011a). For each detected patch, a reference pixel is selected. Fig. 1 shows an example of the identification of homogenous patches for a small region in the town of Lueneburg in Germany. 17 TerraSAR-X images (high resolution spotlight mode) of the test site from 2010-2011 were used. In this demonstration, the region was divided into blocks of 40 × 40 pixels. A minimum patch size of 20 pixels and a coherence threshold of 0.3 was applied.

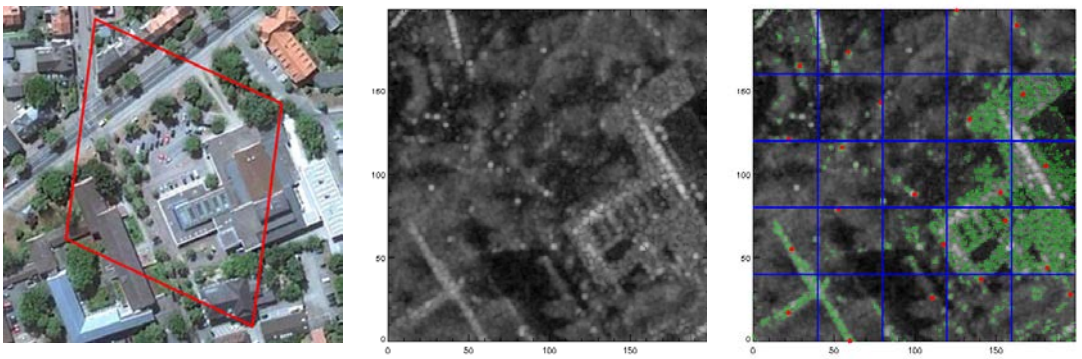

(a) (b) (c)

Figure 1: Identification of homogenous patches. (a) is a Google Earth image of a small part of Lueneburg in Germany, the region of interest is enclosed in red. (b) is the mean amplitude image of the region of interest. (c) shows the division of the region into blocks by the blue lines, wherein, the points in green represent the homogenous pixels and the points in red represent the reference pixels.

2.2 Tilt and Slope Estimation

The single look small baseline differential interferograms can now be exploited for estimation of tilts of deformation velocity and slopes of residual DEM for each patch with respect to the reference pixel of that patch. First, the phase values of each patch are corrected with respect to the reference pixel so that the atmospheric effects and orbital errors are negligible. Second, these are then used for parameter estimation using a 4D periodogram.

For each object patch, to estimate the local tilts of deformation velocity m_{v_x} and m_{v_y} in range and azimuth directions resp. (in mm/year/pixel) and the local slopes of residual DEM m_{h_x} and m_{h_y} in range and azimuth directions resp. (in m/pixel), M periodograms are generated in spatial domain from the $(M * L)$ interferometric phase values of the patch, where L is the number of homogenous pixels. A periodogram $\xi^k, k = 1,...,M$, is a function of the local tilts of deformation velocity and local slopes of residual DEM for the object patch:

$$\xi^k(m_{v_x}, m_{v_y}, m_{h_x}, m_{h_y}) = \frac{1}{L}\left|\sum_{i=1}^{L} e^{j\begin{pmatrix}\phi^{i,k} - T^k m_{v_x} p_x^i - T^k m_{v_y} p_y^i \\ -B^k m_{h_x} p_x^i - B^k m_{h_y} p_y^i\end{pmatrix}}\right| \quad (2)$$

where, L is the number of homogenous pixels for the patch, $\phi^{i,k}$ is the single look interferometric phase for homogenous pixel i and interferogram k, T^k is the velocity conversion factor for interferogram k, B^k is the height conversion factor for interferogram k, m_{v_x} and m_{v_y} are local tilts of deformation velocity in range and azimuth directions resp. (in mm/year/pixel), m_{h_x} and m_{h_y} are local slopes of residual DEM in range and azimuth directions resp. (in m/pixel), p_x^i and p_y^i are pixel indices in range and azimuth directions resp. for homogenous pixel i. The velocity conversion factor for an interferogram k is given by:

$$T^k = \frac{4\pi}{\lambda} B_t^k \quad (3)$$

where, λ is the transmitted wavelength, B_t^k is the temporal baseline for interferogram k. The height conversion factor for an interferogram k is given by:

$$B^k = \frac{4\pi}{\lambda} \frac{B_\perp^k}{R \sin\theta} \quad (4)$$

where, $B_\perp^k$ is the perpendicular baseline for interferogram k, R is the sensor-target distance, θ is the local incidence angle (for flat terrain).

Further on, we make the parameter estimation robust by averaging all the periodograms for a patch to reduce side lobes. We finally get an averaged periodogram ξ as follows:

$$\xi(m_{v_x}, m_{v_y}, m_{h_x}, m_{h_y}) = \frac{1}{M}\sum_{k=1}^{M} \xi^k \quad (5)$$

The local tilts of the deformation velocity m_{v_x} and m_{v_y} and the local slopes of the residual DEM m_{h_x} and m_{h_y} for each patch are estimated from the peak of the averaged periodogram i.e.:

$$(\hat{m}_{v_x}, \hat{m}_{v_y}, \hat{m}_{h_x}, \hat{m}_{h_y}) = \underset{m_{v_x}, m_{v_y}, m_{h_x}, m_{h_y}}{\arg\max} (\xi) \quad (6)$$

2.3 Network Inversion

Since the independent estimated neighboring patches are close and deformation is assumed to be smooth, a 2D-model-deformation integration can finally be performed to get the absolute deformation. A simple 1D case is shown in Fig. 2.

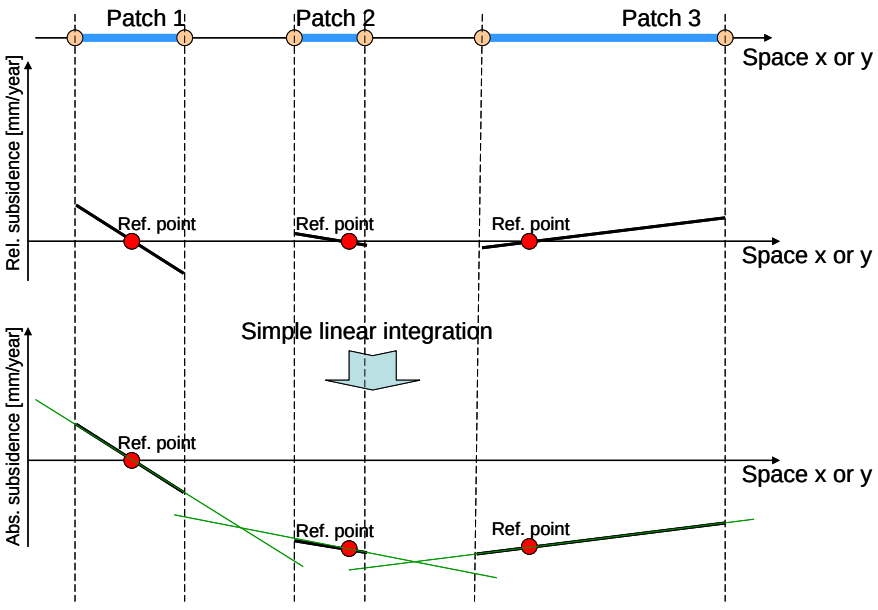

Figure 2: A simple 1D example of integrating the relative deformation of the various patches to get the absolute values.

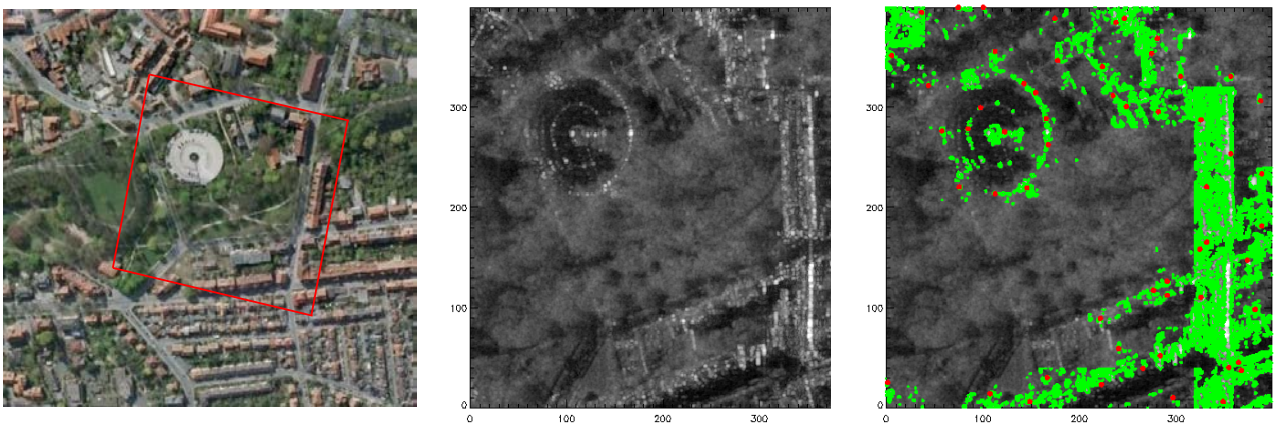

(a) (b) (c)

Figure 3: Identification of homogenous patches for a part of Lueneburg which has deformed highly in the considered time period. (a) is a Google Earth image of a small part of Lueneburg in Germany, the region of interest is enclosed in red. (b) is the mean amplitude image of the region of interest. (c) shows the homogenous pixels in green and the reference pixels in red.

3. APPLICATION TEST CASE AND RESULTS

The town of Lueneburg in Germany has been used to demonstrate our technique. It is situated in the German state of Lower Saxony. The old part of this town lies on a salt dome. As a result of constant salt mining dating back to the 19th century, various areas of the town have experienced a gradual or high subsidence, became unstable and had to be demolished. The sinking still continues even today. Many ground stations have been established since 1946 to monitor the deformation, but due to the changing subsidence patterns and locations, space-borne differential SAR interferometric technique is better suited for deformation mapping of Lueneburg (Goel et al., 2011).

We used 17 high resolution spotlight TerraSAR-X images of Lueneburg from October, 2010 to September, 2011 with a look angle of 29.6 degrees and 'HH' polarization. We generated 89 small baseline differential interferograms. Fig. 3 shows the identification of homogenous patches for a part of Lueneburg which has deformed highly in the considered time period. In Fig. 4, we present deformation estimation results for this region using a different approach so that we can compare the new technique with them. The approach which we used for comparison is object adaptive phase filtering, followed by an L1 norm based SBAS technique (Goel and Adam, 2011b).

Fig. 5 shows the preliminary tilt estimation results for the deformation velocity in range and azimuth directions in mm/year/pixel using the newly developed technique. We can see that the results compare well with the SBAS results. Fig. 6 shows the preliminary slope estimation results for the residual DEM in range and azimuth directions in m/pixel. The comparison of the results with ground truth data is foreseen in the future. We are in contact with the local government of Lueneburg for the levelling data.

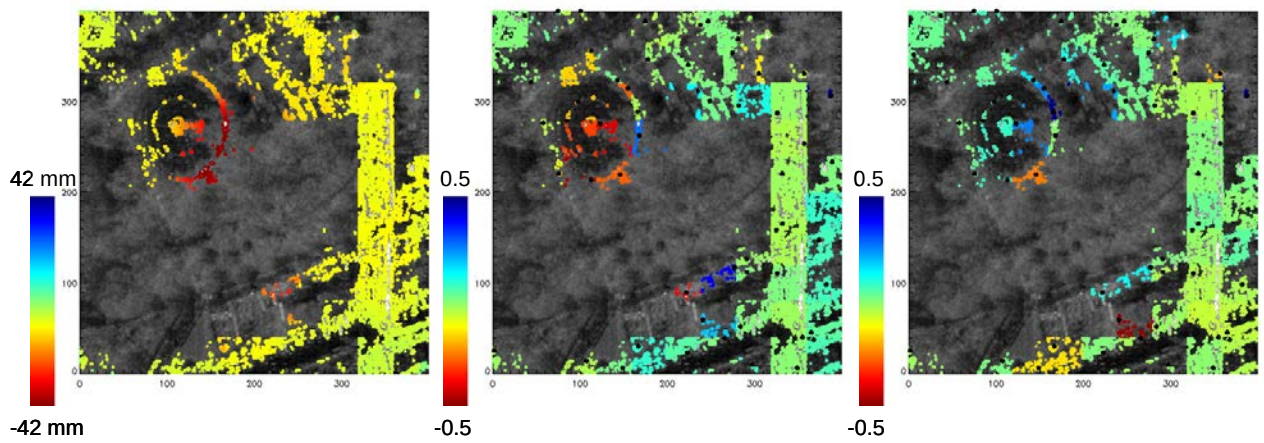

(a) (b) (c)

Figure 4: Deformation estimation results using a different approach (adaptive spatial phase filtering and L1 based SBAS technique). (a) The total deformation in mm. (b) Local tilts of deformation velocity in range (x) direction in mm/year/pixel calculated from (a). (c) Local tilts of deformation velocity in azimuth (y) direction in mm/year/pixel calculated from (a).

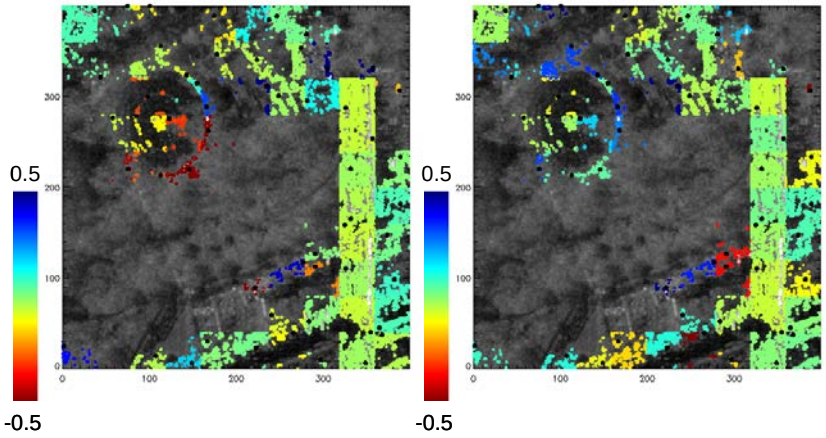

(a) (b)

Figure 5: Deformation estimation results using the newly developed technique. (a) Estimates of local tilts of deformation velocity in range (x) direction in mm/year/pixel. (b) Estimates of local tilts of deformation velocity in azimuth (y) direction in mm/year/pixel.

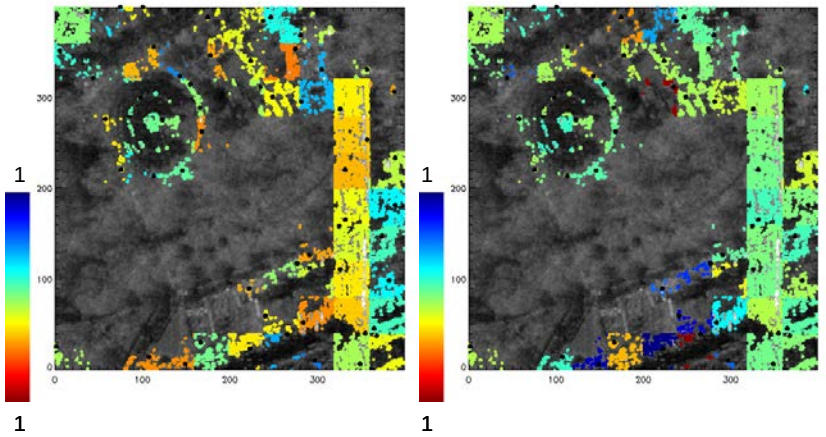

(a) (b)

Figure 6: Residual DEM estimation results using the newly developed technique. (a) Estimates of local slopes of residual DEM in range (x) direction in m/pixel. (b) Estimates of local slopes of residual DEM in azimuth (y) direction in m/pixel.

4. CONCLUSION

A new concept has been developed to estimate deformation of DSs at full resolution without any phase unwrapping. Even in the presence of high phase noise, the algorithm compensates DEM errors and additionally, atmospheric artifacts are removed automatically for each patch as the phase values are referred to one pixel within the patch. A demonstration has been provided using TerraSAR-X data of Lueneburg in Germany. Future work will concentrate on network inversion algorithms to retrieve the absolute LOS deformation velocities and residual DEM.

REFERENCES

Adam, N., Eineder, M., Yague-Martinez, N. & Bamler, R., 2008. High resolution interferometric stacking with TerraSAR-X. In: Proc. *Intl. Geosci. Rem. Sens. Symp. (IGARSS)*, Boston.

Berardino, P., Fornaro, G., Lanari, R. & Sansosti, E., 2002. A new algorithm for surface deformation monitoring based on small baseline differential SAR interferograms. *IEEE TGRS*, vol. 40, no. 11, p. 2375.

Bishop, C. M., 2006. *Pattern recognition and machine learning*. Springer, New York.

Constantini, M., 1998. A novel phase unwrapping method based on network programming. *IEEE TGRS*, vol. 36, no. 3, pp. 813-821.

Eineder, M., Hubig, M. & Milcke, B., 1998. Unwrapping large interferograms using the minimum cost flow algorithm. In: *Proc. IGARSS*, Seattle.

Ferretti, A., Prati, C. & Rocca, F., 2000. Nonlinear subsidence rate estimation using permanent scatterers in differential SAR interferometry. *IEEE TGRS*, vol. 38, no. 5, pp. 2202–2212.

Ferretti, A., Prati, C. & Rocca, F., 2001. Permanent scatterers in SAR interferometry. *IEEE TGARS*, vol. 39, No. 1, pp. 8-20.

Ferretti, A., Fumagalli, A., Novali, F., Prati, C., Rocca, F. & Rucci, A., 2011. A New Algorithm for Processing Interferometric Data-Stacks: SqueeSAR. IEEE TGRS, vol. 49, no. 9, p. 3460.

Goel, K. & Adam, N., 2011a. High resolution differential interferometric stacking via adaptive spatial phase filtering. In: *Proc. IGARSS*, Vancouver, Canada.

Goel, K. & Adam, N., 2011b. Deformation estimation in non-urban areas exploiting high resolution SAR data. In: *Proc. FRINGE*, Frascati, Italy.

Goel, K., Parizzi, A. & Adam, N., 2011. Salt mining induced subsidence mapping of Lueneburg (Germany) using PSI and SBAS techniques exploiting ERS and TerraSAR-X data. In: *Proc. FRINGE*, Frascati, Italy.

Goodman, J. W., 1976. Some fundamental properties of speckle. *J. Opt. Soc. Am. A*, vol. 66, no. 11, pp. 1145–1150.

Golub, G. & Loan, C., 1996. *Matrix Computations*, 3rd ed. Baltimore: John Hopkins University Press.

Kampes, B. M., 2006. *Radar Interferometry - Persistent Scatterer Technique*. Springer.

Mora, O., Mallorqui, J.J., Broquetas, A., 2003. Linear and nonlinear terrain deformation maps from a reduced set of interferometric SAR images. *IEEE TGRS*, vol. 41, no. 10, p. 2243.

Papoulis, A. & Pillai, S. U., 1984. *Probability, random variables, and stochastic processes*. Second Edition, McGraw-Hill, New York.

Parizzi A. & Brcic, R., 2011. Adaptive InSAR stacks multilooking exploiting amplitude statistics: A comparison between different techniques and practical results. *IEEE GRSL*, vol. 8, no. 3.

Pettitt, A. N., 1976. A two-sample Anderson–Darling rank statistic. *Biometrika*, vol. 63, no. 1, pp. 161–168.

Zan, F. D., 2008. Optimizing SAR interferometry for decorrelating scatterers. *Doctoral dissertation*, Politecnico di Milano, Italy.

Zebker, H. A. & Villasenor, J., 1992. Decorrelation in interferometric radar echoes. *IEEE TGRS*, vol. 30, no. 5, pp. 950–959.

A.3 Goel, K., Adam, N., 2013a. A distributed scatterer interferometry approach for precision monitoring of known surface deformation phenomena. IEEE Transactions on Geoscience and Remote Sensing PP (99), 1-15, DOI: 10.1109/TGRS.2013.2289370.

A Distributed Scatterer Interferometry Approach for Precision Monitoring of Known Surface Deformation Phenomena

Kanika Goel and Nico Adam

***Abstract*—This paper presents a new technique for mapping mean deformation velocity in highly decorrelated areas with known deformation patterns, exploiting high-resolution synthetic aperture radar (SAR) data. The implemented method is based on distributed scatterers and first makes use of the Anderson–Darling (AD) statistical test to identify homogenous patches of pixels based on SAR amplitude images. Then, a robust object adaptive parameter estimation is performed to estimate the local gradients of deformation velocity and the local gradients of residual DEM in range and azimuth directions for these patches, utilizing small baseline differential interferograms. Finally, the information obtained from different patches is connected to get the deformation velocity, via a 2-D model-based deformation integration using Bayesian inference. Compared with published multitemporal interferometric work, the main advantage of the newly developed algorithm is that it does not require any phase unwrapping, and because of this, the method is largely insensitive to decorrelation phenomenon occurring in natural terrains and the availability of persistent scatterers (PSs), in contrast to the coherent stacking techniques such as PS interferometry, small baseline subset algorithm, and SqueeSAR. The method is computationally inexpensive with respect to SqueeSAR as only the small baseline interferograms are used for the processing. The method provides spatially dense deformation velocity maps at a suitable object resolution, as compared with a few measured points provided by the stacking techniques in difficult decorrelated regions. High Resolution Spotlight TerraSAR-X data set of Lueneburg in Germany is used as a processing example of this technique.**

***Index Terms*—Differential interferometric synthetic aperture radar (DInSAR), distributed scatterer (DS), high-resolution SAR, small baseline subset algorithm (SBAS), SqueeSAR, synthetic aperture radar (SAR), TerraSAR-X.**

I. Introduction

DIFFERENTIAL interferrometric synthetic aperture radar (DInSAR) is an effective technique for measuring surface displacements [1], [2]. Various multitemporal DInSAR techniques have been developed that exploit permanently coherent, i.e., phase-stable persistent scatterers (PSs). PS interferometry (PSI) utilizes long-time-span differential interferograms with respect to a single master image and provides a parametric estimation of the displacement and 3-D location based on the assumption of one or two dominant scatterers in the resolution cell [3], [4]. However, it has some limitations in nonurban/rural areas due to low density of PSs, their inhomogenous spatial distribution, and phase ambiguities. There is an increasing focus on utilizing distributed scatterers (DSs) to extract geophysical parameters of interest [i.e., line-of-sight (LOS) deformation and residual digital elevation model (DEM)] for surfaces characterized by fields, soil, and rock surfaces. In recent years, several SAR satellites such as TerraSAR-X, COSMO-SkyMed, and Radarsat-2 have been providing high-resolution data suitable for sophisticated interferometric applications. With shorter repeat cycles, smaller orbital tubes and higher bandwidths of the satellites, DS interferometry (DSI) is now supported by a practical data basis. The distributed scattering mechanism involves a coherent sum of many independent small scatterers (and no dominant scatterer) within a resolution cell [5] and is modeled by a complex circular Gaussian radar return [1]. DSs tend to decorrelate temporally, and the phase quality is not on par with the PSs. They usually span several image pixels where the backscattered energy is less strong but statistically homogeneous within the area. It is possible to process DSs with high precision using advanced stacking techniques such as the small baseline subset algorithm (SBAS) and SqueeSAR.

Differently to PSI, SBAS [6] makes use of differential interferograms with small geometric and temporal baselines to limit the decorrelation phenomena. Essentially, in conventional SBAS, the phase is averaged/multilooked in an estimation window to reduce the phase noise [7]. The interferograms are then spatially unwrapped, and the deformation is estimated via the singular value decomposition method (based on $L2$-norm minimization) [8]. Advantageously, SBAS provides complete nonlinear deformation time series of the scatterers. However, a drawback of the straightforward rectangular estimation window is a loss of resolution and a superposition of different objects on ground. Techniques presented in [9] and [10] have been proposed to counter this and extend standard SBAS. The approach implemented in [9] uses both single-look and multilook data and provides deformation at two spatial scales, i.e., regional and local. In contrast, the technique presented in [10] first performs an adaptive spatial phase filtering to preserve object resolution, followed by an $L1$-norm-based deformation retrieval, which results in a more robust solution with respect to the phase unwrapping errors frequently occurring in nonurban areas. In fact, spatial phase unwrapping via the minimum cost flow

Manuscript received March 26, 2013; revised September 7, 2013; accepted October 25, 2013.

The authors are with the Remote Sensing Technology Institute (IMF), German Aerospace Center (DLR), 82234 Wessling, Germany.

Digital Object Identifier 10.1109/TGRS.2013.2289370

(MCF) algorithm [11], [12] is an important step in SBAS, and local phase unwrapping errors are often encountered in natural terrains and are difficult to detect. Although some endeavors have been made to limit the impact of severe phase unwrapping errors on the estimated deformation time series, for example, techniques proposed in [13] and [14], exploit both the temporal and the spatial structure of the data by a 3-D phase unwrapping and further extend the MCF phase unwrapping technique, nonetheless, phase unwrapping still remains a major source of error in spotted coherent areas and is time consuming too.

SqueeSAR [15], on the other hand, makes use of all $N \times (N-1)/2$ interferograms that are possible with N acquisitions to yield the best possible estimates of the $N-1$ phases associated with the deformation of each DS. It first employs adaptive spatial multilooking to reduce the phase noise and estimate the covariance matrix for each DS. Afterward, a phase triangulation algorithm is applied to each DS to retrieve the optimized $N-1$ phase values. The DSs are then processed jointly with the PSs using the traditional PS interferometric chain. Following the basic concept of SqueeSAR, a demonstration of the estimation of DSs' phase histories in urban areas is provided in [16]. SqueeSAR provides motion parameter estimates for DSs with significantly enhanced signal-to-noise ratio (SNR). Although, it can be computationally expensive as it utilizes all possible interferograms.

Nonetheless, highly decorrelated regions still pose a challenge in displacement monitoring. New algorithms are required for measuring difficult areas characterized by high temporal decorrelation and for providing spatially dense deformation maps. With respect to the aforementioned techniques, we have developed and implemented an alternative method for deformation velocity monitoring in difficult decorrelated areas whose deformation velocity can be described by a suitable model, exploiting high-resolution SAR data. Typical application examples include subsurface mining areas, subsurface construction sites, and oil/gas/water reservoirs. The proposed method utilizes DSs and first involves the identification of DSs, i.e., homogenous object patches of pixels, by a similarity test algorithm using a stack of SAR amplitude images [15], [17]. Then, a robust object adaptive parameter estimation is performed to estimate the local gradients of deformation velocity and the local gradients of residual DEM in range and azimuth directions for these patches, utilizing small baseline differential interferograms. Finally, since the independent estimated neighboring patches are close and deformation is assumed to be smooth, 2-D model-based deformation integration is performed to get the LOS deformation velocity. To implement this inversion, a Bayesian estimation framework [18], [19] is applied, which makes use of directed graphs [20] and particle filters [21], [22]. The new concept with respect to the existing DS algorithms is that:

1) There is no need for spatial phase unwrapping, and the mean deformation velocity is estimated at a suitable resolution on the order of the dimension of objects.
2) The computational complexity is reduced, as compared to SqueeSAR, by making use of only small baseline differential interferograms.
3) Even in the presence of high-phase noise, the algorithm compensates DEM errors and atmospheric artifacts.
4) Due to model-based deformation integration, a spatially dense deformation velocity map is estimated, instead of just a few measured points.

The objective of this paper is to present the developed algorithm and its application on a real TerraSAR-X data set of Lueneburg in Germany, which has undergone salt-mining-induced subsidence. We demonstrate its effectiveness to robustly provide deformation velocity maps in areas with high decorrelation and also, counteract some of the limitations of conventional coherent SAR techniques such as PSI, SBAS, and SqueeSAR.

II. Methodology

Assuming that N SAR images and M single-look small baseline differential interferograms are available, the implemented methodology for deformation estimation of DSs involves the following steps.

A. Identification of Homogenous Patches

We start with the identification of independent homogenous patches i.e., DSs using the stack of coregistered and calibrated SAR amplitude images. A DS object covers several pixels in high-resolution SAR images, and these pixels exhibit similar scattering properties and belong to the same distribution. These statistically homogenous patches are dependent on the reflectivity and typically have a constant local slope and clear boundaries (e.g., fields and roads).

Various statistical tests have been proposed in recent years to identify homogenous pixels based on the amplitude of coregistered and calibrated stack of SAR images. These include the Kullback–Leibler divergence test [20], the Kolmogorov–Smirnov test [18] (used in the SqueeSAR approach [15]), and the Anderson–Darling (AD) test [23]. The AD test has been proven to be the most effective [17]. It gives the best detection rate at a constant false alarm rate. It performs reasonably well even for a stack of acquisitions containing as small as ten images. This is the reason we use this algorithm in our implementation. For a pair of pixels a and b, the AD statistic A^2 is

$$A^2 = \frac{N}{2} \sum_{F_{a,b}(x)} \frac{[F_a(x) - F_b(x)]^2}{[F_{a,b}(x) \cdot (1 - F_{a,b}(x))]} \tag{1}$$

where N is the number of SAR amplitude images, $F_a(x)$ and $F_b(x)$ are the empirical cumulative distribution functions of amplitudes x for pixels a and b, and $F_{a,b}(x)$ is the empirical distribution function of the pooled distribution $[a, b]$. If the AD statistic is less than a threshold value, the two pixels are assumed to belong to the same homogenous area.

In this step, the area is divided into nonoverlapping rectangular blocks. Then, within each rectangular block, a homogenous patch of pixels is identified. The patch should have a minimum size since the estimation takes advantage of large homogenous

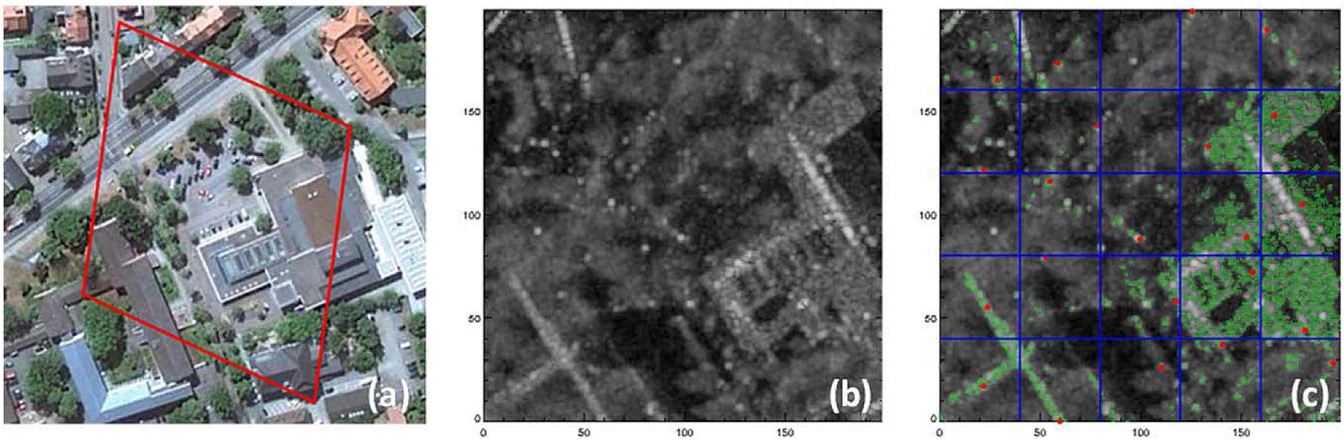

Fig. 1. Identification of homogenous patches. (a) Google Earth image of a small part of Lueneburg in Germany. The region of interest is enclosed in red. (b) Mean amplitude TerraSAR-X image of the region of interest. (c) Division of the region into blocks by the blue lines, wherein the points in green represent the homogenous pixels and the points in red represent the reference pixels.

areas. In addition, the average spatial coherence of the patch should be larger than a certain threshold to counter phase noise. For each detected patch, a reference pixel is selected. Any pixel in the homogenous patch can be assigned as the reference pixel (since, ideally, all the pixels in the homogenous patch have the same coherence). The block size is chosen in such a way that the atmosphere is mitigated if we subtract the phase of the reference pixel from the phases of the other pixels in the block and also considering that the patch size should be large enough to provide us with a reliable estimation. Fig. 1 shows an example of the identification of homogenous patches for a small region in the town of Lueneburg in Germany. In addition, 17 TerraSAR-X High Resolution Spotlight mode images of the test site from 2010 to 2011 were used. In this demonstration, the region is divided into blocks of 40 pixels $\times$ 40 pixels, i.e., 24 m $\times$ 24 m approximately. A minimum patch size of 20 pixels and a coherence threshold of 0.3 have been applied.

B. Gradient Estimation for Deformation Velocity and Residual DEM

The single-look differential interferograms with small spatial and temporal baselines are now exploited for the parameter estimation of DSs in order to reduce the residual topography and temporal decorrelation. In addition, the computational complexity is reduced. The single-look differential interferometric phase of a pixel i for interferogram k, with respect to a reference pixel, is composed of the phase components related to deformation, residual topography, atmosphere, and noise

$$\phi^{i,k} = \phi^{i,k}_{\text{defo}} + \phi^{i,k}_{\text{topo}} + \phi^{i,k}_{\text{atmo}} + \phi^{i,k}_{\text{noise}} \tag{2}$$

where $\phi^{i,k}_{\text{defo}}$ is the deformation phase, $\phi^{i,k}_{\text{topo}}$ is the residual topographic phase, $\phi^{i,k}_{\text{atmo}}$ is the atmospheric phase, and $\phi^{i,k}_{\text{noise}}$ is the phase noise. The deformation phase is given as follows (assuming a constant velocity model):

$$\phi^{i,k}_{\text{defo}} = T^k v^i \tag{3}$$

where v^i is the mean deformation velocity of the pixel i with respect to the reference pixel, and T^k is the velocity conversion factor for interferogram k given by

$$T^k = \frac{4\pi}{\lambda} B^k_t \tag{4}$$

where λ is the transmitted wavelength, and B^k_t is the temporal baseline for interferogram k. The residual topographic phase is given as follows:

$$\phi^{i,k}_{\text{topo}} = B^k \Delta h^i \tag{5}$$

where Δh^i is the residual topography of the pixel i with respect to the reference pixel, and B^k is the height conversion factor for interferogram k given by

$$B^k = \frac{4\pi}{\lambda} \frac{B^k_\perp}{R \sin\theta} \tag{6}$$

where $B^k_\perp$ is the perpendicular baseline for interferogram k, R is the sensor–target distance, and θ is the local incidence angle. The atmospheric phase is minimized if the reference pixel is in close spatial proximity, i.e., less than 1 km away [24], [25]. The phase noise is due to temporal decorrelation, uncompensated spectral shift decorrelation, orbital errors, and thermal noise. Similar to atmosphere, the orbital errors become negligible if the reference pixel is located nearby.

Accordingly, the homogenous patch can be described by the model parameters, LOS deformation velocity, and residual DEM. Since each patch is composed of many neighboring pixels, we do not assign a single average deformation velocity or residual DEM to the homogenous pixels. In fact, the deformation velocities and residual DEMs of the homogenous pixels can be, to the first order, well approximated by a linear spatial behavior in range and azimuth directions, respectively, with respect to the reference pixel. Given the differential phase data, the local gradients of deformation velocity m_{v_x}, m_{v_y} (in millimeters per year per pixel) and the local gradients of residual DEM m_{h_x}, m_{h_y} (in meters per pixel) in range x and azimuth y directions, respectively, are estimated for the

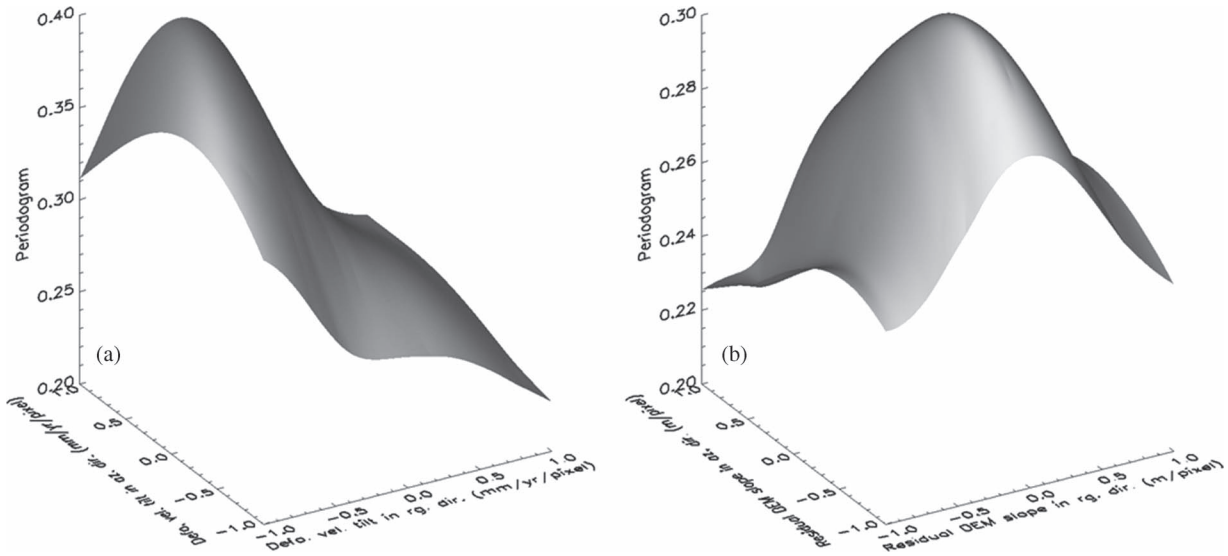

Fig. 2. Periodogram demonstration using Lueneburg data set for a highly deforming patch. (a) Periodogram ξ for $m_{v_x} = [-1, 1]$ (in millimeters per year per pixel), $m_{v_y} = [-1, 1]$ (in millimeters per year per pixel), $m_{h_x} = 0$ (in meters per pixel), and $m_{h_y} = 0$ (in meters per pixel). (b) Periodogram ξ for $m_{v_x} = 0$ (in millimeters per year per pixel), $m_{v_y} = 0$ (in millimeters per year per pixel), $m_{h_x} = [-1, 1]$ (in meters per pixel), and $m_{h_y} = [-1, 1]$ (in meters per pixel).

homogenous patches at subobject resolution. Then, the local gradients of deformation velocity are integrated to obtain the deformation velocity for each DS pixel, as explained in the next section.

Practically, first, the phase values of each patch for every differential interferogram are corrected with respect to the patch's reference pixel so that the atmospheric effects and orbital errors are negligible. Second, these are then used for parameter estimation by adjusting to the data a phase model $\phi^{i,k}_{\text{model}}$, which is given as follows:

$$\phi^{i,k}_{\text{model}} = T^k m_{v_x} p^i_x + T^k m_{v_y} p^i_y + B^k m_{h_x} p^i_x + B^k m_{h_y} p^i_y \quad (7)$$

where $i = 1, \ldots, L$ (L being the number of homogenous pixels in the patch), $k = 1, \ldots, M$ (M being the number of interferograms), and p^i_x and p^i_y are pixel indices (related to the reference pixel indices) in range and azimuth directions, respectively, for homogenous pixel i. Since a DS pixel's phase quality is not on par with a PS, the phase model is not adjusted to the data pixelwise. Instead, all the homogenous pixels inside the DS object patch are simultaneously used for the model fitting by maximizing the following model coherence function (periodogram) ξ:

$$\xi\left(m_{v_x}, m_{v_y}, m_{h_x}, m_{h_y}\right) = \frac{1}{M}\sum_{k=1}^{M}\left(\frac{1}{L}\left|\sum_{i=1}^{L} e^{j\left(\phi^{i,k} - \phi^{\text{i,k}}_{\text{model}}\right)}\right|\right) \quad (8)$$

where $\phi^{i,k}$ is the single-look interferometric phase for homogenous pixel i and interferogram k calibrated with respect to the respective reference pixel, and $\phi^{i,k}_{\text{model}}$ is the phase model given by (7). Of course, the gradients of deformation velocity and the residual topography for each patch are estimated from the peak of this periodogram, i.e.,

$$\left(\hat{m}_{v_x}, \hat{m}_{v_y}, \hat{m}_{h_x}, \hat{m}_{h_y}\right) = \underset{m_{v_x}, m_{v_y}, m_{h_x}, m_{h_y}}{\arg\max}\ (\xi). \quad (9)$$

The maximum of ξ is the temporal coherence of the DS object. Note that usually it is not as good as the temporal coherence of a PS due to temporal decorrelation phenomenon. The range of the gradients of linear deformation and residual DEM, over which the maximum is searched, is based on prior knowledge. Usually, $m_v = [-1, 1]$ (in millimeters per year per pixel) and $m_h = [-1, 1]$ (in meters per pixel) is a suitable search range. The precision of the estimation depends upon the number of homogenous pixels and spatial extension of the patch, in addition to the average spatial coherence of the patch. Further on, the more the number of interferograms, the better is the estimation as the sidelobes (i.e., ambiguous solutions) are reduced and a clear peak is obtained. An illustration of the periodogram is provided in Fig. 2 using Lueneburg data set for a highly deforming patch. In addition, 89 small baseline differential interferograms were utilized for processing. A minimum patch size of 400 and an average spatial coherence threshold of 0.3 were set. A distinct peak is clearly noticeable. At this point, the algorithm has compensated residual DEM and the atmospheric phase screen. The gradients of deformation velocity have been estimated at subobject resolution using only small baseline differential interferograms.

C. Deformation Velocity Integration

Since the independent estimated neighboring patches are close and deformation velocity is assumed to vary smoothly in space, a 2-D deformation velocity integration can finally be performed to get the deformation velocity. A simple 1-D case is shown in Fig. 3. A 2-D model-based deformation integration proves useful as it is straightforward and easy to implement. Depending on the source of the subsidence, e.g., mining, oil/gas extraction, volcano, and earthquake, a suitable model can be adopted and its parameters estimated. The advantage here is that the estimated model parameters can be further used to assess and analyze the impacts of such geophysical phenomena.

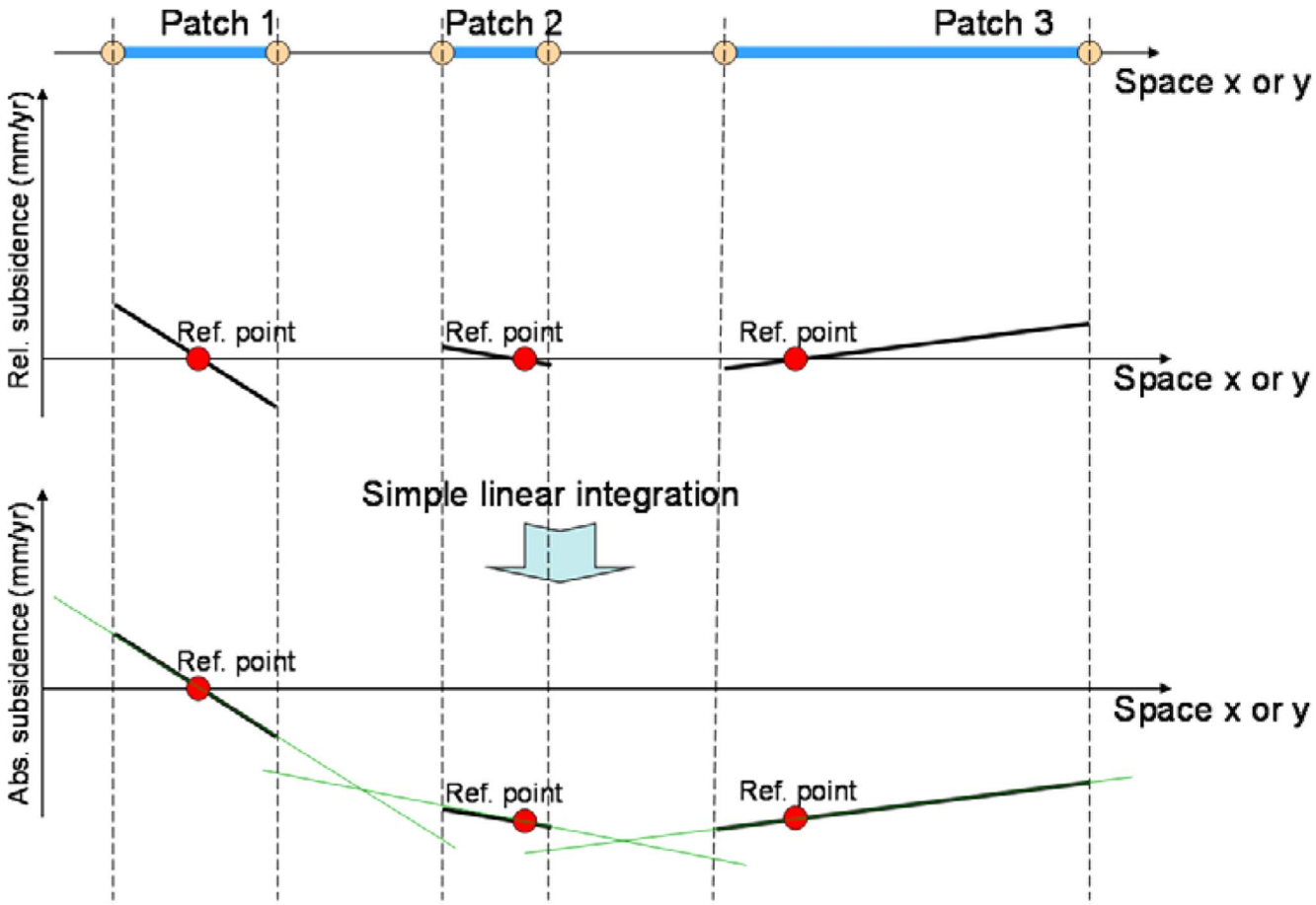

Fig. 3. Simple 1-D example of integrating the relative deformation of the various patches to get the integrated values.

Due to model-based deformation retrieval, the final resolution of deformation velocity is on the order of the dimensions of objects.

In our practical implementation, we have assumed an elliptical subsidence bowl for the test site Lueneburg, which has undergone salt-mining-induced subsidence. This is because the most common shape of surface deformation due to mining is a circular or elliptical sag [26]–[29]. A 2-D elliptical Gaussian deformation velocity field $g(x, y)$ (in millimeters per year) along the x- and y-directions is given by

$$g(x,y) = p \cdot e^{-\left(a(x-x_0)^2+2b(x-x_0)(y-y_0)+c(y-y_0)^2\right)} \tag{10}$$

where p is the height/depth of the peak/valley, and (x_0, y_0) is the center of the deformation trough. Coefficients a, b, and c are given as follows:

$$a = \frac{\cos^2\theta}{2\sigma_x^2} + \frac{\sin^2\theta}{2\sigma_y^2} \tag{11}$$

$$b = -\frac{\sin 2\theta}{4\sigma_x^2} + \frac{\sin 2\theta}{4\sigma_y^2} \tag{12}$$

$$c = \frac{\sin^2\theta}{2\sigma_x^2} + \frac{\cos^2\theta}{2\sigma_y^2} \tag{13}$$

where θ is the rotation of the ellipse from the x-axis in the clockwise direction, and σ_x and σ_y are the spreads in the x- and y-directions, respectively. The deformation model is shown in Fig. 4. For simplicity, it has been assumed that the vertical deformation derived from the model expresses surface subsidence along the satellite's LOS. Equation (10) allows the possibility to model an elliptical (or circular) subsidence bowl or even a nondeforming zone. The deformation integration is thus a model parameter estimation problem, wherein the 2-D Gaussian deformation field parameters p, x_0, y_0, θ, σ_x, and σ_y have to be estimated given the gradients of the deformation velocity $m^j_{v_x}$ and $m^j_{v_y}$ for the reference points x^j_{ref} and y^j_{ref}, respectively, corresponding to the P patches $j = 1, \ldots, P$.

It is important to note that nonlinear least squares curve fitting cannot be directly performed as the observations are the *gradients* of the deformation velocity in the range and azimuth directions. In fact, the model parameter estimation can be expressed as a multidimensional nonlinear optimization problem, where the sum of the absolute errors between the observed gradients of deformation velocity and the modeled gradients of deformation velocity has to be minimized. Conventional methods for multidimensional nonlinear minimization include Powell's conjugate gradient descent method [30], the downhill simplex method of Nelder and Mead [31], and the truncated Newton method by Stephen Nash [32]. However, most of these iterative methods need an initial starting point and find a local minimum of the function to be minimized and thus may not be robust for the deformation integration. In addition, many of

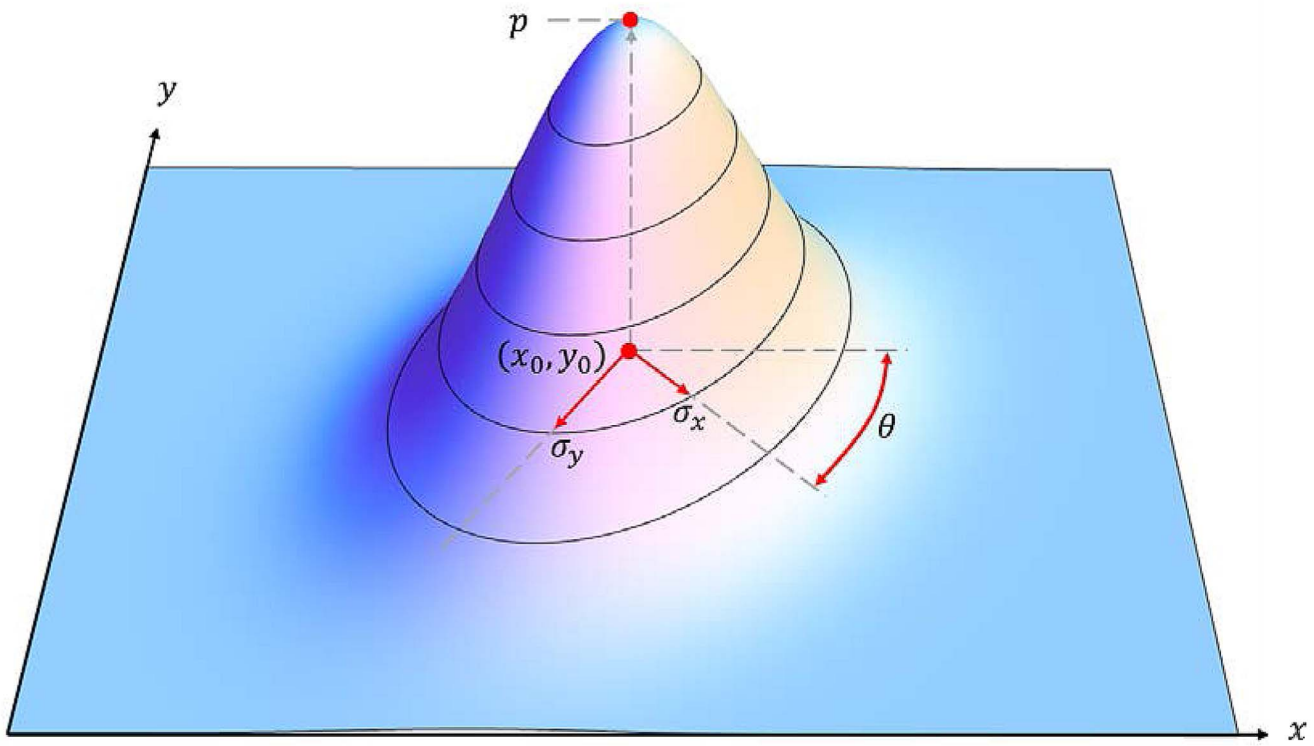

Fig. 4. Two-dimensional elliptical Gaussian deformation velocity model along the x (range)- and y (azimuth)-directions. It is defined by the parameters p, x_0, y_0, θ, σ_x, and σ_y. p is the height/depth of the peak/valley, (x_0, y_0) is the center of the deformation, θ is the rotation of the ellipse from the x-axis in the clockwise direction, and σ_x and σ_y are the spreads in the x- and y-directions, respectively.

these optimization algorithms require derivatives' evaluations, but the function to be minimized is not totally differentiable.

Instead, we have applied Bayesian inference for the multidimensional nonlinear regression [18], [19] by means of directed graphs and particle filters. It is a statistical approach in which all forms of uncertainty are expressed in terms of probability and parameter estimation is performed based on measured or empirical data. Bayesian inference has been successfully demonstrated for 3-D positioning of PSs based on radargrammetry [33].

We construct the directed graphical model (DGM) for deformation estimation, as shown in Fig. 5 [20]. DGMs reduce complex Bayesian inference computations into simple graph manipulations. The parameters that are either observed, known, or need to be estimated are considered as random variables (RVs) and represented by nodes. In our case, $m^j_{v_x}$ and $m^j_{v_y}$ are observed RVs and are consequently represented by blue nodes in Fig. 5. x^j_{ref} and y^j_{ref} are white nodes because they are known parameters, whereas p, x_0, y_0, θ, σ_x, and σ_y are gray nodes because they have to be estimated. $m^j_{v_x}$, $m^j_{v_y}$ and x^j_{ref}, y^j_{ref} are enclosed in a box that represents multiple nodes (i.e., a sequential estimation) for the P patches $j = 1, \ldots, P$. The directions of the arrows/arcs describe the dependence values between the RVs. For the patch j, the gradients of the deformation velocity $m^j_{v_x}$ and $m^j_{v_y}$ in the range and azimuth directions respectively depend on the 2-D Gaussian deformation velocity field parameters p, x_0, y_0, θ, σ_x, and σ_y, as well as on the location x^j_{ref} and y^j_{ref} of the reference point. The probabilistic relation between the RVs can be evaluated using the DGM (obtainable also from Bayes' theorem) in (14), shown at the bottom of the page, where l is the likelihood function given by

$$l = \prod_{j=1}^{P} f(m^j_{v_x}|p, x_0, y_0, \theta, \sigma_x, \sigma_y, x^j_{\text{ref}}, y^j_{\text{ref}}) \cdot \prod_{j=1}^{P} f(m^j_{v_y}|p, x_0, y_0, \theta, \sigma_x, \sigma_y, x^j_{\text{ref}}, y^j_{\text{ref}}). \quad (15)$$

In (14) above, the term on the left-hand side of the equation is the joint posterior probability density function (PDF) of the elliptical Gaussian model parameters p, x_0, y_0, θ, σ_x, and σ_y. The numerator on the right-hand side of

$$f(p, x_0, y_0, \theta, \sigma_x, \sigma_y | m^{1,\ldots,P}_{v_x}, m^{1,\ldots,P}_{v_y}, x^{1,\ldots,P}_{\text{ref}}, y^{1,\ldots,P}_{\text{ref}}) = \frac{l \cdot f(p) \cdot f(x_0) \cdot f(y_0) \cdot f(\theta) \cdot f(\sigma_x) \cdot f(\sigma_y)}{\int_{\sigma_y}\int_{\sigma_x}\int_{\theta}\int_{y_0}\int_{x_0}\int_{p} l \cdot f(p) \cdot f(x_0) \cdot f(y_0) \cdot f(\theta) \cdot f(\sigma_x) \cdot f(\sigma_y) \cdot dp \cdot dx_0 \cdot dy_0 \cdot d\theta \cdot d\sigma_x \cdot d\sigma_y} \quad (14)$$

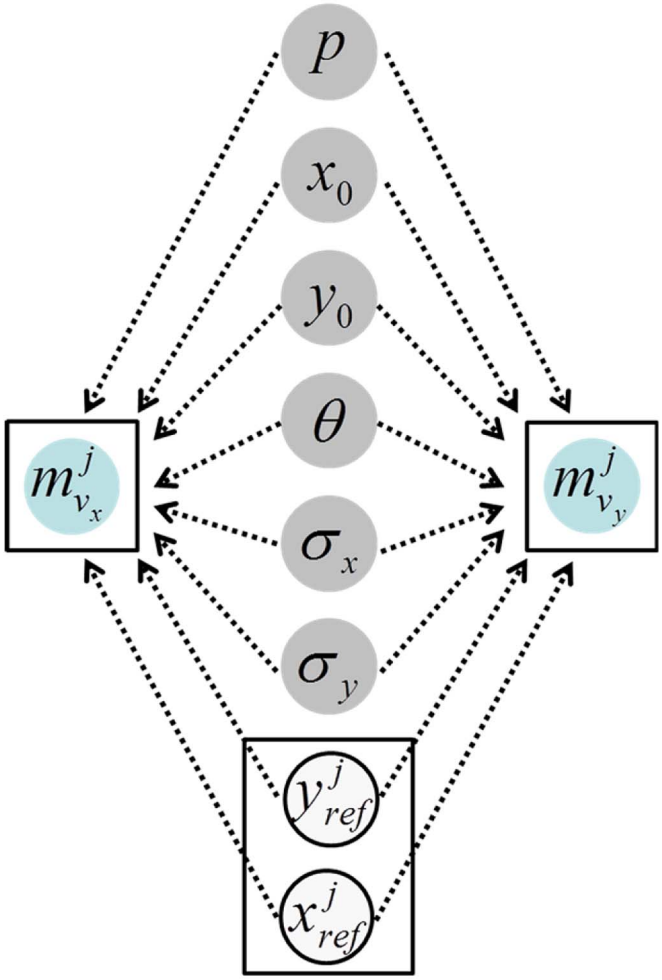

Fig. 5. DGM for the estimation of 2-D Gaussian deformation velocity field parameters. We have P patches denoted by $j = 1, \ldots, P$. For each patch j, the gradients of the deformation velocity $m^j_{v_x}$ and $m^j_{v_y}$ in the range and azimuth directions, respectively (known RVs, blue nodes) depend on the 2-D Gaussian deformation velocity field parameters p, x_0, y_0, θ, σ_x, and σ_y (RVs to be estimated, gray nodes) and also on the location x^j_{ref} and y^j_{ref} of the reference point (known RVs, white nodes) and, hence, the direction of the arrows/arcs. We enclose $m^j_{v_x}$, $m^j_{v_y}$, x^j_{ref}, and y^j_{ref} in the box, representing the multiple nodes for the P patches.

(14) is composed of the conditional PDFs or likelihood $f(m^j_v|p, x_0, y_0, \theta, \sigma_x, \sigma_y, x^j_{\mathrm{ref}}, y^j_{\mathrm{ref}})$ of the measured/observed gradients of the deformation velocity for the different patches and the prior PDFs $f(p)$, $f(x_0)$, $f(y_0)$, $f(\theta)$, $f(\sigma_x)$, and $f(\sigma_y)$ of the Gaussian model parameters. The conditional PDF or likelihood of an observed gradient m^j_v (in range or azimuth direction) of deformation velocity for a patch j is computed using the normalized absolute error between the observed gradient of deformation velocity and the modeled gradient of deformation velocity as follows:

$$f\left(m^j_v|p, x_0, y_0, \theta, \sigma_x, \sigma_y, x^j_{\mathrm{ref}}, y^j_{\mathrm{ref}}\right) = 1 - normalized\left(\left|m^j_v - m\_gauss^j_v\right|\right). \quad (16)$$

Here, $m\_gauss^j_v$ is the modeled gradient (in range or azimuth direction) of deformation velocity for the patch j; this is to say that it is calculated from the Gaussian model parameters p, x_0, y_0, θ, σ_x, and σ_y. The prior PDFs of the Gaussian model parameters depend upon the prior knowledge (e.g., they can be taken as a uniform distribution in a suitable range). The denominator on the right side of (14) is the evidence and can be neglected for the parameter estimation. It is only important if model selection has to be performed.

For the deformation estimation, the joint posterior PDF is computed and maximized to give us the parameter estimates p^{MAP}, x_0^{MAP}, y_0^{MAP}, θ^{MAP}, σ_x^{MAP}, and σ_y^{MAP}. This estimator is called the maximum *a posteriori* (MAP) estimator

$$\left(p^{\mathrm{MAP}}, x_0^{\mathrm{MAP}}, y_0^{\mathrm{MAP}}, \theta^{\mathrm{MAP}}, \sigma_x^{\mathrm{MAP}}, \sigma_y^{\mathrm{MAP}}\right) = \underset{p,x_0,y_0,\theta,\sigma_x,\sigma_y}{\arg\max} \left(f\left(p, x_0, y_0, \theta, \sigma_x, \sigma_y | m^{1,\ldots,P}_{v_x}, m^{1,\ldots,P}_{v_y}, x^{1,\ldots,P}_{\mathrm{ref}}, y^{1,\ldots,P}_{\mathrm{ref}}\right)\right). \quad (17)$$

Our applied framework employs bootstrap particle filtering (i.e., condensation algorithm) for the MAP parameter estimation [21], [22]. Particle filter is a sequential Monte Carlo technique for implementing recursive Bayesian filter using the concepts of importance sampling (and resampling). The basic idea is to represent the required distribution by a set of discrete N_P random particles (i.e., samples and weights associated to each sample), thus inherently dealing with complex multimodal/non-Gaussian PDFs, which are difficult to represent analytically. The MAP estimation via (17) is performed based on these particles. The assessment of the estimation quality is performed by computing the standard deviation of the estimated parameters by means of the posterior PDF. It is also possible to estimate more than one deformation bowls by dividing the SAR scene into smaller areas and performing the parameter estimation for these individually.

Note that, in case we have to optimally choose between different spatial models for the deformation, it can be easily done via Bayesian inference. A good model balances goodness of fit with simplicity. The model that best describes the Bayesian problem is the one that has the highest evidence. Following the basic concept of Monte Carlo integration, our practical implementation of Bayesian inference using particle filters can easily calculate the evidence by converting the integral into some kind of average of the discrete random particles.

To end with, the algorithm provides the deformation velocity at a resolution approximately in the scale of homogenous objects and that too, without any phase unwrapping in typically decorrelated areas. Due to model-based deformation integration, the deformation velocity for the whole subsidence bowl is estimated, including its center, as compared with conventional techniques such as PSI, SBAS, and SqueeSAR, which have a lesser number of estimated points.

III. Application Test Case and Results

A. Application Test Case

We provide practical demonstration of our technique using High Resolution Spotlight 300-MHz TerraSAR-X data of the town of Lueneburg, which is situated in the German state of

Fig. 6. Google Earth image of the test site Lueneburg in Germany (enclosed in red).

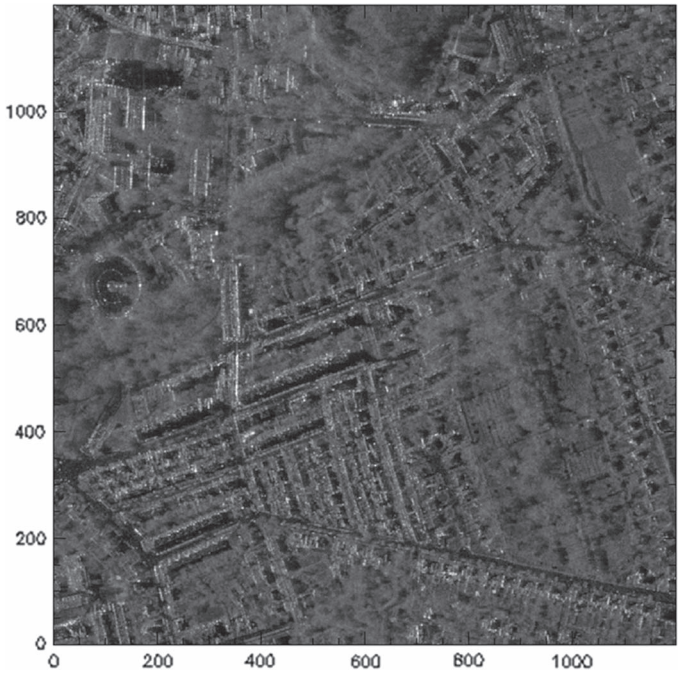

Fig. 7. TerraSAR-X mean amplitude image of the test site Lueneburg.

Lower Saxony. The old part of this town lies on a salt dome. As a result of constant salt mining dating back to the 19th century and continuing until 1980, various areas of the town experienced a gradual or high subsidence, became unstable, and had to be demolished. The sinking still continues even today. Many ground stations have been established since 1946 to monitor the deformation, but due to the changing subsidence patterns and locations, spaceborne differential SAR interferometric technique is better suited for deformation mapping of Lueneburg.

Since October 2010, stacks of the X-band SAR satellite TerraSAR-X have been ordered to monitor the subsidence. TerraSAR-X provides a resolution of 0.6 m in slant range direction and 1.1 m in azimuth direction in the High Resolution Spotlight mode, and even single buildings can be mapped from space. With a short repeat cycle of 11 days, stack of acquisitions can be acquired rapidly for time-series analysis. We have used 17 TerraSAR-X images of Lueneburg from October 2010 to September 2011 with a look angle of 29.6° and "HH" polarization to monitor the highly localized salt-mining-induced subsidence phenomenon. The pixel spacing is approximately 0.6 m in range direction and 0.58 m in azimuth direction (adapted to oversampling). In Fig. 6, we can see the Google Earth image of the test site. Fig. 7 shows its corresponding SAR mean amplitude image. Important to note is the presence of vegetated and low-reflectivity homogenous areas, due to which, the density of PSs is low.

The data set has been processed using our new technique. The stack of TerraSAR-X images was coregistered and calibrated. The calibration constants are provided with the L1b products; TerraSAR-X is a very stable precision instrument for radar imaging [34], [35]. We generated 89 differential interferograms based on a maximum spatial baseline of 150 m and a maximum temporal baseline of 150 days. As aforementioned, small baseline interferograms are used to limit the effects of topography on the DSs but, more importantly, to reduce the computational complexity. For coregistration and DInSAR processing, DLR's operational PSI-GENESIS processor was employed [36], [37]. The coregistration module of the processor uses a geometry-based algorithm, which utilizes precise orbits and a DEM from shuttle radar topography mission (SRTM). Fig. 8 shows the baseline time plot for the scenes and the interferograms. As can be noticed, we have a well-connected network because of short repeat cycle of TerraSAR-X and highly reproducible scene repetition of the spotlight acquisitions, consequently ensuring the temporal continuity of the deformation measurements. The coherence matrix of the data set is illustrated in Fig. 9. It demonstrates the combinations of acquisitions used (i.e., the interferograms), each of which is color coded according to its average spatial coherence. We can see that only small baseline combinations have been used for the processing. Moreover, the average coherence of this region can be observed as low, typical for rural areas, thus advocating the need for DSI.

B. Results

The identification of homogenous patches for Lueneburg using the 17 TerraSAR-X amplitude images is shown in Fig. 10. The region was divided into rectangular blocks of 40 pixels $\times$ 40 pixels, i.e., 24 m $\times$ 24 m approximately. Within each block, homogenous pixels were identified by means of the AD statistical test based on a minimum patch size of 400 pixels and a coherence threshold of 0.3.

Fig. 11 visualizes the gradient estimation results for the residual DEM in the range and azimuth directions in meters per pixel for the test site. Estimation of residual DEM gradients

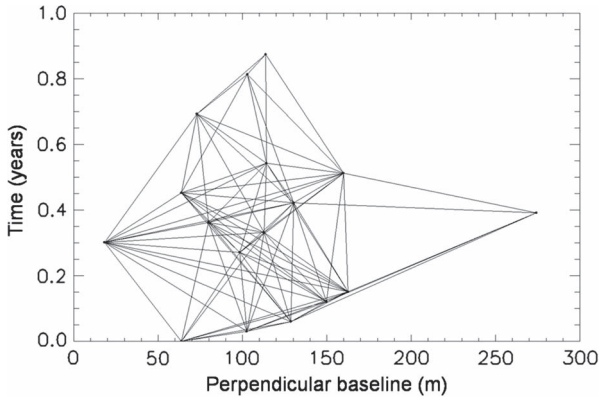

Fig. 8. Baseline-time plot of the TerraSAR-X data set of Lueneburg. Each dot represents a SAR image, and each line represents an interferogram.

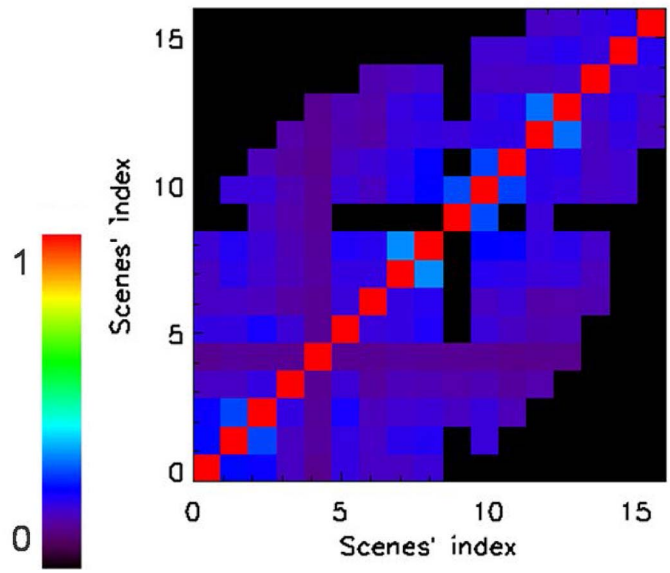

Fig. 9. Coherence matrix of the TerraSAR-X data set of Lueneburg. It depicts the average spatial coherence of the small baseline differential interferograms used in the processing.

is essential for an accurate estimation of deformation velocity gradients. Fig. 12 visualizes the gradient estimation results for the deformation velocity in the range and azimuth directions in millimeters per year per pixel. The number of homogenous pixels and temporal coherence (i.e., peaks of the periodograms) for the patches are illustrated in Fig. 13. The gradients have been estimated for a total of 536 456 points in an area of 1200 pixels $\times$ 1200 pixels.

The deformation integration results using our technique, i.e., DSI, are presented in Fig. 14. The scene was divided into nine equal areas of 400 pixels $\times$ 400 pixels each, and deformation integration was independently performed for these, wherein ten million particles were used for representing the posterior distribution in (14). The results obtained for surface deformation velocity show two Gaussian subsidence bowls, one having a larger deformation than the other and also covering a larger area. The Gaussian subsidence bowls with spreads smaller than a certain threshold (i.e., 20 pixels) were not taken into account. This is because, practically, at least three patches need to be fed into the integration model for an elliptical Gaussian subsidence (it has six parameters). Other types of deformation, e.g., structural stress of buildings, can spatially be fully described by two parameters only, i.e., a single homogeneous patch is sufficient for the deformation estimation.

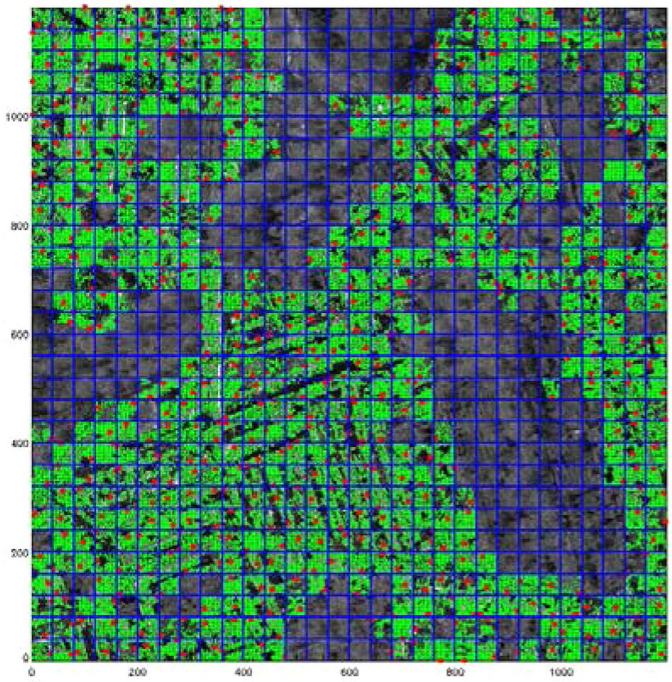

Fig. 10. Identification of homogenous patches for Lueneburg using 17 TerraSAR-X amplitude images via AD test. The region is divided into blocks by the blue lines, where the points in green represent the homogenous pixels and the points in red represent the reference pixels.

The data set was also processed using another technique, i.e., the high-resolution advanced SBAS technique, which was briefly explained in Section I [10]. It makes use of small baseline differential interferograms and incorporates an object adaptive spatial phase filtering and residual topography removal for an accurate phase and coherence estimation while preserving the object resolution. This is followed by retrieval of deformation via the SBAS approach, wherein the phase inversion is performed using an $L1$-norm minimization, which is more robust to the typical phase unwrapping errors encountered in nonurban areas. Again, the 17 TerraSAR-X images and the 89 small baseline differential interferograms were utilized to obtain the deformation time series for Lueneburg. We used pixels that have an average spatial coherence of at least 0.3 (i.e., 121 024 points in an area of 1200 pixels $\times$ 1200 pixels). The mean deformation velocities estimated using this SBAS technique are presented in Fig. 15. The high density of information that can be extracted using our DSI technique can be seen by comparing Fig. 15 with Fig. 12 (which has 536 456 estimated points).

The features that have been identified as deforming in Fig. 15 are also deforming in Fig. 14. The DSI approach, significantly, provides spatially dense deformation velocity estimates instead of just a few measured points using advanced SBAS. The main reason is that the model-based gradient inversion is advantageous compared with phase unwrapping in such areas as the volume of the deformation model is known. It is thus possible to better define the areas that are subsiding and also even identify new ones not previously detected using conventional techniques in nonurban areas.

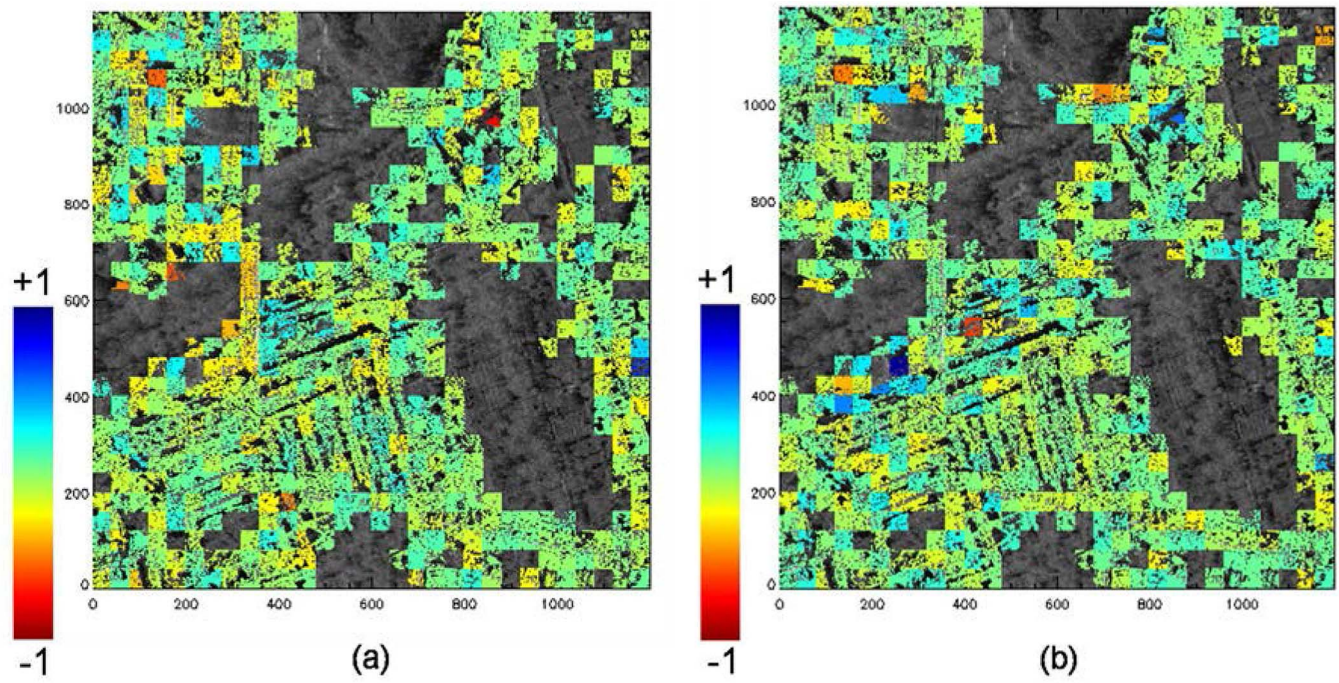

Fig. 11. Residual DEM gradient estimation results for Lueneburg using 89 small baseline differential interferograms. (a) Local gradients of residual DEM in the range x-direction in meters per pixel. (b) Local gradients of residual DEM in the azimuth y-direction in meters per pixel.

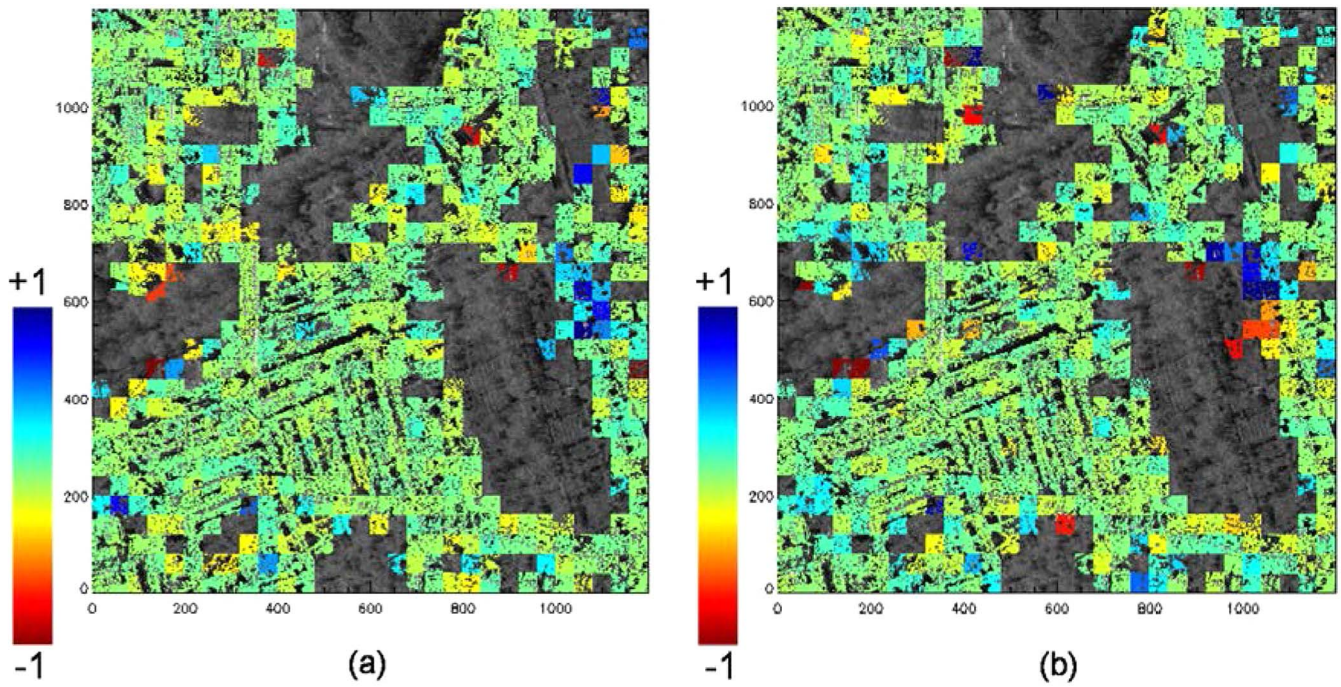

Fig. 12. Deformation gradient estimation results for Lueneburg using 89 small baseline differential interferograms. (a) Local gradients of deformation velocity in the range x-direction in millimeters per year per pixel. (b) Local gradients of deformation velocity in the azimuth y-direction in meters per pixel.

Deformation time series are visualized in Fig. 16 for some of the pixels marked in Fig. 15. We have compared the time series using advanced SBAS and DSI (assuming a constant velocity model). The estimated mean deformation velocities using DSI show a good fit to the nonlinear deformation time series measured using SBAS.

The density histograms of the mean deformation velocity estimates utilizing the two techniques are shown in Fig. 17. What can be seen is the advantage provided by DSI, which measures even the points with highest subsidence (i.e., centers of subsidence bowls), which are not measured by advanced SBAS due to high temporal decorrelation. It also shows that the points, where the subsidence has not been detected using DSI, have zero deformation velocities. This of course does not mean that there is no deformation outside the identified subsidence bowls. It just shows the absence of motion

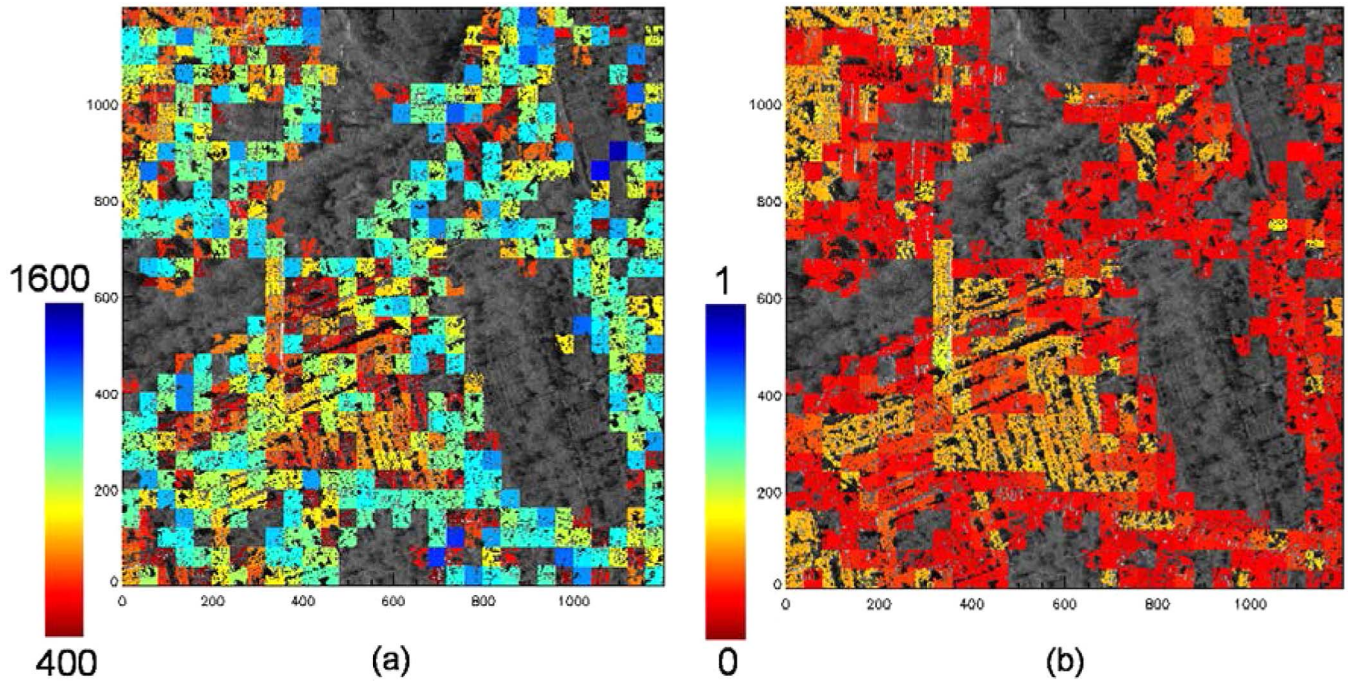

Fig. 13. (a) Number of homogenous pixels for the patches of Lueneburg. (b) Temporal coherence (i.e., peaks of the periodograms) for the patches.

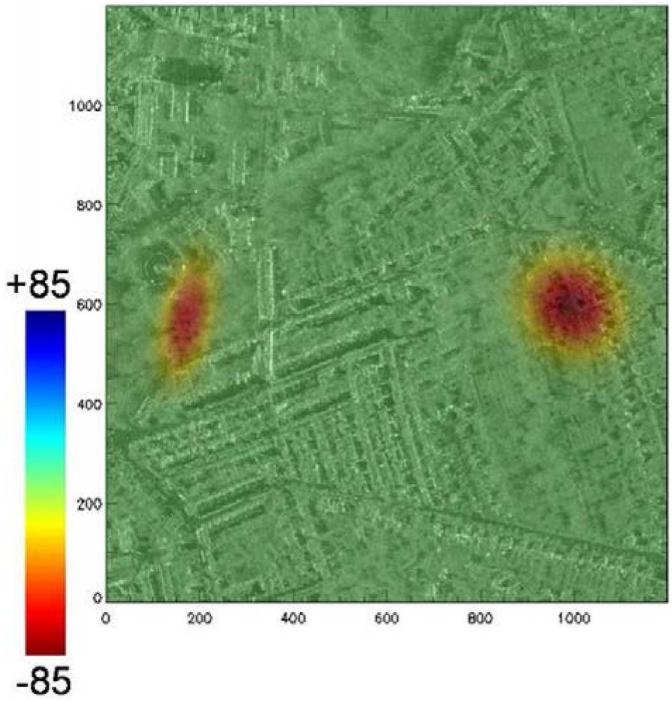

Fig. 14. Deformation velocity in mm/year estimated for Lueneburg using the new DSI technique.

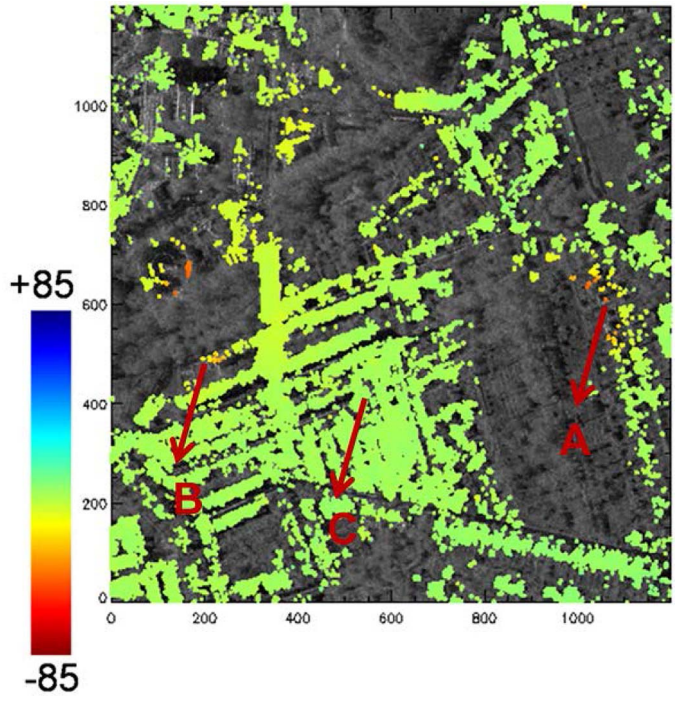

Fig. 15. Deformation velocity in mm/year estimated for Lueneburg using the high-resolution advanced SBAS technique [10]. Deformation time-series comparison for points A, B, and C using advanced SBAS and DSI is shown in Fig. 16.

patterns that follow the Gaussian elliptical deformation velocity model.

Additionally, we have collected ground truth for Lueneburg. Fig. 18 shows the pictures of the area of the bigger subsidence bowl in Lueneburg, "Ochtmisser Kirchsteig," which has been detected using our technique (i.e., the region surrounding point A marked in Fig. 15). The effects of subsidence are encircled in yellow. Fig. 19 shows the picture of the area of the smaller subsidence bowl in Lueneburg, "Frommestrasse," which has been detected (i.e., the region surrounding point B marked in Fig. 15). We can see that both these regions have undergone high subsidence (and have suffered considerable damage), as measured by our technique too.

We have also calculated the standard deviation of the estimated parameters from the posterior PDF. It provides information about the precision of estimation. The standard deviation values for p^{MAP}, x_0^{MAP}, y_0^{MAP}, θ^{MAP}, σ_x^{MAP}, and σ_y^{MAP} are on the order of 0.37 mm/year, 5.96 pixels, 5.96 pixels,

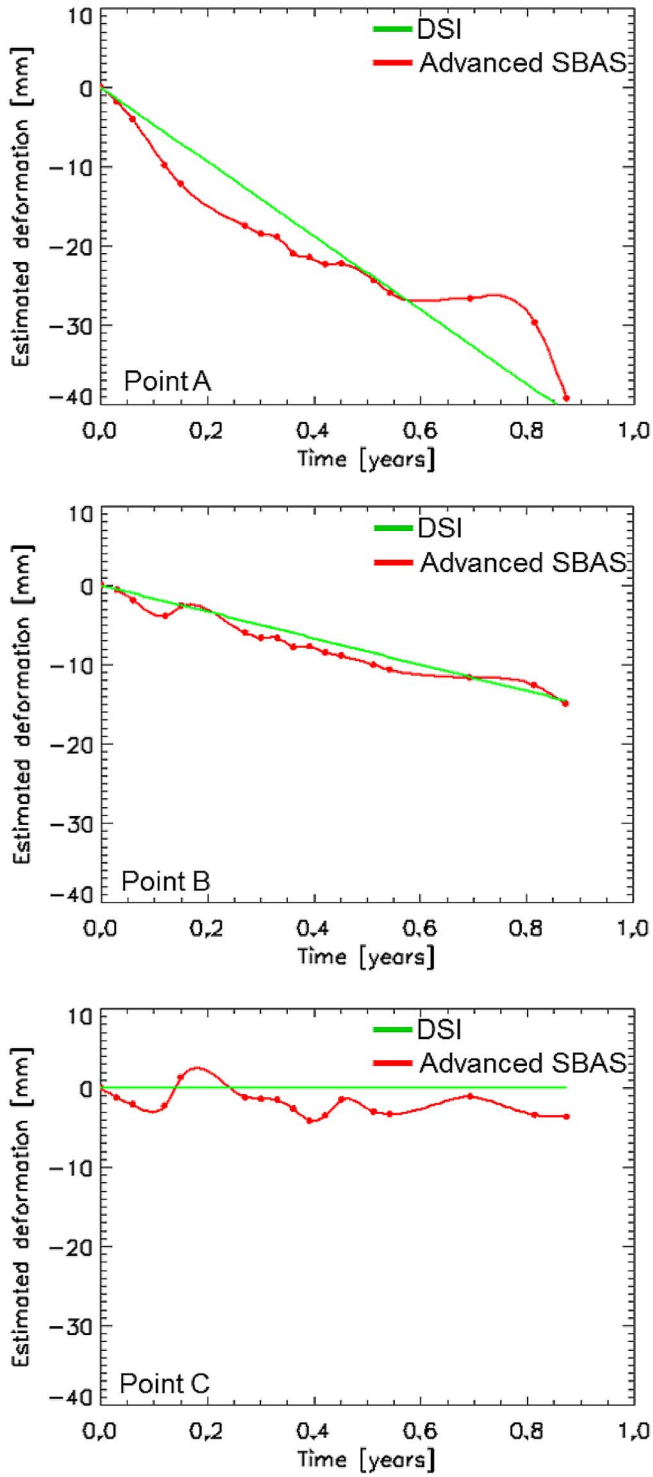

Fig. 16. Deformation time-series comparison for points A, B, and C in Lueneburg marked in Fig. 15 using DSI (assuming a constant velocity model) and advanced SBAS.

0.01 rad, 1.28 pixels, and 1.28 pixels, respectively. Evidently, the precision of this technique is good for high-resolution sensors such as TerraSAR-X.

IV. Discussion

The results demonstrate the potential of this new technique for providing the deformation velocity and parametric modeling of the deformation bowls at a suitable resolution in highly decorrelated areas utilizing DSs. We make a first-order approximation that the deformation velocities and residual topographies of the homogenous pixels show a linear spatial behavior in the range and azimuth directions, respectively, with respect to the reference pixel.

Essentially, this assumption is true for deformation as long as it is not varying spatially faster in comparison to the pixel size (otherwise, a higher SAR resolution would be beneficial), and moreover, it is also based on the sensor characteristics. In other words, the maximum deformation gradient, which is measurable in an interferogram, is determined by the signal wavelength and pixel spacing [38]. However, this is only valid under an ideal condition that there is no noise in the SAR observations. Phase noise due to uncompensated geometrical decorrelation, temporal decorrelation, thermal noise, atmospheric effects, etc., can significantly affect the detectable deformation gradients. As a result, very small and large deformation gradients become undetectable if the level of noise is too high. In [39], a new functional model has been proposed for the maximum and also for the minimum detectable deformation gradients in an interferogram, taking into account the interferometric coherence, which is a measure of the interferometric SNR, thus making the models more realistic. This way of modeling the spatial behavior of surface deformation (assuming that it linearly changes over short distances) is particularly valid for natural terrains, where most surface deformation signals are smooth.

With regard to topography, the aforementioned assumption is a typical attribute of statistically homogenous pixels since radar brightness is strongly dependent on the orientation and slope of a resolution cell. Explicitly, only those pixels would be selected as homogenous, which exhibit a smoothly varying topography. Thus, the identification of homogenous patches is crucial. Again, in natural areas, the topography is mostly smooth.

Given that the above conditions are satisfied, our technique estimates the deformation velocity at a suitable object resolution. This is advantageous in contrast to conventional SBAS, which estimates the deformation at a low resolution and, moreover, does not provide the deformation at points that have undergone high temporal decorrelation. More points are estimated using our technique because no phase unwrapping is required. However, it is worth mentioning that SBAS estimates the nonlinear deformation times series, whereas our technique is concentrated on providing the mean deformation velocity. This is the reason that SBAS requires phase unwrapping operations, which might be difficult in such sparsely urbanized areas. With respect to SqueeSAR, the computational complexity is greatly reduced since only the small baseline differential interferograms are used. With regard to conventional SBAS, our method is computationally costly in identification of homogenous patches and the gradient estimation, whereas SBAS is computationally expensive in phase unwrapping.

The precision of the estimates is quite good for high-resolution satellites, e.g., TerraSAR-X. This method is more appropriate for high-resolution sensors. For conventional sensors, e.g., ERS, the homogenous objects need a large dimension, and thus, the applicability of the method is test site dependent. It

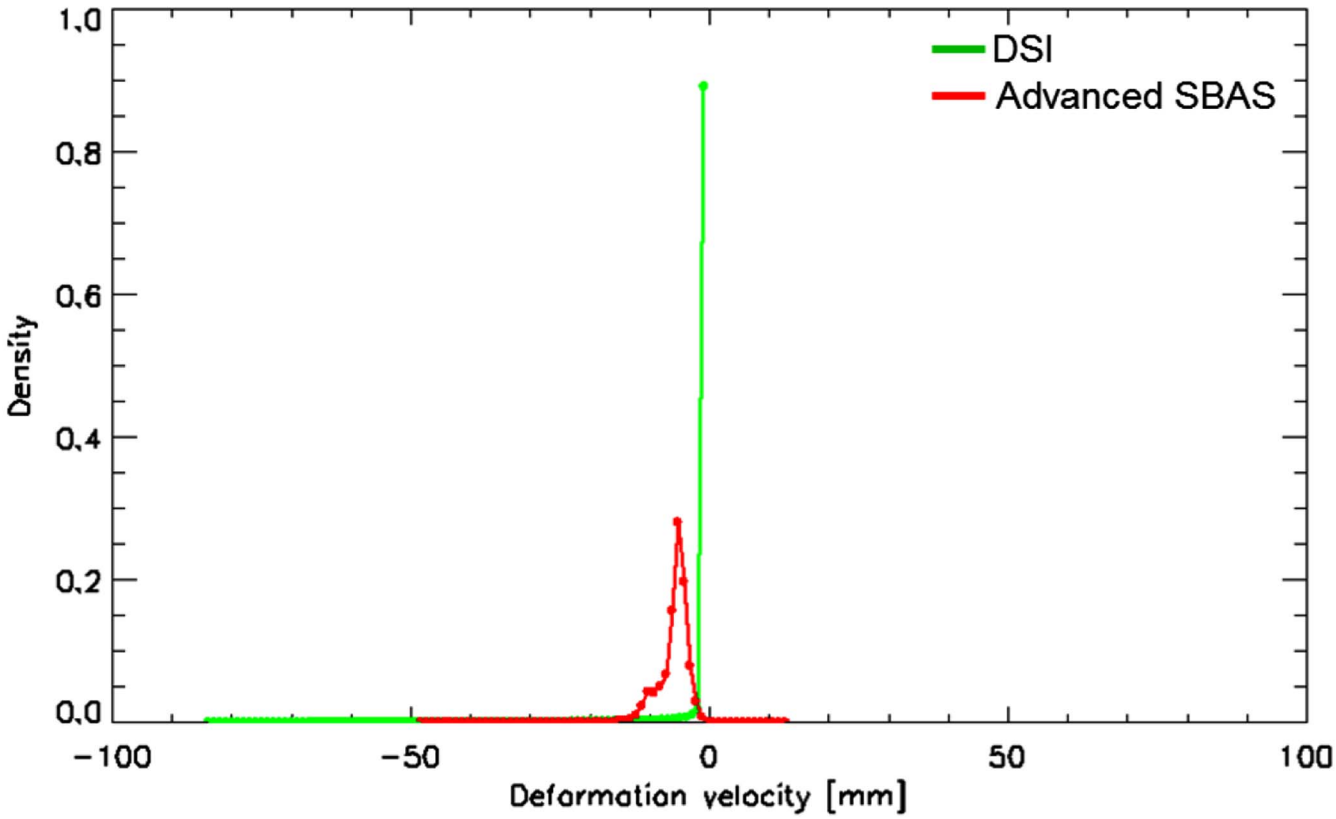

Fig. 17. Density histograms of the mean deformation velocity estimates for Lueneburg utilizing DSI and advanced SBAS.

Fig. 18. Pictures of the area of the bigger subsidence bowl in Lueneburg, "Ochtmisser Kirchsteig," which has been detected using DSI (i.e., the region surrounding point A marked in Fig. 15).

is to be noted that a minimum number of scenes are required for the detection of homogenous patches. The precision of the gradient estimation depends upon the number of homogenous pixels and spatial extension of the patch, number of interferograms, and also the average coherence of the patch. The following aspects need to be taken into consideration.

Fig. 19. Picture of the area of the smaller subsidence bowl in Lueneburg, "Frommestrasse," which has been detected using DSI (i.e., the region surrounding point B marked in Fig. 15).

We have used single-look differential interferograms for processing. Multilooked interferograms generally should not be used since the basis of this technique is using homogenous pixels for the estimation. Anyhow, conventional rectangular multilooking can work if homogenous areas are larger, and we restrict the multilooking and subsequent estimation to small fixed averaging areas. Adaptive multilooking [10], [17] is better as larger patches are possible (if the test site allows) and it leads to a better precision. However, multilooking/averaging can lead to smoothing of the deformation estimates. In addition, we have used nonoverlapping blocks for the identification of homogenous patches. Overlapping blocks can be considered also in the future to increase the resolution.

The smallest deformation pattern that can be measured depends on the type of subsidence effect and the resolution of the sensor. For example, as aforementioned in this section, if elliptical Gaussian subsidence occurs, the minimum size of the bowl should be at least three patches. Anyhow, usually, such a bowl has a larger dimension than this. In case of deformation due to structural stress of buildings or thermal dilation of bridges, even a single patch is enough.

For our test site in Lueneburg, which had been a salt mine, an elliptical subsidence has occurred. Subsidence bowls over mines usually occur when the overburden sags downward due to failure of mine pillars. It results in a depression in the ground, which is usually elliptical or circular in shape. The subsidence is nearly temporally linear and is normally greatest at the center of the bowl and progressively decreases until the boundaries of the impacted surface area are reached. Note that we can assume any appropriate model and estimate its parameters in the same way using Bayesian inference, as described for the elliptical trough (just the number of unknowns should be less than or equal to the number of observations). For instance, sinkhole subsidence can instead occur in areas lying above underground mines, which are located very close to the ground surface. This type of subsidence is pretty localized in extent and causes an abrupt depression of the ground surface as overburden material collapses into the mine. In addition, Bayesian inference also facilitates model selection for choosing the best model from different deformation models. We would like to remark that our approach is suitable to be applied to such phenomena as mining-induced surface deformation and similar geological effects, which can be described by an appropriate model.

This paper, in fact, is a "principle demonstration" of a new technique that avoids the necessity of phase unwrapping, which is often an issue with DInSAR time-series analysis. The current limitation of this technique is the model-based implementation, which requires the surface deformation pattern to be known before starting the data analysis. In the future, more advanced integration methods can be model free, thus making this DSI approach more general.

V. Conclusion

A novel concept has been developed for a robust deformation velocity mapping and parametric modeling in highly decorrelated regions, at a suitable object resolution without any phase unwrapping. The increased density and quality of the deformation estimates is the clear advantage. This new DSI technique is based on an object adaptive parameter estimation that makes use of the high resolution provided by modern sensors. Only the small baseline differential interferograms are utilized in order to reduce the computational burden. The algorithm compensates the DEM errors and atmosphere. The technique's application using High Resolution Spotlight 300-MHz TerraSAR-X data of Lueneburg in Germany demonstrates its high potential.

This technique can benefit from better prior information, e.g., the suitable deformation integration model to be applied and from future SAR systems with 600-MHz chirp bandwidth. Future work can concentrate on integrating the topography gradients and correcting the exploited DEM. Note that this requires a non-model-based approach since, usually, the residual DEM cannot be modeled. Afterward, nonlinear surface displacements, as well as the atmosphere, can be estimated from the residual phase by taking into account their different frequency characteristics in space and time. More importantly, non-model-based deformation velocity integration would be the upcoming focus.

Acknowledgment

The authors thank Prof. Dr. R. Bamler and the anonymous reviewers for the constructive suggestions that greatly helped to improve this paper.

References

[1] R. Bamler and P. Hartl, "Synthetic aperture radar interferometry—Topical review," in *Inverse Problems 14*. Bristol, U.K.: IOP Publishing Limited, 1998, pp. R1–R54.

[2] P. A. Rosen, S. Hensley, I. R. Joughin, F. K. Li, S. N. Madsen, E. Rodriguez, and R. M. Goldstein, "Synthetic aperture radar interferometry," *Proc. IEEE*, vol. 88, no. 3, pp. 333–382, Mar. 2000.

[3] A. Ferretti, C. Prati, and F. Rocca, "Permanent scatterers in SAR interferometry," *IEEE Trans. Geosci. Remote Sens.*, vol. 39, no. 1, pp. 8–20, Jan. 2001.

[4] A. Ferretti, C. Prati, and F. Rocca, "Nonlinear subsidence rate estimation using permanent scatterers in differential SAR interferometry,"

IEEE Trans. Geosci. Remote Sens., vol. 38, no. 5, pp. 2202–2212, Sep. 2000.
[5] J. W. Goodman, "Some fundamental properties of speckle," *J. Opt. Soc. Amer. A*, vol. 66, no. 11, pp. 1145–1150, Nov. 1976.
[6] P. Berardino, G. Fornaro, R. Lanari, and E. Sansosti, "A new algorithm for surface deformation monitoring based on small baseline differential SAR interferograms," *IEEE Trans. Geosci. Remote Sens.*, vol. 40, no. 11, pp. 2375–2383, Nov. 2002.
[7] H. A. Zebker and J. Villasenor, "Decorrelation in interferometric radar echoes," *IEEE Trans. Geosci. Remote Sens.*, vol. 30, no. 5, pp. 950–959, Sep. 1992.
[8] G. Golub and C. Loan, *Matrix Computations*, 3rd ed. Baltimore, MD, USA: The Johns Hopkins Univ. Press, 1996.
[9] R. Lanari, O. Mora, M. Manunta, J. J. Mallorquí, P. Berardino, and E. Sansosti, "A small baseline approach for investigating deformations on full resolution differential SAR interferograms," *IEEE Trans. Geosci. Remote Sens.*, vol. 42, no. 7, pp. 1377–1386, Jul. 2004.
[10] K. Goel and N. Adam, "An advanced algorithm for deformation estimation in non-urban areas," *ISPRS J. Photogramm. Remote Sens.*, vol. 73, pp. 100–110, Sep. 2012.
[11] M. Constantini, "A novel phase unwrapping method based on network programming," *IEEE Trans. Geosci. Remote Sens.*, vol. 36, no. 3, pp. 813–821, May 1998.
[12] M. Eineder, M. Hubig, and B. Milcke, "Unwrapping large interferograms using the minimum cost flow algorithm," in *Proc. IGARSS*, Seattle, WA, US, 1998, pp. 83–87.
[13] A. Pepe and R. Lanari, "On the extension of the minimum cost flow algorithm for phase unwrapping of multitemporal differential SAR interferograms," *IEEE Trans. Geosci. Remote Sens.*, vol. 44, no. 9, pp. 2374–2383, Sep. 2006.
[14] G. Fornaro, A. Pauciullo, and D. Reale, "A null-space method for the phase unwrapping of multi-temporal SAR interferometric stacks," *IEEE Trans. Geosci. Remote Sens.*, vol. 49, no. 6, pp. 2323–2334, Jun. 2011.
[15] A. Ferretti, A. Fumagalli, F. Novali, C. Prati, F. Rocca, and A. Rucci, "A new algorithm for processing interferometric data-stacks: SqueeSAR," *IEEE Trans. Geosci. Remote Sens.*, vol. 49, no. 9, pp. 3460–3470, Sep. 2011.
[16] Y. Wang, X. X. Zhu, and R. Bamler, "Retrieval of phase history parameters from distributed scatterers in urban areas using very high resolution SAR data," *ISPRS J. Photogramm. Remote Sens.*, vol. 73, pp. 89–99, Sep. 2012.
[17] A. Parizzi and R. Brcic, "Adaptive InSAR stacks multilooking exploiting amplitude statistics: A comparison between different techniques and practical results," *IEEE Geosci. Remote Sens. Lett.*, vol. 8, no. 3, pp. 89–99, May 2011.
[18] A. Papoulis and S. U. Pillai, *Probability, Random Variables, and Stochastic Processes*, 4th ed. New York, NY, USA: McGraw-Hill, 2002.
[19] D. S. Sivia, *Data Analysis: A Bayesian Tutorial*. New York, NY, USA: Oxford Univ. Press, 1996.
[20] C. M. Bishop, *Pattern Recognition and Machine Learning*. New York, NY, USA: Springer-Verlag, 2006.
[21] M. Isard and A. Blake, "Condensation—Conditional density propagation for visual tracking," *Intl. J. Comput. Vis.*, vol. 29, no. 1, pp. 5–28, Aug. 1998.
[22] S. Arulampalam, S. Maskell, N. Gordon, and T. Clapp, "A tutorial on particle filters for on-line non-linear/non-Gaussian Bayesian tracking," *IEEE Trans. Signal Process.*, vol. 50, no. 2, pp. 174–188, Feb. 2002.
[23] A. N. Pettitt, "A two-sample Anderson–Darling rank statistic," *Biometrika*, vol. 63, no. 1, pp. 161–168, Apr. 1976.
[24] R. Hanssen, *Atmospheric Heterogeneities in ERS Tandem SAR Interferometry*. Delft, The Netherlands: Delft Univ. Press, 1998.
[25] R. Hanssen, *Radar Interferometry*. Amsterdam, The Netherlands: Kluwer, 2001.
[26] V. Spreckels, "Monitoring of coal mining subsidence by HRSC-A data," in *Proc. ISPRS*, Amsterdam, The Netherlands, 2000, vol. XXXIII, pp. 1452–1458, [CD-ROM].
[27] D. Raucoules, C. Maisons, C. Carnec, S. Le Mouelic, C. King, and S. Hosford, "Monitoring of slow ground deformation by ERS radar interferometry on the Vauvert salt mine (France): Comparison with ground-based measurement," *Remote Sens. Environ.*, vol. 88, no. 4, pp. 468–478, Dec. 2003.
[28] F. J. van Leijen and R. F. Hanssen, "Persistent scatterer density improvement using adaptive deformation models," in *Proc. IGARSS*, Barcelona, Spain, 2007, pp. 2102–2105.
[29] Z. Perski, R. Hanssen, A. Wojcik, and T. Wojciechowski, "InSAR analyses of terrain deformation near the Wieliczka Salt Mine, Poland," *Eng. Geol.*, vol. 106, no. 1/2, pp. 58–67, May 2009.
[30] M. J. D. Powell, "An efficient method for finding the minimum of a function of several variables without calculating derivatives," *Comput. J.*, vol. 7, no. 2, pp. 155–162, 1964.
[31] J. Nelder and R. Mead, "A simplex method for function minimization," *Comput. J.*, vol. 7, no. 4, pp. 308–313, 1965.
[32] S. G. Nash, "Truncated-Newton methods," Ph.D. dissertation, Dept. Computer Science, Stanford Univ., Stanford, CA, USA, 1982.
[33] K. Goel and N. Adam, "Three-dimensional positioning of point scatterers based on radargrammetry," *IEEE Trans. Geosci. Remote Sens.*, vol. 50, no. 6, pp. 2355–2363, Jun. 2012.
[34] M. Schwerdt, B. Bräutigam, M. Bachmann, B. Döring, D. Schrank, and J. H. Gonzalez, "Final TerraSAR-X calibration results based on novel efficient methods," *IEEE Trans. Geosci. Remote Sens.*, vol. 48, no. 2, pp. 677–689, Feb. 2010.
[35] S. Buckreuss, R. Werninghaus, and W. Pitz, "The German satellite mission TerraSAR-X," *IEEE Aerosp. Electron. Syst. Mag.*, vol. 24, no. 11, pp. 4–9, Nov. 2009.
[36] N. Adam, B. Kampes, M. Eineder, J. Worawattanamateekul, and M. Kircher, "The development of a scientific permanent scatterer system," presented at the ISPRS Hannover Workshop, Inst. Photogramm. Geoinf., Hannover, Germany, 2003.
[37] N. Adam, B. Kampes, and M. Eineder, "Development of a scientific permanent scatterer system: Modifications for mixed ERS/ENVISAT time series," in *Proc. ESA Spec. Publ.*, 2005, pp. 457–465, ESA SP-572.
[38] D. Massonnet and K. L. Feigl, "Radar interferometry and its application to changes in the earth's surface," *Rev. Geophys.*, vol. 36, no. 4, pp. 441–500, Nov. 1998.
[39] I. Baran, M. Stewart, and S. Claessens, "A new functional model for determining minimum and maximum detectable deformation gradient resolved by satellite radar interferometry," *IEEE Trans. Geosci. Remote Sens.*, vol. 43, no. 4, pp. 675–682, Apr. 2005.

Kanika Goel received the B.E. degree in electronics and communications engineering from Manipal Institute of Technology, Manipal, India, in 2006 and the M.Sc. degree in Earth-oriented space science and technology (ESPACE) from the Technical University of Munich, Munich, Germany, in 2009. Since 2010, she has been working toward the Ph.D. degree in the Remote Sensing Technology Institute (IMF), German Aerospace Center (DLR), Wessling, Germany, in the field of advanced high-resolution SAR interferometric stacking techniques.

Since April 2013, she has been a Full-Time Scientific Researcher with IMF. Her main research interests include signal processing with applications to spaceborne SAR data processing, radargrammetry, interferometry, and differential interferometry.

Nico Adam received the Diploma degree in electrical engineering and telecommunication science from the University of Rostock, Rostock, Germany, in 1995.

Since 1995, he has been with the Remote Sensing Technology Institute, German Aerospace Center (DLR), Wessling, Germany, where he leads the SAR Interferometry Team at DLR's Remote Sensing Technology Institute. His research interests include signal and image processing in the persistent scatterer interferometry framework and the development of algorithms and software for advanced remote sensing radar systems.

A.4 Goel, K., Adam, N., 2013b. Fusion of monostatic/bistatic InSAR stacks for urban area analysis via distributed scatterers. IEEE Geoscience and Remote Sensing Letters PP (99), 1-5, DOI: 10.1109/LGRS.2013.2278204.

Fusion of Monostatic/Bistatic InSAR Stacks for Urban Area Analysis via Distributed Scatterers

Kanika Goel and Nico Adam

***Abstract*—Interferometric synthetic aperture radar (SAR) is a powerful technique providing meter-precision elevation maps and millimeter-precision surface displacement maps. Since 2007, the high-resolution SAR satellite TerraSAR-X allows monitoring of even single buildings from space using advanced monostatic repeat-pass stacking techniques. Furthermore, the launch of its twin satellite TanDEM-X in 2010 facilitates bistatic single-pass SAR interferometry. The main objective of this mission is the generation of a global digital elevation model. It also provides a configurable SAR platform for demonstrating new interferometric techniques and applications. However, in dense urban areas, standard TanDEM-X elevation models are inaccurate because ambiguities in radar layover areas cannot be solved. This letter describes the potential of joint monostatic and bistatic (motion-free and atmosphere-free) SAR interferometric stacking for an improved scene elevation and surface deformation estimation in complex urban areas. It involves exploiting distributed scatterers (DSs) using an advanced high-resolution small-baseline subset algorithm. Since most of the scatterers within a radar image can be classified as DSs, there is an increasing focus on an optimal processing of DSs for urban area monitoring. The fusion technique and an application test case are presented using a high-resolution spotlight mixed TerraSAR-X/TanDEM-X data stack of Las Vegas, USA.**

***Index Terms*—Digital elevation model (DEM), distributed scatterer (DS), interferometric synthetic aperture radar (SAR) (InSAR), TanDEM-X, TerraSAR-X, urban area monitoring.**

I. Introduction

THE NEW generation of high-resolution X-band synthetic aperture radar (SAR) sensors such as TerraSAR-X and COSMO-SkyMed is providing imagery with unique characteristics, enabling multitemporal interferometric SAR (InSAR) for 3-D mapping and deformation monitoring. In urban areas, these data facilitate monostatic repeat-pass interferometry [1] and allow analysis of individual structures on the ground with a high level of detail [2]. With the launch of the TanDEM-X satellite, high-resolution bistatic single-pass interferometry is now possible in conjunction with TerraSAR-X [3]. TanDEM-X allows the acquisition of highly accurate bistatic across-track interferograms which are free from motion, atmospheric disturbances, and temporal decorrelation. Thus, adding a few bistatic data pairs to the existing monostatic data stack can be used for an improvement in the accuracy of 3-D localization and deformation estimation of objects in urban areas. Basically, the TerraSAR-X/TanDEM-X mission represents a specific sensor availability scenario in space where the two satellites were launched one after the other. There was a long monostatic acquisition period at the beginning of the mission, followed by a bistatic acquisition period which is going on currently, and finally, there would be a monostatic acquisition period again. Consequently, fusion of monostatic and bistatic data is essential to fully exploit the mission potential.

However, in complex metropolitan areas, interpretation of the SAR images and interferometric phase is problematic due to phase discontinuities (e.g., due to height discontinuities, noise, etc.) and complex scattering situations such as radar layover and shadow. Spatial phase unwrapping proves to be a challenge, and ambiguities in layover areas cannot be solved. Therefore, the standard Shuttle Radar Topography Mission (SRTM)/TanDEM-X digital elevation models (DEMs) are erroneous or even useless in urban areas, and advanced multibaseline phase unwrapping algorithms are needed [4]. Hence, there is a need to bypass geometrical limitations (such as layover) of radar and thus enhance the precision and quality of TanDEM-X height models.

Coherent phase-based multitemporal techniques, for instance, persistent scatterer (PS) interferometry (PSI) [1] and SAR tomography [5], make use of points with stable phase to counter some of the aforementioned problems for urban area monitoring. These long-time coherent points are called PSs and are characterized by one or two dominant scatterers in a resolution cell. On buildings, there can be many such points. However, availability of such scatterers is opportunistic. To improve the spatial sampling of the measured points, partially coherent distributed scatterers (DSs) can be exploited, since DSs also make up a significant percentage in X-band. The complex response of a DS in a SAR acquisition involves a coherent sum of many independent small scatterers (no dominant scatterer) within a resolution cell [6] and is modeled as a complex circular Gaussian variate [7]. On man-made structures like roofs, building walls, asphalt roads, and concrete surfaces, the DSs also provide a long-time coherent radar return, although the phase quality is not on par with the PSs. It is possible to estimate the parameters (elevation and deformation) for DSs with good precision using advanced algorithms such as the small-baseline subset (SBAS) algorithm [8] and SqueeSAR [9].

This letter provides the first demonstration of the integration of monostatic and bistatic high-resolution InSAR stacks for complex urban area monitoring and bypassing scattering scenarios, for instance, radar layover. The technique exploits DSs to estimate the topography and full deformation time series using an advanced high-resolution SBAS algorithm. It first utilizes motion-free and atmosphere-free bistatic single-pass

Manuscript received January 17, 2013; revised May 7, 2013 and July 12, 2013; accepted July 29, 2013.

The authors are with the Remote Sensing Technology Institute (IMF), German Aerospace Center (DLR), 82234 Wessling, Germany (e-mail: kanika.goel@dlr.de; nico.adam@dlr.de).

Color versions of one or more of the figures in this paper are available online at http://ieeexplore.ieee.org.

Digital Object Identifier 10.1109/LGRS.2013.2278204

interferograms and then utilizes small-baseline monostatic repeat-pass interferograms (no external DEM is used). The objective of this letter is to present the fusion technique and a test case using high-resolution spotlight mixed TerraSAR-X/TanDEM-X data of Las Vegas, USA.

II. Methodology

Based on N SAR images (including both bistatic and monostatic data), we generate M single-look bistatic interferograms and M' single-look small-baseline monostatic interferograms. The interferograms are first spatially adaptive multilooked, and DSs are selected. The bistatic interferograms are then exploited for topography estimation of each DS. These topographic phases are removed from the monostatic interferograms, and the SBAS technique is applied to retrieve the residual topography and deformation time series for each DS. The various steps involved in the fusion algorithm are as follows.

A. Spatially Adaptive Phase Multilooking and DS Selection

The fusion algorithm first involves the identification of image pixels (i.e., resolution cells) with distributed scattering mechanism, hereafter called DSs. The DSs are characterized by a low SNR, which has to be improved by local spatial averaging/multilooking. A DS object usually spans several image pixels where the backscattered energy is lower/weaker, but is statistically homogeneous within the area. Spatially adaptive filters which average these statistically homogeneous pixels can be used to enhance the amplitude, interferometric phase, and coherence. Rectangular windows can be used too; however, they result in a loss of resolution and usually bias the estimates, for example, when there is a PS present in the rectangular window (which is usually the case in high-resolution images of urban areas).

The amplitudes of the complex returns are a good indicator for distinguishing between different backscatters. Statistically similar pixels can thus be selected for multilooking based on their amplitude distributions using various statistical tests [9], [10]. The Anderson–Darling (AD) test has proven to be the most effective for identifying if two pixels arise from the same distribution, given the stack of N SAR amplitude images (coregistered and calibrated). It gives the best detection rate at a constant false alarm rate. It performs reasonably well even for a stack of acquisitions containing as small as ten images.

The AD test is performed for each image pixel, and the homogeneous pixels surrounding it are identified (i.e., a spatially adaptive estimation window which can have any size and shape). A pixel can be included in different estimation windows, as compared to segmentation wherein each pixel is assigned to a single class. The estimation window for each pixel is then used for complex phase multilooking of the interferograms (bistatic and monostatic) for an improved phase and coherence estimation. Of course, there is a slight reduction of resolution due to the adaptive multilooking, but the object resolution is preserved. Then, we select the DSs for further processing based on a minimum average spatial coherence and a minimum number of looks (so as to exclude PSs). Additionally, in the next step (i.e., Section II-B), a further selection of DSs is done based on the temporal coherence.

B. Bistatic Stacking Interferometry

The bistatic interferograms are now exploited for height estimation of DSs. An external DEM is not used, since it has artifacts in urban areas and is of low resolution (e.g., SRTM DEM). Also, the standard TanDEM-X DEM suffers from the side-looking geometry of SAR, due to which issues like radar layover and shadow remain unsolved, unless multiaspect data or a stack of acquisitions are used. The spatially adaptive multilooked interferometric phase for a generic pixel in the kth bistatic interferogram is composed of the phase components due to topography (ϕ^k_{topo}) and noise (ϕ^k_{noise}) only

$$\phi^k_{\text{ML}} = \phi^k_{\text{topo}} + \phi^k_{\text{noise}}. \tag{1}$$

The topographic phase depends on the perpendicular baseline $B^k_\perp$, the distance R between the target and master sensor, and the local incidence angle (for flat terrain) θ as follows:

$$\phi^k_{\text{topo}} = x^k h = \left(\frac{2\pi}{\lambda}\frac{B^k_\perp}{R\sin\theta}\right)h = \frac{2\pi}{a^k}h \tag{2}$$

where λ is the transmitted wavelength, h is the height of the pixel, and a^k is the height of ambiguity. The phase noise is due to possible uncompensated geometrical decorrelation and thermal noise effects.

Given a few spatially adaptive multilooked bistatic interferograms with different perpendicular baselines/heights of ambiguities and referenced with respect to a single pixel, it is possible to retrieve the height information for each DS by using its wrapped interferometric phase vector. The height h of a DS here refers to the average height of the DS area which has been multilooked. Since a pixelwise adaptive multilooking has been performed, as described in Section II-A, areas with sloping or complex topography are appropriately handled. The following model coherence function (periodogram) ξ is maximized for height estimation:

$$\xi(h) = \frac{1}{M}\left|\sum_{k=1}^{M} e^{j\left(\phi^k_{\text{ML}} - \phi^k_{\text{topo}}\right)}\right|. \tag{3}$$

Since there is no deformation phase in the bistatic interferograms, the periodogram is a 1-D function dependent just on the DS's height (and not on its velocity), and its values are known over an irregular grid defined by the available spatial baselines ($B^k_\perp$). The topography estimate for each DS is estimated from the peak of this periodogram, i.e.,

$$(\hat{h}) = \arg\max_h(\xi). \tag{4}$$

The maximum of the periodogram is the temporal coherence of the DS. The reference pixel is usually a high coherent point located in a nondeforming zone (note that the same reference point is used later on for the monostatic interferograms in Section II-C). The precision of the estimation depends on the number of bistatic interferograms and the baseline distribution, since the sidelobes of the periodogram reduce by using more bistatic interferograms with varying perpendicular baselines [11]. It also depends on the phase stability of the DS and the

sensor characteristics. The variance of the height estimate of a DS is approximately given as follows [12]:

$$\sigma_h^2 \cong \frac{\sum_{k=1}^{M}\left(\frac{1}{\sigma_\phi^k}\right)^2}{\sum_{k=1}^{M}\left(\frac{1}{\sigma_\phi^k}\right)^2 \sum_{k=1}^{M}\left(\frac{x^k}{\sigma_\phi^k}\right)^2 - \left(\sum_{k=1}^{M}\frac{x^k}{\left(\sigma_\phi^k\right)^2}\right)^2} \quad (5)$$

where σ_ϕ^k is the phase standard deviation of the DS for interferogram k. It is a function of the spatial coherence and the number of looks [7]. Assuming that $\sigma_\phi = 20^\circ$ and the height of ambiguities of the TerraSAR-X data set described in Section III, we get $\sigma_h \cong 1.5$ m.

Important to note is that, first, since the DS pixel has been multilooked using its statistically homogeneous pixels, the possibility of a layover (e.g., building and ground) inside a resolution cell is quite low, and usually, a clear periodogram peak is obtained. This is because the radar amplitude is strongly dependent on the orientation and slope of a resolution cell. Explicitly, only those pixels would be selected as homogeneous, which exhibit a smoothly varying topography. Note that the periodogram approach works well for single PSs too; however, we must stress that the periodogram can lead to a wrong estimation in the case of PSs which are characterized by double (or more) dominant scatterers inside a resolution cell. Anyhow, we choose only DSs for the processing, as mentioned in Section II-A. Second, since wrapped phase data are used for height estimation of DSs and no phase unwrapping is required, radar layover is bypassed and does not affect the algorithm.

We then select those DSs for subsequent processing, which exhibit a temporal coherence greater than a certain threshold.

C. Monostatic Stacking Interferometry

The monostatic interferograms are now exploited for deformation time series mapping using the SBAS technique. The DEM phase components estimated via the bistatic interferograms are used to compute the differential monostatic interferograms. There might still be residual topography present in the flattened monostatic interferograms, since the baseline spread of bistatic interferograms is restricted by the number of data pairs and their perpendicular baseline separation. We use only small-baseline monostatic interferograms so as to reduce the effects of residual topography and decorrelation on the DSs. The spatially adaptive multilooked interferometric phase for a generic pixel in the kth flattened monostatic interferogram is composed of the phase components due to residual topography ($\phi^k_{\text{topo\_flat}}$), deformation ($\phi^k_{\text{defo\_flat}}$), atmosphere ($\phi^k_{\text{atm\_flat}}$), and noise ($\phi^k_{\text{noise\_flat}}$)

$$\phi^k_{\text{ML\_flat}} = \phi^k_{\text{topo\_flat}} + \phi^k_{\text{defo\_flat}} + \phi^k_{\text{atm\_flat}} + \phi^k_{\text{noise\_flat}}. \quad (6)$$

The residual topography phase is given as follows:

$$\phi^k_{\text{topo\_flat}} = x^k \Delta h = \frac{4\pi}{\lambda}\frac{B^k_\perp}{R\sin\theta}\Delta h = \frac{2\pi}{a^k}\Delta h \quad (7)$$

where Δh is the residual topography of the pixel. The phase-to-height sensitivity of a monostatic interferogram is double as compared to that of a bistatic interferogram. The phase noise here is due to temporal decorrelation, in addition to uncompensated baseline decorrelation and thermal noise effects.

Fig. 1. Mean SAR amplitude image and its corresponding Google Earth optical image of the test site Las Vegas.

SBAS is explained in detail in [8]. The main steps are as follows.

1) The interferograms are spatially unwrapped, and all coherent pixels are calibrated with respect to the reference pixel (which has been used in Section II-B).
2) Next, the residual DEM and mean deformation velocity are estimated for the DSs via the least squares solution of the computed sequence of differential InSAR interferograms.
3) After this operation, the estimated residual topography and mean deformation velocity are subtracted modulo 2π from each interferogram, resulting in a fringe rate reduction.
4) Accordingly, a new unwrapping step is then applied to the residual wrapped phase, with the phase unwrapping being considerably simplified. By adding back the subtracted mean deformation velocity, refined unwrapped differential interferograms are obtained.
5) The interferogram subsets are afterward linked using the singular-value decomposition method, and a minimum-norm least squares solution (i.e., $L2$ norm minimization) is obtained. Advantageously, SBAS provides complete nonlinear deformation time series of the scatterers, incorporating the linear as well as the seasonal motion (e.g., for buildings), without using any model.
6) Finally, the atmospheric effects are estimated and removed via a spatial low-pass and a temporal high-pass filtering.

However, $L2$ norm minimization (step 5 above) performs poorly in case of difficult-to-detect phase unwrapping errors (spike noise). These might be present in urban areas due to tall and closely located buildings, which result in radar layover and shadow. Instead, a more robust phase inversion solution can be obtained by using an $L1$ norm minimization [13], [14]. Thus, the $L1$ norm cost function is applied to estimate the deformation time series for each DS at object resolution.

III. Application Test Case and Results

We have applied the proposed algorithm on a test site approximately 4 km by 2.5 km centered at the Las Vegas Convention Center in Las Vegas, USA. Eighty-four "high-resolution spotlight" TerraSAR-X/TanDEM-X images from February 2008 to December 2011 with a look angle of 36.04° and "VV" polarization have been used. The mean amplitude image of the test site and its corresponding Google Earth optical image are shown in Fig. 1. The pixel spacing is approximately 0.38 m

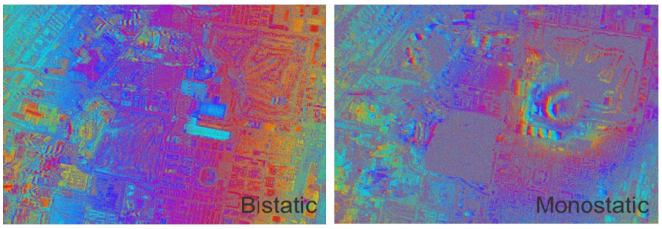

Fig. 2. Comparison of a bistatic and a monostatic interferogram of Las Vegas.

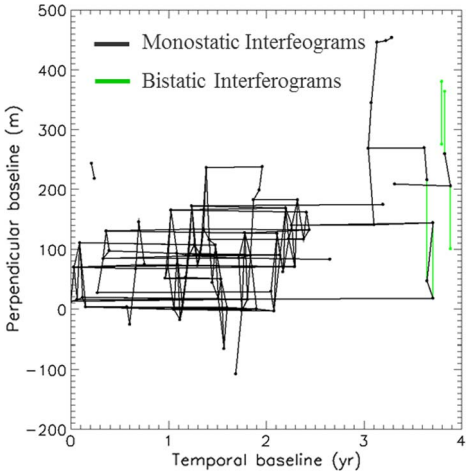

Fig. 3. Baseline–time plot of the TerraSAR-X/TanDEM-X data of Las Vegas.

in the range direction and 0.42 m in the azimuth direction (adapted to oversampling). Fig. 2 shows a comparison between a multilooked bistatic and a monostatic interferogram of the test site Las Vegas. The bistatic interferogram is free from fringes due to deformation and atmosphere and has no temporal decorrelation, as compared to the monostatic interferogram.

The SAR images have been used to generate five bistatic interferograms with height of ambiguities −33.3927, −44.6864, −54.2698, 53.9007, and −53.7940 m/cycle, respectively. Next, 174 monostatic interferograms have been generated. These include, first, small-baseline interferograms based on a maximum perpendicular baseline of 150 m and a maximum temporal baseline of 30 days. Second, these also include a few long-time-span (approximately 750 days) interferograms with very small perpendicular baselines (approximately 5 m) so as to include the full cycles of seasonal motion on buildings in these interferograms; the very small perpendicular baseline ensures that the effect of topographic phase on the interferograms is minimal. For coregistration and InSAR processing, the German Aerospace Center (DLR)'s operational PSI-GENESIS processor has been employed [15]. Fig. 3 shows the baseline–time plot for the scenes and interferograms, wherein each dot represents a SAR image and each line represents an interferogram used in the processing.

We then apply the adaptive spatial filtering algorithm on the single-look interferograms, as demonstrated in Fig. 4. The minimum and maximum sizes of the homogeneous patch are set to 20 and 200 pixels, respectively. We clearly see the reduction in the phase noise and the improvement in the interferometric phase.

This is followed by height estimation of the DSs for the test site by means of 1-D ensemble coherence maximization using

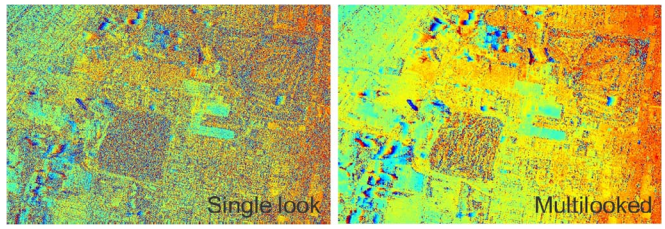

Fig. 4. Single-look monostatic interferogram of Las Vegas and its spatially adaptive multilooked version.

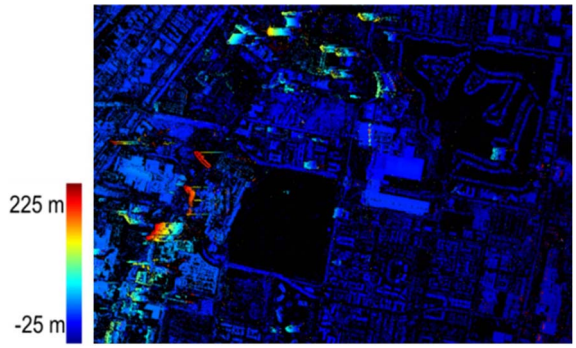

Fig. 5. DS height estimates for Las Vegas using bistatic interferograms via ensemble coherence maximization.

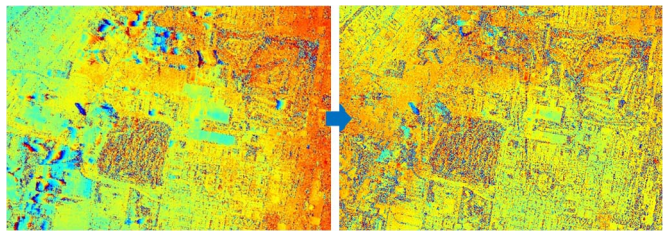

Fig. 6. Illustration of the removal of the topographic phase from a monostatic interferogram of Las Vegas.

only the five bistatic single-pass interferograms, as presented in Fig. 5. We have selected DSs which have an average spatial coherence of at least 0.7 and a temporal coherence of at least 0.5 so as to exclude decorrelated areas. A total of 6 361 670 points have been processed (approximately 600 000 DSs per square kilometer). Assuming a best case scenario of 100 000 PSs per square kilometer, this is a six times increase in the density of measured points. The subsequent flattening of the monostatic repeat-pass interferograms is illustrated in Fig. 6. Evidently, the fringes due to very high buildings in Las Vegas have been removed. It is worth mentioning that the residual DEM is still present in the monostatic interferograms and has to be removed. The better the precision of the height estimation (as described in Section II-B), the lower the magnitude of the residual DEM.

The flattened monostatic interferograms are now unwrapped using the minimum-cost flow algorithm [16]. These are subsequently used for residual topography and deformation monitoring using the SBAS approach via the $L1$ norm minimization. The algorithm proposed by Barrodale and Roberts [17] is used for $L1$ norm minimization. The estimated residual DEM for the DSs of Las Vegas is on the order of a few meters, although there are some DSs which have a significantly high DEM error which is greater than 10 m (approximately 2.8% of the selected DSs). The estimated root-mean-square (rms) deformation and

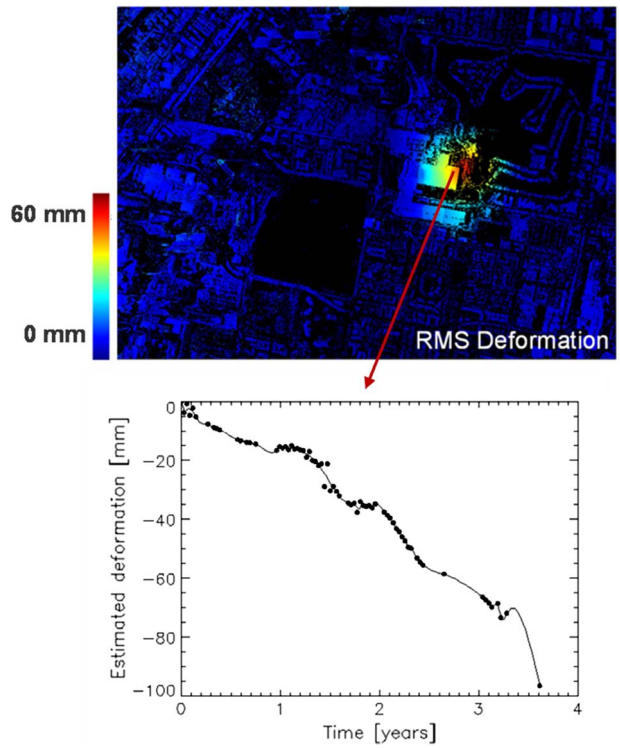

Fig. 7. DS deformation estimates for Las Vegas using flattened monostatic interferograms via $L1$-norm-based SBAS. The deformation time series is visualized for a DS, where the dots represent the estimated deformation at the time of SAR acquisitions and the solid line is a line fitting using cubic spline interpolation.

an example of a deformation time series for a DS are shown in Fig. 7. We have used the rms deformation for visualizing the results as it is visually effective and provides integral information about the displacement with respect to time. As can be seen, even nonlinear deformation time series can be estimated, which include the linear as well as seasonal deformation on buildings due to thermal dilation [18]. The variance of the deformation estimates using the $L1$ norm inversion is between 0 and 10 (mm $\times$ mm), and thus, this method provides millimeter precision. The variance is higher for DS points in layover regions or having a seasonal motion.

We would like to remark that no standard TanDEM-X/external DEM has been used in our processing. Since the same multilooking window is used for topography and deformation estimation of DSs, error propagation is minimal. The fusion algorithm is easy to implement without much add-ons to the existing techniques and is computationally efficient.

IV. Conclusion

High-resolution SAR sensors TerraSAR-X and TanDEM-X enable bistatic and monostatic interferometry. In particular, the bistatic interferograms have a high data quality and are free from deformation, atmosphere, and temporal decorrelation. By properly integrating the data stacks, an improved estimation of topography and deformation time series at object resolution is possible. We have investigated in particular an advanced fusion of TerraSAR-X and TanDEM-X InSAR data utilizing DSs in dense metropolitan areas, where the standard TanDEM-X elevation models are inaccurate. It complements PS-based techniques such as PSI and SAR tomography. The results of processing a TerraSAR-X/TanDEM-X data set of Las Vegas, USA, show the millimeter precision which can be obtained. The topic of further investigation is the potential of jointly processing TerraSAR-X/TanDEM-X data using PSs.

References

[1] A. Ferretti, C. Prati, and F. Rocca, "Permanent scatterers in SAR interferometry," *IEEE Trans. Geosci. Remote Sens.*, vol. 39, no. 1, pp. 8–20, Jan. 2001.

[2] M. Eineder, N. Adam, R. Bamler, N. Yague-Martinez, and H. Breit, "Spaceborne spotlight SAR interferometry with TerraSAR-X," *IEEE Trans. Geosci. Remote Sens.*, vol. 47, no. 5, pp. 1524–1535, May 2009.

[3] G. Krieger, A. Moreira, H. Fiedler, I. Hajnsek, M. Younis, M. Werner, and M. Zink, "The TanDEM-X mission: A satellite formation for high resolution SAR interferometry," *IEEE Trans. Geosci. Remote Sens.*, vol. 45, no. 11, pp. 3317–3341, Nov. 2007.

[4] M. Lachaise, M. Eineder, and T. Fritz, "Multi baseline SAR acquisition concepts and phase unwrapping algorithms for the TanDEM-X mission," in *Proc. IEEE IGARSS*, Barcelona, Spain, 2007, pp. 5272–5276.

[5] X. Zhu and R. Bamler, "Very high resolution spaceborne SAR tomography in urban environment," *IEEE Trans. Geosci. Remote Sens.*, vol. 48, no. 12, pp. 4296–4308, Dec. 2010.

[6] J. W. Goodman, "Some fundamental properties of speckle," *J. Opt. Soc. Amer. A, Opt. Image Sci.*, vol. 66, no. 11, pp. 1145–1150, Nov. 1976.

[7] R. Bamler and P. Hartl, "Synthetic aperture radar interferometry—Topical review," *Inverse Prob.*, vol. 14, no. 4, pp. R1–R54, Aug. 1998.

[8] P. Berardino, G. Fornaro, R. Lanari, and E. Sansosti, "A new algorithm for surface deformation monitoring based on small baseline differential SAR interferograms," *IEEE Trans. Geosci. Remote Sens.*, vol. 40, no. 11, pp. 2375–2383, Nov. 2002.

[9] A. Ferretti, A. Fumagalli, F. Novali, C. Prati, F. Rocca, and A. Rucci, "A new algorithm for processing interferometric data-stacks: SqueeSAR," *IEEE Trans. Geosci. Remote Sens.*, vol. 49, no. 9, pp. 3460–3470, Sep. 2011.

[10] A. Parizzi and R. Brcic, "Adaptive InSAR stacks multilooking exploiting amplitude statistics: A comparison between different techniques and practical results," *IEEE Trans. Geosci. Remote Sens.*, vol. 8, no. 3, pp. 441–445, May 2011.

[11] F. Rocca, "Diameters of the orbital tubes in long-term interferometric SAR surveys," *IEEE Geosci. Remote Sens. Lett.*, vol. 1, no. 3, pp. 224–227, Jul. 2004.

[12] P. R. Bevington, *Data Reduction and Error Analysis for the Physical Sciences*. New York, NY, USA: McGraw-Hill, 1969.

[13] T. Lauknes, H. Zebker, and Y. Larsen, "InSAR deformation time series using an L_1-norm small-baseline approach," *IEEE Trans. Geosci. Remote Sens.*, vol. 49, no. 1, pp. 536–546, Jan. 2011.

[14] K. Goel and N. Adam, "An advanced algorithm for deformation estimation in non-urban areas," *ISPRS J. Photogramm. Remote Sens.*, vol. 73, pp. 100–110, Sep. 2012.

[15] N. Adam, B. Kampes, M. Eineder, J. Worawattanamateekul, and M. Kircher, "The development of a scientific permanent scatterer system," in *Proc. ISPRS Hannover Workshop*, Hannover, Germany, 2003, pp. 1–6.

[16] M. Constantini, "A novel phase unwrapping method based on network programming," *IEEE Trans. Geosci. Remote Sens.*, vol. 36, no. 3, pp. 813–821, May 1998.

[17] I. Barrodale and F. D. K. Roberts, "An improved algorithm for discrete L1 linear approximation," *SIAM J. Numer. Anal.*, vol. 10, no. 5, pp. 839–848, Oct. 1973.

[18] X. Zhu and R. Bamler, "Let's do the time warp: Multi-component nonlinear motion estimation in differential SAR tomography," *IEEE Geosci. Remote Sens. Lett.*, vol. 8, no. 4, pp. 735–739, Jul. 2011.

A.5 Goel, K., Adam, N., 2013c. Advanced stacking of TerraSAR-X and TanDEM-X data in complex urban areas. Proceedings of Joint Urban Remote Sensing Event, JURSE 2013, Sao Paulo, Brazil, 21-23 April, 115-118.

Advanced Stacking of TerraSAR-X and TanDEM-X Data in Complex Urban Areas

Kanika Goel and Nico Adam

Remote Sensing Technology Institute (IMF)
German Aerospace Center (DLR), Oberpfaffenhofen
Wessling- 82234, Germany
Email: kanika.goel@dlr.de

Abstract—**This paper presents the fusion of monostatic repeat-pass and bistatic single-pass SAR data for an improved 3D positioning and deformation monitoring of objects in urban areas. Addition of a few TanDEM-X data pairs (which are free from displacement, atmosphere and temporal decorrelation) to the existing TerraSAR-X data stack can improve the results of stacking techniques such as Persistent Scatterer Interferometry (PSI). However, in dense urban areas, geometrical limitations such as layover make it difficult for an accurate mapping using the standard TanDEM-X elevation models. In this paper, we investigate the potential of jointly processing TerraSAR-X and TanDEM-X data for resolving single or double scattering mechanisms present in the same resolution cell. The technical details and demonstration are provided using high resolution spotlight mixed TerraSAR-X /TanDEM-X data of Las Vegas, US.**

Index Terms— **SAR Interferometry, Persistent Scatterer (PS), TanDEM-X, TerraSAR-X.**

I. INTRODUCTION

SAR interferometry is a well-established technique for measuring Earth's topography and deformation. TerraSAR-X allows millimetric accuracy with its High Resolution Spotlight mode using advanced stacking techniques such as Persistent Scatterer Interferometry (PSI) [1], [2]. The launch of TanDEM-X mission in 2010 facilitates high resolution single pass SAR interferometry [3]. The main objective of this mission is the generation of a global digital elevation model (DEM). Furthermore, it also provides a configurable SAR platform for demonstrating new interferometric techniques and applications. It enables the acquisition of highly accurate across-track interferograms which are free from motion, atmospheric disturbances and temporal decorrelation, as compared to repeat-pass interferometry. Adding a few TanDEM-X data pairs to the existing TerraSAR-X data stack can be used to improve the results of the stacking techniques. Though, the combination of bistatic and monostatic data can be difficult.

Essentially, the TerraSAR-X/Tandem-X case represents a typical sensor availability scenario in space, where, the satellites in a mission are launched one after the other. Typically, there is a long monostatic acquisition period at the beginning of the mission, followed by a short bistatic acquisition period and finally, again a monostatic acquisition period. Thus, fusion of bistatic and monostatic data is essential to fully exploit the potential of high resolution SAR missions.

Also, there is an increased focus on monitoring urban infrastructure from space. In dense metropolitan areas, it is difficult to interpret the SAR images and interferometric phase due to discontinuities and complex scattering situations such as layover and shadow. Spatial phase unwrapping is a challenge. This is the reason that standard TanDEM-X height models are incapable of providing an accurate 3D positioning of objects in urban areas.

This paper explores the integration of monostatic repeat-pass and bistatic single-pass SAR data in complex urban areas for an improved 3D positioning and deformation mapping of persistent scatterers (PSs). Our approach jointly processes TerraSAR-X and TanDEM-X data for resolving single or double scattering mechanisms present in the same resolution cell. It complements coherent phase-based techniques such as conventional PSI, SAR tomography [4] and multi-baseline phase unwrapping [5]. The developed method is more robust because it uses repeat-pass amplitude data and single-pass interferometric phase data only for enhancing the quality and precision of TanDEM-X elevation models. Subsequently, repeat-pass differential interferometric phase data can be used for displacement monitoring. The technical details and first results are presented using high resolution spotlight mixed TerraSAR-X/TanDEM-X data of Las Vegas, US.

II. METHODOLOGY

Standard interferometric processing systems such as PSI are developed to cope with a single scatterer inside a resolution cell. The periodogram (ensemble coherence maximization) based on a common master image is the optimal estimator in case of a single scatterer surrounded by incoherent clutter. The TanDEM-X data pairs acquired simultaneously result in single-pass interferograms which have a high data quality and are free from deformation, atmosphere and temporal decorrelation. Fig. 1 shows a comparison between a single-pass and a repeat-pass interferogram. Given a few single-pass interferograms with different height of ambiguities and calibrated with respect to a single pixel, it is possible to retrieve the height information in

978-1-4799-0211-8/13/$31.00 ©2013 IEEE

case of a single scatterer inside a resolution cell using the periodogram method (without the need of a common master image). In this case, the ensemble coherence as a function of height h for a pixel is given by:

$$\gamma(h) = \frac{1}{M}\left|\sum_{k=1}^{M} e^{j\left(\phi^k - \frac{4\pi}{\lambda}\frac{B_\perp^k}{R\sin\theta}h\right)}\right| \quad (1)$$

where, M is the number of single-pass interferograms, ϕ^k is the interferometric phase of the pixel for interferogram k, λ is the transmitted wavelength, $B_\perp^k$ is the perpendicular baseline for interferogram k, R is the sensor-target distance and θ is the local incidence angle (for flat terrain). Important to note is the fact that since there is no deformation phase in the single-pass interferograms, the ensemble coherence is a 1D function dependent just on the scatterer's height (and not on the scatterer's velocity). Fig. 2 presents the height estimation of PSs for the test site Las Vegas, using only 5 bistatic interferograms with height of ambiguities -33.3927, -44.6864, -54.2698, 53.9007 and -53.7940 m/cycle respectively. The maximum of γ is called temporal coherence (shown in Fig. 3). The height estimates can then be used for the removal of topographic phase from the monostatic interferograms. Afterwards, the flattened monostatic interferograms can be used for deformation mapping using standard stacking algorithms.

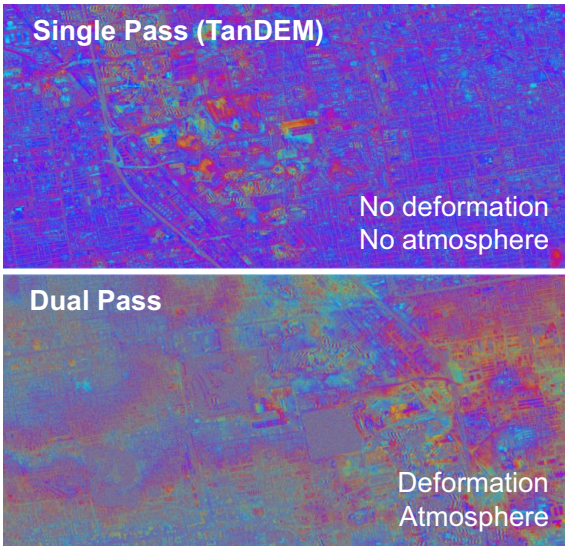

Figure 1. Comparison of a single-pass interferogram (TanDEM-X) and a repeat-pass interferogram (TerraSAR-X) of Las Vegas, US.

We can visualize in Fig. 3 and 4 that some of the results are not correct (lower temporal coherence). This is because of the presence of double scatterers inside a resolution cell. An example of a periodogram for a single scatterer is shown in Fig. 4 (a). What can be seen is the presence of strong side lobes due to the use of only 5 TanDEM-X interferograms. Of course, an ideal situation would be many bistatic interferograms with varying height of ambiguities to reduce the side lobes. Practically, this is not always possible. The periodogram estimates the height accurately only when a single scatterer is present in a resolution cell. The case of multiple scatterers in a resolution cell leads to biased or even a wrong estimation as demonstrated in Fig. 4 (b).

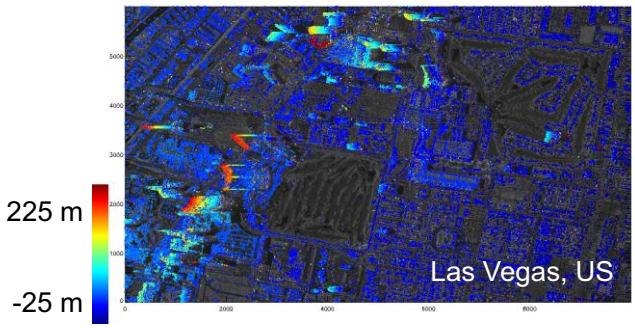

Figure 2. PS height estimation results for Las Vegas via a 1D ensemble coherence maximization approach using 5 TanDEM-X interferograms.

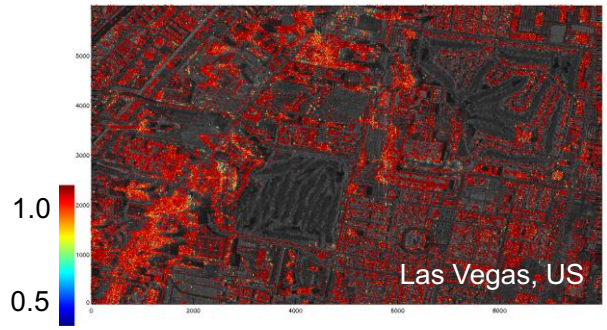

Figure 3. PS temporal coherence results for Las Vegas via a 1D ensemble coherence maximization approach using 5 TanDEM-X interferograms.

Complex urban structures and the side-looking radar observation geometry make it likely that more than one scatterer are inside a resolution cell [6]. Typical example is layover of building and ground. Around 15% of the persistent scatterers (PSs) are multiple scatterers in an urban area [7]. To resolve this ambiguity, the proposed algorithm increases the number of observations by making use of repeat-pass TerraSAR-X amplitude data [7], [8], in addition to the single-pass TanDEM-X interferemetric phase data. The use of only the repeat-pass amplitudes is to avoid deformation and atmospheric interference. The technique utilizes the baseline dependency of the amplitude. It provides the number of dominant scatterers inside a resolution cell and consequently solves the model selection problem. It can be applied in the early stages of interferometric processing and complements coherent techniques such as PSI and SAR tomography which include the phase information and thus require the correction of displacement and atmospheric phase beforehand.

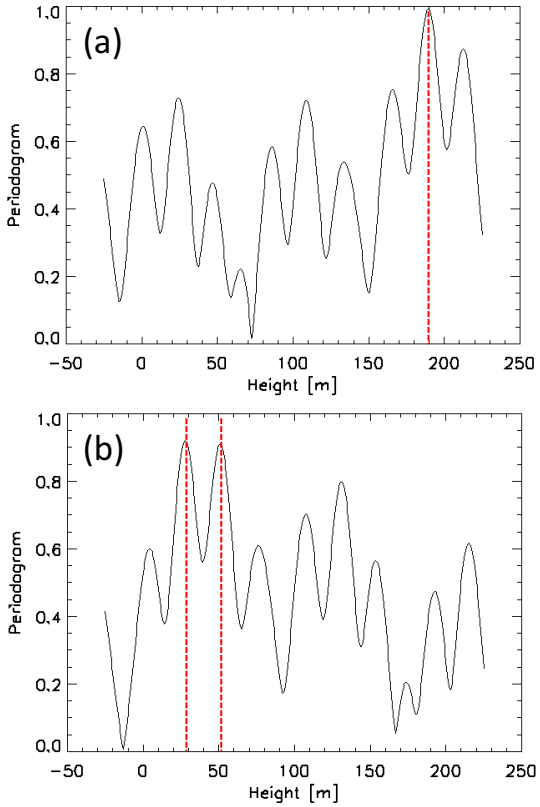

Figure 4. (a) is the periodogram for a single scatterer. (b) is the periodogram for a double scatterer (biased or wrong estimation of height).

Given N amplitude images (coregistered and calibrated) and M bistatic interferograms (referenced to a single pixel), the model selection is based on the following two mechanisms:

A. Single Scattering Mechanism

A single scatterer i.e. a panel made of metal can be described by the following amplitude (baseline dependent):

$$a_i(B_i, s, \Delta, \phi) = s \cdot \left(\left| \frac{\sin(B_i \Delta + \phi)}{(B_i \Delta + \phi)} \right| \right) \tag{2}$$

where, $i = 1,\ldots,N$ is the image index, B_i is the height-to-phase conversion factor for image i given by:

$$B_i = \frac{4\pi}{\lambda} \frac{B_\perp^i}{R \sin\theta} \tag{3}$$

s is the reflectivity of the scatterer, Δ is the extension of the panel and ϕ the orientation of the panel. The ensemble coherence of the single scatterer using only the bistatic interferograms is given by (1).

B. Double Scattering Mechanism

The alternative model describing the amplitude (baseline dependent) of two dominant scatterers inside a resolution cell results from the amplitude of the sum of two complex sinusoids and describes a fading. It is given by:

$$a_i(B_i, s_1, s_2, h_1, h_2, \phi) = \\ sqrt\left(s_1^2 + s_2^2 + 2 \cdot s_1 \cdot s_2 \cdot \cos\left(B_i (h_1 - h_2) + \phi\right)\right) \tag{4}$$

It models the reflectivities s_1 and s_2 of the two scatterers, their heights h_1 and h_2 respectively and the orientation ϕ. The ensemble coherence of the double scatterer using only the bistatic interferograms can be derived from [6].

Based on the above two models, we perform a robust joint maximum a-posteriori (MAP) estimation of the unknown parameters and model selection exploiting the monostatic amplitude and bistatic interferometric phase observations. This is done via Bayesian inference making use of directed graphs and particle filters [9], [10]. It is a statistical approach in which all forms of uncertainty are expressed in terms of probability and parameter estimation is performed based on measured or empirical data. Our practically applied framework estimates the posterior distribution by making use of bootstrap particle filtering (condensation algorithm), which is a computationally efficient method.

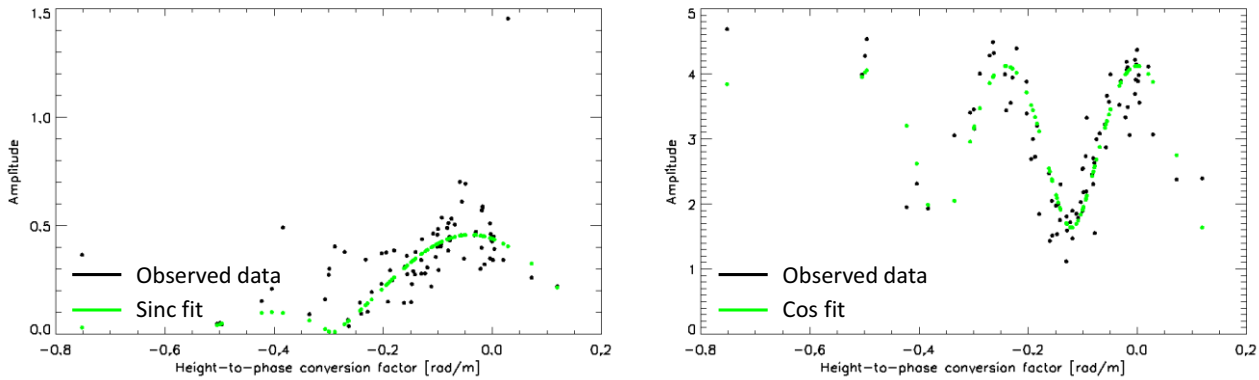

Figure 5. Demonstration of parametric sinc and cos fits for two pixels (PSs) of the test site respectively.

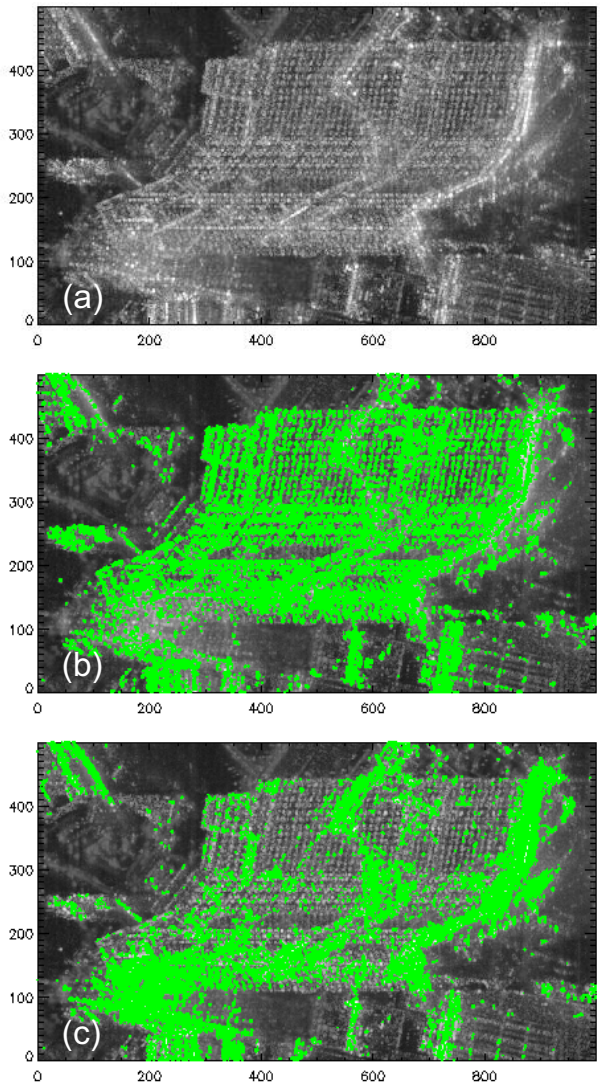

Figure 6. (a) Amplitude image of a part of the test site, Las Vegas, US. (b) Detected single scatterer resolution cells are overplotted and shown in green. (c) Detected double scatterer resolution cells are overplotted and shown in green.

III. Application Test Case

The test site is the city of Las Vegas in US. The data stack comprises of 84 High Resolution Spotlight acquisitions from 2008–2011. For the processing, we used these 84 amplitude images and 5 bistatic interferograms with height of ambiguities -33.3927, -44.6864, -54.2698, 53.9007 and -53.7940 m/cycle. The number of amplitude images required for a reliable estimation can be even less, but the number of unknowns should be less than the number of observations during the MAP estimation and model selection. In this section, we provide the first preliminary results of our approach.

Fig. 5 compares the parameter fits for the two resolution cell configuration models for two pixels (PSs) of the test site. As can be seen, the parametric modeling and fit allows the optimal estimation of the resolution cell configuration. Fig. 6 shows the detected single scatterer and double scatterer resolution cells in green for a part of the test site. The areas where double scatterers exist can be visualized in Fig. 6 (a), which is the amplitude image of the test area. Fig. 6 (c) is plausible, it shows the double scattering resolution cells in areas where it's expected, thus, validating the algorithm.

Based on the number of scatterers inside a resolution cell, the optimal removal of topographic residuals can finally be implemented, followed by improved deformation monitoring using standard techniques.

IV. Conclusion

A new concept has been developed for the fusion of repeat-pass monostatic and single-pass bistatic SAR data. It makes use of single-pass interferograms and repeat-pass SAR amplitude images to cope with the typical PS resolution cell configurations and detects one or two scatterers inside a SAR resolution cell. It is insensitive to deformation and atmospheric disturbances. It complements phase based techniques, e.g., PSI and SAR tomography. A preliminary demonstration has been provided using TerraSAR-X and TanDEM-X data of Las Vegas in US. Future work will concentrate on providing processing examples for this technique. Also, fusion of TerraSAR-X and TanDEM-X data for distributed scatterers (DSs) would be investigated.

Acknowledgment

We would like to thank Prof. Dr. Richard Bamler for his valuable and constructive suggestions.

References

[1] A. Ferretti, C. Prati, and F. Rocca, "Permanent scatterers in SAR interferometry," *IEEE TGRS*, vol. 39, No. 1, pp. 8-20, 2001.

[2] N. Adam, M. Eineder, N. Yague-Martinez, and R. Bamler, "High resolution interferometric stacking with TerraSAR-X," In: Proc. *IEEE IGARSS*, Boston, 2008.

[3] G. Krieger, A. Moreira, H. Fiedler, I. Hajnsek, M. Younis, M.Werner, and M. Zink, "The TanDEM-X mission: A satellite formation for high resolution SAR interferometry," *IEEE TGRS*, vol. 45, no. 11, pp. 3317–3341, 2007.

[4] X. Zhu and R. Bamler, "Very high resolution spaceborne SAR tomography in urban environment," *IEEE TGRS*, vol. 48, no. 12, pp. 4296–4308, Dec. 2010.

[5] M. Lachaise, M. Eineder, and T. Fritz, "Multi baseline SAR acquisition concepts and phase unwrapping algorithms for the TanDEM-X Mission," In: Proc. *IEEE IGARSS*, pp. 5272–5276, 2007.

[6] A. Ferretti, m. Bianchi, C. Prati, and F. Rocca, "Higher-order permanent scatterers analysis," *EURASIP Journal on Applied Signal Processing*, 20, 3231–3242, 2005.

[7] N. Adam, R. Bamler, M. Eineder, and B. Kampes, "Parametric Estimation and Model Selection Based on Amplitude-Only Data in PS_Interferometry". In: Proc. *FRINGE*, Frascati, Italy, 2005.

[8] N. Adam, and M. Eineder, "A three dimensional dominant scatterer map extends the DEM information in urban areas," In: *Symposium of ISPRS Commission I*, Paris, France, 2005.

[9] K. Goel, and N. Adam, "Three-dimensional positioning of point scatterers based on radargrammetry," *IEEE TGRS*, vol. 50. No. 6, pp. 2355-2363, 2012.

[10] K. Goel, and N. Adam, "Parameter estimation of distributed scatterers using high resolution SAR data," In: Proc. *IEEE IGARSS*, Munich, Germany, 2012.

Errata Sheet

This errata sheet lists an error in the paper:
A.5 Goel, K., Adam, N., 2013b. Advanced stacking of TerraSAR-X and TanDEM-X data in complex urban areas. Proceedings of Joint Urban Remote Sensing Event, JURSE 2013, Sao Paulo, Brazil, 21-23 April, 115-118.

The Equation (1) in this paper is corrected to:

$$\gamma(h) = \frac{1}{M}\left|\sum_{k=1}^{M} e^{j\left(\phi^k - \frac{2\pi}{\lambda}\frac{B_\perp^k}{R\sin\theta}h\right)}\right| \tag{1}$$

List of Abbreviations

APS: Atmospheric Phase Screen

BF: Beamforming

CPT: Coherent Pixels Technique

Compressive Sensing: CS

DEM: Digital Elevation Model

DGM: Directed Graphical Model

DInSAR: Differential Interferometric Synthetic Aperture Radar

DTomoSAR: Differential SAR Tomography

DS: Distributed Scatterer

DSI: Distributed Scatterer Interferometry

InSAR: Interferometric Synthetic Aperture Radar

LOS: Line-of-Sight

LS: Least Squares

MAP: Maximum A-Posteriori

MCF: Minimum Cost Flow

ML: Maximum Likelihood

NLS: Non-linear Least Squares

NWP: Numerical Weather Prediction

PDF: Probability Density Function

PS: Persistent Scatterer

PSI: Persistent Scatterer Interferometry

PSI-GENESIS: PSI module of the GENEric System for Interferometric SAR

Radar: RAdio Detection And Ranging

RMS: Root-Mean-Square

RV: Random Variable

SAR: Synthetic Aperture Radar

SBAS: Small Baseline Subset Algorithm

SCR: Signal to Clutter Ratio

SNR: Signal to Noise Ratio

SVD: Singular Value Decomposition

TomoSAR: SAR Tomography

References

Adam, N., Bamler, R., Eineder, M., Kampes, B., 2005. Parametric estimation and model selection based on amplitude-only data in PS-interferometry. In: Proceedings of ESA FRINGE Workshop 2005, Frascati, Italy, 28 November-2 December, on CD.

Adam N., Eineder M., Schatter B., Yague-Martines N., 2007. First TerraSAR-X interferometry evaluation. In: Proceedings of ESA FRINGE Workshop 2007, Frascati, Italy, 26-30 November, on CD.

Adam, N., Eineder, M., Yague-Martinez, N., Bamler, R., 2008. High resolution interferometric stacking with TerraSAR-X. In: Proceedings of IEEE International Geoscience and Remote Sensing Symposium, IGARSS 2008, Boston, US, 7-11 July, 117-120.

Adam, N., Kampes, B., Eineder, M., 2004. Development of a scientific permanent scatterer system: Modifications for mixed ERS/ENVISAT time series. In: Proceedings of ENVISAT/ERS Symposium 2004, Salzburg, Austria, 6-10 September, on CD.

Adam, N., Kampes, B., Eineder, M., Worawattanamateekul, J., Kircher, M., 2003. The development of a scientific permanent scatterer system. In: Proceedings of ISPRS Workshop on High Resolution Mapping from Space, Hannover, Germany, 6-8 October, on CD.

Adam, N., Parizzi, A., Eineder, M., Crosetto, M., 2009. Practical persistent scatterer processing validation in the course of the Terrafirma project. Journal of Applied Geophysics 69 (1), 59-65.

Arulampalam, S., Maskell, S., Gordon, N., Clapp, T., 2002. A tutorial on particle filters for online nonlinear/non-gaussian Bayesian tracking. IEEE Transactions on Signal Processing 50 (2), 174-188.

Bamler, R., Hartl, P., 1998. Synthetic aperture radar interferometry. Inverse problems 14, R1-R54, IOP Publishing Limited.

Bamler, R., Kampes, B., Adam, N., Suchandt, S., 2006. Assessment of slow deformations and rapid motions by radar interferometry. Zeitschrift für Geo-Informationssysteme (GIS) 7, 22-27.

Baran, I., Stewart, M., Claessens, S., 2005. A new functional model for determining minimum and maximum detectable deformation gradient resolved by satellite radar interferometry. IEEE Transactions on Geoscience and Remote Sensing 43 (4), 675-682.

Barrodale, I., Roberts, F., 1973. An improved algorithm for discrete L1 linear approximation. SIAM Journal on Numerical Analysis 10, 839-848.

Berardino, P., Fornaro, G., Lanari, R., Sansosti, E., 2002. A new algorithm for surface deformation monitoring based on small baseline differential SAR interferograms. IEEE Transactions on Geoscience and Remote Sensing 40 (11), 2375-2383.

Bevington, P., Robinson, D., 1969. Data reduction and error analysis for the physical sciences. McGraw-Hill.

Bishop, C., 2006. Pattern recognition and machine learning. Springer.

Blanco-Sanchez, P., Mallorquí, J., Duque, S., Monells, D., 2008. The coherent pixels technique (CPT): An advanced DInSAR technique for nonlinear deformation monitoring. Pure and Applied Geophysics 165 (6), 1167-1193.

Breit, H., Schattler, B., Fritz, T., Damerow, H., Schwarz, E., Balss, U., 2008. TerraSAR-X payload data processing: Results from commissioning and early operational phase. In: Proceedings of IEEE International Geoscience and Remote Sensing Symposium, IGARSS 2008, Boston, US, 7-11 July, II-209-II-212.

Buckreuss, S., Werninghaus, R., Pitz, W., 2009. The German satellite mission TerraSAR-X. IEEE Aerospace and Electronic Systems Magazine 24 (11), 4-9.

Budillon, A., Evangelista, A., Schirinzi, G., 2009. SAR tomography from sparse samples. In: Proceedings of IEEE International Geoscience and Remote Sensing Symposium, IGARSS 2009, Cape Town, South Africa, 12-17 July, 865-868.

Colesanti, C., Ferretti, A., Novali, F., Prati, C., Rocca, F., 2003. SAR monitoring of progressive and seasonal ground deformation using the permanent scatterers technique. IEEE Transactions on Geoscience and Remote Sensing 41 (7), 1685-1701.

Costantini, M., 1998. A novel phase unwrapping method based on network programming. IEEE Transactions on Geoscience and Remote Sensing 36 (3), 813-821.

Cumming, I., Wong, F., 2005. Digital signal processing of synthetic aperture radar data: Algorithms and implementation. Artech House.

Curlander, J., McDonough, R., 1991. Synthetic aperture radar: Systems and signal processing. John Wiley and Sons.

Davidson, G., Bamler, R., 1999. Multiresolution phase unwrapping for SAR interferometry. IEEE Transactions on Geoscience and Remote Sensing 37 (1), 163-174.

Desai, M., 1997. Spotlight mode SAR stereo technique for height computation. IEEE Transactions on Image Processing 10 (6), 1400-1411.

Eineder, M., Adam, N., Bamler, R., Yague-Martinez, N., Breit, H., 2009. Spaceborne spotlight SAR interferometry with TerraSAR-X. IEEE Transactions on Geoscience and Remote Sensing 47 (5), 1524-1535.

Eineder, M., Hubig, M., Milcke, B., 1998. Unwrapping large interferograms using the minimum cost flow algorithm. In: Proceedings of IEEE International Geoscience and Remote Sensing Symposium, IGARSS 1998, Seattle, US, 6-10 July, 83-87.

Ferretti, A., Bianchi, M., Prati, C., Rocca, F., 2005. Higher-order permanent scatterers analysis. EURASIP Journal on Applied Signal Processing, 2005 (20), 3231-3242.

Ferretti, A., Fumagalli, A., Novali, F., Prati, C., Rocca, F., Rucci, A., 2011. A new algorithm for processing interferometric data-stacks: SqueeSAR. IEEE Transactions on Geoscience and Remote Sensing 49 (9), 3460-3470.

Ferretti, A., Perissin, D., Prati, C., Rocca, F., 2005. On the physical nature of SAR permanent scatterers. In: Proceedings of URSI Commission Symposium 2005, Ispra, Italy, 20-21 April, 6-11.

Ferretti, A., Prati, C., Rocca, F., 2000. Nonlinear subsidence rate estimation using permanent scatterers in differential SAR interferometry. IEEE Transactions on Geoscience and Remote Sensing 38 (5), 2202-2212.

Ferretti, A., Prati, C., Rocca, F., 2001. Permanent scatterers in SAR interferometry. IEEE Transactions on Geoscience and Remote Sensing 39 (1), 8-20.

Fornaro, G., Franceschetti, G., Lanari, R., 1996. Interferometric SAR phase unwrapping using Green's formulation. Geoscience and Remote Sensing, IEEE Transactions on Geoscience and Remote Sensing 34 (3), 720-727.

Fornaro, G., Pauciullo, A., Reale, D., 2011. A null-space method for the phase unwrapping of multitemporal SAR interferometric stacks. IEEE Transactions on Geoscience and Remote Sensing 49 (6), 2323-2334.

Fornaro, G., Reale, D., Serafino, F., 2009. Four-dimensional SAR imaging for height estimation and monitoring of single and double scatterers. IEEE Transactions on Geoscience and Remote Sensing 47 (1), 224-237.

Ghiglia, D., Romero, L., 1994. Robust two-dimensional weighted and unweighted phase unwrapping that uses fast transforms and iterative methods. Journal of Optical Society of America A, 11 (1), 107-117.

Goel, K., Adam, N., 2011. High resolution differential interferometric stacking via adaptive spatial phase filtering. In: Proceedings of IEEE International Geoscience and Remote Sensing Symposium, IGARSS 2011, Vancouver, Canada, 24-29 July, 1341-1344.

Goel, K., Adam, N., Minet, Christian, 2011. Long term analysis of strong non-linear deformations induced by coal mining using the SBAS technique. In: Proceedings of ESA FRINGE Workshop 2011, Frascati, Italy, 19-23 September, on CD.

Goel, K., Adam, N., 2012a. An advanced algorithm for deformation estimation in non-urban areas. ISPRS Journal of Photogrammetry and Remote Sensing 73, 100-110.

Goel, K., Adam, N., 2012b. High resolution deformation time series estimation for distributed scatterers using TerraSAR-X data. ISPRS Annals of the Photogrammetry, Remote Sensing and Spatial Information Sciences, XXII ISPRS Congress, Commission VII, Melbourne, Australia, 25 August-01 September 2012, I-7, 29-34, Copernicus Publications.

Goel, K., Adam, N., 2012c. Three-dimensional positioning of point scatterers based on radargrammetry. IEEE Transactions on Geoscience and Remote Sensing 50 (6), 2355-2363.

Goel, K., Adam, N., 2012d. Deformation estimation via object adaptive phase filtering and L1-norm based SBAS technique. In: Proceedings of IEEE International Geoscience and Remote Sensing Symposium, IGARSS 2012, Munich, Germany, 22-27 July, 4014-4017.

Goel, K., Adam, N., 2013a. A distributed scatterer interferometry approach for precision monitoring of known surface deformation phenomena. IEEE Transactions on Geoscience and Remote Sensing PP (99), 1-15, DOI: 10.1109/TGRS.2013.2289370

Goel, K., Adam, N., 2013b. Fusion of monostatic/bistatic InSAR stacks for urban area analysis via distributed scatterers. IEEE Geoscience and Remote Sensing Letters PP (99), 1-5, DOI: 10.1109/LGRS.2013.2278204.

Goel, K., Adam, N., 2013c. Advanced stacking of TerraSAR-X and TanDEM-X data in complex urban areas. Proceedings of Joint Urban Remote Sensing Event, JURSE 2013, Sao Paulo, Brazil, 21-23 April, 115-118.

Goldstein, R., Zebker, H., Werner, C., 1988. Satellite radar interferometry: Two-dimensional phase unwrapping. Radio Science 23 (4), 713-720.

Golub, G., Loan, C., 1996. Matrix Computations. John Hopkins University Press.

Goodman, J., 1976. Some fundamental properties of speckle. Journal of the Optical Society of America A 66 (11), 1145-1150.

Hanssen, R., 1998. Atmospheric heterogeneities in ERS tandem SAR interferometry. Delft University Press.

Hanssen, R., 2001. Radar interferometry: Data interpretation and error analysis. Kluwer.

Hooper, A., Zebker, H., Segall, P., Kampes, B., 2004. A new method for measuring deformation on volcanoes and other natural terrains using InSAR persistent scatterers. Geophysical Research Letters 31 (23), L23611, 1-5.

Isard, M., Blake, A., 1998. CONDENSATION- Conditional density propagation for visual tracking. International Journal of Computer Vision 29 (1), 5-28.

Just, D., Bamler, R., 1994. Phase statistics of interferograms with applications to synthetic aperture radar. Applied Optics, 33 (20), 4361-4368.

Kampes, B., 2006. Radar interferometry: Persistent scatterer technique. Springer.

Kass, R., Raftery, A., 1995. Bayes factors. Journal of the American Statistical Association 90 (430), 773-795.

Krieger, G., Moreira, A., Fiedler, H., Hajnsek, I., Younis, M., Werner, M., Zink, M., 2007. The TanDEM-X mission: A satellite formation for high resolution SAR interferometry. IEEE Transactions on Geoscience and Remote Sensing 45 (11), 3317-3341.

Lachaise, M., Eineder, M., Fritz, T., 2007. Multi baseline SAR acquisition concepts and phase unwrapping algorithms for the TanDEM-X mission. In: Proceedings of IEEE International Geoscience and Remote Sensing Symposium, IGARSS 2007, Barcelona, Spain, 23-27 July, 5272-5276.

Lanari, R., Mora, O., Manunta, M., Mallorquí, J., Berardino, P., Sansosti, E., 2004. A small baseline approach for investigating deformations on full resolution differential SAR interferograms. IEEE Transactions on Geoscience and Remote Sensing 42 (7), 1377-1386.

Lauknes, T., Zebker, H., Larsen, Y., 2011. InSAR deformation time series using an L1-norm small-baseline approach. IEEE Transactions on Geoscience and Remote Sensing 49 (1), 536-546.

Leijen, F., Hanssen, R., 2007. Persistent scatterer density improvement using adaptive deformation models. In: Proceedings of IEEE International Geoscience and Remote Sensing Symposium, IGARSS 2007, Barcelona, Spain, 23-27 July, 2102-2105.

Li, F., Goldstein, R., 2002. Studies of multibaseline spaceborne interferometric synthetic aperture radars. IEEE Transactions on Geoscience and Remote Sensing 28 (1), 88-97.

Lombardini, F., 2005. Differential tomography: A new framework for SAR interferometry. IEEE Transactions on Geoscience and Remote Sensing 43 (1), 37-44.

Massonnet, D., Feigl, K., 1998. Radar interferometry and its application to changes in the earth's surface. Reviews of Geophysics 36 (4), 441-500.

Massonnet, D., Rossi, M., Carmona, C., Adragna, F., Peltzer, G., Feigl, K., Rabaute, T., 1993. The displacement field of the Landers earthquake mapped by radar interferometry. Nature 364, 138-142.

Mora, O., Mallorqui, J., Broquetas, A., 2003. Linear and nonlinear terrain deformation maps from a reduced set of interferometric SAR images. IEEE Transactions on Geoscience and Remote Sensing 41 (10), 2243-2253.

Nash, S., 1982. Truncated-Newton methods. Doctoral dissertation, Stanford University, US.

Nelder, J., Mead, R., 1965. A simplex method for function minimization. The Computer Journal 7 (4), 308-313.

Papoulis, A., Pillai, S., 2002. Probability, random variables, and stochastic processes. McGraw-Hill.

Parizzi A., Brcic, R., 2011. Adaptive InSAR stacks multilooking exploiting amplitude statistics: A comparison between different techniques and practical results. IEEE Geoscience and Remote Sensing Letters 8 (3), 441-445.

Pepe, A., Lanari, R., 2006. On the extension of the minimum cost flow algorithm for phase unwrapping of multitemporal differential SAR interferograms. IEEE Transactions on Geoscience and Remote Sensing 44 (9), 2374-2383.

Perski, Z., Hanssen, R., Wojcik, A., Wojciechowski, T., 2009. InSAR analyses of terrain deformation near the Wieliczka Salt Mine, Poland. Engineering Geology 106 (1), 58-67.

Pettitt, A., 1976. A two-sample Anderson–Darling rank statistic. Biometrika 63 (1), 161-168.

Powell, M., 1964. An efficient method for finding the minimum of a function of several variables without calculating derivatives. The Computer Journal 7 (2), 155-162.

Raucoules, D., Maisons, C., Carnec, C., Le Mouelic, S., King, C., Hosford, S., 2003. Monitoring of slow ground deformation by ERS radar interferometry on the Vauvert salt mine (France): Comparison with ground-based measurement. Remote Sensing of Environment 88 (4), 468-478.

Raggam, H., Gutjahr, K., Perko, R., Schardt, M., 2010. Assessment of the stereo-radargrammetric mapping potential of TerraSAR-X multibeam spotlight data. IEEE Transactions on Geoscience and Remote Sensing 48 (2), 971-977.

Reigber, A., Moreira, A., 2000. First demonstration of airborne SAR tomography using multibaseline L-band data. IEEE Transactions on Geoscience and Remote Sensing 38 (5), 2142-2152.

Rocca, F., 2004. Diameters of the orbital tubes in long-term interferometric SAR surveys. IEEE Geoscience and Remote Sensing Letters 1 (3), 224-227.

Rodriguez-Gonzalez, F., Bhutani, A., Adam, N., 2011. L1 network inversion for robust outlier rejection in persistent scatterer interferometry. In: Proceedings of IEEE International Geoscience and Remote Sensing Symposium, IGARSS 2011, Vancouver, Canada, 24-29 July, 75-78.

Rosen, P., Hensley, S., Joughin, I., Li, F., Madsen, S., Rodriguez, E., Goldstein, R., 2000. Synthetic Aperture Radar Interferometry. Proceedings of the IEEE 88 (3), 333-382.

Schreier, G. (Ed.), 1993. SAR geocoding: Data and systems. Wichmann.

Sivia D., Skilling, J. 2006. Data analysis: A Bayesian tutorial. Oxford University Press.

Soergel, U., Michaelsen, E., Thiele, A., Cadario, E., Thoennesse, U., 2009. Stereo analysis of high-resolution SAR images for building height estimation in cases of orthogonal aspect directions. ISPRS Journal of Photogrammetry and Remote Sensing 64 (5), 490-500.

Soumekh, M., 1999. Synthetic aperture radar signal processing. John Wiley and Sons.

Spreckels, V., 2000. Monitoring of coal mining subsidence by HRSC-A data. In: International Archives of Photogrammetry and Remote Sensing, XIX ISPRS Congress, Commission VII, Amsterdam, The Netherlands, 16-23 July, XXXIII-B7, 1452-1458.

Thiele, A., Cadario, E., Schulz, K., Thonnessen, U., Soergel, U., 2007. Building recognition from multi-aspect high-resolution InSAR data in urban areas. IEEE Transactions on Geoscience and Remote Sensing 45 (11), 3583-3593.

Touzi, R., Lopes, A., Bruniquel, J., Vachon P., 1999. Coherence estimation for SAR imagery. IEEE Transactions on Geoscience and Remote Sensing 37 (1), 135-149.

Wang, Y., Zhu, X., Bamler, R., 2012. Retrieval of phase history parameters from distributed scatterers in urban areas using very high resolution SAR data. ISPRS Journal of Photogrammetry and Remote Sensing 73, 89-99.

Wilkinson, A., 1999. Synthetic aperture radar interferometry: A statistical model for layover areas. In: Proceedings of IEEE International Geoscience and Remote Sensing Symposium, IGARSS 1999, Hamburg, Germany, 28 June-2 July, 2392-2394.

Zan, F., 2008. Optimizing SAR interferometry for decorrelating scatterers. Doctoral dissertation, Politecnico di Milano, Italy.

Zebker, H., Chen, K., 2005. Accurate estimation of correlation in InSAR observations. IEEE Geoscience and Remote Sensing Letters 2 (2), 124-127.

Zebker, H., Goldstein, R., 1986. Topographic mapping from interferometric synthetic aperture radar observations. Journal of Geophysical Research 91 (B5), 4993-4999.

Zebker, H., Rosen, P., Goldstein, R., Gabriel, A., Werner, C., 1994. On the derivation of coseismic displacement fields using differential radar interferometry: The Landers earthquake. Journal of Geophysical Research: Solid Earth 99 (B10), 19617-19634.

Zebker, H., Villasenor, J., 1992. Decorrelation in interferometric radar echoes. IEEE Transactions on Geoscience and Remote Sensing 30 (5), 950-959.

Zhu, X., 2011. Very high resolution tomographic SAR inversion for urban infrastructure monitoring - A sparse and nonlinear tour. Doctoral dissertation, Technische Universitaet Muenchen, Germany.

Zhu, X., Bamler, R., 2010a. Very high resolution spaceborne SAR tomography in urban environment. IEEE Transactions on Geoscience and Remote Sensing 48 (12), 4296-4308.

Zhu, X., Bamler, R., 2010b. Tomographic SAR inversion by L1 norm regularization - The compressive sensing approach. IEEE Transactions on Geoscience and Remote Sensing 48 (10), 3839-3846.

Zhu, X., Bamler, R., 2011. Let's do the time warp: Multicomponent nonlinear motion estimation in differential SAR tomography. IEEE Geoscience and Remote Sensing Letters 8 (4), 735-739.